Year : 2022

Sub-Quaternary Himalayan tectonics inferred from luminescence thermochronometry

Bouscary Chloé

Bouscary Chloé, 2022, Sub-Quaternary Himalayan tectonics inferred from luminescence thermochronometry

Originally published at : Thesis, University of Lausanne

Posted at the University of Lausanne Open Archive http://serval.unil.ch
Document URN : urn:nbn:ch:serval-BIB_ABA730EAC5515

UNIL | Université de Lausanne

Faculté des Géosciences et de l'Environnement (FGSE)
Institut des Dynamiques de la Surface Terrestre (IDyST)
Université de Lausanne

SUB-QUATERNARY HIMALAYAN TECTONICS INFERRED FROM LUMINESCENCE THERMOCHRONOMETRY

Thèse de doctorat

présentée à la Faculté des Géosciences et de l'Environnement de l'Université de Lausanne, pour l'obtention du grade de Docteure en Sciences de la Terre par

Chloé Bouscary

Master / Diplôme d'ingénieur de l'École Nationale Supérieure en Environnement, Géoressources et Ingénierie du Développement durable de l'INstitut Polytechnique de Bordeaux – ENSEGID - Bordeaux INP, France

Directrice de thèse

Prof. Dr. Georgina E. King, University of Lausanne, CH

Jury

Présidente: Prof. Dr. Marie-Elodie Perga, University of Lausanne, CH
Expert interne: Prof. Dr. Frédéric Herman, University of Lausanne, CH
Expert interne: Prof. Dr. György Hetényi, University of Lausanne, CH
Expert externe: Prof. Dr. Jean-Louis Mugnier, University of Grenoble, FR
Expert externe: Prof. Dr. Edwards Rhodes, University of Sheffield, UK

LAUSANNE
2022

UNIL | Université de Lausanne

Faculté des Géosciences et de l'Environnement (FGSE)
Institut des Dynamiques de la Surface Terrestre (IDyST)
Université de Lausanne

SUB-QUATERNARY HIMALAYAN TECTONICS INFERRED FROM LUMINESCENCE THERMOCHRONOMETRY

Thèse de doctorat

présentée à la Faculté des Géosciences et de l'Environnement de l'Université de Lausanne, pour l'obtention du grade de Docteure en Sciences de la Terre par

Chloé Bouscary

Master / Diplôme d'ingénieur de l'École Nationale Supérieure en Environnement, Géoressources et Ingénierie du Développement durable de l'INstitut Polytechnique de Bordeaux – ENSEGID - Bordeaux INP, France

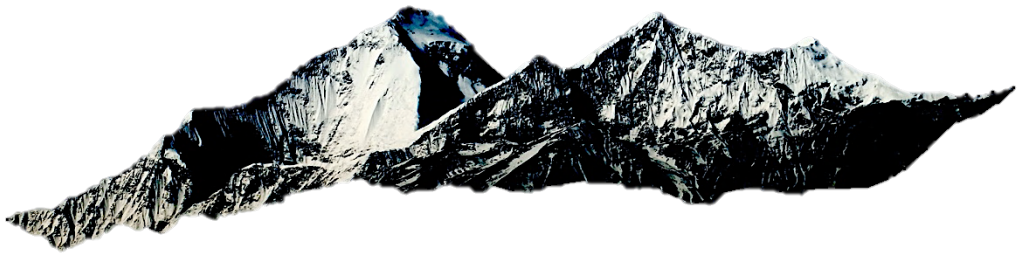

Jury

Directrice de thèse	Prof. Dr. Georgina E. King	Université de Lausanne, CH
Présidente du jury	Prof. Dr. Marie-Elodie Perga	Université de Lausanne, CH
Expert interne	Prof. Dr. Frédéric Herman	Université de Lausanne, CH
Expert interne	Prof. Dr. György Hetényi	Université de Lausanne, CH
Expert externe	Prof. Dr. Jean-Louis Mugnier	Université de Grenoble, FR
Expert externe	Prof. Dr. Edwards Rhodes	University of Sheffield, UK

Lausanne, 2022

UNIL | Université de Lausanne
Faculté des géosciences et de l'environnement
bâtiment Géopolis bureau 4631

IMPRIMATUR

Vu le rapport présenté par le jury d'examen, composé de

Présidente de la séance publique :	Mme la Professeure Marie-Elodie Perga
Présidente du colloque :	Mme la Professeure Marie-Elodie Perga
Directrice de thèse :	Mme la Professeure Georgina King
Rapporteur de thèse :	M. le Professeur Frédéric Herman
Expert interne :	M. le Professeur György Hetényi
Expert externe :	M. le Professeur Jean-Louis Mugnier
Expert externe :	M. le Professeur Edwards Rhodes

Le Doyen de la Faculté des géosciences et de l'environnement autorise l'impression de la thèse de

Madame Chloé BOUSCARY

Titulaire d'un
Master of Science
de l'ENSEGID à Bordeaux

intitulée

SUB-QUATERNARY HIMALAYAN TECTONICS INFERRED FROM LUMINESCENCE THERMOCHRONOMETRY

Lausanne, le 9 décembre 2022

Pour le Doyen de la Faculté des géosciences et de l'environnement

Professeure Marie-Elodie Perga

Year : 2022

SUB-QUATERNARY HIMALAYAN TECTONICS INFERRED FROM LUMINESCENCE THERMOCHRONOMETRY

Chloé Bouscary

Bouscary Chloé, 2022, Sub-Quaternary Himalayan tectonics inferred from luminescence thermochronometry

Originally published at: Thesis, University of Lausanne

Posted at the University of Lausanne Open Archive http://serval.unil.ch
Document URN:

“The more detours you encounter, the more paths you discover.”

— Anonymous

"C’est le temps que tu as perdu pour ta rose qui fait ta rose si importante."

— Le Petit Prince, Antoine de Saint-Exupéry

Acknowledgements

This has been a long journey, following the meanders of research, through the multiple peaks and abysses of PhD life. This introspective journey, sometimes experienced as a solitary adventure, and sometimes as a travel accompanied by friends, family, and colleagues, helped me grow and become the scientist that I am today.

Firstly, I would like to thank my supervisor, **Georgina King**, for the opportunity she gave me to conduct this research on the Himalayas, for her guidance, intellectual support, and feedbacks. Thanks for your patience and scientific enthusiasm.

This work has also benefited from insightful scientific discussions with **Frédéric Herman**, **György Hetényi**, **Jérôme Lavé**, **Djordje Grujic**, **Rafael Almeida**, and all the other researchers that I met during my time in Bern and Lausanne, and at conferences. Thank you!

I am also really grateful to the students who helped me in the lab. This PhD would not have been possible without you. Thanks **Sebastian Schaller**, **Sébastien de Meris**, and **Keyvan Diba**, I could not have prepared all my ~100 samples on my own and finished this PhD on time. And also thank you to **Shiba Subedi**, **Kristel Chanard**, **Ananta Gajurel**, and **Jérôme Lavé**, who took the time to accompany me in the field in Nepal to collect my samples.

Special thanks also go to my thesis committee for taking the time to read my work and for coming to my private PhD defence, for inspiring questions and the interesting discussions afterwards.

On a more personal note, I am also really lucky to have good friends and family which have been constantly encouraging, motivating, and cheering me in all situations. Merci! Thank you! Danke! Grazie!

To the **sweet Powerpuff girls of office 3151**, our moral support office plants (or at least the ones that survived Covid), and to all my **Lausanne friends**, thanks for your friendship and moral support. I especially want to thank **Joanne Elkadi**, my PhD sister, almost twin, who has showered me with kindness over the past 5 years, you are the best 'girl in my office' that anyone could ask for. And **Xiaoxia Wen**, thanks a lot for being a really good friend, for the climbing, the hiking, the skiing, the ice-skating …

To my Lausanne family: **'La Coloc'**, les actuels et les immortels: **Philibert**, **Armand**, **Steve**, **Lea**, **Marie-Louise et Clemens** ... Mon Repos 38 a été un havre de paix, mon expérience de thèse en Suisse n'aurait pas été la même sans vous. Merci !

Marine 'Maurice' Guichard, tu es là depuis mon premier terrain en géologie lorsque nous étions au lycée, et tu es restée malgré tous les cailloux que je te ramenais des différents endroits que je visitais. Je ne sais comment te remercier pour tout le soutien moral que tu m'as apporté au cours de ces dernières années. Merci beaucoup !
Rémi Bérard, **Coline Ariagno**, **Philippe Razin** et bien d'autres, je vous remercie de m'avoir accompagné et soutenu durant mes années d'étude, et encore après. Merci pour votre amitié.

I am also grateful to have found really good friends/family in Bern. **Fabio 'Pablo' Magrani**, obrigado for sharing my craziness, and all those late nights doing puzzles, fighting Peperoni gelb (R.I.P.), crawling below museum exhibitions, building ice-igloos ... **Julien Reynes**, milles merci pour les soirées vin-fromage-gaufres, et les parties interminables de Carcassonne, et pour nos explorations du patrimoine français et des montagnes suisses. **Tito Arosio**, grazie pour ton amitié, pour les soirées à parler de tout et de rien, et pour le Braulio.
To **Alessandro 'Sandro' Maltese**, vielen Dank d'avoir été patient et de m'avoir soutenu et réconforté dans les moments de frustration, et d'avoir partagé mon enthousiasme et mon excitation dans les moments de succès. Merci aussi pour les moments de détente, d'escalade, de randonnées, de jeux de société … de vie. Grazie mille!

Je dois également un grand merci à **mes parents** et à **ma famille** pour avoir contribué au développement de mon amour pour la Nature et la montagne, pour avoir supporté mes choix professionnels, et pour avoir été d'un soutien indéfectible tout au long de ma thèse.

Lastly, I express my hearty thanks to those whom I might have missed to mention by name, who helped directly and indirectly throughout all these years.

Thank you all for accompanying me on this adventure, I look forward to the next one!

Chloé Bouscary
Lausanne, 2022

"Je suis le pâtre des montagnes, j'aime l'air pur et la liberté." — Interprétation d'Emile Bouscary.

Synopsis

La chaîne de montagnes de l'Himalaya est le résultat de la collision continentale entre l'Inde et l'Eurasie. La convergence entre les deux plaques tectoniques a généré des stresses qui ont éventuellement conduit à la cassure de la croûte terrestre en différents fragments et blocs bougeant les uns relativement aux autres le long de plans de failles sub-métriques à pluri-kilométriques. Dans un orogène compressif comme l'Himalaya, le glissement le long de plans de faille légèrement inclinés, appelés chevauchements, amène les blocs sus-jacents (séries chevauchantes) à se déplacer au-dessus des blocs inférieurs (séries chevauchées). La plupart des failles produisent des déplacements répétés au cours des temps géologiques. Lorsque la contrainte accumulée le long des plans de faille dépasse un certain seuil, un glissement soudain se produit, libérant des ondes d'énergie qui se traduisent par des tremblements de terre. Comprendre la structure et l'évolution des failles et chevauchements permet de mieux déterminer et contraindre l'occurrence d'une telle activité sismique, également responsable de la formation de glissements de terrain, éboulements, chutes de pierres, coulées de boue et tsunamis.

Au Népal, le tremblement de terre de Gorkha en 2015, qui a causé de nombreux ravages et pertes en vies humaines, a révélé certaines lacunes dans notre compréhension de la tectonique de l'Himalaya, notamment sur la connaissance de la tectonique Quaternaire (derniers 2,6 millions d'années). En effet, peu de techniques actuelles permettent de résoudre les déformations de la Terre en surface et sub-surface sur cette échelle de temps.

La thermochronométrie par luminescence est une nouvelle méthode développée dans les quinze dernières années, qui permet de contraindre l'histoire de refroidissement des roches lorsqu'elles remontent vers la surface depuis les profondeurs de la Terre plus chaudes. L'avantage de cette méthode est que la luminescence est la seule technique sensible à des températures entre 30 et 100 °C, permettant d'avoir des informations cruciales sur le parcours des roches au cours des derniers 300 milles ans, sur les derniers kilomètres de leur parcours vers la surface terrestre. Ces indications sur les changements de températures vécus par la roche au cours du temps permettent de retracer les mouvements de la surface terrestre, que ce soit dû à l'érosion par le climat ou à des mouvements tectoniques, i.e. des mouvements de failles.

En me basant sur les données de thermochronométrie par luminescence recueillies lors de ma thèse, je propose d'améliorer la précision des modèles tectoniques (étude des structures géologiques et de leurs déformations) en reconstruisant l'histoire des mouvements des failles népalo-himalayennes au cours du Quaternaire récent (derniers 200 milles ans). Cela permettra à terme d'avoir une meilleure compréhension de l'évolution temporelle et spatiale des systèmes de failles himalayens, et fournira des informations cruciales sur l'activité sismique des failles népalaises au Quaternaire, permettant l'amélioration des modèles d'aléa sismique.

Dans cette thèse, un nouveau jeu de plus de 100 échantillons de roches de l'Himalaya, répartis sur le sud de la chaîne himalayenne entre l'ouest du Népal et l'est du Bhutan, et aussi le long de quatre vallées du Haut-Himalaya népalais aux alentours des sommets de l'Annapurna et du Ganesh, a permis de contraindre les déformations liées à la convergence himalayenne depuis plus de 200 milles ans. Ces taux d'exhumation ont permis de démontrer que bien que les failles de la chaine himalayenne soient actives au sud de l'Himalaya, des mouvements sont aussi enregistrés dans le Haut-Himalaya, ce qui pourrait démontrer une activité tectonique de la faille centrale himalayenne (MCT), mettant potentiellement en danger toute une population.

Contents

Abstract

A system of successively forming north-dipping crustal-scale thrusts, extending along the Himalayan arc, and merging at depth into the Main Himalayan Thrust (MHT), have accommodated most of the convergence between the Indian and Eurasian tectonic plates since at least the early Miocene. While deformation of the Himalayan fold-and-thrust belt is well documented over recent ($\leq 10^2$ yr), Holocene ($10^{3\text{-}4}$ yr) and Myr ($\geq 10^6$ yr) timescales, almost no quantitative data are available to constrain sub-Quaternary ($10^{4\text{-}5}$ yr) deformation, despite the proposal that deformation rates vary episodically over geological timescales and that there is out-of-sequence activity of some faults. Filling this timescale gap is thus crucial to better understand Himalayan tectonics that underpin seismic hazard models in this densely populated region.

In this PhD thesis, I first start by optimising and validating the luminescence thermochronometry method, in order to be able to have accurate constrains on rock thermal history. I then present an extensive new dataset of more than 100 luminescence thermochronometry samples to provide a new perspective on Late Pleistocene exhumation (timescales of 10^4 to 10^5 years), a timescale until now largely inaccessible to other techniques, by offering high-resolution constraints of rock cooling histories within the upper kilometres of the Earth's crust. The samples, distributed across the hinterland (High Himalaya) and the foothills (Sub-Himalaya) of the Himalayas, were specifically selected to resolve deformation across the main geological structures shaping the Himalayan orogen, namely the Main Frontal Thrust (MFT), and the Main Central Thrust (MCT).

Results show that although the faults of the Sub-Himalayan fold-and-thrust belt are active during the late Quaternary, movements are also recorded in the High Himalayas on the same timescale, which may indicate tectonic activity of the Main Central Thrust (MCT), potentially endangering an entire population.

Keywords: Himalaya, Tectonics, Thrust, Quaternary, Luminescence thermochronometry

Résumé

Un système de chevauchements successifs à pendage nord, s'étendant le long de l'arc himalayen et fusionnant en profondeur avec le chevauchement principal de l'Himalaya (MHT), a accommodé la majeure partie de la convergence entre les plaques tectoniques indienne et eurasienne depuis au moins le début du Miocène. Bien que les déformations de la ceinture de plis et de chevauchements himalayenne soient bien documentées sur les échelles de temps récentes ($\leq 10^2$ ans), Holocène (10^{3-4} ans), et sur des millions d'années ($\geq 10^6$ ans), presque aucune donnée quantitative n'est disponible pour contraindre les déformations sous-Quaternaires (10^{4-5} ans), malgré la proposition selon laquelle les taux de déformation varient épisodiquement sur les échelles de temps géologiques et qu'il existe une activité hors séquence de certaines failles. Combler cet écart temporel est donc crucial pour mieux comprendre la tectonique himalayenne qui entre dans la composition des modèles d'aléa sismique dans cette région densément peuplée.

Dans cette thèse, je commence d'abord par optimiser et valider la méthode de thermochronométrie par luminescence, afin de pouvoir contraindre précisément l'histoire thermique des roches. Je présente ensuite un nouveau jeu de données de plus de 100 échantillons de thermochronométrie par luminescence afin d'avoir une nouvelle perspective sur l'exhumation du Pléistocène supérieur (échelles de temps de 10^4 à 10^5 ans), une échelle de temps jusqu'à présent largement inaccessible aux autres techniques, le but étant d'avoir une contrainte haute résolution de l'histoire de refroidissement des roches dans les kilomètres supérieurs de la croûte terrestre. Les échantillons, répartis dans l'arrière-pays (Haut Himalaya) et l'avant-pays (Sous-Himalaya) de l'Himalaya, ont été spécifiquement sélectionnés pour résoudre les déformations des principales structures géologiques façonnant l'orogène himalayen, à savoir le chevauchement frontal himalayen (MFT) et le chevauchement central himalayen (MCT).

Les résultats montrent que bien que les failles de la ceinture de plis et chevauchements sous-himalayenne soient actives à la fin du Quaternaire, des mouvements sont également enregistrés dans le Haut Himalaya à la même échelle de temps, pouvant indiquer une activité tectonique de la faille centrale himalayenne (MCT), mettant potentiellement en danger toute une population.

Mots clés : Himalaya, Tectonique, Chevauchement, Quaternaire, Thermochronométrie par luminescence

Introduction

1. General introduction

The Earth is in constant movement. Interactions between tectonics, erosion, and climate shape our landscapes and are key factors in the formation of orogens (Molnar and England, 1990; Reiners et al., 2003; Whipple, 2009; Champagnac et al., 2012). Thermochronometry, the quantification of the thermal history of rocks as they exhume from depth to the Earth's surface, is a set of methods that is often used to understand the interplay between tectonic uplift and erosion (e.g., Willett and Brandon, 2002; Finnegan et al., 2008; Whipple, 2009; Fox et al., 2015). In this thesis, the newly developed luminescence thermochronometry method is used to resolve exhumation over sub-Quaternary timescales in the Himalayas; to gain a better understanding of tectonics, earth surface processes and landscape evolution, focusing on active mountainous regions.

Most thermochronometric applications involve quantification of cooling that happens as rocks move towards the Earth's surface. This cooling rate depends on the local geothermal gradient of the Earth's crust (below several kilometres, the thermal structure of the continental crust is primarily governed by radiogenic heat production, conduction of heat to the surface, and, in regions where the crust has vertical velocity, advection), and on the velocity at which the rocks exhume towards the surface, which depends on the dynamic balance between rock uplift and exhumation.

Different thermochronometric systems have different thermal sensitivities (Fig. 1), enabling the reconstruction of time-temperature histories over different crustal depths, allowing geomorphological and geological processes to be constrained on different timescales specific to their closure temperature. Only a few thermochronometers are able to constrain low-temperature paths (temperatures below ~120 °C) for the reconstruction of thermal histories within the upper first few kilometres of the Earth's crust (e.g., U-Th/He, $^{4}He/^{3}He$, ESR; e.g., Ault et al., 2019), offering the potential to study recent (Quaternary) landscape evolution. Luminescence thermochronometry (Herman et al., 2010; Li and Li, 2013; Guralnik et al., 2015a; King et al., 2016a; Herman and King, 2018) is a recently developed very-low-temperature thermochronometer with a high sensitivity to temperatures below ~120 °C. It has a very low closure temperature (~30-100 °C, depending on the signal) (Guralnik et al., 2013; King et al., 2016b) that offers the potential to resolve rock cooling, and thus exhumation, over timescales of 10^{3} to 10^{6} years, i.e. at sub-Quaternary timescales (Rhodes, 2011; Guralnik et al., 2013, 2015b; King et al., 2016a). The uniqueness of this technique, which fills the gap between the other existing thermochronometers for low temperature systems, allows the cooling histories of rocks to be constrained on km-spatial scales and 100-kyr timescales, allowing neotectonics and sub-Quaternary deformation (uplift rates, exhumation rates), feedbacks between glacial-interglacial climate fluctuations and catchment-scale erosion rates and fluvial downcutting during the Late Pleistocene-Holocene, etc., to be constrained.

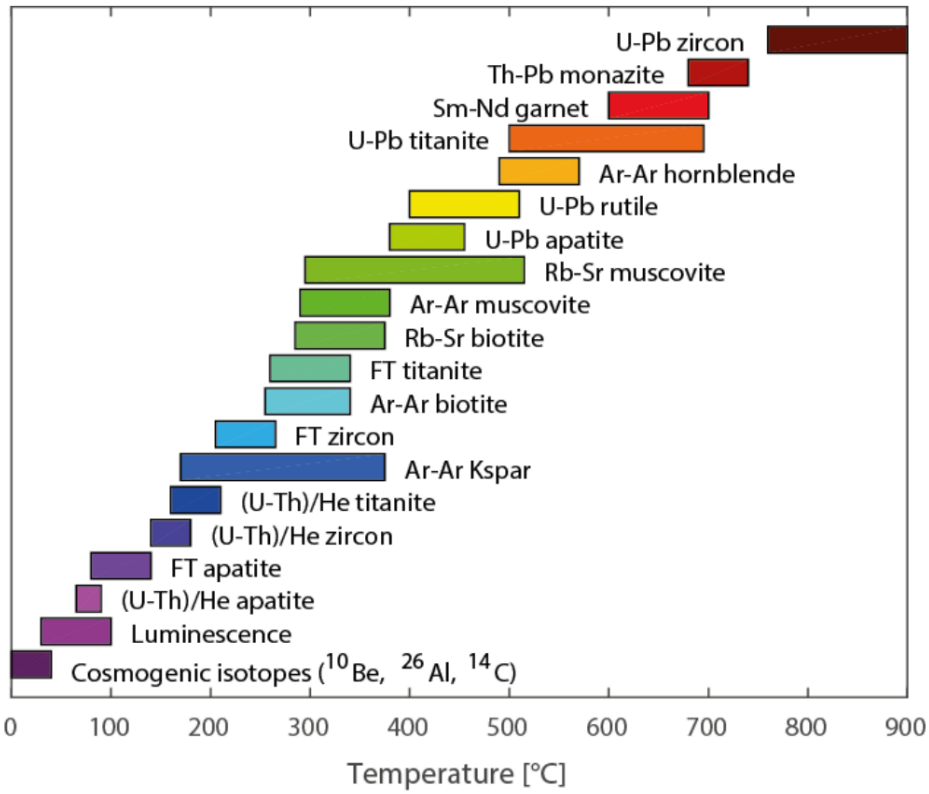

Fig. 1: *Different thermochronometric systems and their closure temperatures (Lambert, 2018). Each closure temperature range allows geologic questions to be resolved over different depths and timescales.*

This PhD thesis addresses the following objectives:

- **To optimize and validate the multi-luminescence thermochronometry method.**

- **To fill the temporal gap in geological constraint between Holocene and geologic data by constraining the recent thermal and exhumation history of the Sub-Himalayas and the High Himalayas on 100 kyr timescales using luminescence thermochronometry.**

- **To improve the Himalayan tectonic models for the sub-Quaternary, in order to increase knowledge on tectonics and the seismic cycle.**

The remainder of this introductory chapter will first present the Himalayas, their tectonic and structural evolution, and the open questions that are relevant to this thesis. Then a brief description of luminescence thermochronometry will be given, before presenting the area of study and the trajectory of this thesis dissertation.

2. The Himalayas

The Himalayan mountain range, stretching from the Brahmaputra to the Indus river in central Asia, is one of the most active intra-continental orogens in the world. It runs west-northwest to east-southeast in a southward-convex arc of ~2500 km length and 200-400 km width. It separates the plains of the Indian subcontinent in the south from the Tibetan Plateau in the north, and is situated between the Nanga Parbat syntaxis, Pakistan, in the west, and the Namche Barwa syntaxis, Tibet, in the east. The Himalayas has nine of the ten highest peaks in the world, including the highest: Mount Everest, culminating at 8848 m.

The Himalayan orogen is one of the youngest mountain range on the planet, and is still uplifting. Its formation is the result of compressional orogeny due to the continental collision between the Indian and the Eurasian tectonic plates, that started during the (Cenozoic) Paleocene - Early Eocene (Chirouze et al., 2012; Bernet et al., 2006; Mathew et al., 2013; Yin and Harrison, 2000). This collision caused intense crustal shortening and thickening, and the imbrication of southward-displaced thrust sheets, resulting in the formation of the Himalayan mountain belt and the Tibetan Plateau (Chirouze et al., 2012; Bernet et al., 2006; Hodges, 2000; Yin and Harrison, 2000). Today, the Himalayas is subdivided into four major lithotectonic units (Bernet et al., 2006; van der Beek et al., 2006; Hodges, 2000; Yin and Harrison 2000): the Tethyan Himalayan zone (TH), the Higher or Greater Himalayan zone (HH), the Lesser Himalayan zone (LH), and the Sub-Himalaya (SH). These units are separated by Late Cenozoic north-dipping crustal-scale faults systems: the South Tibetan Detachment system (STDS), the Main Central Thrust (MCT), the Main Boundary Thrust (MBT), and the Main Frontal Thrust (MFT), from north to south. All of these faults are branched on the main detachment overlying the underthrusted Indian plate, the Main Himalaya Thrust (MHT) (Yin and Harrison, 2000; Avouac, 2003) (Fig. 2).

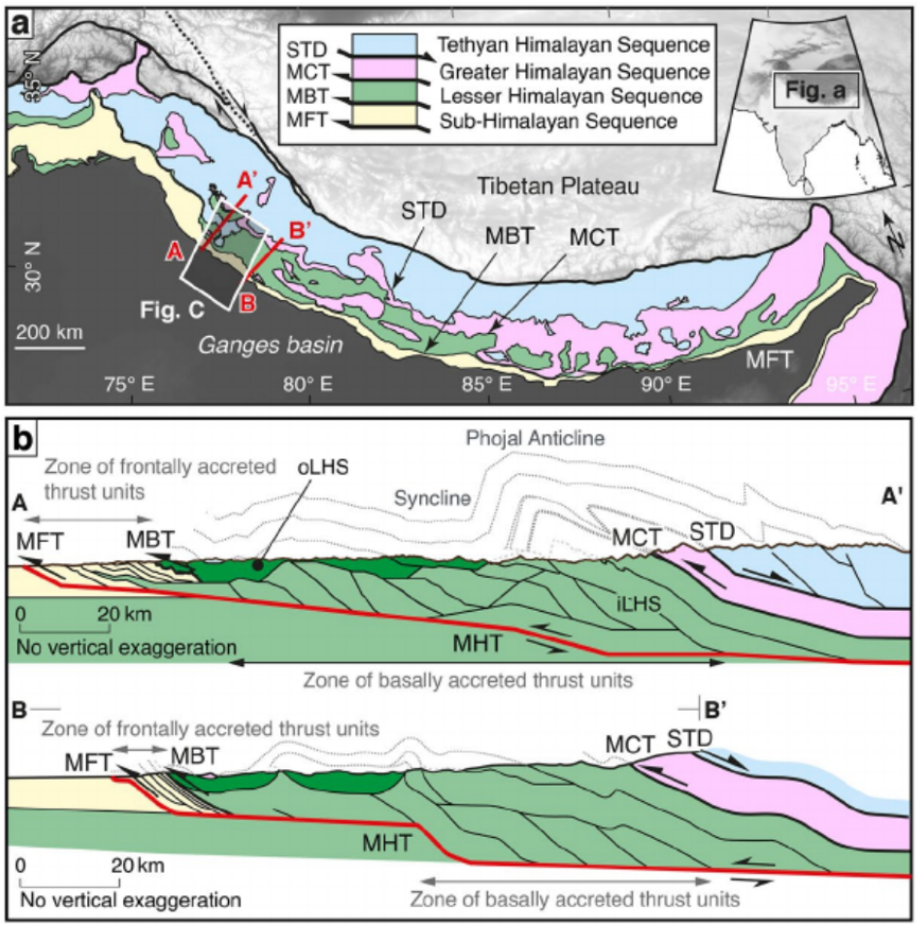

Fig. 2: ***A.*** *Simplified geological map of the Himalayas, showing major tectonostratigraphic units and faults. The inset shows the location of the Himalayas in Asia.* ***B.*** *Balanced structural cross sections along the A-A' and B-B' transects, modified from Srivastava and Mitra (1994) and Webb (2013). MFT, Main Frontal Thrust; MBT, Main Boundary Thrust; MCT, Main Central Thrust; STD, South Tibetan Detachment. MHT, Main Himalayan Thrust (from Mandal et al., 2021).*

2.1. Structural evolution of the Himalayas

Around 120-130 Ma ago, during the Early Cretaceous, what is now India broke off from the supercontinent of Gondwana (e.g., Metcalfe, 1996), and started migrating north, at about 10 to 15 cm/yr, progressively closing the Tethys Ocean by subduction beneath the Eurasian plate in an oceanic-continental convergence setting (e.g., O'Brien, 2001; Dhital, 2015). Most of the sediments of the Indian margin of the Tethysian ocean were scraped off and accreted onto the Eurasian continent as an accretionary wedge. Some of these sediments are now part of the Himalayan mountain range.

Around 60-50 Ma, during the Paleocene-Eocene, the rate of northward drift of the Indian continental plate slowed to around 4-6 cm/yr (e.g., Guillot et al., 2003; Molnar and Stock, 2009; Dhital, 2015) due to the subduction of the passive continental margin of India beneath the

active continental margin of Eurasia (Fig. 3). The collision between the Eurasian and Indian continental plates began, first in the west and then in the east (e.g., Rowley, 1996; De Sigoyer et al., 2000; Ding et al., 2005), completely closing the former Tethys Ocean (Indus Suture) and initiating the uplift of the Himalayas. From there on, the Himalayas are the product of ~55 million years of tectonic compression and structural deformation at the collision boundary between the Indian and Eurasian tectonic plates.

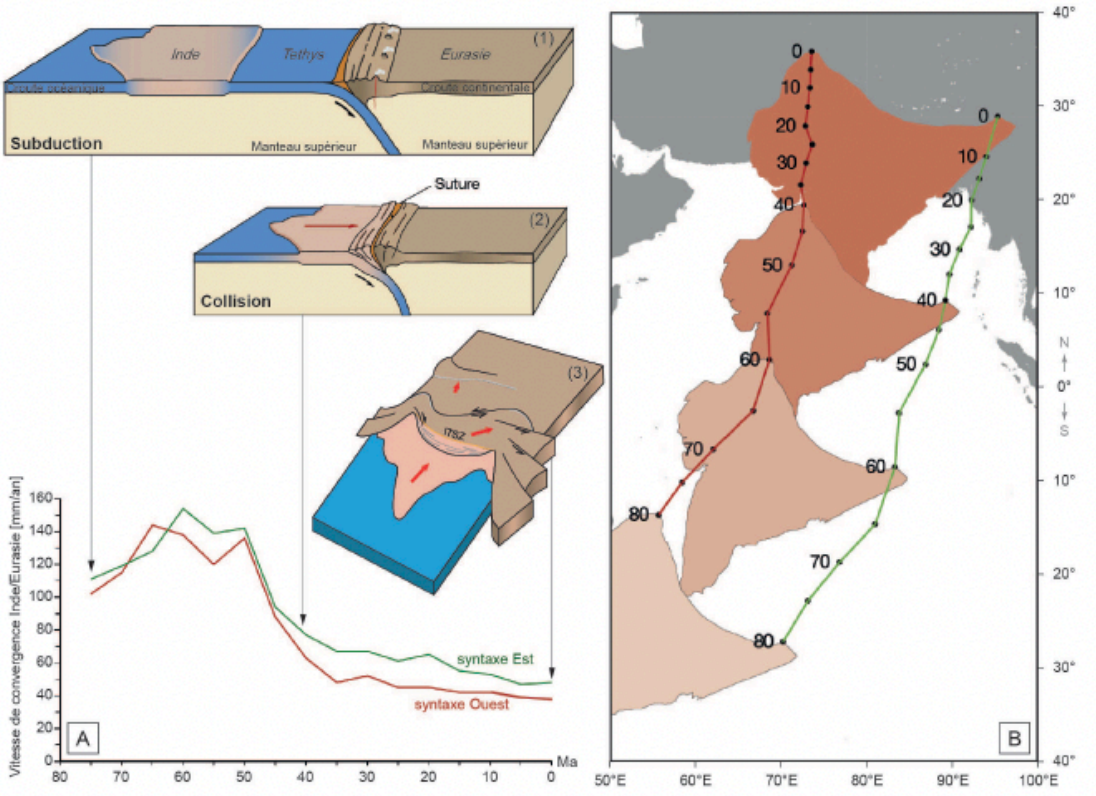

Fig. 3: *Convergence speed of India relative to Asia since ~80 Ma. The red and green lines in* ***A.*** *correspond respectively to the west and east syntaxis positions (west and east ends of the suture) shown in* ***B.*** *The geodynamic diagrams in A. illustrate (1) the oceanic subduction of the Tethys under the Asian continent (~80 Ma), (2) the entry into subduction of the Indian continental margin, and (3) the current India-Eurasia collision. (From Le Roux-Mallouf (2019), modified from Malavieille et al. (2002)).*

Between 55-35 Ma, a first mountain range, the Trans-Himalayan igneous arc, emerged, and tectonic deformation affected the Tethyan Himalaya. The emergence from the accretionary wedge and folding of these sediments occurred shortly after the India-Eurasia collision and continued for millions of years. Since the India-Asia collision occurred in a diachronous, oblique manner, the deformations first began in the north-western Himalayas (in Pakistan and Ladakh) around 55-45 Ma, and then affected the eastern parts of the Himalayas at around 35 Ma (Fig. 3).

During the early Miocene (24-17 Ma), the Higher Himalayan rocks began a rapid uplift along the MCT, after being metamorphosed and partially melted under temperatures of 600-800 °C and pressures of 6-10 kilobars at 20-25 km depth. Concurrent with the activity of the MCT, the Tethyan Himalayan zone was detached from the Higher Himalaya along the normal fault of the STDS, that forms the northern boundary of the Higher Himalaya. The STDS caused tectonic extension / spreading, gravitational gliding and back-folding of the Tethyan Himalayan sediments (down-thrown block), while the Higher Himalayan rocks (upthrown block) were uplifted and exhumed. At the same time, leucogranites were formed and rapidly uplifted along the upthrown edge of the STDS, indicating that their formation and exhumation to the surface was related to the activity of the fault. Furthermore, the slip on the MCT is more than 150 km and has transported the Higher Himalayan metamorphic rocks onto the Lesser Himalaya where they can nowadays be found as klippes.

During the Late Miocene (11-7 Ma), sedimentation rates in the Sub-Himalayas (Siwalik basin) drastically increased with the rapid erosion of the Himalayas. The MBT also began its activity during this period. By 10-7 Ma, the Himalayas had attained sufficient height to act as a topographic barrier and have an effect on climate circulation; the region began to experience seasonal monsoons. In addition to this, as a result of uplift, the Himalayas began to experience high altitude glaciation.

The Quaternary period (2.6-0 Ma) is an important renewed phase of tectonic uplift for the Himalayas. Some signs testify to intense neotectonic movements in the Himalayan region: presence of active faults and large earthquakes, geochronologic evidence of rapid erosion from various parts of the Higher Himalaya (young fission-track ages of 1-3 Ma, van der Beek et al., 2006), with deep and narrow gorges, uplift of the Sub-Himalayan fold-and-thrust belt (FTB) range (Siwalik foothills) along the MFT over the past few million years, with uplifted terraces of young sediments, and enormous amounts of coarse-grained fluvial sediments in the Quaternary record of the Himalayan foreland basins.

Today, the Indian plate continues to be driven horizontally at the Eurasian plate, which forces the Tibetan plateau and the Himalayas to continue to rise. The Indian plate is still moving at ~58-67 mm/yr. Approximately one-third of the present-day convergence-rate between India and Eurasia (i.e., ~12-23 mm/yr; e.g., Vernant et al., 2014; Stevens and Avouac, 2015; Bilham et al., 2017) is absorbed by thrusting along the Himalaya southern front, and leads to the Himalayas rising by about 5 mm/yr, making them geologically active. The movement of the Indian plate into the Asian plate also makes this region seismically active, leading to earthquakes (van der Beek et al., 2006).

2.2. Major tectonic subdivisions

The Himalayas can be divided into different major longitudinal zones or northwest-northeast trending belts, separated by north-dipping crustal-faults (Fig. 4):

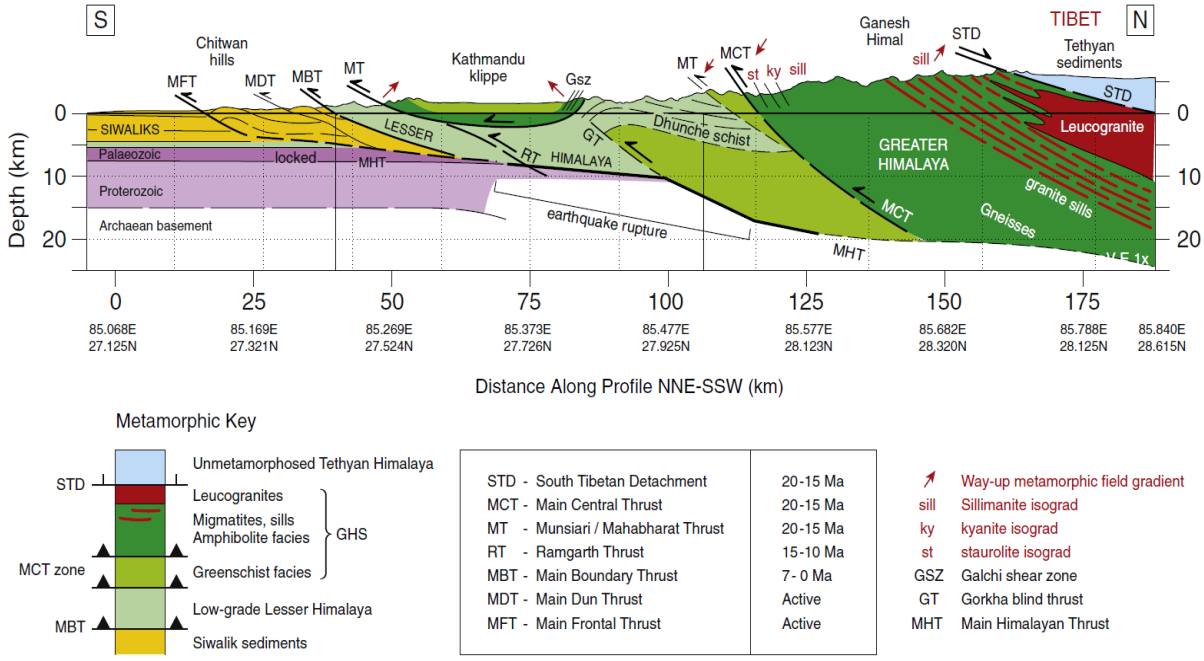

Fig. 4: *Geological cross-section of the Langtang-Kathmandu Himalayas showing major structural units, metamorphic grade, thrust faults and extent of the rupture during the 25th April 2015 Gorkha earthquake (Searle et al., 2017).*

- The northernmost section, the **Tethys Himalayan Zone**, is an approximately 100 km large synclinorium formed by strongly folded and imbricated sedimentary series. The stratigraphic succession of sediments in this zone can reach up to 12 km of thickness, and consists of fossiliferous Cambrian to Eocene marine sedimentary (sandstone, shale and limestone to low-grade metasedimentary rocks). These rocks are sediments that were deposited on the north-facing passive margin of the continental shelf of the Indian plate. Some klippes of ophiolite complexes with ultramafic-serpentinite and local volcanics represent the remnant of the abducted oceanic crust slab from the Indus-Tsangpo Suture zone. Within the Tethys Himalayan zone, there is also a series of dome-shaped structures made up of Cambrian granite gneiss or of Miocene white granites / leucogranites. These rocks and structural domes have been uplifted by the North Himalayan Thrust fault, situated at their base.

  The stratigraphic analyses of these sediments yield important indications on the geological history of the northern margin of the Indian continent from its Gondwanian evolution to its continental collision with Eurasia.

  The transition between the Tethys Himalaya and the Higher Himalaya can be progressive, but in many places, this transition zone is marked by a major extensional structure, the major normal fault of the South Tibetan Detachment System (STDS).

- The **Higher Himalaya (HH)** unit or Greater Himalayan Sequence (GHS) is a 10 to 30 km thick crystalline zone of medium- to high-grade metamorphic sequence of metasedimentary rocks and granitoids.
  These crystalline rocks represent the remobilization of the basement of the Indian crust (e.g., Hodge, 2000; Yin, 2000; Robinson et al., 2006; Dhital, 2015), and are made up of Late Proterozoic to early Cambrian metasedimentary rocks, kyanite-sillimanite bearing schist and paragneiss, as well as orthogneiss. These metasediments are frequently intruded by Ordovician and Lower Miocene granites / leucogranites. The metamorphic sequence shows a progressive metamorphism ranging from biotite to sillimanite grade.
  The South Tibetan Detachment System (STDS) constitutes the northern boundary of the Higher Himalaya, and along its southern boundary, the major nappe of the Higher Himalaya is thrust over the Lesser Himalaya along the Main Central Thrust (MCT).

- The **Lesser Himalaya (LH)** consists mainly of 10 to 20 km of Precambrian (Upper Proterozoic to Lower Cenozoic) clastic sediments and metasedimentary rocks (quartzite, marble, slate, phyllite, schist and gneiss), with minor volcanic and granitic rocks. The metamorphism in the Lesser Himalaya was less severe (lower temperatures) than for the Higher Himalayan metamorphic rocks. And, within the Lesser Himalaya, there is an inverted metamorphic grade, with lower grade metamorphic rocks to the south, overlain by higher-grade metamorphic rocks to the north, close to the MCT. This upward increase in metamorphism is related to deformation and/or heating in the footwall of the MCT and tectonic imbrications (Bernet et al., 2006).
  The Lesser Himalaya is bounded at the base, in the south, by the Main Boundary Thrust (MBT), which has uplifted the rocks for the Lesser Himalaya atop of the Sub-Himalayan rocks. The Higher Himalaya also often appears in isolated tectonic windows within the Lesser Himalaya Crystalline Sequence. These Higher Himalayan klippes were transported on the back of the MCT and isolated from the autochthone rocks.

- The **Sub-Himalaya (SH)** geographically corresponds to the Siwalik range in the Himalayan foreland. It forms the foothills of the Himalayan range and is essentially composed of the clastic sediments of the Siwalik Group, which consists of 5 to 19 km thick middle Miocene to Pliocene molassic siliciclastic foreland basin sediments (conglomerates, sandstones, and mudstones carried and deposited by rivers). These molasses are internally folded and imbricated.
  The Sub-Himalayan fold-and-thrust belt constitutes the active deformation front of the Himalayas and the deformed part of its Neogene foreland basin. This belt can be subdivided in two: a structurally simple outer belt - composed of laterally propagating

fault-bends or fault-propagation folds associated with the Main Frontal Thrust (MFT) and their hanging-wall synclines -, and a more complex inner belt - composed of a series of laterally relayed and transported thrust sheets (Mugnier et al., 1999; Champel et al., 2002; van der Beek et al., 2006).

The Sub-Himalayas of central Nepal started to uplift ~2.4-1.8 Ma (Mugnier et al., 2004) along high-angle reverse faults (some of which are still active), which are collectively termed the MFT. This fault system marks the boundary between the Sub-Himalaya in the north and the north Indian plain in the south. The Sub-Himalaya is thrusted along the MFT over the Quaternary alluvium deposited by the rivers coming from the Himalayas (Ganges, Indus, Brahmaputra...), which demonstrates that the Himalayas is still a very active orogen.

2.3. Main structural elements

From north to south, the Himalayan belt can be divided by four north-dipping main structural elements. All of these crustal-scale faults are branched on the **Main Himalayan Thrust (MHT)**, the main detachment overlying the underthrusted Indian plate, and representing the plate boundary between the Indian and Eurasian plates. The MHT extends below the Himalayan orogen from depths of 2-5 km beneath the foreland to more that 40 km below Tibet (e.g., Schelling, 1992; Power et al., 1998; Mugnier et al., 1999; Almeida et al., 2018), with a shallow dip of maximum 2-6°.

- The **South Tibetan Detachment System (STDS)** represents a major set of orogen-parallel normal faults and shear zones that strike the entire Himalayan orogen (e.g., Yin, 2006; Burg and Chen, 1984), at the boundary between the High Himalaya and the Tethys Himalaya. Deformations along this structure were accommodated either by dextral strike-slip or by extensional shearing. Various strands belonging to this structure have been identified and classified in different shear zones that each accommodate the deformation differently (structural detachment between the HH and the TH, ductile dextral strike-slip …).

- The **Main Central Thrust (MCT)** zone is one of the most important tectonic elements associated with the Himalayan orogen. This broad fault zone is currently defined by three different independent definitions. It can be defined as a metamorphic-rheological boundary, where the MCT is the thrust that marks a break in metamorphic grade between the higher-grade metamorphic rocks of the Higher Himalaya (hanging-wall), and the lower-grade metamorphic rocks of the Lesser Himalaya (footwall), the deformations along the MCT were mainly ductile (Heim and Gansser, 1939; Searle et al., 2008). The MCT zone can also be defined as an age of motion-structural boundary in which the MCT is the foreland-vergent thrust that was active in early to middle

Miocene time (Webb et al., 2013). The third MCT zone definition is as a protolith boundary-structural, with the MCT being the Cenozoic foreland-vergent thrust that juxtaposed the pre-latest Cretaceous Himalayan Assemblage A and B, at a high strain zone and protolith boundary (Martin, 2017). Depending on which definition of the MCT is taken by authors, and due to along-strike variations in geology, the location and width of the MCT can vary up to several kilometres (Long et al., 2016; Gibson et al., 2016; Mukherjee, 2015; Law et al., 2013; Yin et al., 2010; Vannay et al., 2004). In this study, we took the metamorphic-rheological MCT that can be traced along the entire frontal zone of the Himalayan belt and appears in tectonic windows as well as in klippes.

- The **Main Boundary Thrust (MBT)** separates the metasediments of the Lesser Himalaya (hanging wall) from the molassic sediments of the Sub-Himalaya (footwall). The south-west-directed movements associated with this structure are characterised by brittle deformation (cataclastites).

- The **Main Frontal Thrust (MFT)**, also called the Himalayan Frontal Fault or Thrust, is a series of thrusts that represent the surface expression of the outer ramp part of the MHT. Some of these faults are 'blind' and are often concealed under debris washed down from the hillsides. In the landscape, a series of isolated fault-related folds mark individual imbricated MFT fault splays from the MHT (Yeats and Thakur, 2008; Delcaillau et al., 2006; Mugnier et al., 2004; Champel et al., 2002; Lavé and Avouac, 2000; Power et al., 1998; Schelling, 1992). It is along this still active structure that the Sub-Himalaya is thrusted towards the south-west over the Quaternary fluvial deposits of the north Indian plains.

2.4. Open questions, open debates

2.4.1. Tectonic model

Despite decades of research, the tectonic evolution of the Himalayas is still debated, particularly the 'recent' tectonic evolution, in part due to the difficulty of constraining quantitative rates of tectonic change over the Quaternary, and also because different models conflict in their explanation of the tectonic processes that build the High Himalaya.

The present-day convergence rates across the Himalayas of ~12-23 mm/yr (e.g., Vernant et al., 2014; Stevens and Avouac, 2015; Bilham et al., 2017) are equal to the Holocene shortening rates across the north-dipping crustal-scale thrusts that separate the different major lithotectonic units of the Himalayas. Depending on where the more recently active thrust faults are located, two hypotheses can explain the tectonics of the Himalayas during the Quaternary.

(1) The **in-sequence or duplex model** accommodates all the convergence on an active MHT expressed as the MFT and the development of duplex structures (e.g., Lavé and Avouac, 2000; DeCelles et al., 2001; Robinson et al., 2003; Mugnier et al., 2004; Herman et al., 2010). **(2)** Others argue that the slip on the MHT is insufficient to accommodate this convergence, and they suggest an **out-of-sequence model** (Catlos et al., 2001; Hodges et al., 2001; Wobus et al., 2003; Hodges et al., 2004; Whipple et al., 2016), with more recent activity of the thrusts towards the MCT (Fig. 5).

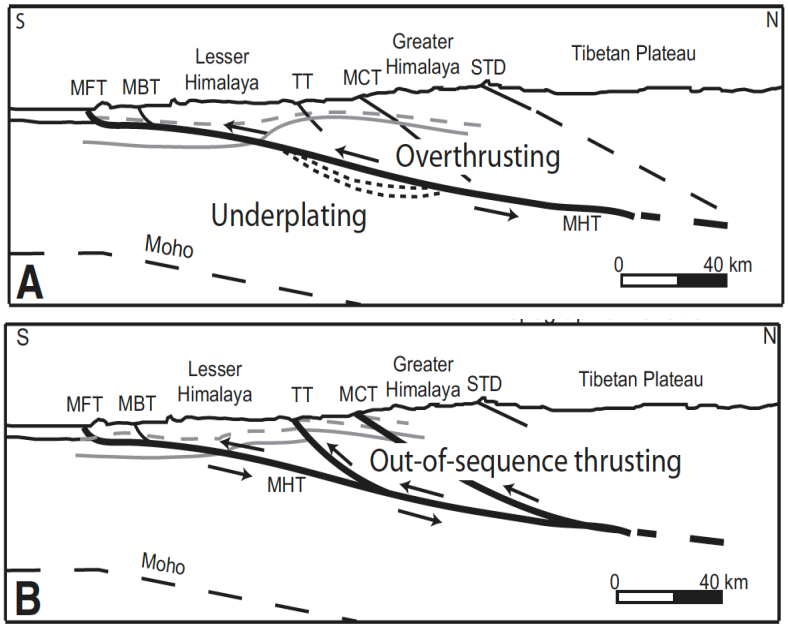

Fig. 5: *Schematic tectonic end-member models with the present-day kinematics of the Central Nepal Himalayas. In model **A** (Avouac, 2003), in-sequence faulting, the shortening is concentrated on the MHT with a crustal ramp below the topographic transition between the Lesser and Greater Himalaya. In model **B** (Hodges et al., 2004), out-of-sequence faulting occurs in the TT zone. MFT = Main Frontal Thrust; MBT = Main Boundary Thrust; MCT = Main Central Thrust; MHT = Main Himalaya Thrust; STD = South Tibetan Detachment; TT = Topographic transition (modified from Robert et al., 2009).*

These two competing models have been proposed to describe the present-day kinematics of the central Nepal Himalayas. They differ in their interpretations of which surface breaking faults accommodate current shortening and the kinematics responsible for driving rapid exhumation in the topographic transition zone around the MCT. These locally higher uplift and erosion rates in the High Himalaya could reflect (1) thrusting over a midcrustal ramp (e.g., Cattin and Avouac, 2000; Lavé and Avouac, 2001) with the growth of a Lesser Himalaya duplex at midcrustal depth causing underplating along the MHT ramp (e.g., Schelling and Arita, 1991; DeCelles et al., 2001; Robinson et al., 2003; Avouac, 2003; Bollinger et al., 2004, 2006), or (2) out-of-sequence thrusting along the front of the High Himalaya, possibly driven

by climatically controlled localized exhumation (e.g., Harrison et al., 1998; Hodges et al., 2004; Wobus et al., 2003).

Many previous studies have tried to discriminate between these two hypotheses by doing global analyses of thermometric, barometric and thermochronological data, and combining them with geomorphic observations. In addition, numerous thermo-kinematic and thermo-mechanical numerical models have also been built by modelling of the tectonics and topography based on these data (e.g., Huerta et al., 1999; Herman et al., 2010; Dal Zilio et al., 2018).

A wide range of low- and medium-temperature thermochronometric systems (defined by their different closure temperatures) have been applied to bedrock rock samples and detrital samples (sediments) from the High Himalaya hinterland: $^{40}Ar/^{39}Ar$ in muscovite and biotite (Copeland et al., 1991; Macfarlane et al., 1992, 1993; Edwards et al., 1996; Arita et al., 1997; Coleman and Hodges, 1998; Rai, 1998; Catlos, 2000; Hodges et al., 2004; Bollinger et al., 2004; Wobus et al., 2005; Huntington and Hodges, 2006), fission-track in zircon and apatite (Arita and Ganzana, 1997; Burbank et al., 2003; Blythe et al., 2007), and (U-Th)/He in apatite and zircon ages (Blythe et al., 2007; Adams et al., 2009). For the Siwaliks sediments and fluvial terrace deposits from the Nepalese foreland, ages and exhumation/erosion rates are calculated from complementing geochronologic and thermochronometric techniques: e.g., ^{14}C, terrestrial cosmogenic nuclide dating, optically-stimulated and infrared-stimulated luminescence dating, electron spin resonance dating, isotopes analysis (Lavé and Avouac, 2000, 2001; Burgess et al., 2012; Lénard, 2019; Lénard et al., 2020; etc), as well as from U-Pb, apatite and zircon fission-track and $^{40}Ar/^{39}Ar$ (Bernet et al., 2006; Szulc et al., 2006; van der Beek et al., 2006). The conclusions of all of these studies are variable despite focusing on the same region. Some show the validity of the duplex model (Schelling and Arita, 1991; Cattin and Avouac, 2000; DeCelles et al., 2001; Lavé and Avouac, 2001; Avouac, 2003; Robinson et al., 2003; Bollinger et al., 2004, 2006; Herman et al., 2010), whereas others support the out-of-sequence model, with activity recorded in the MCT zone over the past 2 Myr (Harrison et al., 1998; Hodges et al., 2001, 2004; Wobus et al., 2003; Blythe et al., 2007). However, most of these studies did not fully explore the range of possible kinematic models, nor the range of possible thermal parameters. Whipp et al. (2007) and Wobus et al. (2006) question the reliability of these studies and concluded that the existing low-temperature thermochronological data from the High Himalaya are insufficient to discriminate among the various models of crustal deformation. Also, despite the dense thermochronological data available from the Himalayas of central Nepal, few thermochronologic data collected in the Lesser Himalaya are reliable due to unfavourable lithologies, and there is a lack of precision and accuracy in the youngest thermochronometric data (closure temperature too high).

This is the departure and insertion point of this thesis project. More than 100 samples were collected across the Himalayas, to accurately constrain exhumation rates on sub-

Quaternary timescales. Specifically, samples were taken across the two fault systems of the MFT and the MCT, in order to provide a better resolution of the difference in exhumation and thrust activity between the two areas, and to discriminate between the two tectonic models/hypothesis for the late Quaternary.

2.4.2. Climate, tectonics, erosion

The interplay between climate, tectonics, and surface processes controls the morphology of mountainous settings. However, constraining the relative effects of these three controlling factors remains challenging, particularly due to the difficulty of constraining changes in exhumation rates at sub-Ma timescales.

Exhumation refers to the processes by which rocks are brought vertically from depth to the Earth's surface. Exhumation can be caused by the removal of overburden mass by denudation or/and by tectonic processes such as crustal ductile thinning or normal faulting (Gallagher, 2012; England and Molnar, 1990, Ring et al., 1999; Stüwe and Barr, 1998). Denudation is a surface process that removes material for the Earth's surface, either by mechanical processes (erosion) or by chemical processes (weathering). It generally leads to a lowering of the Earth's surface with respect to sea-level (Gallagher, 2012). In a simple monotonically exhuming setting, exhumation is equal to erosion (Ring et al., 1999).

However, has exhumation of the Himalayas been continuous or episodic since the mid-Miocene? During the late Quaternary? And, is the exhumation history of the Himalayas governed purely by tectonics or can climatic effects be distinguished?

The Himalayas experienced phases of glaciations during the last 2 Myr, and climatic variations of the Late Pleistocene have been primarily due to glacial-interglacial fluctuations. For the same amount of precipitation, glaciers generate erosion rates equivalent or even superior to fluvial incision rates, glacial erosion being very proficient and being able to influence topography and tectonics systems (Hallet et al., 1996; Brocklehurst and Whipple, 2002; Berger et al, 2008).

On a broader spatial and temporal scale, tectonics and climate are considered interdependent, both having an impact on topography by erosion and weathering. Topography (creation of a mountain range), as a result of uplift and erosion, can affect global atmospheric circulation patterns (e.g. Molnar et al., 2010), affecting precipitation patterns and therefore causing regional variations in climate (e.g. Bookhagen and Burbank, 2010). On the contrary, climate moderates tectonics through erosion and weathering (e.g. Willett, 1999; Whipple, 2009).

Within the Himalayan foreland fold-and-thrust belt, tectonic shortening and fluvial incision modulated by the Indian monsoon interact to govern the morphology of the Siwalik

foothills. Hirschmiller et al. (2014) found that the width of the fold-and-thrust belt correlates inversely with rainfall amount, inferring that surface processes may control the morphology of the fold-and-thrust belt (Fig. 6). Whilst compelling, few direct measurements of rates of surface erosion are available from the fold-and-thrust belt, which in part reflects the recent (i.e. Quaternary) deformation of this region.

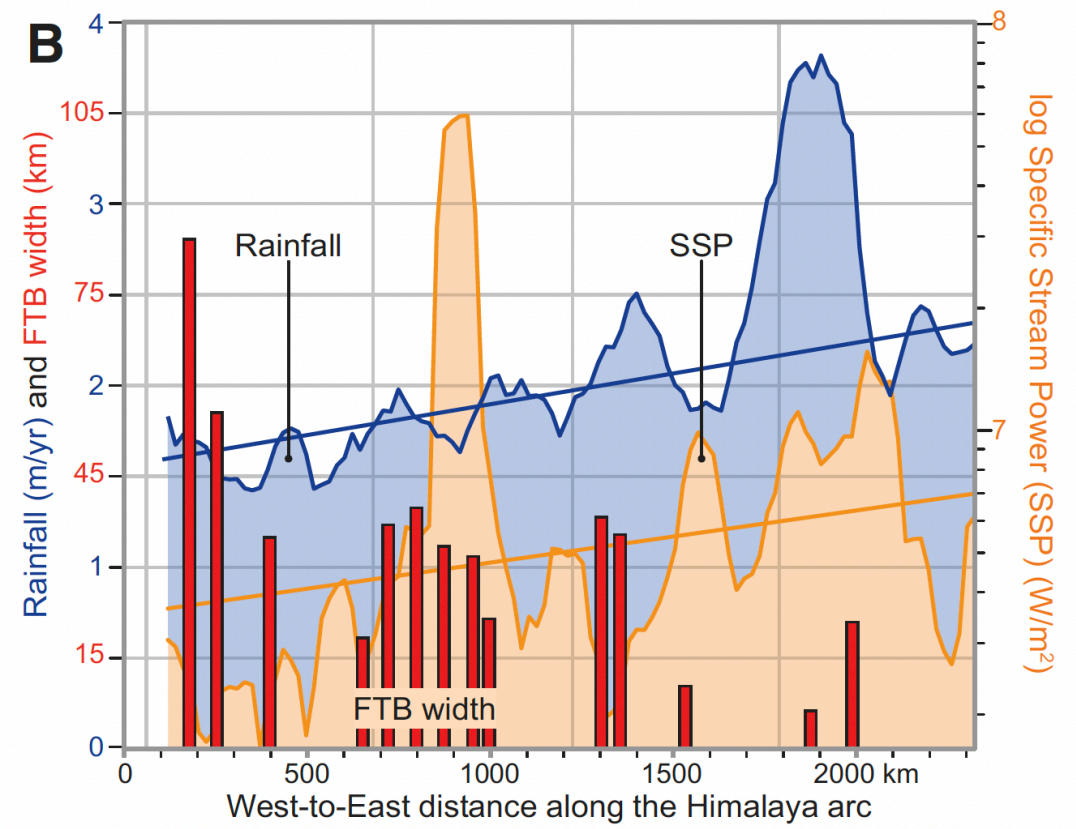

Fig. 6: *Width of the Himalayan fold-and-thrust belt (FTB) along the Himalayan arc, against total annual rainfall and specific stream power (SSP) (Hirschmiller et al., 2014).*

3. Luminescence thermochronometry

3.1. Theory

Luminescence dating (Aitken, 1985, 1998; Huntley et al., 1985; Duller, 2008; Preusser et al., 2009; Rhodes, 2011) is based on the measurement of trapped electrons, which build up in the crystal defects of some mineral grains such as quartz or feldspar. These defects may comprise crystallographic vacancies when ions are absent from their proper places, crystallographic interstitials when there is an additional ionised charge in the lattice structure of an ionic crystal, and chemical impurities when some atoms are replaced by ionised substitutes. Each individual crystal has a finite number of defects (traps) limiting the amount

of electrons that can be trapped, fixing the saturation limit (maximum trapped charge population) of each crystal.

Upon burial, crystals start to accumulate trapped luminescence signal (electrons). When the energy released by naturally-occurring ionising radiation (i.e., alpha, beta or gamma radiation mainly coming from the decay chain of the radionuclides ^{40}K, ^{232}Th, ^{238}U, ^{235}U, and ^{87}Rb from the neighbouring environment or from within the grain, as well as cosmic radiation) interacts with the crystalline lattice (Fig. 7A), it causes the excitation of atoms within the crystal lattice, leading some electrons to be activated at higher energy states, detaching from their equilibrium state in the valence band (leaving behind a 'hole', charged h+) and diffusing towards positively charged defects and impurities within the crystal, where some become trapped (Fig. 8). The amount of electrons trapped within the crystal defects will increase with time, until saturation is reached (no more traps to fill), unless the crystal is exposed to energy sufficient to evict the electrons from the traps. Energy may be in the form of light or heat, that causes vibration of the crystal lattice, and allows the trapped electrons to escape from their traps and to diffuse through the crystal (Fig. 7B and Fig. 8) until the electrons recombine with trapped holes (recombination centres). With this electron-hole recombination (Fig. 8), excess energy is released either in the form of light (photon) or dissipated as heat in the crystal. It is this luminescent (light) signal that is measured with the luminescence method. As the intensity of light emitted by a crystal is proportional to the number of recombining electrons and, hence, to the amount of electrons trapped prior to stimulation by heat or light, it can be used to estimate the time that has elapsed since the crystal was last heated or exposed to light, providing that the environmental radiation dose rate (rate of charge trapping) is known.

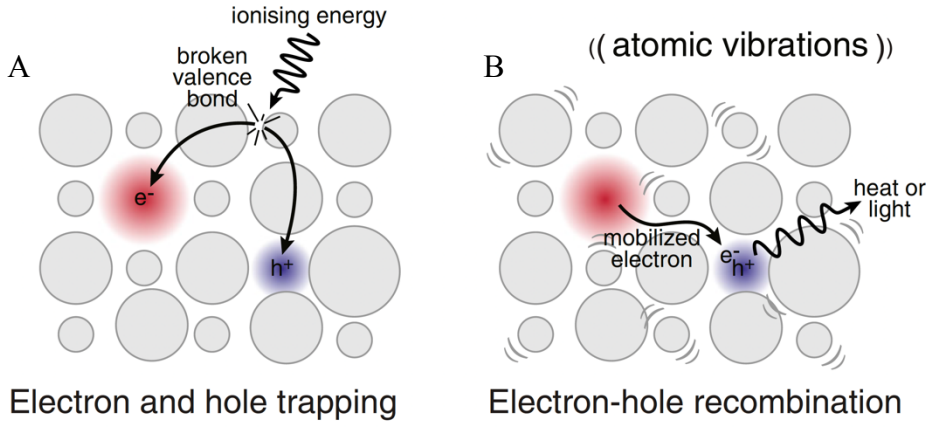

Fig. 7: *Schematic diagram of charge **A.** trapping and **B.** detrapping in the crystal lattice due to the effects of radiation. In (A) ionisation energy results in diffusion of an electron e- to an electron trapping site (in red), and of the creation of luminescence recombination centre of positive charge h+ (in blue). Exposure of the mineral to heat or to light (B) enables the electron to escape the trapping site and to recombine with a hole, leading to a release of excess energy either in the form of measurable light (luminescence signal), or via dissipation by heat (King et al., 2016c).*

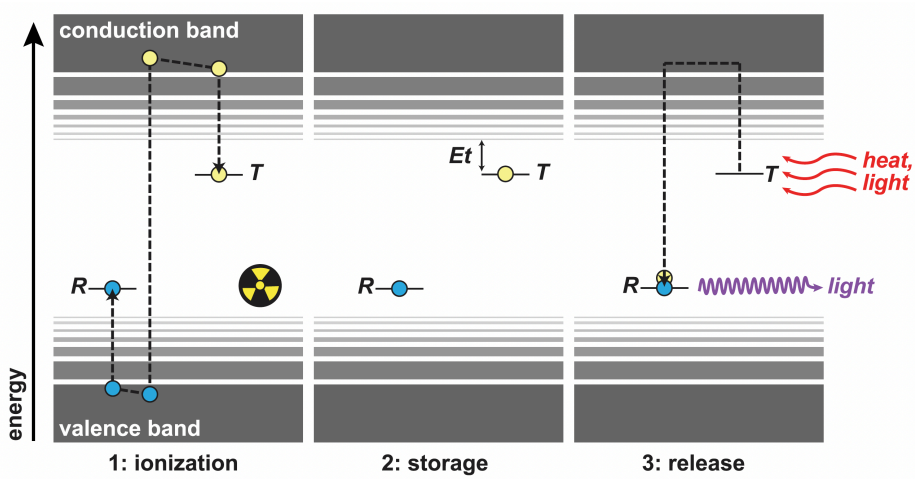

Fig. 8: *Energy level diagram illustrating the luminescence trapping and detrapping processes. **(1)** Ionising radiation interacts with the crystal lattice of quartz or feldspar minerals (ionisation), which causes electrons (yellow circles) to become exited and to migrate from their ground state in the valence band to the conduction band, where they become trapped at lattice defect sites (T). As electrons leave the valence band, they leave behind 'holes' (blue circles), that form recombination centres (R). **(2)** Electrons remain trapped at defect sites T over geological time, requiring energy Et [eV] to escape the electron trap (the deeper the trap below the conduction band, the more stable the electron and the longer it stays trapped). **(3)** The crystal is stimulated by heat or exposure to light, providing sufficient energy to release the electrons from the traps T, which recombine with holes at luminescence centres R, dissipating excess energy by the emission of photons (light) which can be measured (luminescence signal). (Ault et al., 2019).*

For geomorphological or geological processes, the fact that the luminescence signal is zeroed by heat (thermally annealed) or light (optically bleached), means that luminescence dating allows the time that has elapsed since mineral grains crystallised (high temperature), were last exposed to light (daylight), or were heated to ~400 °C to be measured. Luminescence signals accumulate when the crystals are shielded from the light and when it is cold enough (< 120 °C) for the signal not to be zeroed instantaneously. When buried in the ground, naturally occurring radioactivity causes feldspar and quartz minerals to accumulate dose (Fig. 9). The dose that the minerals absorb is directly proportional to the radiation exposure time within the depositional environment. To determine the time since sunlight or heat exposure for a buried grain (age), two pieces of information are needed, the geological environmental dose-rate $\dot{D}$ (i.e., the rate at which the naturally-occurring radiation interacts with the crystal to cause charge accumulation), and the total luminescence signal, also called the equivalent dose D_e (i.e., total radiation dose absorbed by the grain):

Age [kyr] = equivalent dose D_e [Gy] / geological environmental dose-rate $\dot{D}$ [Gy/kyr]

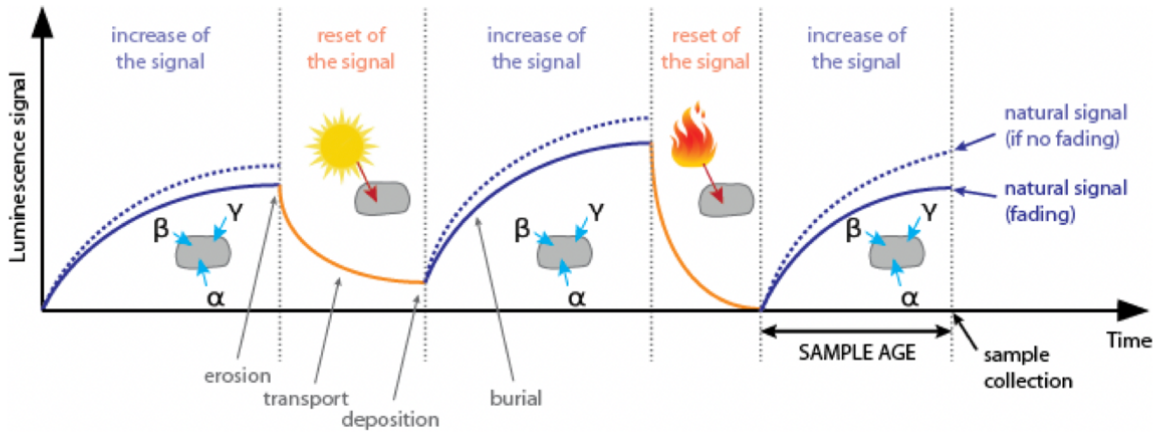

Fig. 9: *Evolution of the luminescence signal stored in feldspar crystals throughout their geological history. Luminescence signal (amount of stored electrons within crystal lattice defects) build-up as crystals are shielded from the light (e.g., during burial), and are exposed to ionising radiations. Light exposure of crystal due to exposure to light (e.g., erosion and transport in shallow water or by the wind) or to high temperature (e.g., wild fire, volcanic eruption) zeros the luminescence signal. The age of the sample corresponds to the time elapse since the last depositional event.*

3.2. Measurements

Luminescence thermochronometry (Guralnik et al., 2015a; King et al., 2016a; Herman et al., 2010; Li and Li, 2013) is a recently developed very-low-temperature thermochronometer, sensitive to temperatures of 30-100 °C, based on the luminescence dating of quartz and feldspar minerals. Luminescence thermochronometry relies on modelling electron trapping and detrapping in quartz or feldspar minerals, using kinetic parameters derived from fitting experimental data with numerical models (c.f. Herman et al., 2010; Guralnik et al., 2015a, 2015b). The charges (electrons) trapped in the defects of the lattice of quartz or feldspar minerals can be evicted by either optical or thermal stimulation, or for feldspar minerals, via athermal processes related to quantum mechanical tunnelling, generally referred to as anomalous fading (Wintle, 1977). Constraining these processes of luminescence signal accumulation and loss allows the sample's thermal history to be determined and is usually done for all samples investigated (e.g., Guralnik et al., 2015b; Wu et al., 2015; King et al., 2016a; Biswas et al., 2018), using three sets of measurement in the laboratory:

- The natural luminescence signal of the sample is first measured, and converted to a dose using a dose response curve. This curve is obtained by bleaching the sample and giving known laboratory radiation doses, from which the resulting luminescence signal is measured. This is repeated for a range of increasing known-doses. As the dose increases, the luminescence response is brighter, until the luminescence signal reaches saturation (same maximum luminescence signal). The dose-response data are then

fitted with a curve, e.g., a single saturating exponential, to derive the dose equivalent to the natural luminescence signal.

- For minerals such as feldspar or quartz of volcanic origin, athermal signal loss due to quantum mechanical tunnelling from the ground state of the trap to the recombination center (hole) needs to be constrained. Because of this anomalous fading, the measured trapped-charge population is significantly smaller than for a non-fading mineral, given an identical thermal history. Anomalous fading is measured by giving a known dose to the samples, and seeing the evolution of the luminescence signal at room temperature after different delay periods (e.g., Huntley, 2006). Once the athermal loss is quantified, the dose response curve and the other luminescence measurements can be corrected for fading, which is necessary before parameter determination.
- Thermal decay, or thermal annealing, which is how the sample reacts to temperature, is measured by giving a known dose to the sample, before holding it at different isothermal temperatures for a range of durations, and measuring the remaining luminescence signal (e.g., Murray and Wintle, 1999; Guralnik et al., 2015a).

3.3. Models

The luminescence signal, or the fraction $\tilde{n} = (\frac{n}{N})$ of n trapped electrons in a total of N electron traps (saturation ratio), as a function of time, t [s], can be synthetized as:

$$\frac{d\tilde{n}}{dt} = (1)\ trapping - (2)\ thermal\ detrapping\ - (3)\ athermal\ detrapping$$

A range of different models have been proposed to describe optically/infrared stimulated luminescence signal growth and decay (e.g., Li and Li, 2013; Guralnik et al., 2015a; Lambert, 2018).

The evolution of the luminescence signal growth through time t [s], term (1), can be described with a single saturating exponential function, 1EXP:

$$\frac{d\tilde{n}}{dt} = \frac{\dot{D}}{D_0}(1-\tilde{n}) \qquad [1]$$

or with a general order kinetic model, GOK:

$$\frac{d\tilde{n}}{dt} = \frac{\dot{D}}{D_0}(1-\tilde{n})^{\alpha} \qquad [2]$$

where $\dot{D}$ [Gy/s] is the environmental radiation dose rate, D_0 [Gy] the fading corrected characteristic dose of saturation, and α the kinetic order of the fit with the GOK model.

The thermal decay, term (2), is signalled either with the band-tail states model (Poolton et al., 2009; Li and Li, 2013; King et al., 2016a), BTS:

$$\frac{d\tilde{n}}{dt} = -s\,\tilde{n}\,e^{-\frac{E_t-E_b}{k_b T}} \qquad [3]$$

with the Gaussian model (Lambert, 2018), GAUSS:

$$\frac{d\tilde{n}}{dt} = -s\,\tilde{n}\,e^{-\frac{E_t}{k_b T}} \quad [4]$$

or with the general order kinetic model (Guralnik et al., 2015a), GOK:

$$\frac{d\tilde{n}}{dt} = -s\,\tilde{n}^{\beta}\,e^{-\frac{E}{k_b T}} \quad [5]$$

where thermal detrapping is a function of the temperature T [K], the Boltzmann constant k_B [eV/K], the thermal frequency factor s [s^{-1}], the activation energy (or trap depth below the conduction band) E_t [eV], and the band-tail state energy level E_b [eV], with E the activation energy, and β the kinetic order (usually $1 \leq \beta \leq 2$).

These different models for thermal trapping and detrapping are based on different interpretations of the distribution of the traps and recombination centres, and the energy level of the conduction band. The band-tail states model BTS (Poolton et al., 2002a, 2002b, 2009; Li and Li, 2013) stipulates that a continuum of energy states is exponentially spatially distributed below the conduction band throughout the crystal. Trapped electrons need less energy to thermally escape, as they can pass via a band-tail energy instead of the conduction band. The Gaussian model is based on the BTS model, but assumes a Gaussian distribution of trap depths around the ground state of the trap (Lambert, 2018).

Athermal decay, term (3), is constrained with the model of Huntley (2006), as:

$$\frac{d\tilde{n}}{dt} = -\tilde{s}\,\tilde{n}\,e^{-\rho'^{\frac{1}{3}} r'} \quad [6]$$

with the athermal frequency factor $\tilde{s}$ = 3 x 10^{15} s^{-1} (Huntley, 2006), the dimensionless density of the recombination centres ρ' [-], and the dimensionless distance r' [-] between trapped electrons and their recombination centres.

In this PhD thesis, we mainly used the 1EXP fit for the dose-response curve, and the BTS model for the thermal decay (Fig. 10). More details on the equations and on the technique can be found in Chapter 1, and in the Appendix.

$$\frac{d[\tilde{n}(r',E_b,t)]}{dt} = \frac{\dot{D}}{D_0}[1-\tilde{n}(r',E_b,t)] - s\,e^{-\frac{E_t-E_b}{k_b T}}[\tilde{n}(r',E_b,t)] - \tilde{s}\,e^{-\rho'^{\frac{1}{3}}r'}[\tilde{n}(r',E_b,t)]$$

Luminescence signal = trapping – thermal detrapping – athermal detrapping

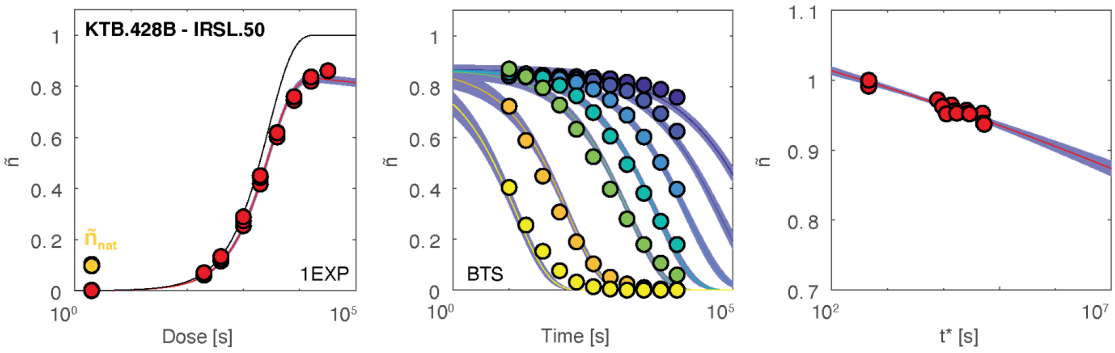

Dose response curve **Isothermal holding experiment** **Anomalous fading**

Fig. 10: *Luminescence equation and measurements with their model fit results for the IRSL.50 signal of sample KTB.428B.* ***A.*** *Luminescence dose response fitted using a single-exponential model. The black solid line is the non-faded corrected dose response curve. The natural luminescence signal is represented in yellow.* ***B.*** *Isothermal decay data fitted using the BTS model (isothermal temperatures from blue =170 °C to yellow = 350 °C).* ***C.*** *Anomalous fading data fitted with the model of Huntley (2006).*

3.4. Multi-luminescence thermochronometry

Multi-luminescence-thermochronometry (Li and Li, 2012; King et al., 2016a) exploits the different thermal stabilities of different temperature infrared stimulated luminescence (IRSL) signals from K-feldspar extracts, using a multi-elevated-temperature (MET) measurement protocol (Li and Li, 2011; King et al., 2016a). This method can be used to derive high-precision cooling histories in geological settings. Through measuring multiple luminescence signals at different temperatures from the same mineral in a multiple-elevated temperature protocol (Li and Li, 2011), it is possible to obtain multiple controls on the cooling history of a single sample. Multi-luminescence-thermochronometry of feldspar is able to resolve rock cooling histories over timescales of more than 200 kyr and provides much tighter constraint on late-stage cooling histories than single-system luminescence-thermochronometry (King et al., 2016a).

Applying this new technique on the feldspar of the synorogenic sediments of the Sub-Himalayas and on the metamorphic sediments of the High Himalayas around the MCT, provides insights into the late Quaternary cooling and thus exhumation/erosion history of the

Himalayan foreland and hinterland, and offer new opportunities to investigate the interactions between climate, tectonics and surface processes over sub-Quaternary timescales.

4. Contribution of this thesis

4.1. Study areas, samples locations

The samples available for this study are relevant considering their location. Contrary to most of the previous studies done in the Himalayas that only focus on a few samples scattered on a relatively small area either in the High Himalayas or the Sub-Himalayas, or along a valley or a few elevations transects, this study has a dense collection of more than 100 samples distributed across a large area of the Himalayas, mainly in Nepal, but also in Bhutan (Fig. 11).

For the Sub-Himalayas, 44 samples were collected, from which exhumation rates of 33 of those samples are presented in Chapter 2, and the results for the 11 others are studied in Chapter 4. These samples were collected along six transects across the Siwalik foothills, specifically selected to constrain exhumation rate and thus shortening rate changes in the Sub-Himalayan fold-and-thrust belt (FTB). From west to east: ten samples (NG.1, 2, 3, 4, 5, 6, 7, 8, 10, and 11) were taken north of Nepalgunj in western Nepal. In central Nepal, five samples (BUT.1, 2, 3, 4, 5) were collected near Butwal along the Tinau Khola, samples SU-9 and BAR-1 were sampled along the Bakaya river nearby the MFT surface expression, and seventeen samples were collected on three thrust sheet along the Kamala Khola (RA-K01, 02, 03, 04, 05, 06) and the Ratu Khola (RA-P01, 02, 03, 04, 05, 06, and RA-B01, 02, 03, 04, 05). In eastern Nepal, samples CA14-4 and CA14-7 were taken along the Koshi river. The easternmost transect of eight samples (SJT.01A, 03, 05, 07, 08, 10, 11, 12) is situated near Samdrup Jongkhar, along the Dungsam Chu river in eastern Bhutan. All samples are fluviatile/molassic sedimentary rocks from the Siwalik Group, collected along rivers situated within the Sub-Himalayan FTB, delimited by the Main Boundary Thrust (MBT) in the North, and the Main Frontal Thrust (MFT) in the South. NG.1 is the only sample that lies south of the MFT.

For the High Himalayas (Chapter 3), the study-area focusses on four valleys around the Annapurna and Ganesh peaks in Nepal. Rock samples were collected in the hinterland – along the Kali Gandaki, Marsyangdi, Buri Gandaki, and Trisuli rivers -, specifically selected to record exhumation rate changes on each side of the Main Central Thrust (MCT) and the South Tibetan Detachment System (STDS). From the 61 samples collected, 56 had enough K-feldspar and could be used for luminescence measurements. From west to east, 13 samples were collected from along the Kali Gandaki, 19 (14 samples had enough K-feldspar to be measured) along the Marsyangdi river, 15 along the Buri Gandaki, and 14 along the Trisuli transect. From these samples, 3 elevation transects were collected, one north of the STDS at the end of the

Marsyangdi valley (HIM.6-6E), and two on the MCT thrust sheet in the Marsyangdi (HIM.4Z-4C) and Buri Gandaki (BG.E-A) valleys. Two samples from the Marsyangdi, HIM.3A and HIM.3B were taken near hot springs. Most of these samples are metamorphic rocks from the Lesser Himalaya and Higher Himalaya, and some are metamorphic-sedimentary rocks and igneous rocks from the Tethyan Himalaya.

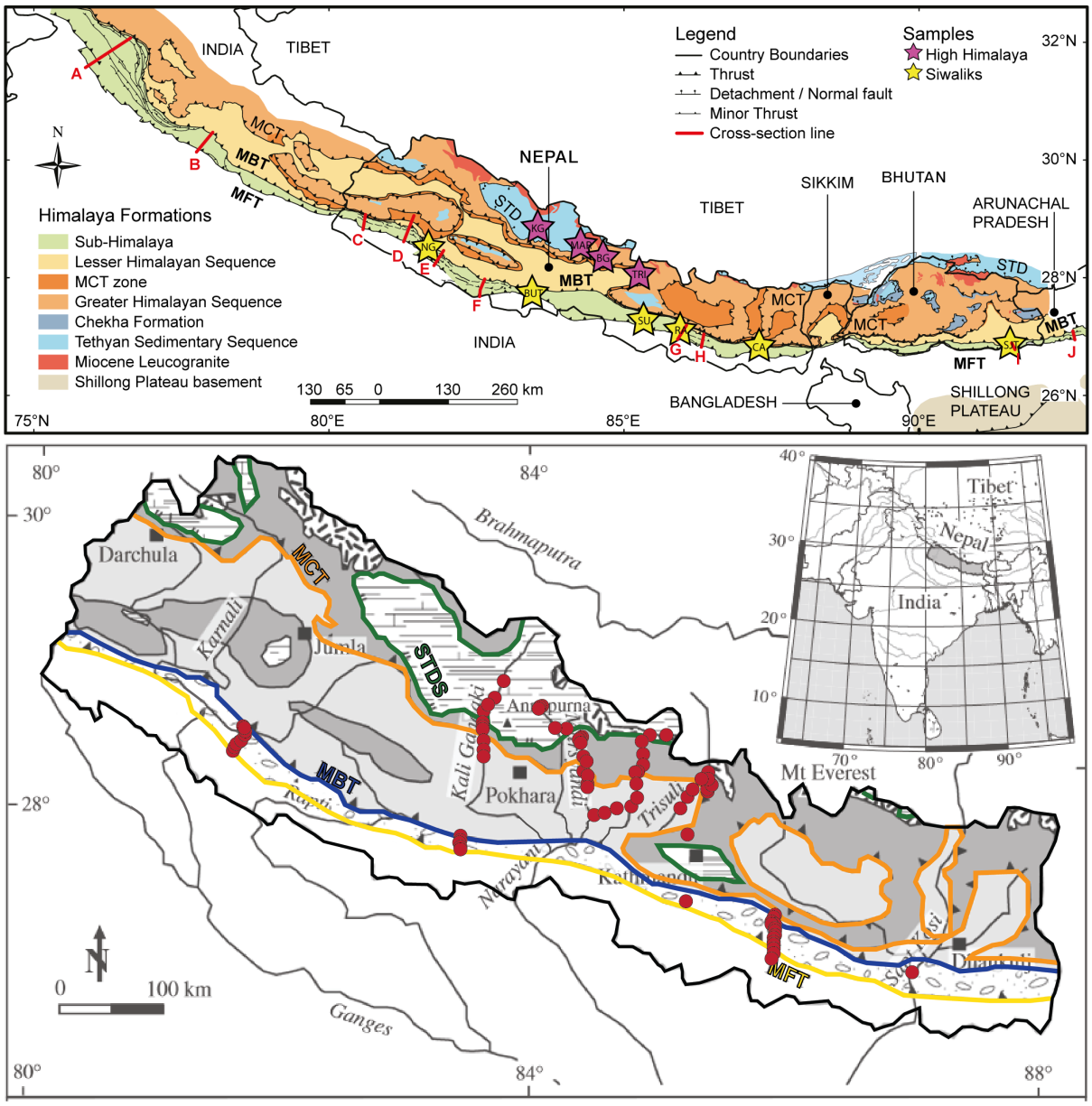

Fig. 11: A. *Simplified geological and tectonic map of Nepal and Bhutan (Hirschmiller et al., 2014). The yellow stars represent the six transects of the Sub-Himalaya, and the purple stars the four transects of the High Himalaya from this study.* ***B.*** *Zoom in on Nepal, with the red dot representing the distribution of the samples of the four High Himalaya transects, and the Sub-Himalayan samples of central Nepal (modified from van der Beek et al., 2006). STDS: South Tibetan Detachment System; MCT: Main Central Thrust; MBT: Main Boundary Thrust; MFT: Main Frontal Thrust.*

4.2. Dissertation structure

Despite the potential of luminescence thermochronometry for deriving changes in landscape and subsurface evolution, it has never been applied to a large-scale study area, or even been validated as a multi-thermochronometer approach. The primary objective of this thesis is to use luminescence thermochronometry to constrain the exhumation histories and thus the tectonic model of the Himalayas over the late Pleistocene to Holocene timescales (late Quaternary).

For this, the thesis is structured in four chapters that address the following sub-objectives:

- **Validate and optimize the multi-luminescence thermochronometry protocol for feldspar minerals.**
- **Constrain the late Quaternary (last 200 kyr) thermal and exhumation history of the Sub-Himalayas and the High Himalayas by applying luminescence thermochronometry on more than a hundred samples distributed throughout the Nepalese and Bhutanese Himalayas, in order to (i) fill the temporal gap in geological constraint between the Holocene and geologic data, (ii) improve the tectonics models of the Himalayas for the Quaternary, and (iii) increase knowledge on the seismic cycle.**

In **Chapter 1**, three sets of samples, samples with independently known thermal histories, synthetic thermal history samples created following irradiation at high temperature in the laboratory, and unknown-thermal history samples, are analysed to improve and validate the multi-elevated-temperature infrared stimulated luminescence (MET-IRSL; Li and Li, 2012) measurement protocol for feldspar thermochronometry. A new protocol to extract thermal kinetic parameters is proposed. This chapter was published in *Quaternary Geochronology*:

> **Bouscary, C., and King, G.E. (2022)**. Luminescence thermochronometry of feldspar minerals: optimisation of measurement conditions for the derivation of thermal kinetic parameters using isothermal holding experiments. *Quaternary Geochronology,* 67, 101240, 1-14, doi:10.1016/j.quageo.2021.101240.

In **Chapter 2**, the improved and validated luminescence thermochronometry method is used to extract the exhumation history of Sub-Himalayan samples. We present an extensive new dataset of more than 30 luminescence thermochronometry samples from six transects across the Siwalik foothills from western Nepal to eastern Bhutan, specifically selected to resolve deformation at sub-Quaternary timescales, a timescale until now largely inaccessible to other techniques. This chapter was submitted to *Geology*:

Bouscary, C., King, G.E., Grujic, D., Lavé, J., Almeida, R., Hetényi, G., and Herman F. (*In review*). Sustained deformation across the Sub-Himalayas since 200 ka. *Geology*.

In **Chapter 3**, luminescence thermochronometry is used to derive exhumation rates for four valleys in the High Himalayas of Nepal to determine exhumation rates on the MHT/MCT, and to try to decipher which of the tectonic model between the in-sequence/duplexing and the out-of-sequence applies during the late Quaternary. The results of this chapter will be submitted for publication in *Journal of Geophysical Research: Solid Earth*:

Bouscary, C., King, G.E., Lavé, J., Hetényi, G., Gajurel, A.P., and Herman, F. (*in prep.*). Late Quaternary exhumation rates of the Nepalese-Himalayan hinterland, duplex vs. out-of-sequence activity of the MCT. *Journal of Geophysical Research: Solid Earth*.

In **Chapter 4**, all the research conducted that did not lead to a publication, i.e., unsuccessful experiments, blind alleys, incomplete datasets due to time-constraints … is gathered into mini sub-chapters/paragraphs that summarise what was done. Some of this research could potentially later lead to publications.

Finally, all the different chapters are synthetized and their implications are discussed in the **Conclusions**. An outlook for further research in this field is also presented in the **Perspectives**.

In the **Appendix**, the basics of luminescence and electron spin resonance (ESR) thermochronometry are presented, and the MATLAB codes developed and improved that are used to analyse the data for trapped-charge thermochronometry are explained. This pseudo-chapter is a collaborative effort to make the luminescence and ESR codes available to the scientific community. This work will be submitted to *AncientTL* or as a *Technical Note for Geochronology*:

Bouscary, C., Bartz, M., Biswas, R., Bossin, L., Duverger, A., Guralnik, B., Lambert, R., Licul, A., Nanni, U., Stalder, N., Valla, P., Visnjevic, V., Wen, X., Herman, F., and King, G.E. *(in prep.)*, LumiThermo and ESRThermo: Libraries of codes for trapped-charge thermochronometry. *AncientTL / Technical Note for Geochronology*.

References are all gathered in a single reference list at the end of the manuscript in order to avoid unnecessary duplicated.

Chapter 1

Luminescence thermochronometry of feldspar minerals: optimisation of measurement conditions for the derivation of thermal kinetic parameters using isothermal holding experiments

---

C. Bouscary [1], G.E. King [1]

[1] Institute of Earth Surface Dynamics, Géopolis, University of Lausanne, Switzerland

Table of contents

This chapter was published in *Quaternary Geochronology*:

Bouscary, C., and King, G.E. (2022). Luminescence thermochronometry of feldspar minerals: optimisation of measurement conditions for the derivation of thermal kinetic parameters using isothermal holding experiments. *Quaternary Geochronology,* 67, 101240, 1-14, doi:10.1016/j.quageo.2021.101240.

Abstract

Luminescence thermochronometry is sensitive to very low temperatures (below ~120 °C), and enables the resolution of thermal histories over sub-Quaternary timescales. Here we apply a multi-elevated-temperature post-infrared infrared-stimulated luminescence (MET-pIR-IRSL) measurement protocol to feldspar minerals to extract thermal histories. These thermal histories depend on the thermal stability of the MET signal, and are based on the thermal kinetic parameters extracted from isothermal decay experiments. However, the derived thermal kinetic parameters vary with experimental conditions, specifically with the number of isothermal holding temperatures (ITL) used. We analyse samples with independently known thermal histories, together with synthetic thermal history samples and samples with unknown thermal histories to test the validity of thermal kinetic parameters obtained from different combinations of isothermal holding data. This approach is tested on feldspars of different mineralogies and lithologies. We find that the temperatures inferred from inverting the data change, depending both on the number and on the highest ITL temperature used for thermal kinetic parameter derivation. Analysed samples validate the MET-pIR IRSL protocol for extracting thermal histories, and we suggest that four isothermal holding temperatures between 190 and 250 °C are used for appropriate thermal kinetic parameter derivation.

Keywords: low-temperature thermochronometry, luminescence, feldspar, kinetic parameters, isothermal holding experiments

1. Introduction

Thermochronometry is the quantification of the thermal history of rocks. Different thermochronometric systems have different thermal sensitivities, enabling the reconstruction of different time-temperature histories. Only some thermochronometers are able to constrain low-temperature paths (temperatures below ~120 °C) for reconstruction of the thermal histories of the upper first few kilometres of the Earth's crust (e.g., U-Th/He, $^{4}He/^{3}He$, ESR; e.g., Ault et al., 2019). Luminescence thermochronometry (Herman et al., 2010; Li and Li, 2013; Guralnik et al., 2015a; King et al., 2016a; Herman and King, 2018) is a recently developed very-low-temperature thermochronometer with a high sensitivity to temperatures below ~120 °C. It has a very low closure temperature (~30-100 °C, depending on the signal) (Guralnik et al., 2013; King et al., 2016b) that offers the potential to resolve rock cooling, and thus exhumation, over timescales of 10^3 to 10^6 years, i.e. at sub-Quaternary timescales (Rhodes, 2011; Guralnik et al., 2013, 2015b; King et al., 2016a).

Luminescence thermochronometry is a trapped charge method based on the modelling of electron trapping and detrapping in quartz or feldspar minerals, using kinetic parameters derived from fitting experimental data with numerical models (c.f. Herman et al., 2010; Guralnik et al., 2015a, 2015b). The charges (electrons) trapped in the defects of the lattice of quartz or feldspar minerals can be evicted by either optical or thermal stimulation, or for feldspar minerals, via athermal processes related to quantum mechanical tunnelling, generally referred to as anomalous fading (Wintle, 1977). Constraining these processes of luminescence signal accumulation and loss allows the sample's thermal history to be determined and is usually done for all samples investigated (e.g., Guralnik et al., 2015b; Wu et al., 2015; King et al., 2016a; Biswas et al., 2018). One method through which the thermal kinetic parameters can be constrained is an isothermal holding experiment. Such an experiment comprises irradiating a sample in the laboratory, before holding it at different isothermal temperatures for a range of durations, and measuring the remaining luminescence signal (e.g., Murray and Wintle, 1999; Guralnik et al., 2015a).

Beyond the calibration study of Guralnik et al. (2015b), the validity of the thermal kinetic parameters extracted from isothermal holding experiments for different thermochronometric samples has not been confirmed. Guralnik et al. (2015b) showed that their approach of using three isothermal holding temperatures (ITL) between 190 and 230 °C resulted in thermal kinetic parameters that accurately recovered the temperature for samples from the KTB borehole. However, no study has investigated whether this approach, or the approach of King et al. (2016a) of using seven isothermal holding temperatures between 170 and 350 °C, is appropriate for other samples. Furthermore no independent validation of the use of multi-signal feldspar protocols for luminescence thermochronometry has been made, despite their use in a number of studies (King et al., 2016a, 2016b; Herman and King, 2018; Lambert,

2018; King et al., 2020). This is at least partly because most geological samples do not have an independently constrained thermal history.

In this contribution, we seek to establish what combination of isothermal temperatures is appropriate for samples of different mineralogies and lithologies by developing an independent method of testing the suitability of multi-signal feldspar methods for luminescence thermochronometry. For this, we use an approach for feldspar extracts (following Li and Li, 2011; King et al., 2016a) that exploits the distinct thermal stabilities of infrared stimulated luminescence (IRSL) signals measured at different stimulation temperatures. This approach has been used previously to derive cooling histories in geological settings (King et al., 2016b; Herman and King, 2018). First, we explore known-thermal history Na-feldspar samples of gneiss and amphibolite from the KTB borehole, before investigating K-feldspar minerals extracted from Nepalese Siwaliks sandstones. We then create calibration samples that mimic the thermal steady-state conditions of the KTB borehole by irradiating samples at high temperatures in the laboratory. We validate the multi-thermochronometric method using these data, before contrasting our results with a set of control samples from different mineralogies (Na-feldspars and K-feldspars) and lithologies (bedrocks, sediments, reference sample, and museum specimens).

2. Luminescence thermochronometry: models and measurements

2.1. Luminescence thermochronometry model and derivation of kinetic parameters

Luminescence thermochronometry exploits the properties of electron traps present in the lattice of quartz and feldspar crystals. A range of different models have been proposed to describe optically stimulated luminescence signal growth and decay (e.g., Li and Li, 2013; Guralnik et al., 2015b; Lambert, 2018). For the purpose of this study, we follow the approach of King et al. (2016a) and describe luminescence signal growth with a single saturating exponential function, signal thermal decay with the band-tail states model (BTS; Poolton et al., 2009; Li and Li, 2013; King et al., 2016a), and athermal decay with the model of Huntley (2006) (Tachiya and Mozumder, 1974). The luminescence signal, or the fraction of occupied electron traps (saturation ratio) $\tilde{n}$ is thus described by: [1]

$$\frac{d[\tilde{n}(r', E_b, t)]}{dt} = \frac{\dot{D}}{D_0}\left[1 - \tilde{n}(r', E_b, t)\right] - s\, e^{-\frac{E_t - E_b}{k_b T}}\left[\tilde{n}(r', E_b, t)\right] - \tilde{s}\, e^{-\rho'^{\frac{1}{3}} r'}\left[\tilde{n}(r', E_b, t)\right]$$

where t [s] and T [K] are the time and temperature. The radiation-induced growth (first term on the right-hand side of the equation) of the ratio $\tilde{n} = (\frac{n}{N})$ of n trapped electrons in a total of N electron traps is characterised by $\dot{D}$ [Gy/s], the environmental radiation dose rate, and D_0 [Gy], the fading corrected characteristic dose of saturation. Thermal detrapping (second term) is a function of the Boltzmann constant k_B [eV/K], the thermal frequency factor s [s^{-1}], the activation energy (or trap depth below the conduction band) E_t [eV], and the band-tail state energy level E_b [eV]. Athermal detrapping (third term) is a function of the athermal frequency factor $\tilde{s}$ = 3 x 10^{15} s^{-1} (Huntley, 2006), the dimensionless density of the recombination centres ρ' [-], and the dimensionless distance r' [-] between trapped electrons and their recombination centres.

The total accumulation of trapped electrons for a given thermal history is obtained by integrating $\tilde{n}(r', E_b, t)$ over the range of dimensionless distances, r', and the range of the band-tail states, E_b:

$$\tilde{n}(t) = \int_{r'=0}^{r'=\infty} \int_{E_b=0}^{E_t} p(r')P(E_b)\,\tilde{n}(r', E_b, t)dE_b dr' \quad [2]$$

where $p(r')$ and $P(E_b)$ are respectively, the probability density distributions of the nearest recombination centres and of the band-tail states.

The kinetic parameters in equation 1 that describe the luminescence signal are estimated for each sample through a series of laboratory experiments: the luminescence dose response curve is used to constrain the parameters $\tilde{n}$ and D_0; measurement of athermal signal loss in a fading measurement is used to constrain the athermal kinetic parameter ρ'; and thermal signal loss is measured using an isothermal holding experiment, that allows constraint of s, E_t, and E_b. The rate of electron trapping, $\dot{D}$, is determined from measuring the concentration of U, Th, and K in the sample using, e.g., inductively coupled plasma mass spectrometry (ICP-MS) or gamma-spectrometry.

2.1.1. Athermal detrapping

Athermal detrapping, also referred to as anomalous fading, is a phenomenon that mainly affects feldspar minerals whereby trapped charges tunnel from the electron traps with time (Wintle, 1973, 1977). This tunnelling process is described by the model of Huntley (2006):

$$\tilde{n}(t^*) = \tilde{n}(0)\varphi(t^*) \quad [3]$$

where φ is a time-dependent factor,

$$\varphi(t^*) = e^{-\rho' ln\,(1.8\,\tilde{s}\,t^*)^3} \quad [4]$$

with $\tilde{n}(0)$ being the initial trapped charge quantity, t^* [s] the fading time, and $\rho' \equiv \frac{4\pi\rho}{3\alpha^3}$, where α [m^{-3}] is a constant (Huntley, 2006; Kars et al., 2008; Li and Li, 2008), and ρ [m^{-3}] is the density of randomly distributed recombination centres within the feldspar minerals.

2.1.2. Electron trapping

The accumulation of the luminescence signal through time is fitted with a single saturating exponential function (Guralnik et al., 2015a, King et al., 2016a).

$$\tilde{n}(t) = \varphi(t^*)\, A \left(1 - e^{-\frac{\dot{D}t}{D_0}}\right) \quad [5]$$

where φ is a time-dependent factor to account for athermal detrapping throughout measurement as defined in section 2.1.1 (equation 4), and A is a pre-exponential multiplier (King et al., 2016a).

2.1.3. Thermal detrapping

Thermal detrapping can be described with different models (Guralnik et al., 2015a), but here we opt to use the BTS (Li and Li, 2013), as implemented by King et al. (2016a):

$$\frac{\tilde{n}(t)}{\tilde{n}(0)} = \varphi(t^*) \int_{E_b=0}^{E_t} P(E_b)\, e^{(-s.t.e^{\frac{E_t - E_b}{k_b T}})}\, dE_b \quad [6]$$

The probability of thermally evicting an electron into the band-tail states of energy $E_b + dE_b$, with a probability of $P(E_b)dE_b$, is given by (Poolton et al., 2009; Li and Li, 2013):

$$P(E_b)dE_b = B.e^{(-\frac{E_b}{E_u})}dE_b \quad [7]$$

where E_u [eV] is the width of the Urbach tail, and B is a pre-exponential multiplier.

2.2. Sample description

2.2.1. KTB borehole samples

Guralnik et al. (2015b) validated the luminescence thermochronometry method by recovering the temperatures of several Na-feldspar samples from the KTB borehole using a

single thermochronometric system (IRSL 50 °C). Guralnik et al. (2015b) used a general order kinetic (GOK) model to derive thermal kinetic parameters from three sets of isothermal holding data measured at 190, 210, and 230 °C. In our study, we pursue a multi-thermochronometer approach (Li and Li, 2012), using the multi-elevated temperature (MET) protocol (IRSL 50, 100, 150, 225 °C) (Li and Li, 2011), and the BTS model (Li and Li, 2013) to fit our isothermal decay data. Following King et al. (2016a), we measure isothermal decay for seven different ITL temperatures between 170 and 350 °C.

To validate the MET luminescence thermochronometry method, previously prepared and studied Na-feldspar samples from the KTB borehole, Germany were used (Guralnik et al., 2015b). These rocks have a known thermal history (Clauser et al., 1997; Wagner et al., 1997), allowing material from this borehole to be used as calibration samples for thermochronometric studies (e.g., apatite fission-track: Coyle et al., 1997; ^{40}Ar-^{39}Ar: Warnock et Zeitler, 1998; luminescence IRSL 50 °C: Guralnik et al., 2015b). Following the previous work of Guralnik et al. (2015b), four samples that reflected borehole temperatures (i.e., were not in luminescence athermal steady-state) were selected: samples KTB.253F, KTB.383C, KTB.428B, and KTB.481B (see Table 1).

Table 1: *KTB borehole sample details after Guralnik et al. (2015b).*

Samples KTB				**Whole-rock radiochemistry**			**Dose Rate**
ID	**Depth**	**In-situ temperature**	**Lithology**	**U**	**Th**	**K**	**Ḋ**
	[m]	**[°C]**		**[ppm]**	**[ppm]**	**[wt.%]**	**[Gy/ka]**
253F	1175	39.8 ± 2.1	Garnet-amphibolite	0.8	2.1	1.25	1.58 ± 0.24
383C	1730	55.1 ± 2.9	Sillimanite-muscovite-biotite-gneiss	2.5	7.7	1.72	3.02 ± 0.45
428B	1892	59.5 ± 3.1	Garnet-sillimanite-biotite-gneiss	2.6	8.9	2.42	3.44 ± 0.52
481B	2097	65.2 ± 3.4	Garnet-sillimanite-biotite-gneiss	2.7	8.7	2.34	3.58± 0.54

2.2.2. Butwal samples

In contrast to the KTB samples which comprise Na-feldspar, K-feldspar is the most frequent mineral used in luminescence thermochronometry studies (e.g., King et al., 2016b; Brown et al., 2017; Biswas et al., 2018). No K-feldspar bearing samples with independent temperature control were readily available for calibration of the luminescence thermochronometry technique. Instead, we used a sample from the Himalayas, for which we developed a synthetic calibration by irradiating the sample at elevated temperature within a modified luminescence reader (e.g., Wallinga et al., 2002).

We selected five samples from the Himalayan foreland, taken along the Tinau river in the Siwalik hills (Table 2): BUT.1, 2, 3, 4, and 5. These five Middle Siwaliks sandstone samples are part of the Butwal transect, and were collected between the Main Frontal Thrust and the Main Boundary Thrust. For a geological description of the area, see Gautam and Apple (1997), and Szulc et al. (2006).

Table 2: *Butwal sample details. Lithologies from Tokuoka et al. (1988). For full details of the dose-rate calculation see section 2.3.2 and Supplementary Tables S3 and S4.*

Samples Butwal			**Whole-rock radiochemistry**			**Dose Rate**
ID	**Alt.**	**Lithology**	**U**	**Th**	**K**	**Ḋ**
	[m]		**[ppm]**	**[ppm]**	**[wt.%]**	**[Gy/ka]**
BUT.5	322	Sandstones, Middle Binai Khola Fm. / Middle Siwalik	1.8	5.2	0.75	2.08 ± 0.11
BUT.4	317	Sandstones, Lower Binai Khola Fm. / Middle Siwalik	1.8	7.3	1.24	2.59 ± 0.14
BUT.3	298	Sandstones, Upper Arung Khola Fm. / Lower Siwalik	1.9	8.3	1.22	2.65 ± 0.14
BUT.2	300	Sandstones, Upper Arung Khola Fm. / Lower Siwalik	1.7	7.6	0.95	2.36 ± 0.12
BUT.1	204	Sandstones, Upper Arung Khola Fm. / Lower Siwalik	1.7	9.2	0.83	2.37 ± 0.12

2.2.3. Control samples

To evaluate whether different feldspar minerals and lithologies require different measurement conditions for the derivation of thermal kinetic parameters, data from ten previously analysed feldspar samples from the literature, and two further museum-specimens of Na-feldspar, are investigated as control samples. The samples were separated into different categories based on their orthoclase (Or, $KAlSi_3O_8$), albite (Ab, $NaAlSi_3O_8$), and anorthite (An, $CaAl_2Si_2O_8$) composition (Table 3, and Ternary plot in Fig. S1 of the Supplementary material).

Table 3: *Mineralogical composition of feldspars of different origins and lithologies. Ternary plot in the Supplementary material (Fig. S1).*

ID	Type	Lithology	Feldspar composition assuming 100 % feldspar			Quartz content
			Or (K)	Ab (Na)	An (Ca)	[%]
NB139 [a]	B	Migmatitic gneiss, Namche Barwa, Nepal	**89.3**	9.4	1.4	4.2
NB120 [a]	B	Migmatitic gneiss, Namche Barwa, Nepal	**86.2**	11.0	2.9	5.0
MBT-I-2430 [a]	B	Calc-alkaline granite, Mont-Blanc Tunnel, Italy	**86.7**	12.0	1.3	4.2
KRG-16-06 [a]	B	Kurobegawa granite, Japanese Alps, Japan	**79.4**	17.3	3.2	3.1
KRG-16-112 [a]	B	Kurobegawa granite, Japanese Alps, Japan	**75.2**	21.3	3.5	3.4
JSH1-13 [a]	S	Sand, Shirasuka Lowlands, Japan	**50.4**	37.6	12.1	38.1
HAM-5 [a]	S	Lake sediment, Lake Hamana, Japan	**64.9**	31.1	4.0	19.3
F1 [a]	R	IAEA AQCS reference feldspar	**61.3**	33.4	5.4	0.3
CLE [a]	M	Pegmatite, Golonca District, Minas Gerais, Brazil	0.5	**99.3**	0.2	3.9
Al-I [b]	M	Metamorphic albite, Pinzele, Trente, Italy	1.0	**97.0**	2.0	5.0
KNR169 62 [c]	M	Albite, Ljosland, Iveland, Agder, Norway	4.6	**81.6**	13.8	64.7
KNR324 91 [c]	M	Albite, Seiland, Alta, Finnmark, Norway	4.3	**71.6**	24.0	61.7
KTB.253F [d]	B	Garnet-amphibolite, KTB borehole, Germany	5.9	**68.8**	25.3	21.9
KTB.383C [d]	B	Sillimanite-muscovite-biotite-gneiss, KTB borehole, Germany	18.2	**67.4**	14.4	52.8
KTB.428B [d]	B	Garnet-sillimanite-biotite-gneiss, KTB borehole, Germany	8.2	**77.9**	13.8	51.5
KTB.481B [d]	B	Garnet-sillimanite-biotite-gneiss, KTB borehole, Germany	15.6	**66.7**	17.8	72.5
BUT.5 [e]	S	Sandstones, Middle Binai Khola Fm. / Middle Siwalik, Nepal	**96.0**	2.6	1.4	81.2
BUT.4 [e]	S	Sandstones, Lower Binai Khola Fm. / Middle Siwalik, Nepal	**89.0**	11.0	0.0	55.3
BUT.3 [e]	S	Sandstones, Upper Arung Khola Fm. / Lower Siwalik, Nepal	**86.3**	13.6	0.1	51.4
BUT.2 [e]	S	Sandstones, Upper Arung Khola Fm. / Lower Siwalik, Nepal	**88.4**	11.4	0.2	70.2
BUT.1 [e]	S	Sandstones, Upper Arung Khola Fm. / Lower Siwalik, Nepal	**95.8**	0.0	4.2	90.8

Notes: Data taken from [a] Riedesel et al., 2019; [b] Riedesel et al., 2021; [c] X-Ray Fluorescence (XRF) at the University of Lausanne; [d] Guralnik et al., 2015b; [e] Mineralogical composition determined using an XRF-attachment fixed to a Risø OSL/TL reader (Kook et al., 2012) at the Leibniz Institute of Applied Geophysics in Hannover. B: Bedrock; S: Sedimentary rocks; R: Reference sample; M: Museum-specimen.

2.3. Luminescence measurements

2.3.1. Sample preparation

Feldspar minerals were extracted using standard methods (e.g., King et al., 2016a) under subdued red-light conditions. The outer part of the samples (1-3 cm) was removed using a water-cooled diamond saw to remove any potentially light exposed material. The light safe samples were then crushed and sieved to extract the grain-size fraction of interest (180-210 µm). Carbonates and organic material were removed using 10 % HCl and 30 % H_2O_2 respectively. Finally, the K-feldspar enriched fraction was isolated using density separation with sodium polytungstate of $\rho < 2.58$ g.cm^{-3}. The two Na-feldspar museum-specimens KNR16962 and KNR32491 prepared for this study were directly hand-crushed to sand-sized fragments.

2.3.2. Environmental dose rate Ḋ

For the Butwal samples, the dose rate $\dot{D}$ was calculated for each sample. A representative sub-sample of the light exposed sample exterior was sent to ActLabs – Activation Laboratories Ltd, Ancaster, Canada, for ICP-MS analysis to determine the concentration of U, Th and K for environmental dose rate determination. Thin-sections of the samples were prepared to quantify grain size, which influences the environmental radiation dose rate due to grain size attenuation effects.

The original grain size (before crushing) was estimated from thin-section images using the software Digital Grain Size developed by Buscombe (2013). When the average grain size of the sample was equivalent to or smaller than the grain size of the feldspar extract analysed (180-210 µm), the latter grain size was adopted for the dose rate calculations. The dose rate was then determined using the Dose Rate and Age Calculator DRAC developed by Durcan et al. (2015), with the conversion factors of Guérin et al. (2011), the alpha grain-size attenuation factors of Brennan et al. (1991), and the beta grain-size attenuation factors of Guérin et al. (2012). An alpha-efficiency (a-value) of 0.15 ± 0.05 (Balescu and Lamothe, 1994), and a water content of 25 ± 10 % were used for the sandstone samples of the Butwal transect. No cosmic dose rate was incorporated in the final dose rate estimations as the samples are thought to have been at the surface for a relatively short period of time.

The DRAC input and output tables for the Butwal samples are provided in Supplementary Table S4. For samples for which it was not possible to calculate an environmental dose rate, such as the museum specimens for which only a limited amount of material was available, a dose rate of 3.00 ± 0.50 Gy/ka was arbitrarily assumed (see Supplementary Table S5).

2.3.3. Luminescence thermochronometry measurement protocol

Samples were measured in the luminescence laboratory at the University of Lausanne, Switzerland. Feldspar grains were mounted on 10 mm diameter stainless steel discs as small aliquots of ~2 mm diameter. Three aliquots were measured for each sample for the luminescence thermochronometry measurements (dose response curve, fading, isothermal decay). The measurements were done on TL/OSL-DA-20 Risø luminescence readers, and signals were detected in the blue part of the visible spectrum using a BG39 and BG3 filter.

A multi-elevated temperature (MET) post-infrared infrared-stimulated luminescence (post-IR IRSL) – MET-pIRIR – protocol (Li and Li, 2011) was used for all measurements. All of the measurements were done under the same conditions. After a preheat at 250 °C for 60 s, four IRSL measurements at 50, 100, 150 and 225 °C were made for a duration of 100 s each (L_x). A test dose of 75-95 Gy (beta radiation) was given to the aliquots, before measuring the test dose signal (T_x) for each stimulation temperature (50, 100, 150, and 225 °C). Each measurement cycle was followed by infrared bleaching at 290 °C for 60 s. All luminescence signals were integrated over the 5 first channels (2 s) of the luminescence decay curve, with a background subtraction calculated over the last 50 channels (20 s). Aliquots were accepted and included in the study when they fulfilled all of the sample acceptance criteria, i.e. signal greater than 3σ above background, recycling ratio within 10 % of unity, maximum test dose uncertainty < 10 %, and recuperation < 10 % of the natural signal.

To constrain the fraction of trapped charge $\tilde{n}$, the natural luminescence signal stored in the feldspar minerals was first measured with the four stimulation temperatures. Nine regenerative doses between 0 and 6000 Gy were then given to the aliquots to construct sample specific dose response curves. Data were fitted using equation 5 to derive D_0.

Athermal signal loss was then measured under the same conditions, using the same aliquots. After the administration of a fixed regenerative dose of 75-95 Gy, equal to the test dose, aliquots were preheated prior to storage following Auclair et al. (2003) and measured following different delay periods. Data were fitted using equations 3 and 4 and the model of Huntley (2006) for the natural samples; the approach of Kars et al. (2008) was used to screen whether the samples were in athermal steady-state, or whether they exhibited disequilibrium (i.e. contained a thermal signal), through comparison of $\tilde{n}_{nat}$ values with those predicted for athermal steady-state $\tilde{n}_{SS}$ calculated using equation 15 of Li and Li (2008).

Finally, thermal signal loss was measured using isothermal decay measurements on one representative aliquot of each of the samples. The isothermal decay of each signal was measured using storage temperatures in the range of 170-350 °C, with isothermal delay times of 1 to 10,000 s. All data were fitted using the band tail states model (Li and Li, 2013), using equations 6 and 7 to extract the thermal kinetic parameters E_t, E_u, and s.

To control the quality of the data, a dose recovery test was done on each of the KTB and Butwal samples. Six new aliquots were prepared and bleached with natural sunlight for

4 h; three discs were then given a laboratory dose, whilst the other three discs were used to measure the unbleached residual signal. Dose recovery ratios were calculated following residual subtraction. Two different doses were given to the samples, either a dose similar to the D_e of the IRSL.50 signal was used, or a dose of 150 Gy. This second approach was used more widely as most of the Butwal samples are saturated or close to saturation, prohibiting the use of a dose equal to their D_e.

2.4. Data inversion for isothermal temperature

Guralnik et al. (2015b) successfully constrained the thermal histories of the KTB samples using the GOK model and three isothermal holding temperatures at 190, 210 and 230 °C. In contrast, King et al. (2016a) used seven different temperatures to determine thermal kinetic parameters for samples from Namche Barwa, ranging in temperature from 170 to 350 °C. To evaluate whether there is any benefit in using a larger range of isothermal holding temperatures, which necessarily increases sample measurement time, luminescence signals using different combinations of ITL measurements were compared using forward and inverse modelling.

To evaluate the sensitivity of the thermal kinetic parameters to the inclusion/exclusion of different ITL measurements, ITL data were excluded or included in different combinations of three to seven temperatures. The resulting kinetic parameters were then used together with the $\tilde{n}_{nat}$ values to invert for isothermal temperature using equations 1 and 2 and the approach described below. Whilst the KTB samples are assumed to have experienced an isothermal history, this is not necessarily the case for the Butwal samples. However, inverting these data for isothermal temperature enables the effect of different ITL combinations to be tested.

For each set of kinetic parameters determined using a different combination of ITL data, a Monte Carlo model with 100 iterations randomly sampled values of the thermal kinetic parameters (E_t, E_u, and s) from within their 1σ uncertainties. Synthetic $\tilde{n}_{mod}$ values for each IRSL signal were then generated for different isothermal histories, using equations 1 and 2, that describe the growth and loss of the luminescence signal through time. The model assumed isothermal holding over a period of 1 Myr to ensure that the luminescence signals generated were in steady-state (i.e., were in a dynamic equilibrium between rates of electron trapping and detrapping), rather than reflecting continued signal growth. Temperatures ranging from 0 to 100 °C in 1 °C intervals were modelled for the natural temperature of the KTB and Butwal samples. Finally, the data were passed through a rejection algorithm (Tarantola, 2005). The final $\tilde{n}_{mod}$ value, $\tilde{n}_{mod}(end)$, was extracted for each synthetic isothermal history, and contrasted with the $\tilde{n}_{nat}$ values to calculate the misfit, after Wheelock et al. (2015), as previously implemented by King et al. (2020) and Biswas et al. (2020):

$$Misfit = \left(0.5 \left(\frac{\tilde{n}_{nat}}{s\tilde{n}_{nat}} . log \frac{\tilde{n}_{nat}}{\tilde{n}_{mod}(end)}\right)\right)^2 \quad [8]$$

with $s\tilde{n}_{nat}$ being the uncertainty on $\tilde{n}_{nat}$. From this, the likelihood is calculated:

$$Likelihood = exp(-Misfit) \quad [9]$$

Likelihood values are compared to a random number between 0 and 1. If the likelihood is greater than this number, the isothermal history is accepted, otherwise it is rejected. In this way, thermal histories from the full range of possibilities can be accepted, but the probability of accepting histories with a bad fit (low likelihood) is low. A probability density function of the inverted temperatures can then be constructed from the retained paths (Fig. 1).

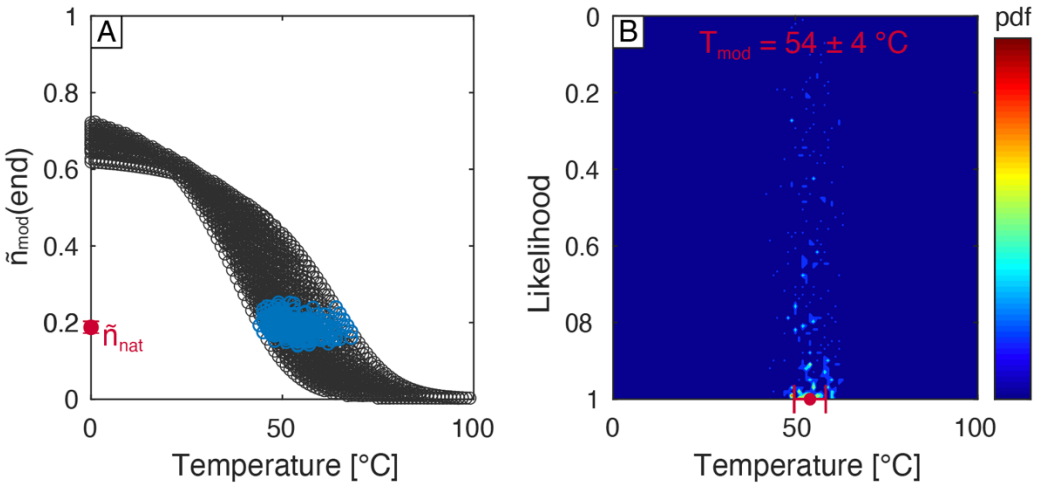

Fig. 1: *Inversion of the IRSL.50 signal of sample KTB.383C, using kinetic parameters derived from four isothermal temperatures between 190 and 250 °C.* ***A.*** *Distribution of the $\tilde{n}_{mod}(end)$ values for different isothermal temperature predictions. The red dot represents the $\tilde{n}_{nat}$ value, and the blue area highlights the data that passed the rejection algorithm.* ***B.*** *Probability density function resulting from the accepted data in A.*

2.5. High temperature irradiation experiments

Natural samples in thermal steady-state that have experienced a known-isothermal history, such as the Na-feldspars of the KTB borehole, are not always readily available. Instead, it may be possible to create artificial calibration samples in the laboratory by irradiating samples at elevated temperatures. Sample BUT.4 (K-feldspar) and sample KTB.428B (Na-feldspar) were chosen as synthetic calibration samples. While BUT.4 was selected as a suitable synthetic calibration sample because of its favourable luminescence properties, sample KTB.428B serves to confirm the validity of the synthetic calibration experiment.

Prior to irradiation of the sample at elevated temperature, it is first necessary to predict luminescence trap occupancy for the specific thermal electron trapping and detrapping rates. The natural dose rate of sample BUT.4 is $\dot{D}_{nat}$ = 2.59 ± 0.14 Gy/ka, however at the time of the experiment in the laboratory, the instrument dose rate was $\dot{D}_{lab} \approx (3.627 \pm 0.095) \times 10^9$ Gy/ka = 0.116 ± 0.003 Gy/s, which is nine orders of magnitude greater. In the same manner, the natural dose rate of sample KTB.428B is $\dot{D}_{nat}$ = 3.44 ± 0.52 Gy/ka, and $\dot{D}_{lab} \approx (3.595 \pm 0.095) \times 10^9$ Gy/ka = 0.114 ± 0.003 Gy/s at the time of the experiment. As laboratory dose rates are so much greater than those in nature, it is practical to rapidly irradiate a sample into a thermal steady-state condition, within a matter of hours.

Using equations 1 and 2, synthetic $\tilde{n}_{mod}$ values were calculated for a range of different isothermal histories, for each IRSL signal. These forward models were run assuming laboratory irradiation and isothermal holding over a period of 24 h to ensure that thermal steady-state was reached, at temperatures ranging from 0 to 300 °C in 10 °C intervals. Note however that thermal equilibrium is reached after only a few minutes to a few hours of irradiation, dependent on the isothermal temperature and on the luminescence signal measurement temperature. The results of the forward modelling are shown in Table 4. The average uncertainty on the $\tilde{n}_{nat}$ values of the samples investigated here is ~0.03, which is effectively the limit of detection for our measurements. For that reason, three temperatures were selected for sample BUT.4, between which the $\tilde{n}_{mod}$ values differed by > 0.03. Irradiations at 200 °C, 250 °C, 300 °C were selected as they result in measurably different $\tilde{n}$ values (Fig. 2). Irradiation at 250 °C only was carried out for sample KTB.428B as this sample provides validation of the approach.

Table 4: *$\tilde{n}_{mod}(end)$ values for the elevated temperature irradiation experiments. Irradiation was done for 24 h, with instrument dose rate of $\dot{D}_{lab} \approx (3.627 \pm 0.095) \times 10^9$ Gy/ka = 0.116 ± 0.003 Gy/s for sample BUT.4, and $\dot{D}_{lab} \approx (3.595 \pm 0.095) \times 10^9$ Gy/ka = 0.114 ± 0.003 Gy/s for sample KTB.428B.*

Sample	Irradiation temperature [°C]	$\tilde{n}_{mod}$(end) IRSL.50	$\tilde{n}_{mod}$(end) IRSL.100	$\tilde{n}_{mod}$(end) IRSL.150	$\tilde{n}_{mod}$(end) IRSL.225
BUT.4	200 °C	0.655	0.764	0.828	0.880
	250 °C	0.211	0.335	0.462	0.638
	300 °C	0.018	0.038	0.073	0.182
KTB.428B	250 °C	0.189	0.389	0.376	0.361

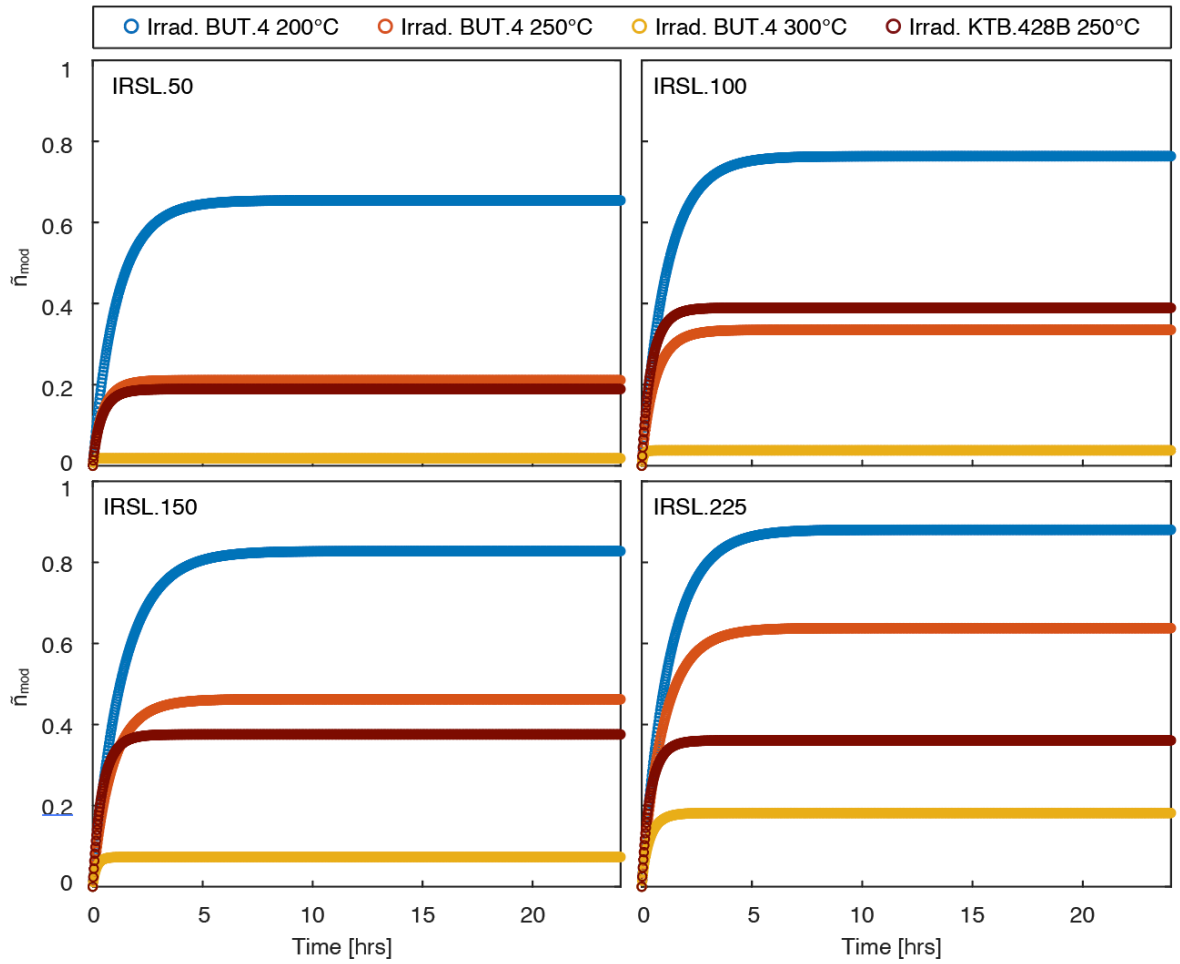

Fig. 2: *Evolution of $\tilde{n}_{mod}$ values for the elevated temperature irradiation experiments. See caption of Table 4 for the irradiation conditions.*

Experimentally, three aliquots of each sample were first bleached with a solar simulator for 1 h, to remove all pre-existing luminescence signals. They were then placed in a Risø TL-DA-20 instrument (instrument 355), where after irradiation for 24 h at high temperature (200, 250, and 300 °C), dose response curves were measured at ambient laboratory temperatures (~20-25 °C) using the protocol described in section 2.3.3 to constrain the laboratory induced trapped charge concentration $\tilde{n}_{synth.lab}$. The samples were then inverted for irradiation temperature using the existing isothermal decay and anomalous fading data, and the modelling approach described in section 2.1. To evaluate which temperature these high temperature irradiation experiments would correspond to under natural environmental irradiation conditions, the data were again inverted, replacing the laboratory dose rate by the natural sample dose rate.

3. Results

3.1. Luminescence measurements

All of the samples were measured following the protocol described in section 2.3. The four KTB borehole (Germany) samples, and the five Butwal transect (Nepal) samples passed the aliquot acceptance criteria for all IRSL measurements, and the measurements were reproducible within error for each sample (n = 3). The IRSL.50 signals were generally brighter than the other IRSL signals. This was particularly evident for the KTB samples, for which post-IR signals were ~75 % less bright, but still yielded good counting statistics.

For the isothermal holding data (Fig. 3C and 3F), the band-tail states model fits the data well for the lower holding temperatures (170-200 °C). However, there is a misfit in the lower part of the curves between the measured and modelled values for the 250, 300, and 350 °C ITL temperatures. This misfit has been reported previously for samples from the Mont-blanc massif (Lambert, 2018).

The two sets of samples exhibit different behaviours regarding their thermal and athermal stabilities (Fig. 3.G and 3.H). Whereas the KTB samples exhibit similar $\tilde{n}$ values between the three post-IR temperatures at 100, 150, and 225 °C, results of the four IRSL measurement temperatures for the Butwal samples are distinct. The $\tilde{n}_{nat}$ values are thermally and athermally dependent, whereas the $\tilde{n}_{SS}$ values are computed considering only athermal signal loss. Here, for the KTB samples, IRSL.50 $\tilde{n}_{nat}$ values are lower than the values of the other IRSL temperatures, which give quasi-identical $\tilde{n}_{nat}$ values. This difference in $\tilde{n}_{nat}$ can be explained by the fact that the IRSL.50 is less thermally stable than the post-IR signals, that have similar thermal stability. This variation in $\tilde{n}_{nat}$ and $\tilde{n}_{SS}$ values also reflects a difference in athermal stability of the IRSL signals for the samples 383C, 428B, and 481B. The IRSL.50 signal of these samples has a higher fading than the rest of the IRSL signals, that have similar rates of anomalous fading. This pattern is confirmed by the fading rates (expressed as g-values normalised to 2 days, $g2d$, Huntley and Lamothe, 2001) presented in Table 5.

In contrast, the Butwal samples show an increase in $\tilde{n}_{nat}$ values with an increase in IRSL measurement temperature. These samples are closer to saturation than the KTB samples, but almost all $\tilde{n}_{nat}$ values are below 86 % of $\tilde{n}_{SS}$, which is the saturation limit ($2D_0$). An exception is the IRSL.150 signal of sample BUT.1 that is fully saturated, and the IRSL.225 signal of sample BUT.5 that is just at the upper limit of saturation.

The kinetic parameters are similar for the different IRSL signals of samples from the same transect. The similarity is more pronounced for the samples of the Butwal transect than for the samples of the KTB borehole. Sample KTB.253F in particular exhibits different behaviour as compared to the other KTB samples. Whereas for most samples fading rates

reduce with increasing measurement temperature, sample KTB.253F shows an increase in $g2d$ values with increasing measurement temperature. Whereas the D_e values reduce with depth because of increasing temperature for the KTB samples, the D_e values are similar between the different surface samples of the Butwal transect

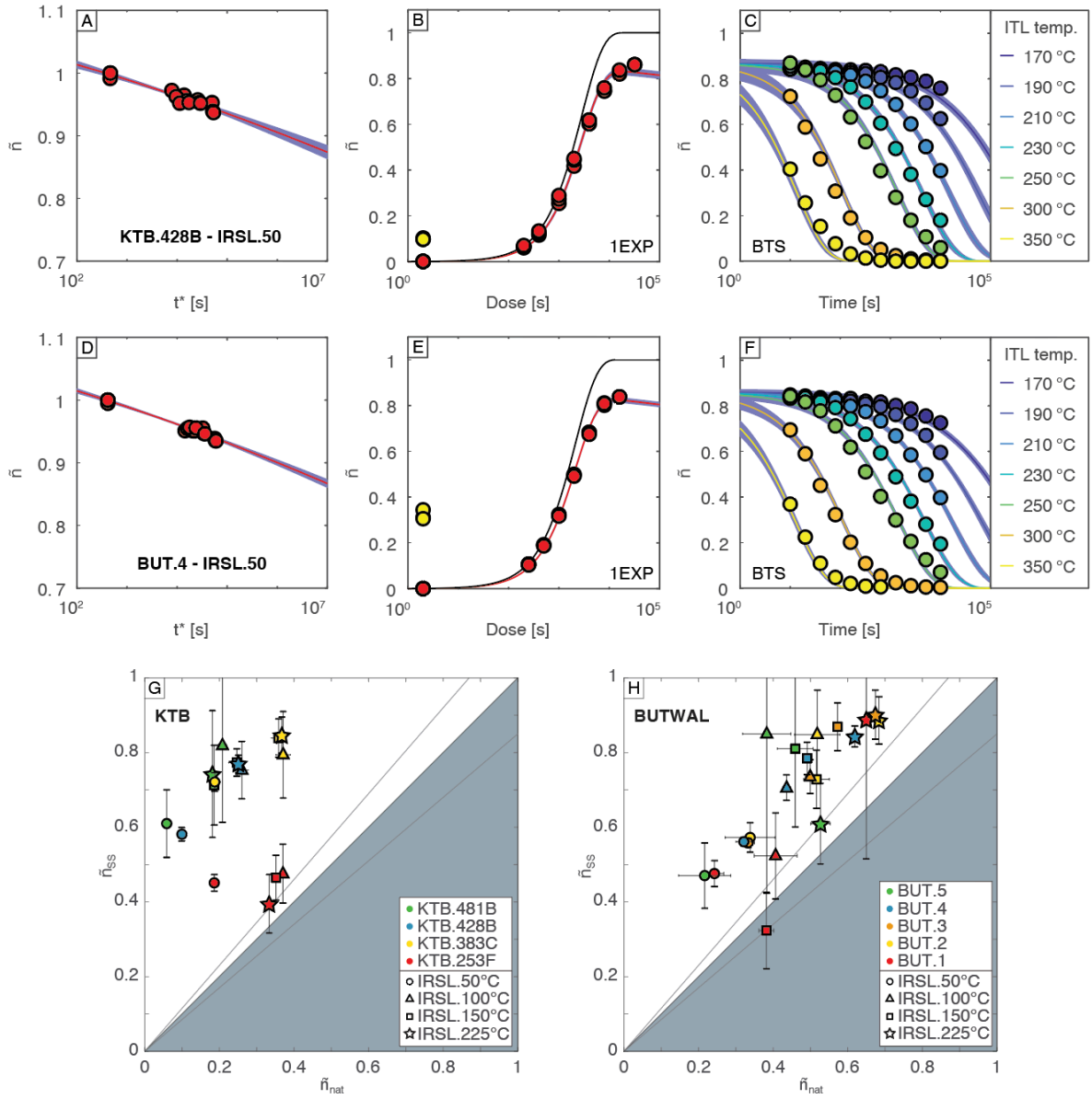

Fig. 3: *Luminescence measurement and model fit results for the IRSL.50 signal of one KTB and one Butwal sample. (A, D) Anomalous fading data fitted using equations 3 and 4. (B, E) Luminescence dose response fitted using equation 5. The black solid line is the unfaded dose response curve. (C, F) Isothermal decay data fitted using equations 6 and 7. (G, H) Saturation plots (Kars plots) contrasting $\tilde{n}_{nat}$ with $\tilde{n}_{SS}$ predicted for each of the KTB and Butwal samples, respectively.*

Table 5: *Kinetic parameters of the KTB and Butwal samples, for all four IRSL temperatures, using kinetic parameters derived from four isothermal temperatures between 190 and 250 °C.*

Sample / IRSL		Et [eV]	Eu [eV]	log10 s [s^{-1}]	log10 ρ' [-]	g2d [%]	De [Gy]	D0 [Gy]	ñ [-]
KTB.253F	**50**	1.58 ± 0.06	0.08 ± 0.01	11.83 ± 0.58	-5.55 ± 0.03	3.73 ± 0.24	197 ± 10	389 ± 14	0.19 ± 0.00
	100	1.63 ± 0.11	0.10 ± 0.01	11.85 ± 1.08	-5.57 ± 0.10	3.67 ± 0.81	336 ± 17	235 ± 7	0.37 ± 0.01
	150	1.61 ± 0.10	0.09 ± 0.01	11.81 ± 1.01	-5.56 ± 0.07	3.87 ± 0.65	330 ± 17	247 ± 9	0.35 ± 0.01
	225	1.60 ± 0.09	0.10 ± 0.01	11.74 ± 0.93	-5.47 ± 0.09	4.50 ± 0.97	364 ± 18	210 ± 9	0.33 ± 0.01
KTB.383C	**50**	1.57 ± 0.06	0.08 ± 0.01	11.58 ± 0.56	-5.92 ± 0.04	1.62 ± 0.17	96 ± 5	326 ± 12	0.19 ± 0.02
	100	1.63 ± 0.08	0.09 ± 0.01	11.75 ± 0.81	-6.06 ± 0.23	1.21 ± 0.63	126 ± 6	204 ± 7	0.37 ± 0.02
	150	1.62 ± 0.09	0.09 ± 0.01	11.65 ± 0.86	-6.18 ± 0.13	0.92 ± 0.28	120 ± 6	218 ± 8	0.36 ± 0.02
	225	1.58 ± 0.08	0.09 ± 0.01	11.35 ± 0.79	-6.20 ± 0.13	0.89 ± 0.27	111 ± 6	198 ± 6	0.37 ± 0.01
KTB.428B	**50**	1.61 ± 0.06	0.08 ± 0.01	11.93 ± 0.54	-5.71 ± 0.02	2.62 ± 0.15	100 ± 5	552 ± 17	0.10 ± 0.00
	100	1.64 ± 0.08	0.09 ± 0.01	11.88 ± 0.81	-5.98 ± 0.14	1.44 ± 0.46	135 ± 7	323 ± 10	0.26 ± 0.02
	150	1.61 ± 0.08	0.08 ± 0.01	11.68 ± 0.73	-6.02 ± 0.08	1.31 ± 0.22	126 ± 6	333 ± 11	0.25 ± 0.02
	225	1.62 ± 0.07	0.08 ± 0.01	11.81 ± 0.67	-6.01 ± 0.05	1.35 ± 0.15	120 ± 6	308 ± 10	0.25 ± 0.02
KTB.481B	**50**	1.55 ± 0.06	0.08 ± 0.01	11.16 ± 0.60	-5.75 ± 0.12	2.39 ± 0.68	52 ± 3	531 ± 21	0.06 ± 0.00
	100	1.60 ± 0.08	0.09 ± 0.01	11.29 ± 0.77	-6.13 ± 0.39	1.02 ± 0.93	79 ± 4	275 ± 9	0.21 ± 0.01
	150	1.58 ± 0.08	0.09 ± 0.01	11.16 ± 0.75	-5.90 ± 0.17	1.72 ± 0.68	83 ± 4	282 ± 10	0.19 ± 0.00
	225	1.59 ± 0.07	0.09 ± 0.01	11.32 ± 0.71	-5.95 ± 0.27	1.51 ± 0.95	77 ± 4	279 ± 13	0.18 ± 0.00
BUT.5	**50**	1.38 ± 0.08	0.10 ± 0.01	9.04 ± 0.80	-5.58 ± 0.11	3.47 ± 0.84	459 ± 23	781 ± 28	0.22 ± 0.07
	100	1.50 ± 0.07	0.09 ± 0.01	9.96 ± 0.69	-6.24 ± 0.73	0.80 ± 1.30	385 ± 19	650 ± 27	0.38 ± 0.06
	150	1.42 ± 0.08	0.08 ± 0.00	8.69 ± 0.72	-6.13 ± 0.39	1.04 ± 0.91	543 ± 27	659 ± 25	0.46 ± 0.05
	225	1.66 ± 0.08	0.09 ± 0.00	10.55 ± 0.79	-5.76 ± 0.14	2.39 ± 0.79	1080 ± 54	561 ± 24	0.53 ± 0.03
BUT.4	**50**	1.54 ± 0.06	0.08 ± 0.01	11.20 ± 0.60	-5.68 ± 0.01	2.78 ± 0.10	361± 18	442 ± 9	0.32 ± 0.02
	100	1.52 ± 0.06	0.08 ± 0.00	10.74 ± 0.53	-5.90 ± 0.06	1.70 ± 0.23	399 ± 20	426 ± 10	0.44 ± 0.01
	150	1.51 ± 0.06	0.08 ± 0.00	10.24 ± 0.59	-6.06 ± 0.09	1.22 ± 0.26	473 ± 24	489 ± 13	0.49 ± 0.01
	225	1.53 ± 0.06	0.08 ± 0.00	9.95 ± 0.54	-6.21 ± 0.08	0.85 ± 0.16	569 ± 28	436 ± 14	0.62 ± 0.02
BUT.3	**50**	1.53 ± 0.06	0.09 ± 0.01	10.90 ± 0.59	-5.68 ± 0.02	2.79 ± 0.11	419 ± 21	480 ± 16	0.33 ± 0.02
	100	1.55 ± 0.06	0.08 ± 0.00	10.96 ± 0.57	-5.95 ± 0.08	1.51 ± 0.28	421 ± 21	378 ± 11	0.50 ± 0.01
	150	1.47 ± 0.06	0.07 ± 0.00	9.92 ± 0.57	-6.29 ± 0.19	0.69 ± 0.31	441 ± 22	414 ± 14	0.57 ± 0.01
	225	1.50 ± 0.06	0.08 ± 0.00	9.59 ± 0.59	-6.42 ± 0.24	0.52 ± 0.29	499 ± 25	365 ± 15	0.67 ± 0.01
BUT.2	**50**	1.54 ± 0.06	0.08 ± 0.00	10.45 ± 0.54	-5.70 ± 0.05	2.64 ± 0.32	472 ± 24	548 ± 19	0.34 ± 0.07
	100	1.55 ± 0.09	0.08 ± 0.01	10.33 ± 0.82	-6.23 ± 0.28	0.83 ± 0.54	392 ± 20	419 ± 16	0.52 ± 0.06
	150	1.56 ± 0.10	0.07 ± 0.01	10.47 ± 0.97	-5.94 ± 0.13	1.54 ± 0.48	522 ± 26	432 ± 18	0.52 ± 0.03
	225	1.60 ± 0.10	0.08 ± 0.01	10.48 ± 0.93	-6.36 ± 0.21	0.60 ± 0.29	492 ± 25	336 ± 17	0.68 ± 0.02
BUT.1	**50**	1.43 ± 0.07	0.09 ± 0.01	9.44 ± 0.64	-5.58 ± 0.04	3.47 ± 0.34	425 ± 21	626 ± 20	0.24 ± 0.03
	100	1.56 ± 0.16	0.08 ± 0.01	10.66 ± 1.54	-5.63 ± 0.14	3.12 ± 1.02	658 ± 33	459 ± 24	0.41 ± 0.06
	150	1.59 ± 0.17	0.09 ± 0.01	10.77 ± 1.61	-5.39 ± 0.12	5.48 ± 1.54	1385 ± 66	407 ± 19	0.38 ± 0.02
	225	1.46 ± 0.11	0.08 ± 0.01	9.29 ± 0.99	-6.37 ± 0.75	0.59 ± 1.02	419 ± 21	322 ± 15	0.65 ± 0.01

3.2. Inversion for isothermal temperature

3.2.1. KTB borehole: known-temperature samples

The results of the temperature inversion using different ITL combinations for the KTB samples are presented in Fig. 4. The difference between the predicted temperature values and the in-situ temperature values for the KTB samples studied can be used to assess which ITL combination should be used to yield reliable thermal histories.

Different ITL combinations yield different inverted temperatures. The higher the end-temperature of the ITL combination, the lower the modelled temperature. When the ITL data for temperatures of 300 or 350 °C are included, or if all seven isothermal holding temperatures are used, the KTB borehole temperatures are not recovered, even within error (grey areas in Fig. 4).

3.2.2. Butwal transect: unknown-temperature samples

The K-feldspar samples of the Butwal transect have no independent temperature control and were collected at the surface, on bedrock outcrops. Their inversion for ambient temperature (Fig. 5) might not reflect the thermal reality of the sample and rather than reflecting surface temperature, it may relate to the cooling history experienced by these rocks.

For the Butwal samples (Fig. 5), there is less variation in the inverted temperatures with different combinations of ITL temperatures, relative to the KTB samples (Fig. 4). All of the inversions give modelled temperatures below 60 °C, with an average for all the ITL combinations of around 30 °C. A visible exception is the IRSL.150 signal of sample BUT.1, that gives inverted temperatures around 17 °C, ~15 °C below the results of the other samples and IRSL signals.

3.2.3. Control samples: unknown-temperature samples

The twelve control samples have a range of trapped charge concentrations. As the natural trapped charge concentration partly controls the inverted temperatures, all inverted temperatures were normalised to an average value to facilitate comparison (Fig. 6). This was done by fitting the data with a linear regression and by moving the origin of the regression lines to the same initial temperature.

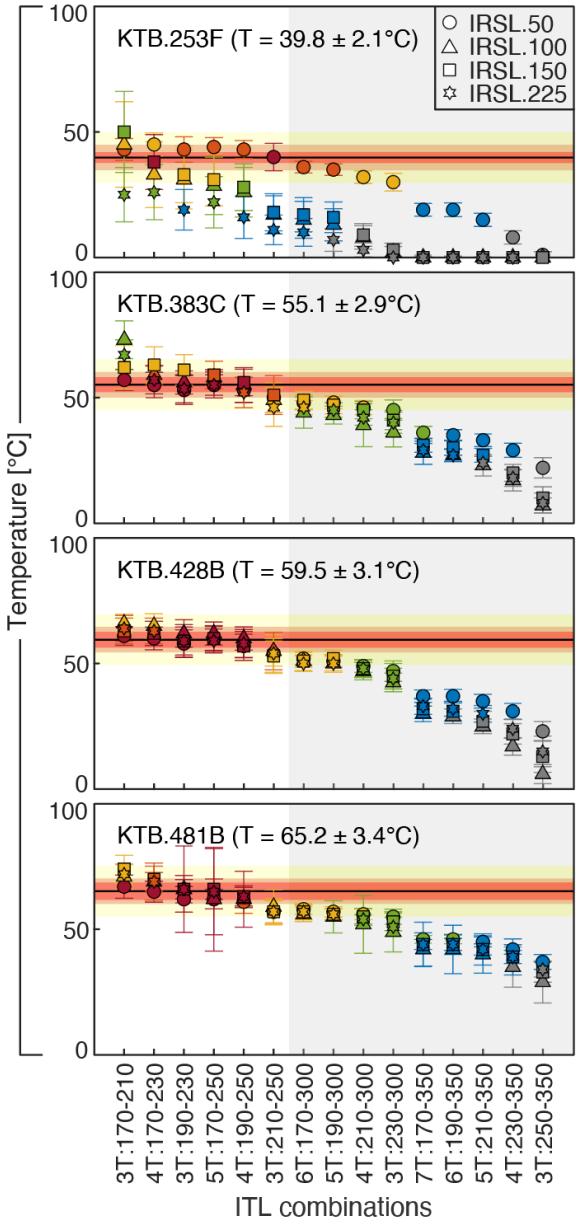

Fig. 4: *Results of the inversion for isothermal temperatures for the KTB borehole samples. Different combinations of ITL temperatures are tested. The different colours represent how close the inverted temperatures are to the target in-situ temperature. The red area and the red dots are modelled temperatures within the error range of the in-situ temperature, the orange area and dots are within 5 °C of the target-temperature, and the yellow area and dots are within 10 °C of the target-temperature. The green dots have a difference of 10 to 20 °C with the in-situ temperature, 20 to 30 °C for the blue dots, and above 30 °C for the grey dots. The solid black line is the target in-situ temperature, and the red-coloured areas represent the error on this temperature. The grey area highlights the ITL combinations that do not successfully recover the in-situ temperature of the KTB borehole, within error.*

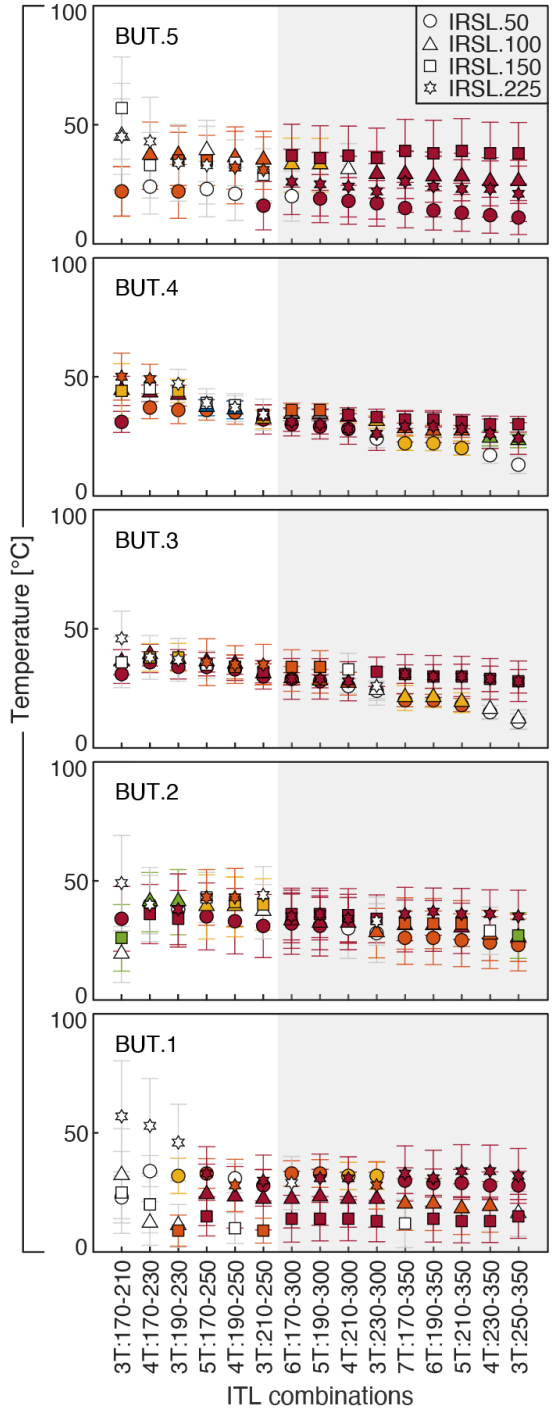

Fig. 5: *Results of the inversion for isothermal temperatures for the Butwal samples. Different combinations of ITL temperatures are tested. The different colours represent different temperature plateaux identified using a nearest neighbour MATLAB cluster function, that regroups temperatures by how close they are to each other, independent of their position on the x-axis. The largest plateaux are in red (then orange, yellow, green, blue, and grey). White data points are ITL combinations for which there is no plateau (only one data point yields this temperature).*

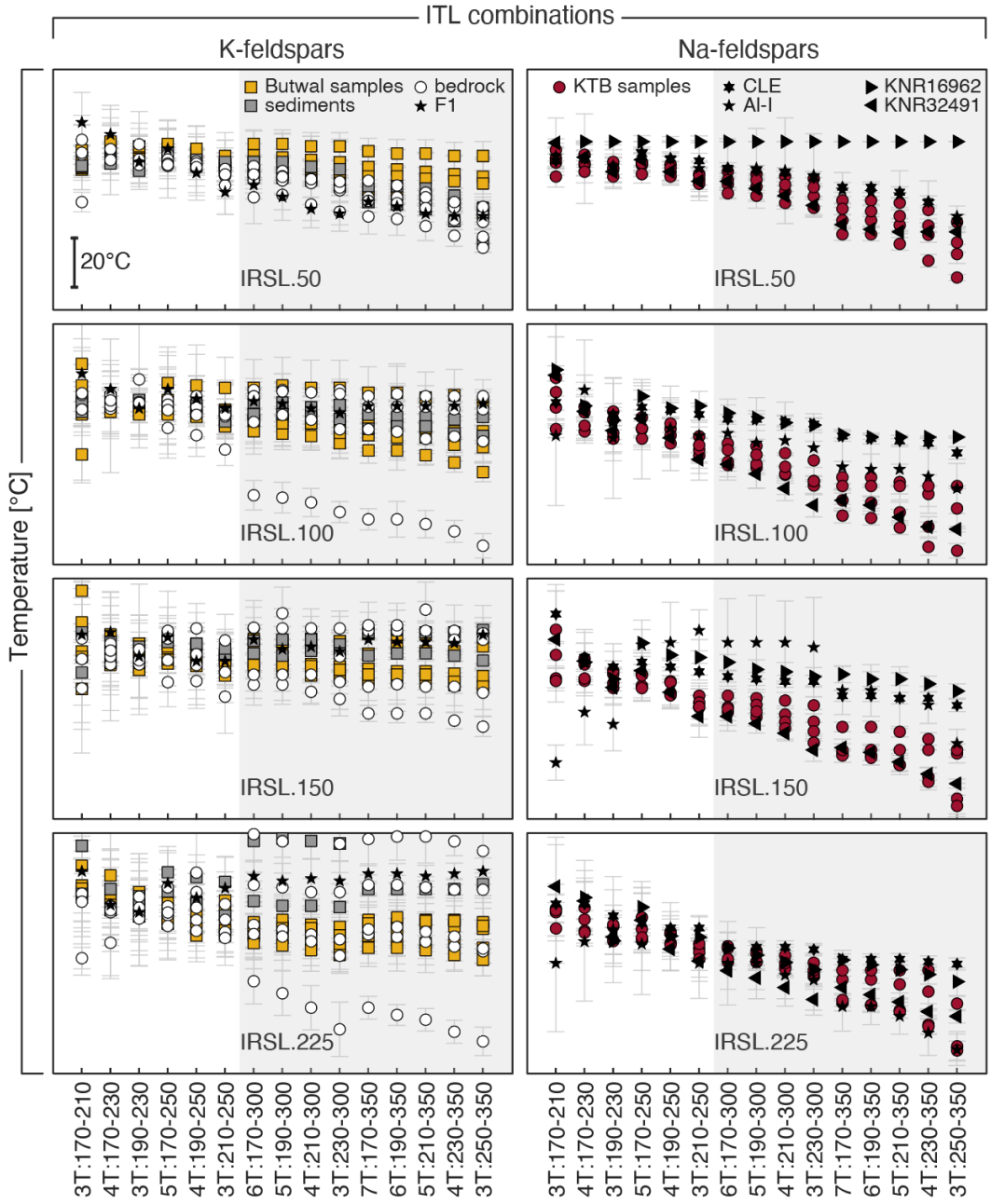

Fig. 6: *Normalised results of the inversion of the control samples, the KTB and Butwal samples. Samples details are given in Table 3.*

Despite their difference in mineralogy and lithology, the samples generally depict the same trend: a decrease in inverted temperature with the inclusion of higher temperature ITL data (Fig. 6). For most samples, there is a change in behaviour in the data when the final temperature of the ITL combination passes from 250 °C to 300 °C. The scatter between the different inverted temperatures increases, and the inverted temperatures generally reduce. Although affected by this trend, the K-feldspar samples seem to exhibit less variation in inverted temperature between different ITL data combinations than the Na-feldspar samples. These results are consistent with that recorded for the Butwal and KTB samples (Figs. 4-6).

3.2.4. Synthetic calibration samples: high temperature irradiations

In contrast to the natural samples, inversion of the laboratory high-temperature irradiation data for both sample BUT.4 and sample KTB.428B exhibited less sensitivity to the different combinations of ITL data (left-hand side of Fig. 7).

All of the ITL combinations recover the irradiation temperature within 10 % error, however, only the 250 °C irradiation of sample BUT.4 recovers the irradiation temperature exactly with all of the IRSL signals. For the 250 °C irradiation of sample KTB.428B, and the 300 °C irradiation of sample BUT.4, there is a consistent underestimation of the modelled temperature compared to the target temperature of 15 and 30 °C respectively. For the 200 °C irradiation of sample BUT.4, only the IRSL.150 perfectly recovers the target-temperature. The IRSL.225 signal shows an underestimation of ~40 °C, and the IRSL.50 and 100 signals overestimate the temperature by 10 to 15 °C, but all signals recover the target-temperature within 1σ error.

When the data are inverted using the natural environmental dose rate (right-hand side of Fig. 7), there are again sensitive to the combination of ITL temperatures used and exhibit a similar trend to that observed for the naturally irradiated samples (Figs. 4 and 5), with sample KTB.428B exhibiting the greatest sensitivity. Despite this, irradiation at 250 °C for both samples yields inverted temperatures of around 40-45 °C for all ITL combinations when ITL data measured at 300 and 350 °C are excluded. The irradiation at 300 °C gives an approximate temperature in the range of 55 to 60 °C, and the lowest temperature of irradiation at 200 °C has a natural equivalent below 20 °C, even reaching temperatures below 0 °C depending on the ITL combination, indicating that the sample would likely be in steady-state in the natural environment. With the exception of the irradiation at 200 °C that yields an equivalently saturated result, the other high temperature irradiations correspond to physically possible temperatures in nature and are in the range of the temperatures recorded for the KTB samples.

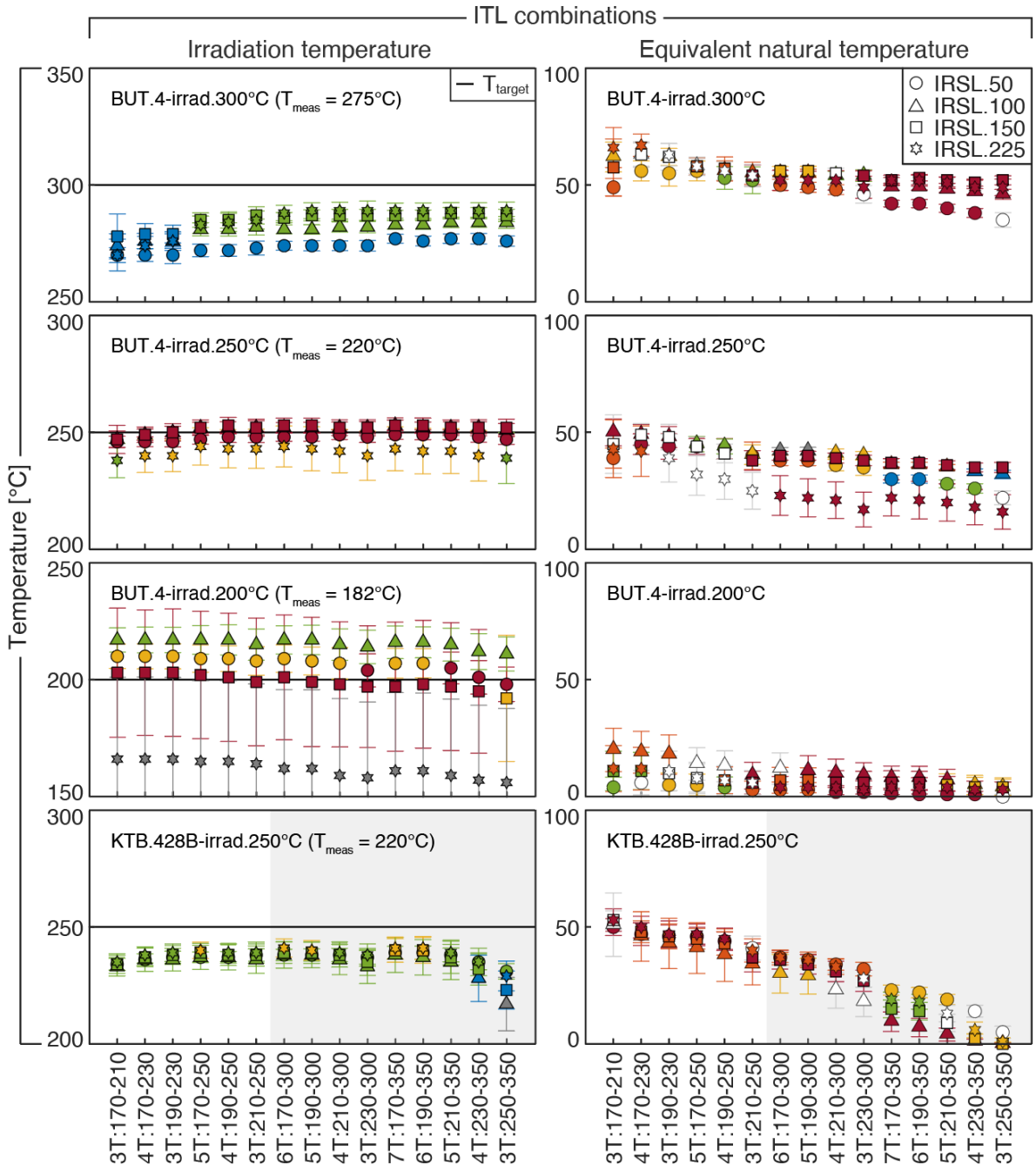

Fig. 7: *On the left-hand side, results of the inversion for isothermal temperatures for the high temperature irradiation measurements on K-feldspar sample BUT.4 and Na-feldspar sample KTB.428B. Solid black lines are the irradiation target temperatures. On the left-hand side, results of inversion of the high temperature irradiation data using the natural environmental dose rate. For the definition of the colours, refer to the caption of Fig. 5.*

4. Discussion

Samples with independently known thermal histories provide an opportunity to validate measurement and modelling approaches relevant for luminescence thermochronometry. Here we use samples from the KTB borehole, together with synthetically developed known-thermal history samples, to test the validity of thermal kinetic parameters obtained from different combinations of isothermal holding data. We find that inverted temperatures change, depending both on the number of ITL temperatures and on the highest ITL temperature used for thermal kinetic parameter derivation (Figs. 4-7). Modelled temperatures reduce as the highest ITL temperature increases, to the extent that the KTB borehole sample temperatures are no longer recovered when the 300 and 350 °C ITL are included to derive the kinetic parameters. Only where these temperatures are excluded are the KTB borehole sample temperatures recovered accurately. The temperature deviation observed when the 300 and 350 °C ITL temperatures are incorporated might be explained by enhanced thermal transfer of charge at temperatures greater than the preheat temperature, which was 250 °C for all of the analyses reported here. The observation that the 300 and 350 °C ITL data are least well fitted by the band-tail states model (Fig. 3C and 3F), is consistent with this result. Where the 300 and 350 °C ITL temperatures are excluded, all of the data combinations between three and five ITL temperatures between 170 °C and 250 °C yield accurate in-situ temperatures for the KTB samples (Fig. 4).

However, the KTB borehole samples are Na-feldspar, whereas K-feldspar is usually targeted in luminescence studies because of its favourable luminescence dating properties (i.e. brighter signal intensities). The Butwal samples are K-feldspars and their response to changing ITL temperature combinations (Fig. 5) is somewhat different to that observed for the KTB samples (Fig. 4). Although it is not known whether the Butwal samples reflect exhumation or isothermal temperature, inverting the samples assuming an isothermal history is useful for exploring the effect of different thermal kinetic parameters obtained from different ITL combinations. It is apparent from contrasting Figs. 4 and 5 that whereas the KTB samples exhibit high sensitivity to the combination of ITL temperatures, and in particular the inclusion of highest temperature ITL measurements, that the Butwal samples are relatively unaffected. Although there is a trend towards reducing temperature and increasing scatter between the different MET signals with the inclusion of higher temperature ITL data, the temperature change is more moderate, especially for samples BUT.2, BUT.3 and BUT.4 which are far from saturation (Fig. 3H). In contrast, the data for BUT.1 and BUT.5 is more scattered, which may reflect the higher saturation level of at least one of the MET signals of these samples.

This difference in behaviour between the Na-feldspars of the KTB samples and the K-feldspars of the Butwal samples is also seen in the control feldspars (Fig. 6). Despite their difference in mineralogy and lithology, all samples generally depict the same trend, with a decrease in inverted temperature with the inclusion of the highest temperature ITL data. The scatter between the different inverted temperatures also increases when the 300 and 350 °C

ITL data are included. The K-feldspars (left-side of Fig. 6) are generally less affected than Na-feldspars (right-side of Fig. 6), with some exceptions. Sample lithology appears to be a controlling factor, with sedimentary samples exhibiting the least sensitivity to changing ITL combinations. However, the most significant trend is between samples from the same location. The KTB samples exhibit similar behaviour, clearly distinguishable from the other Na-feldspars, and the Butwal samples are similar to each other but distinguishable from the other K-feldspars.

The significant differences in inverted temperatures discussed above illustrate the importance of identifying a suitable measurement protocol. If we isolate the ITL combinations that give the most consistent results, i.e., where independently known temperature is recovered (Fig. 4) and the scatter between the data is the least (Fig. 6), based on the results of the KTB borehole samples, we are left with two combinations of four isothermal temperatures between 170 and 230 °C, and 190 and 250 °C. However, in most geological application, independent temperature control is absent, and it is thus usually not possible to select which of these ITL temperature combinations yields the most accurate result. For this reason, we sought to develop synthetic calibration samples through elevated temperature irradiation in the laboratory (e.g., Wallinga et al., 2002).

In contrast to the naturally irradiated samples, inversion of the elevated temperature irradiated samples reveals almost no sensitivity to the number of ITL temperatures incorporated (left-hand side of Fig. 7). Inverting these data again, instead using the sample's respective natural dose rate (right-hand side of Fig. 7), reveals that the laboratory dose rate masks the effect of changes in the thermal kinetic parameters. The laboratory dose rate of our instrument is nine orders of magnitude greater than the natural environmental dose rate. The rate of charge accumulation is thus disproportionally high in comparison to the lifetime of charges in the traps, which is defined by the sample's thermal kinetic parameters. Consequently, relatively little charge is thermally evicted compared to the rate of charge trapping, and variation in the thermal kinetic parameters caused by the differences in ITL combinations (left-hand side of Fig. 7) has almost no impact. In contrast, the natural environment is much more sensitive to these subtle changes in kinetic parameters (Figs. 4, 5 and right-hand side of Fig. 7) because of the comparatively slow rate of charge trapping relative to charge detrapping.

It is thus unfortunately challenging to develop highly sensitive luminescence thermochronometry calibration samples in the laboratory. Despite this, we recover the irradiation temperatures within error for all of our experiments indicating that our measurement and modelling approach is robust. The large uncertainties recorded for the 200 °C irradiation of the IRSL.225 signal of sample BUT.4 reflect the fact that the ñ values are near to saturation for this irradiation temperature, rendering the recovery of a precise thermal history impossible. For the 250 °C and 300 °C irradiations, the modelled temperature slightly underestimates the measured temperatures. This may relate to the precision of the instrument heater-plate. Despite this, as the modelled results are within 10 % uncertainty of the measured value, we consider the results to be robust.

As the synthetic calibration data are not sufficiently sensitive to aid in the selection of an appropriate combination of ITL temperatures, we instead contrasted the results of inverting both the natural data for the KTB and Butwal samples (Figs. 4 and 5) and the inversion of the elevated temperature irradiation data using the natural environmental dose rate (right-hand side of Fig. 7). For the inversion of the natural KTB data, kinetic parameters calculated from four ITL temperatures between 190 and 250 °C recover the in-situ temperature both accurately and precisely for all samples and all IRSL signals, with the exception of the post-IR signals of sample KTB.253F. This sample has a different lithology to the other KTB samples analysed, comprising garnet-amphibolite, rather than biotite-gneiss which may explain its anomalous behaviour. The combination of four ITL temperatures also yields tightly clustered inversion results for the natural samples BUT.2, BUT.3 and BUT.4 (Fig. 5), although the data are more scattered for BUT.1 and BUT.5. As the latter two samples have at least one IRSL signal saturated or near to saturation (Fig. 3H), we do not discard this temperature combination on their account. Similarly, this combination of ITL temperatures yields accurate results for the elevated irradiation temperature data (left-hand side of Fig. 7), and tightly clustered results for the inversion of these data using the natural environmental dose rate (right-hand side of Fig. 7). For this reason, we consider this combination of temperatures as appropriate for both the KTB and Butwal samples. But in the absence of known-thermal history samples for K-feldspars, we acknowledge that this combination of temperatures may not yield accurate results for the Butwal samples.

5. Conclusion

In this study, the impact of different combinations of isothermal holding temperature data was investigated in the context of luminescence thermochronometry, using a combination of numerical modelling and experimental data. Measurement of Na-feldspar minerals from known-thermal history KTB borehole samples allowed validation of the MET-pIR-IRSL measurement protocol for luminescence thermochronometry through the successful recovery of in-situ borehole temperatures. However, these samples also showed that the inclusion of isothermal holding data above 250 °C resulted in kinetic parameters that underestimated temperature. As the majority of luminescence studies are applied to K-feldspar minerals, complimentary investigations on unknown thermal history K-feldspar minerals extracted from samples of the Nepalese Siwaliks (Butwal transect) were made. These experiments yielded similar results, although these samples were notably less sensitive to the inclusion of isothermal holding data above 250 °C, whilst also exhibiting a trend of reducing inverted temperature with the inclusion of higher temperature isothermal data. To evaluate how representative the KTB and Butwal samples are of K-feldspars and Na-feldspars generally, we contrasted our data with a suite of twelve control samples of different chemical compositions and geological origins. The most distinctive trend is that samples from the same locality tend to exhibit similar

behaviour, and that most samples yield lower reconstructed temperatures where high temperature isothermal holding data are used for kinetic parameter derivation.

Finally, we attempted to develop artificial luminescence calibration samples in the laboratory, through irradiating a K-feldspar (BUT) and Na-feldspar (KTB) sample at elevated temperature. However, the laboratory dose rate is nine orders of magnitude greater than that experienced in nature and masked the effect of changes in the kinetic parameters caused by their calculation with different sub-sets of isothermal data. Consequently, through consideration of the trends in all of our data, and in particular the isothermal temperature combinations that yielded accurate in-situ temperatures for the KTB borehole samples, we advocate using four isothermal temperatures at 190, 210, 230 and 250 °C to determine thermal kinetic parameters from isothermal holding experiments. We find that this temperature combination performed accurately for the four MET signals investigated for the KTB samples, and that the decline in inverted temperatures occurred when isothermal decay data above 250 °C were incorporated. However, we acknowledge that in the absence of any independent control on sample thermal history, this may still yield inaccurate results for some feldspar minerals. Generating locality specific plots that explore changes in inverted temperatures for a sub-set of samples using different combinations of isothermal holding temperature data will allow the sensitivity of a sample to be analysed and the selected measurement conditions to be at least partially evaluated.

Acknowledgements

The authors would like to thank A. Finch for providing the sample CLE, H. Friis and the Natural History Museum of Oslo for the KNR16962 and KNR32491 samples, B. Guralnik for the KTB samples, J. Lavé for the Butwal samples, and S. Riedesel for measuring the samples AL-I, HAM-5 and JSH1-13. The authors would also like to thank M. Bartz, S. Riedesel, S. Tsukamoto and F. Oppermann for laboratory support, and F. Herman and C. Schmidt for comments and suggestions on the manuscript. G.E. King has received funding from the European Research Council (ERC) under the European Union's Horizon 2020 research and innovation programme, grant agreement No. 851614.

Supplementary data

Contents

S1. Detailed information on the Butwal samples

Table S1: *Location of the Butwal samples.*

	Latitude	Longitude	Latitude	Longitude	Alt [m]
BUT.1	27°43'8.21"N	83°27'55.94"E	27.718947	83.465539	204
BUT.2	27°43'28.41"N	83°28'10.63"E	27.724558	83.469619	300
BUT.3	27°43'57.02"N	83°28'8.47"E	27.732506	83.469019	298
BUT.4	27°44'23.54"N	83°27'52.17"E	27.739872	83.464492	317
BUT.5	27°44'42.71"N	83°28'6.46"N	27.745197	83.468461	322

Note: Samples collected by Jérôme Lavé.

S2. Chemical composition of the samples and Ternary plot

Table S2: *Chemical composition of the studied samples.*

ID	Type	Lithology	Location	Feldspar composition assuming 100 % feldspar			Quartz content [%]	References
				Or (K)	Ab (Na)	An (Ca)		
NB139 [a]	Bedrock	Migmatitic gneiss	Namche Barwa, Nepal	**89.3**	9.4	1.4	4.2	King et al., 2016; Riedesel et al., 2019
NB120 [a]	Bedrock	Migmatitic gneiss	Namche Barwa, Nepal	**86.2**	11.0	2.9	5.0	King et al., 2016; Riedesel et al., 2019
MBT-1-2430 [a]	Bedrock	Calc-alkaline granite	Mont-Blanc Tunnel, Italy	**86.7**	12.0	1.3	4.2	Lambert, 2018; Riedesel et al., 2019
KRG-16-06 [a]	Bedrock	Kurobegawa granite	Japanese Alps, Japan	**79.4**	17.3	3.2	3.1	Riedesel et al., 2019; King et al., 2020
KRG-16-112 [a]	Bedrock	Kurobegawa granite	Japanese Alps, Japan	**75.2**	21.3	3.5	3.4	Riedesel et al., 2019; King et al., 2020
JSH1-13 [a]	Sediment	Sand	Shirasuka Lowlands, Japan	**50.4**	37.6	12.1	38.1	Riedesel et al., 2018; Riedesel et al., 2019
HAM-5 [a]	Sediment	Lake sediment	Lake Hamana, Japan	**64.9**	31.1	4.0	19.3	Riedesel et al., 2019
F1 [a]	Reference sample	-	IAEA AQCS reference feldspar	**61.3**	33.4	5.4	0.3	IAEA, 1999; Riedesel et al., 2019
CLE [a]	Museum specimen	Pegmatite	Golonca District, Minas Gerais, Brazil	0.5	**99.3**	0.2	3.9	Cassadanne and Roditi, 1996; Rendell and Clarke, 1997;
Al-1 [b]	Museum specimen	Metamorphic albite	Pinzele, Trente, Italy	1.0	**97.0**	2.0	5.0	Govindaraju, 1995; Riedesel et al., 2021
KNR16962 [c]	Museum specimen	Albite	Ljosland, Iveland, Agder, Norway	4.6	**81.6**	13.8	64.7	This study
KNR32491 [c]	Museum specimen	Albite	Seiland, Alta, Finnmark, Norway	4.3	**71.6**	24.0	61.7	This study
KTB.253F [d]	Bedrock	Garnet-amphibolite	KTB borehole, Germany	5.9	**68.8**	25.3	21.9	Guralnik et al., 2015
KTB.383C [d]	Bedrock	Sillimanite-muscovite-biotite-gneiss	KTB borehole, Germany	18.2	**67.4**	14.4	52.8	Guralnik et al., 2015
KTB.428B [d]	Bedrock	Garnet-sillimanite-biotite-gneiss	KTB borehole, Germany	8.2	**77.9**	13.8	51.5	Guralnik et al., 2015
KTB.481B [d]	Bedrock	Garnet-sillimanite-biotite-gneiss	KTB borehole, Germany	15.6	**66.7**	17.8	72.5	Guralnik et al., 2015
BUT.5 [e]	Sediment	Sandstones, Middle Binai Khola Fm. / Middle	Butwal area, Siwaliks, Nepal	**96.0**	2.6	1.4	81.2	This study
BUT.4 [e]	Sediment	Sandstones, Lower Binai Khola Fm. / Middle Siwalik	Butwal area, Siwaliks, Nepal	**89.0**	11.0	0.0	55.3	This study
BUT.3 [e]	Sediment	Sandstones, Upper Arung Khola Fm. / Lower Siwalik	Butwal area, Siwaliks, Nepal	**86.3**	13.6	0.1	51.4	This study
BUT.2 [e]	Sediment	Sandstones, Upper Arung Khola Fm. / Lower Siwalik	Butwal area, Siwaliks, Nepal	**88.4**	11.4	0.2	70.2	This study
BUT.1 [e]	Sediment	Sandstones, Upper Arung Khola Fm. / Lower Siwalik	Butwal area, Siwaliks, Nepal	**95.8**	0.0	4.2	90.8	This study

Notes: Data taken from [a] Riedesel et al., 2019; [b] Riedesel et al., 2021; [c] XRF at the University of Lausanne; [d] Guralnik et al., 2015; [e] Mineralogical composition determined using an X-Ray Fluorescence (XRF) attachment fixed to a Risø OSL/TL reader (Kook et al., 2012) at the Leibniz Institute of Applied Geophysics in Hannover.

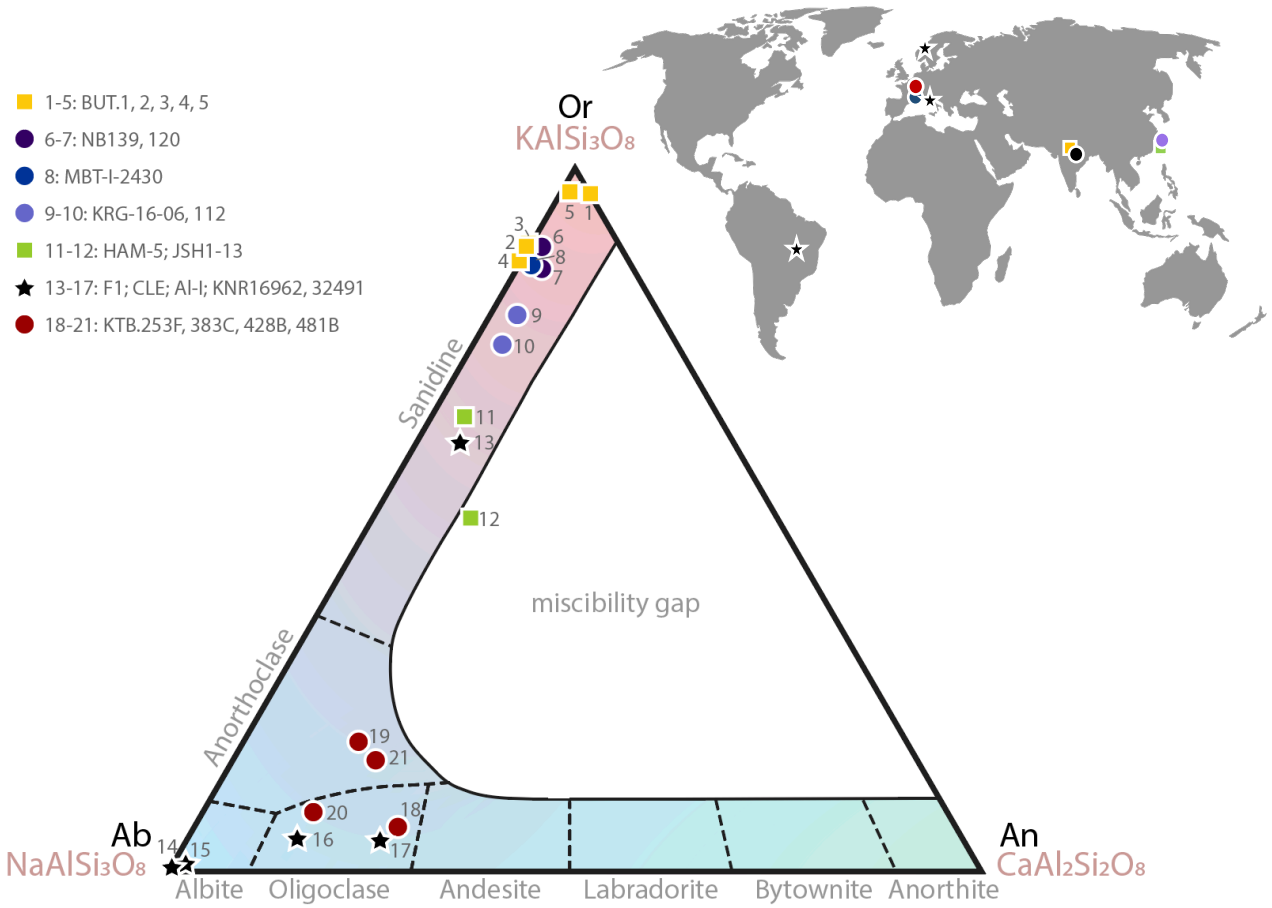

Fig. S2: *Ternary feldspar diagram of the chemical composition of the studied samples.*

S3. Dose rate calculation for the Butwal samples: DRAC input and output tables

Table S3.1: *Radioactive element composition of the Butwal samples.*

		K2O [%]	K [%]	K err.(3%) [%]	Rb [ppm]	Rb err.(3%) [ppm]	Th [ppm]	Th err.(3%) [ppm]	U [ppm]	U err.(3%) [ppm]
BUT	BUT.5	0.90	0.75	0.02	39	1	5.2	0	1.8	0
	BUT.4	1.49	1.24	0.04	68	2	7.3	0	1.8	0
	BUT.3	1.47	1.22	0.04	59	2	8.3	0	1.9	0
	BUT.2	1.15	0.95	0.03	47	1	7.6	0	1.7	0
	BUT.1	1.00	0.83	0.02	39	1	9.2	0	1.7	0

Table S3.2: *DRAC input and output tables for the Butwal samples.*

Table available at an online depository:
>>>> Please ask for the Dropbox link if needed. >>>>

S4. Dose rate, temperatures, and luminescence data of the studied samples

Table S4: *Dose rate, temperatures, and luminescence data of the studied samples.*

ID	Dose rate [Gy/ka]		Temperature [°C]		Mineralogy	Data Luminescence
	Dr	err	T	err	feldspar	
NB139	14.17	0.78	-	-	K	NB.139
NB120	6.27	0.51	-	-	K	NB.120
MBT-I-2430	15.27	3.90	-	-	K	MBT-I-2430
KRG-16-06	7.02	0.45	-	-	K	KRG.06
KRG-16-112	6.23	0.14	-	-	K	KRG.112
JSH1-13	3.65	0.31	-	-	K	JSH1.13
HAM-5	2.80	0.50	-	-	K	HAM.5
F1	3.00	0.50	-	-	K	F1
CLE	3.00	0.50	-	-	Na	CLE
Al-I	3.00	0.50	-	-	Na	Al-I
KNR16962	3.00	0.50	-	-	Na	KNR16962
KNR32491	3.00	0.50	-	-	Na	KNR32491
KTB.253F	1.58	0.24	39.8	2.1	Na	KTB.253F
KTB.383C	3.02	0.45	55.1	2.9	Na	KTB.383C
KTB.428B	3.44	0.52	59.5	3.1	Na	KTB.428B
KTB.481B	3.58	0.54	65.2	3.4	Na	KTB.481B
BUT.5	2.37	0.12	-	-	K	BUT.1
BUT.4	2.36	0.12	-	-	K	BUT.2
BUT.3	2.65	0.14	-	-	K	BUT.3
BUT.2	2.59	0.14	-	-	K	BUT.4
BUT.1	2.08	0.11	-	-	K	BUT.5
BUT.4-irrad200	3.63E+09	9.46E+07	200	-	K	BUT.4-irrad200
BUT.4-irrad250	3.63E+09	9.46E+07	250	-	K	BUT.4-irrad250
BUT.4-irrad230	3.63E+09	9.46E+07	300	-	K	BUT.4-irrad230
KTB.428B-irrad250	3.60E+09	9.46E+07	250	-	Na	KTB.428B-irrad250

Luminescence data available at an online depository:
>>>> Please ask for the Dropbox link if needed. >>>>

S5. Saturation plots of the studied samples

Fig. S5: *Saturation plots, classified by mineralogy and lithology.*

KTB samples: Na-feldspars, bedrock

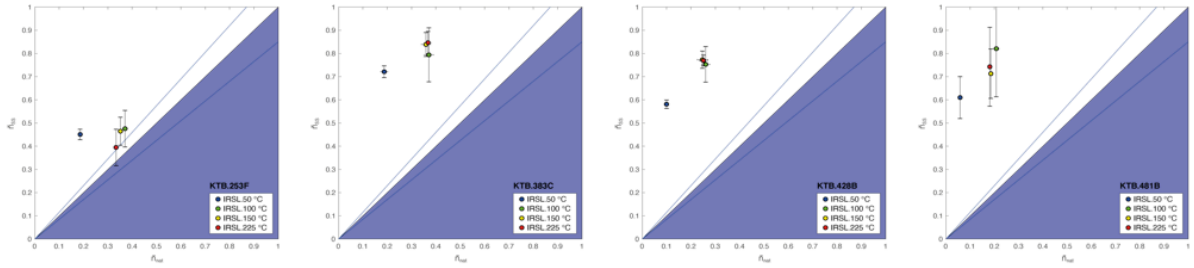

Control samples: Na-feldspars, museum samples

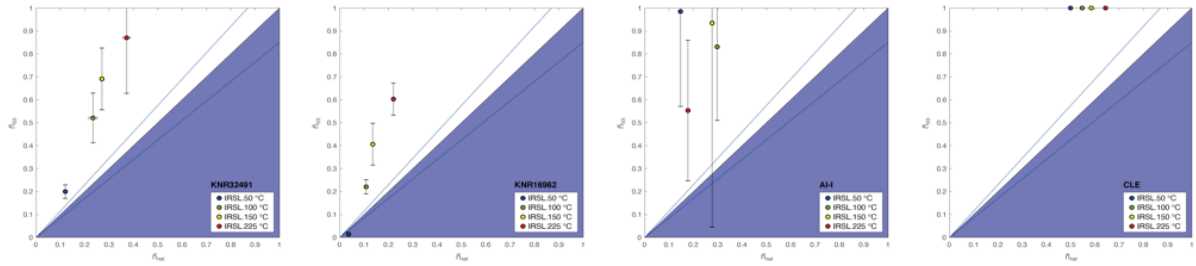

Butwal samples: K-feldspars, sandstones

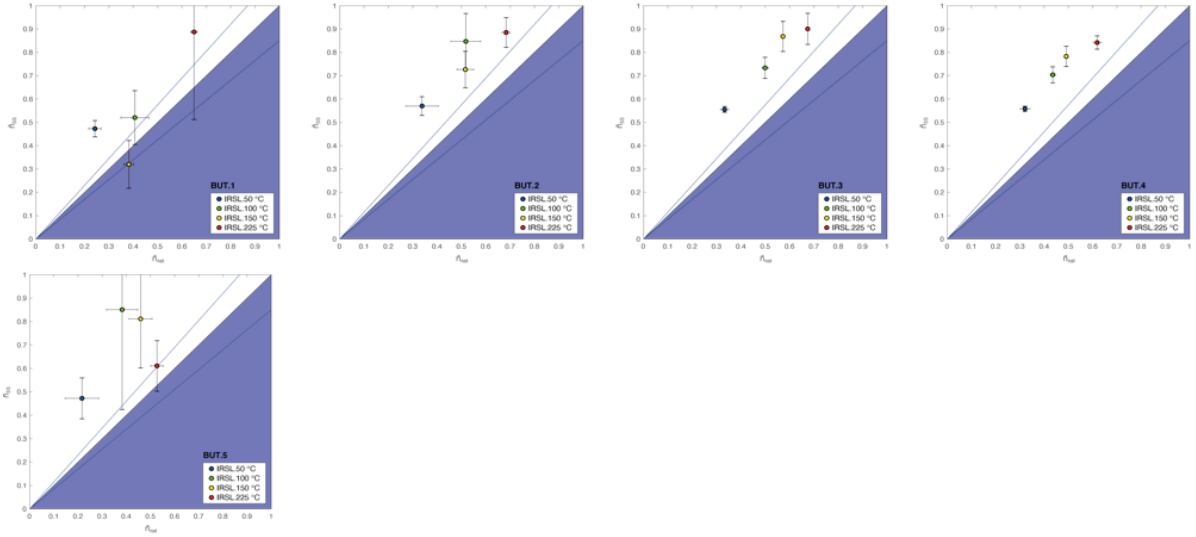

Control samples: K-feldspars, bedrock

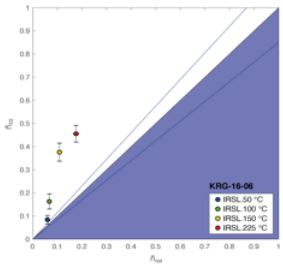

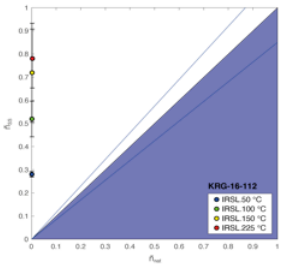

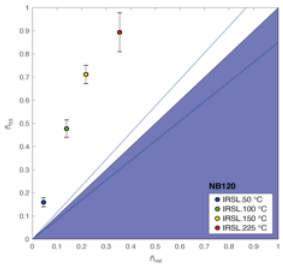

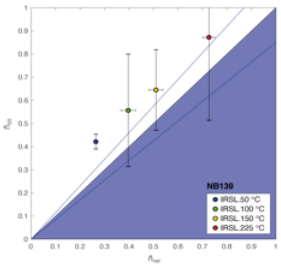

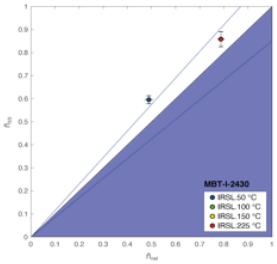

Control samples: K-feldspars, sandstones

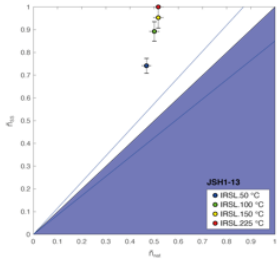

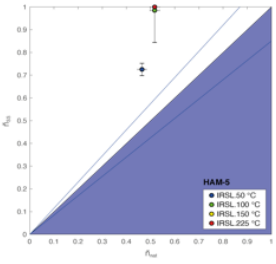

Control samples: K-feldspars, reference sample

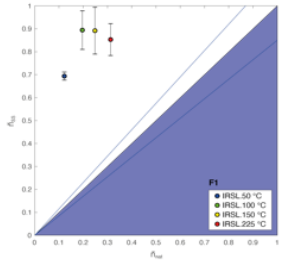

Chapter 2

Sustained deformation across the Sub-Himalayas since 200 ka

C. Bouscary[1], G.E. King[1], D. Grujic[2], J. Lavé[3], R. Almeida[4], G. Hetényi[5], F. Herman[1]

[1] Institute of Earth Surface Dynamics, University of Lausanne, Lausanne, Switzerland
[2] Department of Earth and Environmental Sciences, Dalhousie University, Halifax, Canada
[3] CRPG, UMR 7358 CNRS, University of Lorraine, Nancy, France
[4] School of Earth Sciences Energy and Environment, Yachay Tech University, San Miguel de Urcuquí, Ecuador
[5] Institute of Earth Sciences, University of Lausanne, Lausanne, Switzerland

Table of contents

This chapter was submitted to *Geology*:

Bouscary, C., King, G.E., Grujic, D., Lavé, J., Almeida, R., Hetényi, G., and Herman F. (*In review*). Sustained deformation across the Sub-Himalayas since 200 ka. *Geology*.

Abstract

The Himalayan Main Frontal Thrust (MFT) currently accommodates about half, i.e., 12-23 mm/yr, of the convergence between the Indian and Eurasian tectonic plates by uplift and deformation of the Sub-Himalayas. While deformation is well documented at modern and Myr timescales, almost no quantitative data are available that constrain Quaternary timescale deformation rates along and within this key tectonic unit. Filling this knowledge gap is crucial to better understand Himalayan tectonics and the seismic cycle in this densely populated region. Here we quantify exhumation rates in the Sub-Himalayas using the recently established luminescence thermochronometry technique over timescales of 10^5 yr. The ultra-low closure temperature of luminescence thermochronometry (30-100 °C) enables us to resolve thermal histories from the Siwalik Group rocks, which have experienced maximum burial temperatures of ~120 °C. An extensive set of 33 samples was collected from western Nepal to eastern Bhutan, of which 22 yield exhumation rates of ~3-11 mm/yr over the past ~200 kyr. We convert these values to minimum cumulative thrust slip rates and horizontal shortening rates of ~6-22 mm/yr and ~5-19 mm/yr, assuming a thrust dip angle of 30°. Our luminescence thermochronometry results show that the Sub-Himalayan fold-and-thrust belt (FTB), particularly the MFT, accommodates most of the convergence across the Himalayas since at least 200 kyr. Our data also show activity of the Main Dun Thrusts (MDT) throughout this time period, implying that internal deformation of the orogenic wedge and strain partitioning may have occurred.

1. Introduction

The Himalayan orogen results from the collision between the Indian and Eurasian continental plates where a system of successively forming north-dipping crustal-scale thrusts, extending along the Himalayan arc and merging at depth into the Main Himalayan Thrust (MHT), the basal detachment of the Himalayas (Schelling and Arita, 1991; Pandey et al., 1995), have accommodated most of the convergence since at least the early Miocene (Fig. 1A; Herman et al., 2010). The Sub-Himalayan FTB formed over the past few million years in response to the propagation of deformation into the foreland of the Himalayan orogen, the MFT being the youngest regional fault system and the current active deformation front in most of the Himalayas (Fig. 1A).

The ongoing contraction across the Himalayas and interseismic locking along the MHT causes accumulation of elastic strain that is released by Mw 8+ earthquakes that propagate under the Sub-Himalayan FTB and have catastrophic impact on the local population (Lavé and Avouac, 2000; Bollinger et al., 2014; Stevens and Avouac, 2015; Bilham et al., 2017). Whilst GPS measurements constrain modern deformation rates in the Sub-Himalayan FTB (Vernant et al., 2014; Stevens and Avouac, 2015; Bilham et al., 2017), few studies have succeeded in constraining deformation rates at 10-100 kyr timescales (e.g., Mugnier et al., 2004; van der Beek et al., 2006), despite the proposal that deformation rates vary episodically over geological timescales and that out-of-sequence activity occurs for some faults (e.g., Hodges, 2000; Mugnier et al., 2004; Wobus et al., 2006). Here we apply luminescence thermochronometry (King et al., 2016a) over a large geographical area of the Sub-Himalayan FTB ranging from western Nepal to eastern Bhutan to resolve deformation at sub-Quaternary timescales (Figs. 2 and 3), a timescale hitherto inaccessible to other techniques.

2. Geological setting

The Sub-Himalayan FTB consists of synorogenic terrestrial molassic sediments of the Siwalik Group, sourced from the denudation of the main Himalayan range, and deposited in the Himalayan foredeep during the Neogene-Quaternary. The Siwalik Group sediments were buried to depths of up to ~5 km by continuous deposition and syn-sedimentary tectonics, and exhumed by syn/post-sedimentary tectonics along the MFT and other thrusts within the Sub-Himalayan FTB (Mugnier et al., 1999; van der Beek et al., 2006). The MFT in the south and the MBT in the north bound the tectonic unit of the Sub-Himalayas, whilst several smaller intra-wedge thrusts, referred to as the MDT, formed in-sequence between the two.

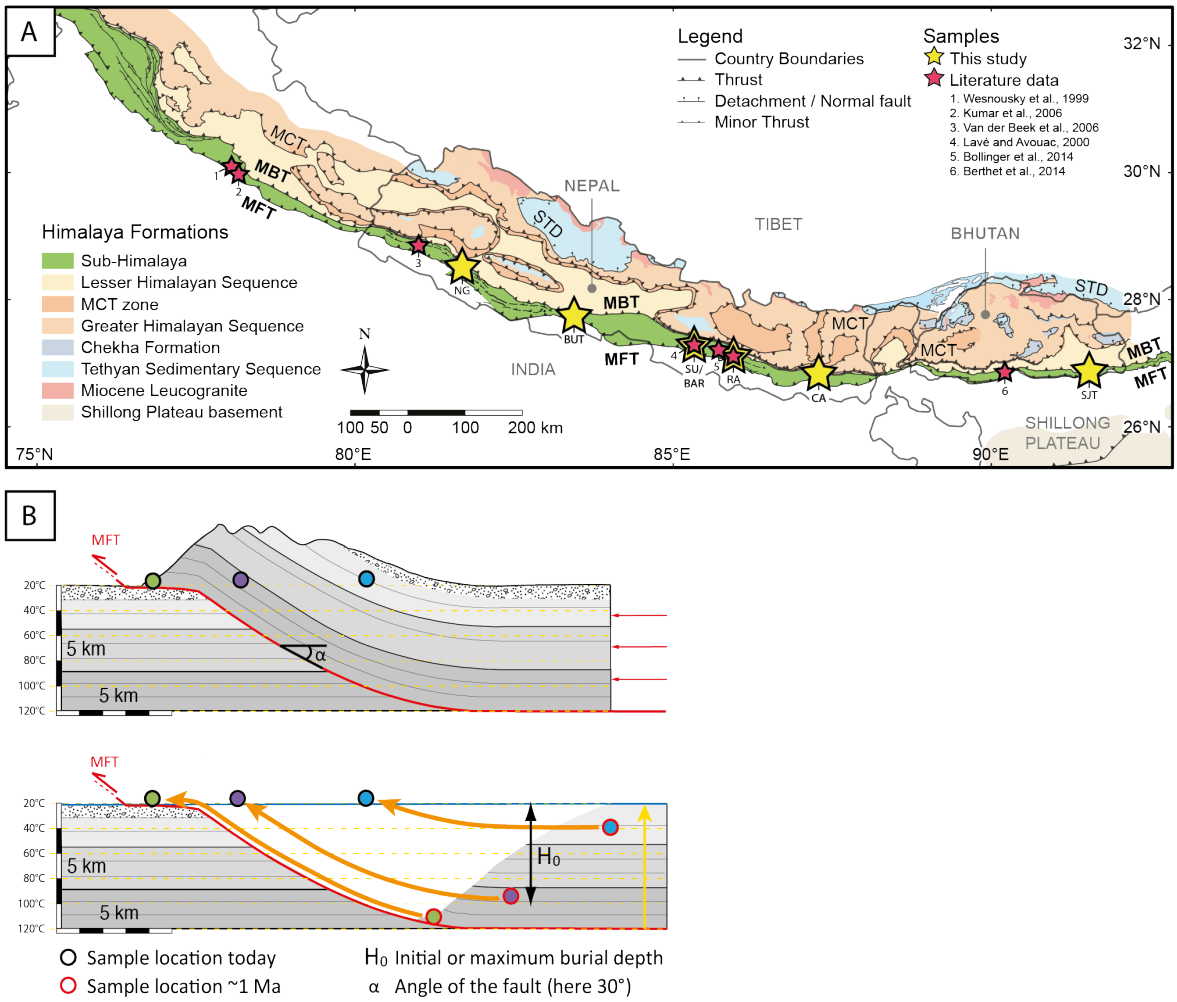

Fig. 1: ***A.*** *Geological map showing the major tectonostratigraphic units and faults of the Himalayan FTB (modified from Hirschmiller et al., 2014). The sedimentary rocks of the Sub-Himalayan FTB are represented in green, between the MFT and the MBT thrusts. Yellow stars show the location of the Sub-Himalayan transects of this study, and purple stars show published transects.* ***B.*** *Schematic cross-section of the MFT, with below, its balanced cross-section, showing the original location of the samples at ~1 Ma, and the trajectory that the samples followed along the thrust to be at the surface today (orange arrows). The vertical geothermal gradient path is represented in yellow.*

Present-day convergence rates across the Himalayas from western Nepal to eastern Bhutan range from 12 to 23 mm/yr (e.g., Vernant et al., 2014; Stevens and Avouac, 2015; Bilham et al., 2017), with the highest rates around 82°E (Fig. 3). These geodetic convergence rates are approximately equal to Holocene shortening rates inferred from fluvial incision rates at specific locations across the MFT (e.g., Lavé and Avouac, 2000; Mugnier et al., 2004), and are broadly consistent with the Miocene-Pliocene estimates of shortening rate throughout the Himalayan Belt of western Nepal of ~19 mm/yr (Mugnier et al., 2004). The consistency of convergence/shortening rates at different timescales implies that the convergence between

India and the Tibetan plateau has occurred at a nearly constant rate for the past 10 Myr (e.g., Lyon-Caen and Molnar, 1985; Molnar and Stock, 2009). However, whether shortening has always been accommodated on the frontal-most thrust, or by several thrusts concurrently during this period is not constrained.

We collected 33 samples from six transects across the Siwalik foothills, specifically selected to constrain exhumation rate and thus shortening rate changes in the Sub-Himalayan FTB (Fig. 1A and Table SD.1). From west to east: ten samples (NG) were taken across MDTs in western Nepal, north of Nepalgunj. In central Nepal, five samples (BUT) were collected along the Tinau Khola, samples SU-9 and BAR-1 were sampled along the Bakaya river nearby the MFT surface expression, and six samples (RA-K) were collected north of the MDT along the Kamala river. In eastern Nepal, samples CA14-4 and CA14-7 were taken along the Koshi river. The easternmost transect of eight samples (SJT) is situated near Samdrup Jongkhar, along the Dungsam Chu river in eastern Bhutan.

3. Constraining Quaternary exhumation rates

Multi-luminescence thermochronometry of feldspar minerals was used to determine the exhumation rates of all samples. They were prepared and measured using the approach of King et al. (2016a) and Bouscary and King (2022). A multi-elevated temperature post-infrared infrared-stimulated luminescence (MET-pIR-IRSL) protocol was applied to single-aliquots of K-feldspar extracted from the samples. Luminescence dose response, the thermal and athermal stability, and the environmental dose rate of each sample was constrained to determine the kinetic parameters that describe luminescence signal growth and decay. These data allow the thermal history of the samples to be modelled (King et al., 2016a; Bouscary and King, 2022). It is worth noting that luminescence thermochronometry is limited by signal saturation, which restricts its application to rapidly exhuming terrain and late Quaternary exhumation histories (Herman and King, 2018). Individual luminescence signals were rejected when their natural signal was in field saturation. Full details of sample preparation and analysis are given in the Supplementary Materials.

We predicted time-temperature paths by prescribing a series of constant exhumation rates between 0 and 20 mm/yr, which were then converted into thermal histories assuming a 20 °C/km geothermal gradient (Mugnier et al., 1995; van der Beek et al., 2006) and an average surface temperature of 20 °C. For each time-temperature history, synthetic luminescence data were generated using the sample specific kinetic parameters. Natural luminescence signals were then compared to the synthetic signals generated for each exhumation rate, and values with the minimum misfit were retained, corresponding to the exhumation rate experienced by the sample, valid for the apparent sample age. Note that we did not account for deformation of

isotherms by heat advection due to thrusting and other tectonic processes, which would yield lower exhumation rates than those presented here (Braun, 2002). However, a uniform geothermal gradient at this timescale seems reasonable, especially given that the geothermal gradient is primarily controlled by the underthrusting plate (Huerta et al., 1996).

Table 1: *Exhumation rates, ages and depths over which the thrust dip angles should be constrained, thrust dip angles, and derived thrust slip rates and shortening rates, for* ***A.*** *the transects of this study, and* ***B.*** *transects from published articles.*

A.						**Fixed angle: 30°**		**Angle range: 25-45°**	
Transect	**Thrust sheet**	**Longitude [°E]**	**Exhumation rate [mm/yr]**	**Apparent age [kyr]**	**Thrust dip depth [m]**	**Thrust slip rate [mm/yr]**	**Shortening rate [mm/yr]**	**Thrust slip rate [mm/yr]**	**Shortening rate [mm/yr]**
NG.1	South of MFT	81.7 ± 0.1	7.1 ± 1.5	201 ± 25	~1400-2000	#	#	#	#
NG.2-5	MFT	81.7 ± 0.1	5.1 ± 1.5	187 ± 20	~900-1400	*10.2 ± 2.9**	*8.8 ± 2.5**	*5.1-15.5**	*3.6-14.1**
NG.11	MDT	81.7 ± 0.1	3.0 ± 0.6	286 ± 4	~800-1100	6.0 ± 1.2*	5.2 ± 1.0*	3.4-8.5*	2.4-7.7*
NG	Sub-H. FTB	81.7 ± 0.1	4.7 ± 1.6	207 ± 48	~900-1600	16.2 ± 3.0*	14.0 ± 2.6*	8.5-24.0*	6.0-21.8*
BUT	MFT	83.5 ± 0.1	6.0 ± 1.0	194 ± 14	~1100-1500	12.0 ± 2.1	10.4 ± 1.8	7.0-16.7	5.0-15.1
SU/BAR	MFT	85.2 ± 0.1	9.1 ± 0.3	175 ± 15	~1500-1800	18.1 ± 0.7	15.7 ± 0.6	12.3-22.2	8.7-20.2
RA-K	MDT	85.9 ± 0.1	10.7 ± 2.7	199 ± 6	~2100-2800	21.4 ± 5.4	18.5 ± 4.7	11.3-31.7	8.0-28.7
CA	MFT	87.2 ± 0.1	6.7 ± 2.4	162 ± 7	~1000-1600	13.4 ± 4.8	11.6 ± 4.2	6.1-21.5	4.3-19.5
SJT	MFT	91.5 ± 0.1	5.9 ± 0.8	204 ± 19	~1100-1500	11.7 ± 1.7	10.2 ± 1.5	7.1-15.9	5.0-14.4

*thrust slip and convergence rates for the NG transect are the sum of the MFT and MDT thrust sheet values (data in italic).
not interpreted in terms of slip and shortening rates due to location of the sample south of the MFT in Upper Siwalik Group detrital material, the recorded exhumation rate is probably inherited from MFT fold denudation.

B.					**Fixed angle**			**Angle range**		
Transect	**Longitude [°E]**	**Exhumation rate [mm/yr]**	**Age [kyr]**	**Depth constrained [m]**	**Thrust angle [°]**	**Thrust slip rate [mm/yr]**	**Shortening rate [mm/yr]**	**Thrust angle [°]**	**Thrust slip rate [mm/yr]**	**Shortening rate [mm/yr]**
Dehra Dun [a]	77.8 ± 0.5	6.9 ± 1.8	< 2.5	~20	30	13.8 ± 3.6	11.9 ± 3.1	25-35	8.9-20.6*	7.3-18.7*
Uttara-khand [b]	78.0 ± 1.3	4-6	~ 1.5	~10	-	-	-	20-45	6-18	4-16
KAR [c]	81.3 ± 0.2	~12	~300	~3600	30	~24*	~20*	-	-	-
Bakaya/ Bagmati [d]	85.2 ± 0.5	~10-15	≤ 9.2	~100	28.5	21.5 ± 1.5	18.4 ± 2.8*	23-34	15.2-29.4*	12.6-27.1*
Sir Khola [e]	85.6 ± 0.1	8.5 ± 1.5	< 2.5	~20-25	25	20.1 ± 3.5*	18.2 ± 3.2*	20-30	14.0-29.2*	12.1-27.5*
RA-B [e]	85.9 ± 0.1	~10 ± 1.5	< 2.5	~25-30	45	18.4 ± 2.8*	15.4 ± 2.3*	40-50	14.8-22.3*	12.1-19.1*
RA-P [e]	85.9 ± 0.1	12.4 ± 2.3	< 2.5	~30-40	33	17.5 ± 3.3*	12.4 ± 2.3*	30-35	13.2-22.9*	8.5-17.5*
Sarpang [f]	90.3 ± 0.1	8.8 ± 2.1	< 6.5	~50-70	25	20.8 ± 8.8	18.9 ± 4.5*	20-30	13.4-31.9*	11.6-29.9*

*calculated for this study from the published exhumation rates and thrust angles.
Notes: Data from [a] Wesnousky et al., 1999; [b] Kumar et al., 2006; [c] van der Beek et al., 2006; [d] Lavé and Avouac, 2000; [e] Bollinger et al., 2014; [f] Berthet et al., 2014.

Considering that the subdued topography of the Siwaliks hills quickly reaches steady-state (see arguments in Lavé and Avouac, 2000), thrust slip rates and horizontal shortening rates were estimated (Table 1) by assuming that the luminescence thermochronometry derived exhumation rates are equal to rock uplift rates. This allows comparison of our data with the modern geodetic convergence rates (Fig. 3). Assuming a constant dip angle along the thrust (Fig. 1B), we calculated thrust slip rates from uplift rate/sin(dip), and horizontal shortening rates from uplift rate/tan(dip). Both calculations are highly sensitive to the dip angle used: the steeper the dip angle, the lower the slip rate obtained (Drukpa et al., 2018). An exhumation rate of 10 mm/yr equates to vertical displacement of 100 m for the Holocene, and 2 km over 200 kyr; the fault geometry should thus be determined over a depth appropriate for the timescale investigated (Table 1). However, precise geological constraints at km depths are scarce and are not available for our sample locations, instead we assume a range of dip angles between 25-45° based on published balanced cross-sections (e.g., Mugnier et al., 1995; Hirschmiller et al., 2014).

4. Results and discussion

Exhumation, slip and shortening rates were determined for 22 samples; the remaining samples were rejected due to signal saturation. Exhumation rates vary between the samples and transects (Table 1), with rates averaged over the different MET-pIR-IRSL signals ranging between 3.0 ± 0.6 and 10.7 ± 2.7 mm/yr. The transect-averaged exhumation rates exhibit no clear east-west pattern, and there is no clear difference between rates for samples in the MDT and MFT (Table 1 and Fig. 2). The average exhumation rate across all samples is 6.2 ± 1.8 mm/yr for the Sub-Himalayas over the last ~200 kyr.

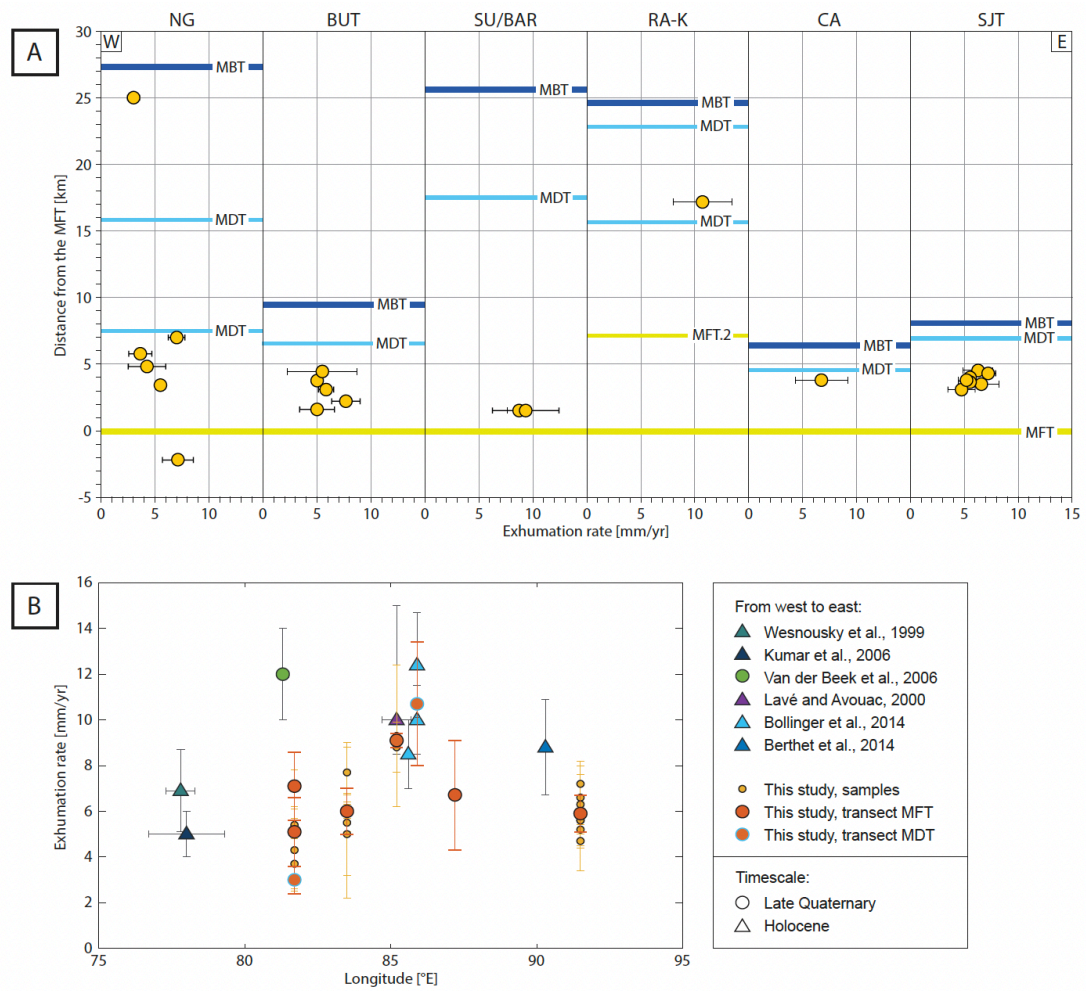

Fig. 2: *Exhumation rates for the Sub-Himalayan FTB.* ***A.*** *Sample specific exhumation rates by transect, the baseline is relative to the MFT (in yellow), distance to the MBT (in dark blue) shows the Sub-Himalayan FTB width.* ***B.*** *Sample specific and transect thrust sheet averaged exhumation rates in comparison to published values.*

The luminescence thermochronometry derived exhumation rates (Figs. 1 and 2) are approximately half of that estimated by van der Beek et al. (2006) for the Karnali River in western Nepal (~12 mm/yr over the past 0.3 Ma). However, van der Beek et al. (2006) calculated this rate using partially annealed apatite fission track data that are complex to interpret. Our exhumation rates are consistent with Holocene rock uplift rates of ~5-7 mm/yr (Wesnousky et al., 1999; Kumar et al., 2006) in Uttarakhand, are slightly lower but in general agreement with the uplift rates of Holocene fluvial terraces of 8.5-15 mm/yr (Lavé and Avouac, 2000; Bollinger et al., 2014) in central Nepal, and are within error of the vertical component of fault slip rates of 8.8 ± 2.1 mm/yr in central Bhutan (Berthet et al., 2014; Figs. 1 and 2).

Assuming a fault dip of 30°, the luminescence thermochronometry derived late Quaternary geological thrust slip rate of 18.1 ± 0.7 mm/yr across the MFT in the Bakaya valley (SU/BAR) is slightly lower than the Holocene slip rate of 21.5 ± 1.5 mm/yr for the same valley

(Lavé and Avouac, 2000). Corresponding shortening rates for this transect yield 15.7 ± 0.6 mm/yr for the late Quaternary and 18.4 ± 2.8 mm/yr for the Holocene, consistent with local GPS convergence velocities of 15-21 mm/yr (e.g., Vernant et al., 2014; Bilham et al., 2017). Whilst transects SU/BAR and RA-K yield shortening rates similar to the geodetic convergence rates at the same location, the remaining transects yield rates ~30-45 % lower (Fig. 3). Assuming a dip angle < 30° would yield higher shortening rates, whilst a dip angle > 30° would yield lower shortening rates (Table 1), impacting the portion of shortening taken by the MFT. Considering steady convergence between India and Eurasia since ~10 Ma (Molnar and Stock, 2009), a palaeo-shortening rate deficit with respect to geodetic convergence rates may imply only partial accommodation of convergence by the MFT during the past ~200 kyr at these locations. This may suggest that convergence was accommodated elsewhere, by internal deformation of the wedge: e.g., by reactivation of faults within the Sub-Himalayan FTB (e.g., Mugnier et al., 1999; Dey et al., 2016), by tectonic structures such as the MBT or within the frontal Lesser Himalaya (e.g., Arun section in Lavé and Avouac, 2001; Hossler et al., 2016), or by fault activation at the foothills of the High Himalaya (e.g., Hodges, 2000). Furthermore, the transects that record the least shortening on the MFT during the late Quaternary are situated in regions where the Sub-Himalayan FTB is very narrow (<10 km, BUT, CA, SJT), while regions where the Sub-Himalayan FTB is wider (~20 km, NG, SU/BAR, RA-K) show MFT rates that accommodate most to all of the convergence (Table 1). Along segments where the Sub-Himalayan FTB narrow, the most frontal folds are more mature, and are fully consumed by overthrusting, which makes further overthrusting above the MFT challenging. Such increased resistance to frontal deformation favors local reactivation of the MDT, MBT, or of thrusts further north (e.g., Mugnier et al., 1999; Thiede et al., 2017), implying shortening distribution across several structures.

However, the calculation of shortening rates is highly dependent on thrust angle (Table 1), and further constraint of thrust geometry at depth is needed to accurately constrain the proportion of late Quaternary convergence accommodated by the MFT relative to the proportion of strain partitioning. Despite this uncertainty, our study shows that the MFT accommodates at least ~55 % of the convergence across the Himalayas since the late Quaternary (Table 1 and Fig. 3), but that strain partitioning cannot be excluded as late Quaternary activity of the MDT is recorded at two sites (NG, RA-K), with thrust slip rates of respectively 6.0 and 21.4 mm/yr for a fault dip of 30° (Table 1). As luminescence thermochronometry thrust slip rates are averaged over ~200 kyr (Table SD.4), it is not possible to determine whether the MDT was active out-of-sequence, accommodating the full convergence rate for a short period, or whether slip on the MFT and the MDT was coeval, with each thrust accommodating part of the convergence.

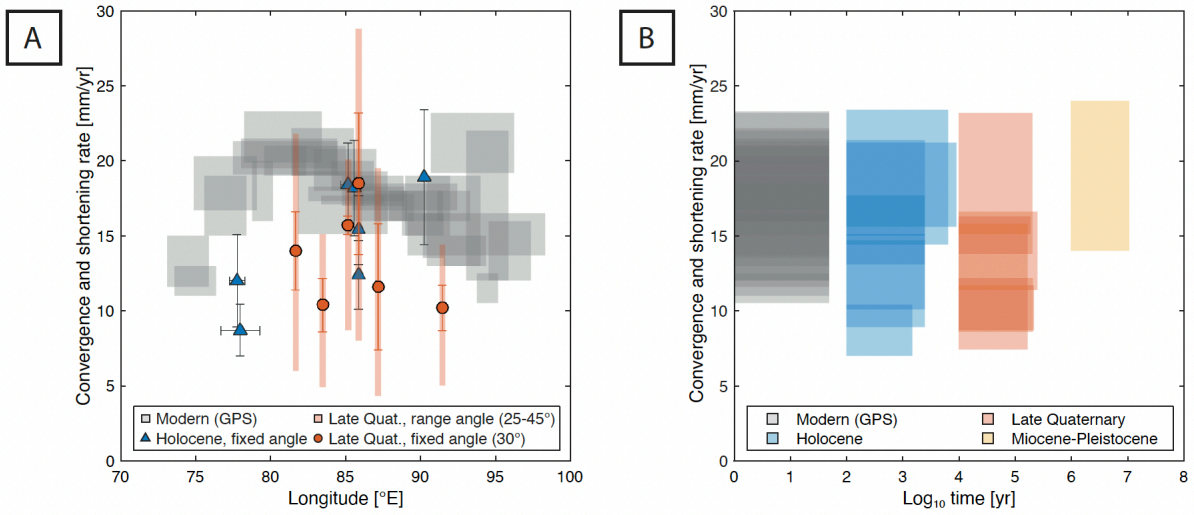

Fig. 3: A. *Compilation of published GPS convergence rates along the Himalayan range (Li et al., 2019; Sreejith et al., 2018; Bilham et al., 2017; Marechal et al., 2016; Stevens and Avouac, 2015; Vernant et al., 2014; Ader et al., 2012), contrasted with Sub-Himalayan FTB shortening rates for the Holocene and the late Quaternary (this study) (Table 1).* ***B.*** *Convergence and shortening rates (fixed angle) from A., and Miocene-Pleistocene shortening rates from Mugnier et al. (2004), plotted relative to timescale.*

5. Conclusions

The application of luminescence thermochronometry yields late Quaternary (10^5 yr) exhumation rates for 22 sedimentary rocks sampled from the Sub-Himalayan FTB. These data enable us to fill the temporal gap between modern GPS measurements (10^1 yr), Holocene fluvial terrace records (10^4 yr) and geological estimates (10^{6+} yr) of exhumation rates. Our results show that the Sub-Himalayas experienced exhumation of 3-11 mm/yr over the past ~200 ka. Converting these data to thrust slip and horizontal shortening rates indicates that at least ~55 % of the Himalayan convergence is accommodated by the MFT, consistent with this fault being a high seismic hazard zone. Our data show that whilst most convergence is accommodated on the MFT since at least ~200 kyr, part of the shortening is also taken by the MDT within the same time period, indicating either out-of-sequence or coeval activity of the two thrust systems within the late Quaternary. Strain partitioning on other thrusts north of the MFT cannot be excluded. Further studies are necessary to image and constrain near-surface (~few hundred m to km) fault geometries, as they have a major influence on the slip and shortening rates estimated from geological records, and consequently on estimates of strain partitioning.

Acknowledgment

Financial support by the Natural Sciences and Engineering Research Council of Canada, RGPIN-2020-05658 to DG.

Supplementary material

S1. Sample selection

A total of 33 samples were collected across the Sub-Himalayan fold-and-thrust belt (FTB), from western Nepal to eastern Bhutan, and analyzed using luminescence thermochronometry. Sample locations are shown in Fig. 1A and are detailed in Table 1 of the main article, and Table SD.1 of the Supplementary data file. All samples are fluviatile/molassic sedimentary rocks from the Siwalik Group, collected along rivers situated within the Sub-Himalayan FTB, delimited by the Main Boundary Thrust (MBT) in the North, and the Main Frontal Thrust (MFT) in the South. NG.1 is the only sample that lies south of the MFT.

Samples NG.1, 2, 3, 4, 5, 6, 7, 8, 10, and 11 were sampled North of Nepalgunj, in western Nepal (see Hirschmiller et al., 2014 for a cross-section of the area). Samples BUT.1, 2, 3, 4, 5 were collected more towards the east, in the Butwal area, central Nepal, along the Tinau Khola. Samples SU-9 and BAR-1 are two sandstones from the Bakaya valley (see Lavé and Avouac, 2000 for a cross-section of the area), south of Kathmandu, central Nepal. Samples RA-K01, 02, 03, 04, 05, 06 were collected across the Kamala thrust sheets, along the Kamala river, central Nepal (see Hirschmiller et al., 2014 for a cross-section of the area). Sandstone samples CA14-4 and CA14-7 (see Lavé and Avouac, 2001 for a cross-section of the area), were taken from along the Koshi Khola, eastern Nepal. Samples SJT.01A, 03, 05, 07 (siltstones), and SJT.08, 10, 11, 12 (sandstones) were collected in the Samdrup Jongkhar region, eastern Bhutan (Coutand et al., 2016). Further details on the samples can be found in the main text of the article, in the Supplementary data file, and below.

S2. Luminescence thermochronometry

S2.1. Sample preparation

All sample preparation and measurements were done under subdued red-light conditions, following the standard approach described in King et al. (2016a). After removing any potentially light exposed material of the samples (outer 1-3 cm) using a water-cooled diamond saw, the light safe part of the samples was crushed and sieved to extract the grain-size fraction of interest (180-212 μm). Carbonates and organic material were then removed using 10 % HCl and 30 % H_2O_2 respectively, before a density separation with sodium polytungstate of $\rho < 2.58$ g.cm^{-3} was used to isolate the K-feldspar enriched fraction of the samples.

S2.2. Environmental dose rate

The environmental dose rates $\dot{D}$ were determined using the Dose Rate and Age Calculator DRAC developed by Durcan et al. (2015). A representative part of each sample was sent to ActLabs – Activation Laboratories Ltd, Ancaster, Canada, for inductively coupled plasma mass spectrometry (ICP-MS) to determine the radioisotope concentrations of U, Th, K and Rb. Thin-section images were used to determine the original grain size of the samples (before crushing) with the Digital Grain Size software developed by Buscombe (2013). The grain size 180-212 µm was used when the average grain size of the sample was equivalent to or smaller than the grain size of the feldspar extract analysed (180-212 µm). The dose rate was then determined using DRAC, using the conversion factors of Guérin et al. (2011), the alpha grain-size attenuation factors of Brennan et al. (1991), the beta grain-size attenuation factors of Guérin et al. (2012), an alpha-efficiency (a-value) of 0.15 ± 0.05 (Balescu and Lamothe, 1994), and a water content of 10 ± 10 weight % (sandstone samples). As the samples are thought to have been at the surface for a relatively short period of time (for less than 2 kyr because of high erosion rates), cosmic dose rates were not incorporated in the final environmental dose rate estimations. Radio-isotopic concentrations, grain size, and final dose rates are listed in Table SD.2 of the Supplementary data file for more information.

S2.3. Luminescence measurements

The samples were measured in the luminescence laboratories at the University of Bern and the University of Lausanne, Switzerland, using a multi-elevated temperature (MET) post-infrared infrared-stimulated luminescence (post-IR IRSL) – MET-pIR-IRSL – single aliquot regenerative dose (SAR) protocol (Li and Li, 2011) on ~2 mm diameter aliquots of K-feldspar grains. Luminescence measurements were conducted on automated TL/OSL-DA-20 Risø luminescence readers. Aliquots were stimulated with infrared LEDs, and signals were detected in the blue part of the visible spectrum using a BG39 and BG3 filter pack.

All measurements were done under the same conditions. After a preheat at 250 °C for 60 s, four IRSL signals (IRSL.50, 100, 150, 225) were measured by infrared stimulation at 50, 100, 150 and 225 °C for a duration of 100 s each (L_x). A test dose of 75-95 Gy (beta radiation) was then given to the aliquots, before another preheat and measurement of the test dose signal (T_x) for each stimulation temperature (IRSL at 50, 100, 150, and 225 °C). Each measurement cycle was followed by an infrared bleaching at 290 °C for 60 s to remove any remaining signal before the measurement cycle. For each sample, three measurements were done to constrain (i) the trapped charge concentration, (ii) the sample specific rate of athermal signal loss (anomalous fading), and (iii) the sample thermal stability (Table S.1 and Fig. SD.1).

(i) Trapped charge concentrations were measured on three aliquots per sample. The natural luminescence signal stored in the feldspar minerals, $\tilde{n}_{nat}$, was first measured, before nine regenerative doses between 0 and 6000 Gy were given to the aliquots to construct sample

specific dose response curves. Data were then fitted using equation 5 of King et al. (2016a) to derive the trapping kinetic parameter D_0.

(ii) Athermal signal loss was measured using the same three aliquots used in the previous step. After the administration of a fixed regenerative dose of 75-95 Gy, equal to the test dose, aliquots were preheated prior to storage at ambient temperature following Auclair et al. (2003), and measured following different delay periods from 0 to 48,000 s. Data were fitted using equations 3 and 4 of King et al. (2016a) and the model of Huntley (2006) for the natural samples, to extract the athermal kinetic parameter ρ'. Dose response curves were then corrected for anomalous fading, and equivalent doses D_e were calculated for each aliquot.

(iii) Thermal loss was measured with isothermal decay measurements on one representative aliquot of each sample. The isothermal decay of each IRSL signal was measured using four isothermal storage temperatures at 190, 210, 230, and 250 °C, following Bouscary and King (2022), with isothermal delay times of 1 to 10,000 s. Data were fitted using the band-tail states model (BTS; Li and Li, 2013), using equations 6 and 7 of King et al. (2016a), to extract the thermal kinetic parameters E_t, E_u, and s.

Table S.1: *(i) Dose response curve, (ii) anomalous fading, and (iii) isothermal decay luminescence measurement protocols for K-feldspars aliquots with the MET-pIR-IRSL protocol.*

Steps	(i) Dose response curve	(ii) Anomalous fading	(iii) Isothermal decay
1	Natural / regenerative dose 0-6000 Gy (Lx)	Fixed regenerative dose Gy (Lx)	Fixed regenerative dose Gy (Lx)
2	Heat to 250 °C for 60 s	Heat to 250 °C for 60 s	Heat to 250 °C for 60 s
3	-	Storage $T°_{ambient}$, 0-48000s	Storage $T°_{190\text{-}250}$, 0-10000s
4	IR stimulation at 50 °C for 100 s		
5	IR stimulation at 100 °C for 100 s		
6	IR stimulation at 150 °C for 100 s		
7	IR stimulation at 225 °C for 100 s		
8	Test dose (Tx)		
9	Heat to 250 °C for 60 s		
10	IR stimulation at 50 °C for 100 s		
11	IR stimulation at 100 °C for 100 s		
12	IR stimulation at 150 °C for 100 s		
13	IR stimulation at 225 °C for 100 s		
14	Hot-bleach, IR stimulation at 290 °C for 60 s		
	Repeat		

Dose recovery tests were done to control the quality of the data. Six new aliquots were prepared and bleached with natural sunlight for 4 h or with a solar simulator for 1 h. Three discs were used to measure the unbleached residual signal, and three discs were given a laboratory dose to obtain dose recovery ratios following residual subtraction. The laboratory

dose used was either a dose similar to the D_e of the IRSL.50 signal, or a dose of 150 Gy for samples close to saturation.

All luminescence signals were extracted from the luminescence decay curves by integrating the signal over the 5 first channels (2 s), and subtracting the background calculated over the last 50 channels (20 s). Aliquots were accepted and included in the study when they fulfilled the sample acceptance criteria, i.e. signal greater than 3σ above background, recycling ratio within 10 % of unity, maximum test dose uncertainty < 10 %, and recuperation < 10 % of the natural signal.

S2.4. Results and data screening

All aliquots of all samples passed the aliquot acceptance criteria for all IRSL measurements, and the measurements were reproducible within error for each sample (n = 3). Dose recovery ratios (after residual subtraction) yielded a dose recovery ratio within 15 % of unity, which was deemed acceptable in this study.

To evaluate aliquot saturation, the approach of Kars et al. (2008) was used to screen whether the samples were in athermal steady-state, or whether they exhibited disequilibrium (i.e. contained a thermal signal). Natural luminescence $\tilde{n}_{nat}$ values were compared with those predicted for athermal steady-state $\tilde{n}_{SS}$. Samples are considered saturated when $\tilde{n}_{nat} \geq 0.86.\tilde{n}_{SS}$. Of the 33 samples measured, 5 are in athermal steady-state for all the measured signals (NG.10, RA-K01, RA-K04, RA-K06, and CA14-4). 15 other samples are within the limit of saturation for at least one IRSL signal. In total, 10 samples have their IRSL.50 signal saturated, 6 their IRSL.100 signal, 10 their IRSL.150 signal, and 15 their IRSL.225 signal. The high number of saturated samples for the IRSL.50 might relate to the high fading rates for this signal. The saturation of the post-IRSL signals, particularly of the IRSL.225, is probably linked to low counting statistics for less bright luminescence emissions or to the higher thermal stability of this signal.

Another screening was done to remove samples that are potentially in thermal equilibrium with surface temperature. A temperature at 20 °C, reflecting the approximate average surface temperature throughout the Holocene (last few meters of exhumation of the rocks) was chosen. Thermal steady-state values for a temperature of 20 °C, $\tilde{n}_{20}$, were calculated for each sample and compared with the natural luminescence values, $\tilde{n}_{nat}$. As above, samples are considered saturated when $\tilde{n}_{nat} \geq 0.86.\tilde{n}_{20}$. All signals that are within the limit of saturation for athermal steady-state, are also all in saturation for surface temperature. Out of the 33 samples measured, 11 are in thermal steady-state for surface temperature for all the measured signals (the 5 that are also in athermal steady-state, as described above, and NG.6, NG.7, NG.8, RA-K02, SJT01A), and 15 other samples are within the limit of saturation for at least one IRSL signal. In total, 18 samples have their IRSL.50 signal saturated, 16 their IRSL.100 signal, 15 their IRSL.150 signal, and 23 their IRSL.225 signal. Only 7 samples

(NG.4, NG.5, BUT.2, BUT.3, BUT.4, SU-9, and BAR-1) have no signals in equilibrium with surface temperature.

S3. Inversion of thermochronometric data

S3.1. Maximum burial temperature

To invert thermochronometric data for exhumation rates, the thermal history of the sample should be considered. In the Ganga plain or the Himalayan foredeep basin, the limited flexure of the rigid lid of the Indian plate (Lyon-Caen and Molnar, 1985) greatly limits the depth of burial of the Himalayan molasses. Consequently, in the Sub-Himalayan FTB, the exhumed rocks of the Siwalik Groups were buried only to depths of up to ~5 km, corresponding to a maximum burial temperature of 120 °C, assuming a homogeneous geothermal gradient of 20 °C/km (Mugnier et al., 1995; van der Beek et al., 2006).

When maximum burial temperatures are not already constrained by vitrinite reflectance data, as for the SJT transect (Coutand et al., 2016), maximum burial temperatures were estimated from each sample maximum burial depth, derived from the stratigraphic location of the sample and balanced cross-section reconstruction, using a fixed geothermal gradient of 20 °C/km and a surface temperature of 20 °C. These maximum burial temperatures are minimum estimates that do not consider the overthrusting rocks from the hanging walls of near thrusts. Maximum burial depth and burial temperatures for each sample are listed in Table SD.5.

S3.2. Exhumation rates

Average exhumation histories are calculated for each non-saturated IRSL signal. The models are run for 1 Myr, between 1 Ma and 0 Ma (today), with a time step of 1000 yr (nstep = 1001), to ensure that the luminescence signals generated are in steady-state, i.e., are in dynamic equilibrium between rates of electron trapping and detrapping for the maximum burial temperature prior to rock cooling. Time-temperature cooling paths were calculated for fixed exhumation rates between 0 mm/yr (no exhumation) and 20 mm/yr, in increments of 0.1 mm/yr, assuming a fixed homogeneous geothermal gradient at 20 °C/km, and a surface temperature of 20 °C. Maximum temperature was fixed as the maximum possible burial temperature for the specific sample under investigation, derived from the maximum burial depth that the sample experienced (see Table SD.5).

For each exhumation rate-derived time-temperature path (Fig. S.1A), a forward model calculates the modelled trap occupancy values, $\tilde{n}_{mod}$, for each IRSL signal, using the sample specific natural kinetic parameters and equation 5 of King et al. (2016a) (Fig. S.1B). Final $\tilde{n}_{mod}$ values, $\tilde{n}_{mod}(end)$, were extracted and compared to the natural luminescence signals of the samples, $\tilde{n}_{nat}$. Only exhumation rates that yielded $\tilde{n}_{mod}(end)$ values within uncertainty

of $\tilde{n}_{nat}$ ($s\tilde{n}_{nat}$, fixed at a minimum of 5 % of $\tilde{n}_{nat}$) were retained (Fig. S.1B). Exhumation rates are then extracted from the minimum difference between $\tilde{n}_{mod}(end)$ and $\tilde{n}_{nat}$ for each IRSL signal. Errors on the exhumation rates values are calculated in the same way, from the minimum and maximum exhumation rates that correspond to the minimum and maximum $\tilde{n}_{nat}$ values including error ($\tilde{n}_{nat}$ - $s\tilde{n}_{nat}$ and $\tilde{n}_{nat}$ + $s\tilde{n}_{nat}$) (Fig. S.1C).

Samples specific exhumation rates are then averaged over the different non-saturated luminescence signals of the samples. See Table 1 of the main article for transect specific exhumation rates, and Table SD.6 for the sample specific thrust slip rates and shortening rates.

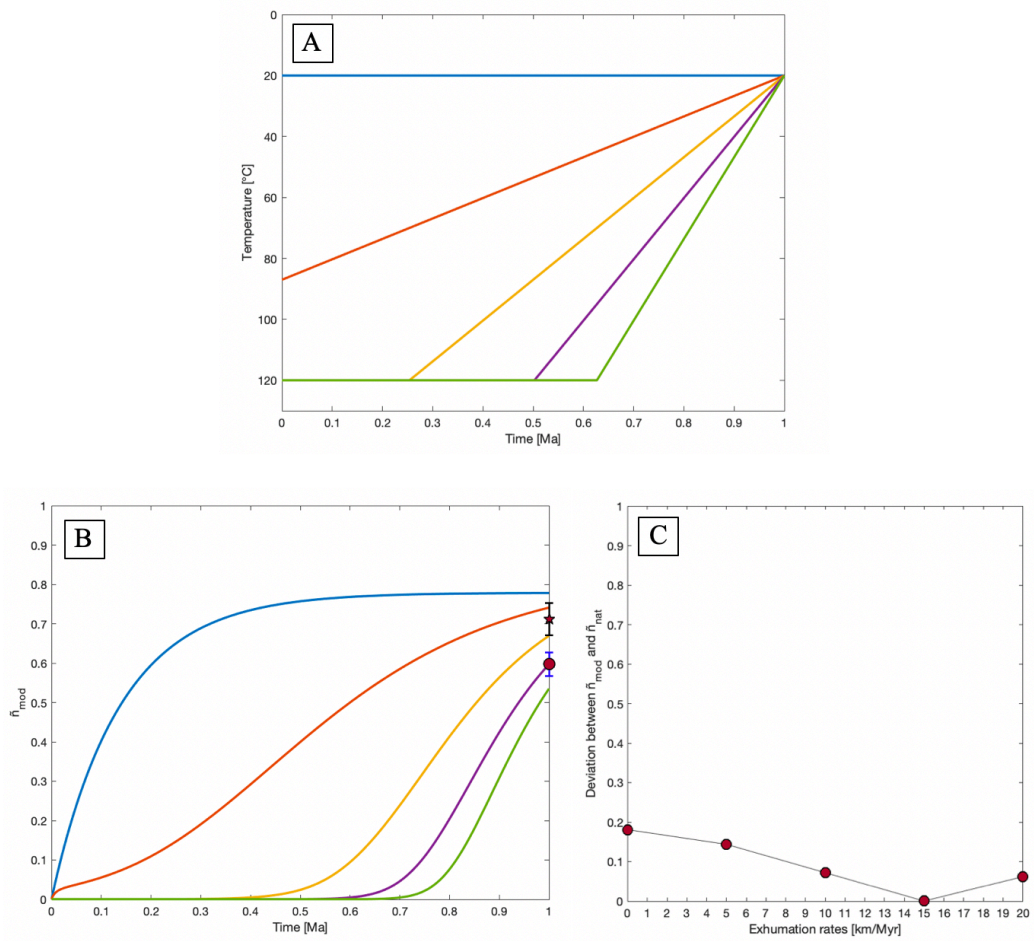

Fig. S.1: *Modelled average exhumation rates for an IRSL signal of a sample.* ***A.*** *Example of a few time-temperature paths corresponding to 5 exhumation rates at 0 (blue), 5 (orange), 10 (yellow), 15 (purple), and 20 mm/yr (green). The time 1 Ma corresponds to the present day.* ***B.*** $\tilde{n}_{mod}$ *signals for each exhumation rate. The red circle and star represent the* $\tilde{n}_{nat}$ *and* $0.86 * \tilde{n}_{SS}$ *values for the IRSL of the sample, and their error range* $s\tilde{n}_{nat}$ *and* $s\tilde{n}_{SS}$ *in blue and black respectively. The time 1 Ma corresponds to the present day.* ***C.*** *Deviation between the final* $\tilde{n}_{mod}$ *value,* $\tilde{n}_{mod}(end)$*, and the natural signal of the sample,* $\tilde{n}_{nat}$*, for each exhumation rate. When the misfit is closest to the x-axis, it corresponds to the exhumation rate that generates an* $\tilde{n}_{mod}(end)$ *value closest to* $\tilde{n}_{nat}$ *for the sample signal, i.e., here to 15 mm/yr.*

Supplementary data

Supplementary data are available at an online depository:
>>>> Please ask for the Dropbox link if needed. >>>>

Table SD.1: Sample names, thrust sheet, locations, elevations, and transect name and location.

Table SD.2: Radioisotope concentrations, grain size range, and calculated total environmental dose rate ($\dot{D}$). Errors are calculated as 3 % of the values.

Table SD.3: Summary of kinetic and fitted parameters for all four IRSL temperatures, using kinetic parameters derived from four isothermal temperatures between 190 and 250 °C (Bouscary and King, 2022). Uncertainties are listed at 1σ for all values, except for D_e, for which errors are listed as 5 % of D_e. Fading rates are expressed both as ρ' and as g-values normalised to 2 days, g_{2d}, Huntley and Lamothe (2001). Saturated samples are shown in grey.

Table SD.4: Saturation indicator values, and age of the samples for all four IRSL temperatures. Saturated samples are shown in grey.

Table SD.5: Samples with their reference thrust, geographical distance to the Main Frontal Thrust (MFT), and stratigraphic burial depth and associated maximum burial temperature, derived from the stratigraphic location of the sample today, and cross-section reconstruction.

Table SD.6: Samples with their IRSL signal specific exhumation rate, and their sample specific exhumation rate, i.e., the average of the non-saturated IRSL signal specific exhumation rates.

Table SD.7: Samples with their averaged apparent age, exhumation rate, and thrust slip rates and shortening rates with a fixed dip angle of 30°, and with a dip angle range between 25 and 45°.

Table SD.8: Compilation of GPS derived geodetic convergence rates from the literature.

Fig. SD.1.1-6: Luminescence measurement and model fit results for all samples. (A, D, G, J) Anomalous fading data fitted using equations 3 and 4 of King et al. (2016a), for the IRSL at 50, 100, 150, and 225 °C respectively. (B, E, H, K) Luminescence dose response accounting for fading, fitted using equation 5 of King et al. (2016a). The black solid line is the unfaded dose response curve, and the yellow dots represent the $\tilde{n}_{nat}$ values of each aliquot. (C, F, I,

L) Isothermal decay data fitted with the BTS model, using equations 6 and 7 of King et al. (2016a).

Fig. SD.2.1-6: Steady-state saturation plots (Kars plots) for all samples, contrasting natural luminescence values, $\tilde{n}_{nat}$, with steady-state luminescence values, $\tilde{n}_{SS}$, predicted for each of the samples. The 1:1 line delimits saturated samples (blue area) to unsaturated samples (white area), with the saturation limit indicated by the blue line.

Fig. SD.3.1-6: Surface temperature saturation plots for all samples, contrasting natural luminescence values, $\tilde{n}_{nat}$, with the luminescence values for a surface temperature of 20 °C, $\tilde{n}_{Tmin} = \tilde{n}_{20}$, predicted for each of the samples. The 1:1 line delimits saturated samples (blue area) to unsaturated samples (white area), with the saturation limit indicated by the blue line.

Chapter 3

Late Quaternary exhumation rates of the Nepalese-Himalayan hinterland, duplex vs. out-of-sequence activity of the MCT

C. Bouscary et al.

Table of contents

The results of this chapter will be submitted to *Journal of Geophysical Research: Solid Earth*:
Bouscary, C., King, G.E., Lavé, J., Hetényi, G., Gajurel, A.P., and Herman, F. (*in prep.*). Late Quaternary exhumation rates of the Nepalese-Himalayan hinterland, duplex vs. out-of-sequence activity of the MCT. *Journal of Geophysical Research: Solid Earth*.

Abstract

The tectonic evolution of the Himalayas throughout the Quaternary period (last 2.6 Myr) remains disputed. Two end-member models have been proposed. The first posits that in-sequence thrusting has resulted in the most recent tectonic activity occurring on the southernmost thrust of Nepal, in the Siwaliks foothills, and is associated with the development of a duplex structure at depth below the High Himalayas. The second model proposes that some faults evolved out-of-sequence in the High Himalaya area, resulting in thrusting both at the Himalayas front and hinterland. Both models explain the observed inverted metamorphism, but they lead to drastically different distribution of strain within the Himalayas. Understanding how strain is distributed remains essential for the accuracy of seismic hazard models.

To address this debate, existing low and medium-temperature thermochronometric data (Herman et al., 2013) were contrasted with 61 new luminescence thermochronometry samples distributed across the hinterland of the central Nepal, and luminescence thermochronometric data from the Sub-Himalayas (Bouscary et al., In review). The luminescence thermochronometry samples provide a new perspective on Late Pleistocene exhumation rates (timescales of 10^4 to 10^5 years) of the Nepalese Himalayas, by offering high-resolution constraints of rock cooling histories within the upper kilometres of the Earth's crust.

Results show that high exhumation rates are recorded both in the hinterland and the foreland of the Nepalese-Himalayas, with exhumation rates of ~3-11 mm/yr for the Sub-Himalayas over the last ~200 kyr, and ~3-16 mm/yr for the High Himalayas over the last ~0.1 Myr. Enhanced exhumation since ~200 kyr, with the location of the highest exhumation rates varying spatially and temporally since the Miocene, suggest an intermittency of exhumation due to geomorphological processes, favouring the in-sequence model with the development of a duplex structure below the High Himalayas. However, sharp differences in apparent age and exhumation rates on each side of the MCT fault system during the late Quaternary indicate fault movement along the MCT, proving that the Himalayas are active out-of-sequence on 100 kyr-timescales.

1. Introduction

The Himalayan orogen is the largest and one of the youngest and most active mountain ranges on the planet. Its formation is the result of continental collision between the Indian and the Eurasian tectonic plates, that started during the Paleocene - Early Eocene (Yin and Harrison, 2000; Bernet et al., 2006; Chirouze et al., 2012; Mathew et al., 2013; Dhital, 2015). This collision caused intense crustal shortening and thickening, and imbrications of southward-displaced thrust sheets, resulting in the formation of the Himalayan mountain belt and the Tibetan Plateau (Hodges, 2000; Yin and Harrison, 2000; Bernet et al., 2006; Chirouze et al., 2012). Today, the Himalayas is subdivided into four major lithotectonic units (Hodges, 2000; Yin and Harrison 2000; Bernet et al., 2006; van der Beek et al., 2006; Dhital, 2015): the Tethyan Himalayan zone, the Higher Himalayan zone, the Lesser Himalayan zone, and the Sub-Himalaya. These units are separated by Late Cenozoic north-dipping crustal-scale fault systems that formed in-sequence from north to south: the South Tibetan Detachment system (STDS), the Main Central Thrust (MCT), the Main Boundary Thrust (MBT), and the Main Frontal Thrust (MFT). These faults are all branched on the main detachment overlying the underthrusted Indian plate, the Main Himalaya Thrust (MHT) (Yin and Harrison, 2000; Avouac, 2003; Dhital, 2015) (Fig. 1 and Fig. 2).

In central Nepal, depending on where the more recently active thrust faults are located, two hypotheses can explain the tectonics of the Himalayas during the Quaternary. (1) The in-sequence model accommodates all the convergence on an active MHT expressed as the MFT and the development of duplex structures (e.g., Lavé and Avouac, 2000; DeCelles et al., 2001; Robinson et al., 2003; Bollinger et al., 2004; Mugnier et al., 2004; Herman et al., 2010). (2) Others argue that the slip on the MHT is insufficient to accommodate this convergence, and they suggest an out-of-sequence model (Catlos et al., 2001; Hodges et al., 2001; Wobus et al., 2003; Hodges et al., 2004; Whipple et al., 2016), with more recent activity of the thrusts towards the MCT area (Fig. 1).

These two end-member competing models have been proposed to describe the present-day kinematics of the central Nepal Himalayas. They differ in their interpretations of which surface breaking faults accommodate current shortening and the kinematics responsible for driving rapid exhumation in the topographic transition zone around the MCT. The locally higher uplift and erosion rates in the High Himalaya could reflect (1) thrusting over a mid-crustal ramp (e.g., Cattin and Avouac, 2000; Lavé and Avouac, 2001) with the growth of a Lesser Himalaya duplex at mid-crustal depth causing underplating along the MHT ramp (e.g., Schelling and Arita, 1991; DeCelles et al., 2001; Robinson et al., 2003; Avouac, 2003; Bollinger et al., 2004, 2006), or (2) out-of-sequence thrusting along the front of the High Himalaya, possibly driven by climatically controlled localized exhumation (e.g., Harrison et al., 1998; Wobus et al., 2003; Hodges et al., 2004).

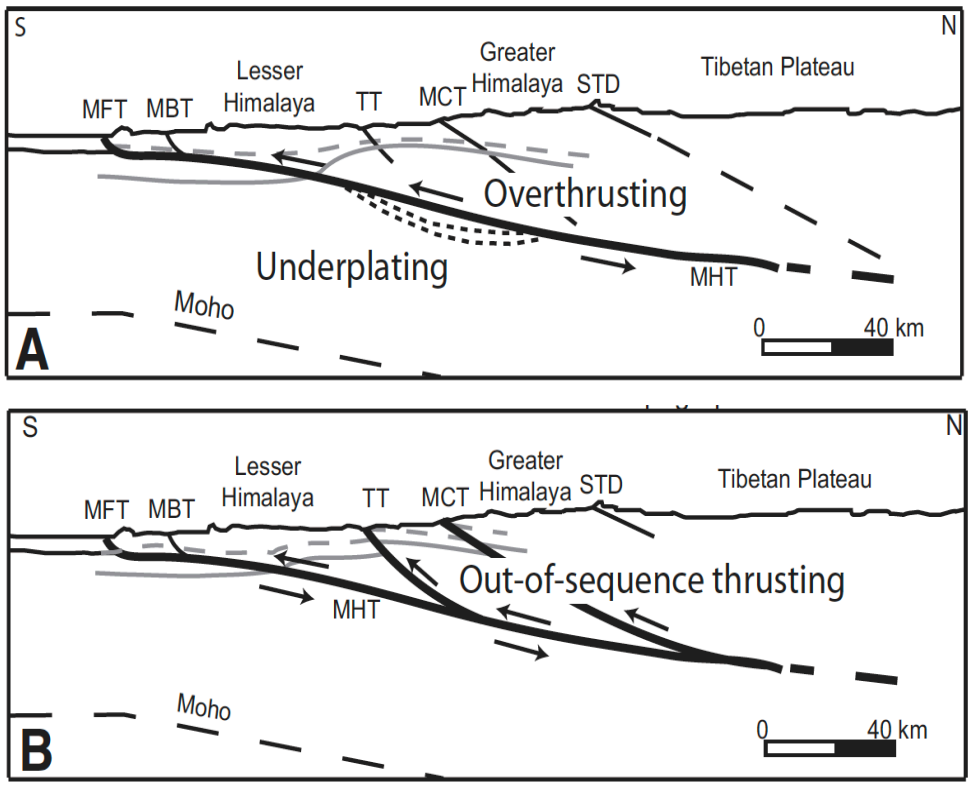

Fig. 1: *Schematic tectonic end-member models with the present-day kinematics of the Central Nepal Himalayas. In model* ***A*** *(Avouac, 2003), in-sequence faulting, the shortening is concentrated on the MHT with a crustal ramp below the topographic transition between the Lesser and Greater Himalaya. In model* ***B*** *(Hodges et al., 2004), out-of-sequence faulting occurs in the TT zone. MFT = Main Frontal Thrust; MBT = Main Boundary Thrust; MCT = Main Central Thrust; MHT = Main Himalaya Thrust; STD = South Tibetan Detachment; TT = Topographic transition (modified from Robert et al., 2009).*

Many previous studies have tried to discriminate between these two hypotheses by interpretation of thermometric, barometric and thermochronological data, and combining them with geomorphic observations. In addition, numerous thermo-kinematic and thermo-mechanical numerical models have also been built by modelling of the tectonics and topography based on these data (e.g., Huerta et al., 1999; Herman et al., 2010; Dal Zilio et al., 2018). A wide range of low- and medium-temperature thermochronometric systems (defined by their different closure temperatures) have been applied to bedrock rock samples and detrital samples (sediments) from the High Himalaya hinterland: $^{40}Ar/^{39}Ar$ in muscovite and biotite (e.g., Copeland et al., 1991; Macfarlane et al., 1992, 1993; Edwards et al., 1996; Arita et al., 1997; Coleman and Hodges, 1998; Rai, 1998; Catlos, 2000; Bollinger et al., 2004; Hodges et al., 2004; Wobus et al., 2005; Huntington and Hodges, 2006), fission-track in zircon and apatite (e.g., Arita and Ganzana, 1997; Burbank et al., 2003; Blythe et al., 2007), and (U-Th)/He in apatite and zircon ages (e.g., Blythe et al., 2007; Adams et al., 2009). For the Siwaliks, sediments and fluvial terrace deposits from the Nepalese foreland, ages and exhumation/erosion rates have been calculated from complementing geochronologic and

thermochronometric techniques: e.g., ^{14}C, terrestrial cosmogenic nuclide dating, optically-stimulated and infrared-stimulated luminescence dating, electron spin resonance dating, isotopic analysis (e.g., Lavé and Avouac, 2000, 2001; Burgess et al., 2012; Lénard, 2019; Lénard et al., 2020; etc), as well as from U-Pb, apatite and zircon fission-track and $^{40}Ar/^{39}Ar$ dating (e.g., Bernet et al., 2006; Szulc et al., 2006; van der Beek et al., 2006).
The conclusions of these studies are variable despite focusing on the same region. Some show the validity of the duplex model (e.g., Schelling and Arita, 1991; Cattin and Avouac, 2000; DeCelles et al., 2001; Lavé and Avouac, 2001; Avouac, 2003; Robinson et al., 2003; Bollinger et al., 2004, 2006; Herman et al., 2010), whereas others support the out-of-sequence model, with activity in the MCT zone over the past 2 Myr (e.g., Harrison et al., 1998; Hodges et al., 2001, 2004; Wobus et al., 2003; Blythe et al., 2007). However, most of these studies did not explore the full range of possible kinematic models, nor the range of possible thermal parameters. Whipp et al. (2007) and Wobus et al. (2006) question the reliability of these studies and concluded that the existing low-temperature thermochronological data from the High Himalaya are insufficient to discriminate among the various models of crustal deformation. Also, despite the dense thermochronological data available from the Himalayas of central Nepal, few of the thermochronologic ages reported for the Lesser Himalaya are reliable due to unfavourable lithologies, and the youngest thermochronometric data lack precision and accuracy (closure temperature too high).

To tackle this debate, we combine new luminescence thermochronometric data applied to 61 new samples that were collected all across the High Himalayas of central Nepal, with existing classical thermochronometers from the High Himalayas (Herman et al., 2013) and luminescence thermochronometric data from the Sub-Himalayas (Bouscary et al., In review). Our objective is to accurately constrain exhumation rates on sub-Quaternary timescales across the two fault systems of the MFT and the MCT, to provide a better resolution of the difference in exhumation and thrust activity, and to discriminate between the two tectonic models/hypotheses for the late Quaternary (timescales of 10^4 to 10^5 years).

2. Area of study

This study focusses on the High Himalayas of central Nepal in the Annapurna and Ganesh regions. Existing low and medium-temperature thermochronometric data for the High Himalayas of central Nepal were extracted from the world thermochronometric data file of Herman et al. (2013). These data comprise thermochronometric ages from $^{40}Ar/^{39}Ar$ on muscovite, apatite (U-Th)/He (AHe), zircon (U-Th)/He (ZHe), apatite fission track (AFT), and zircon fission track (ZFT), with ages extending to the Oligocene (~23-34 Ma).

To complement these existing published data, 61 new rock samples were collected to be analysed with luminescence thermochronometry. They were specifically selected to record exhumation rate changes on each side of the major thrusts and faults that shape the Nepalese hinterland landscape in central Nepal (Fig. 2). From west to east, 13 samples were collected along the Kali Gandaki, 19 samples along the Marsyangdi river, 15 samples along the Buri Gandaki, and 14 samples in the Trisuli valley. Samples from these transects were taken from metamorphic rocks from the Lesser Himalaya and Higher Himalaya, as well as metamorphic-sedimentary rocks and igneous rocks from the Tethyan Himalaya, to provide information on the MCT zone and the STDS, and on associated tectonic structures. Three elevation transects were collected, one north of the STDS at the end of the Marsyangdi valley (HIM.6-6E), and two on the MCT thrust sheet in the Marsyangdi (HIM.4Z-4C) and Buri Gandaki (BG.E-A) valleys. Two samples from the Marsyangdi, HIM.3A and HIM.3B, were also sampled near the hot springs of Jagat and Shirchaur in the Marsyangdi valley. Sample KG.2 was also sampled close to Tatopani, another hot spring in the Kali Gandaki valley.

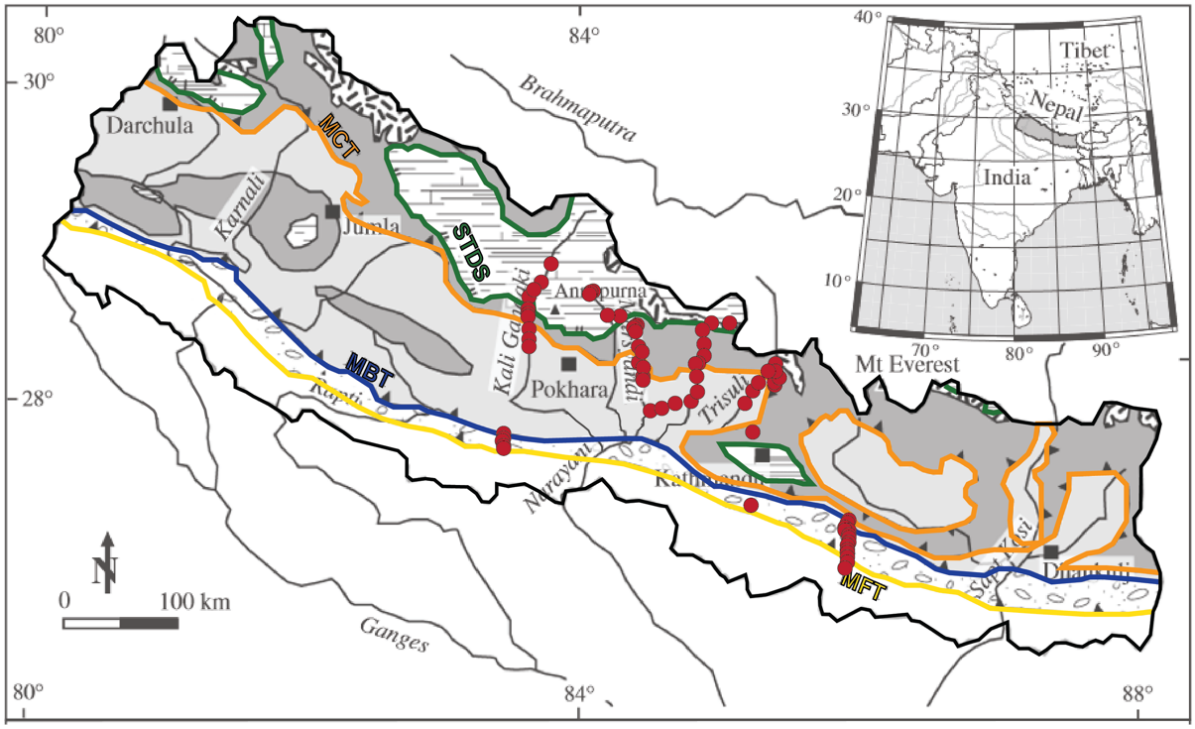

Fig. 2: *Simplified geological and tectonic map of Nepal (modified from van der Beek et al., 2006). The red dots represent the luminescence thermochronometry samples used in this study, with in the hinterland (High Himalaya), the 61 samples measured in this study, and in the Sub-Himalayas, between the MFT and MBT thrusts, samples from three transects of Bouscary et al. (In review). MFT – Main Frontal Thrust; MBT – Main Boundary Thrust; MCT – Main Central Thrust; STDS – South Tibetan Detachment System.*

Deformation along the frontal part of the Himalayan range were taken from the study of Bouscary et al. (In review) / Chapter 2. The luminescence thermochronometry derived apparent ages and exhumation rates from the five BUT samples, the samples SU-9 and BAR-1, and the six RA-K samples, highlight the deformation/tectonic activity of Sub-Himalayan fold-and-thrust belt along the MFT in central Nepal (c.f., Bouscary et al., In review).

3. Method

3.1. Quaternary exhumation rates derived with GLIDE

The existing low and medium-temperature thermochronometric data from the world data file of Herman et al. (2013) (Fig. 3) were inverted for exhumation rates and projected on the studied area using the Bayesian inversion method of Fox et al. (2014) with GLIDE (Fig. 4). This approach converts thermochronometric ages to exhumation rates based on the fact that the depth to the closure isotherm is the integral of exhumation rates from the cooling age to the present. Time is discretized over a finite number of time intervals, and exhumation rate is determined for each of these intervals. A full description of the procedure is provided in Fox et al. (2014). As these thermochronometers constrain cooling, and thus exhumation rates, on longer timescales than luminescence thermochronometry, exhumation rates were extracted for the last 2 Myr, more or less covering the exhumation rates of the Quaternary period (2-0 Ma; Fig. 4).

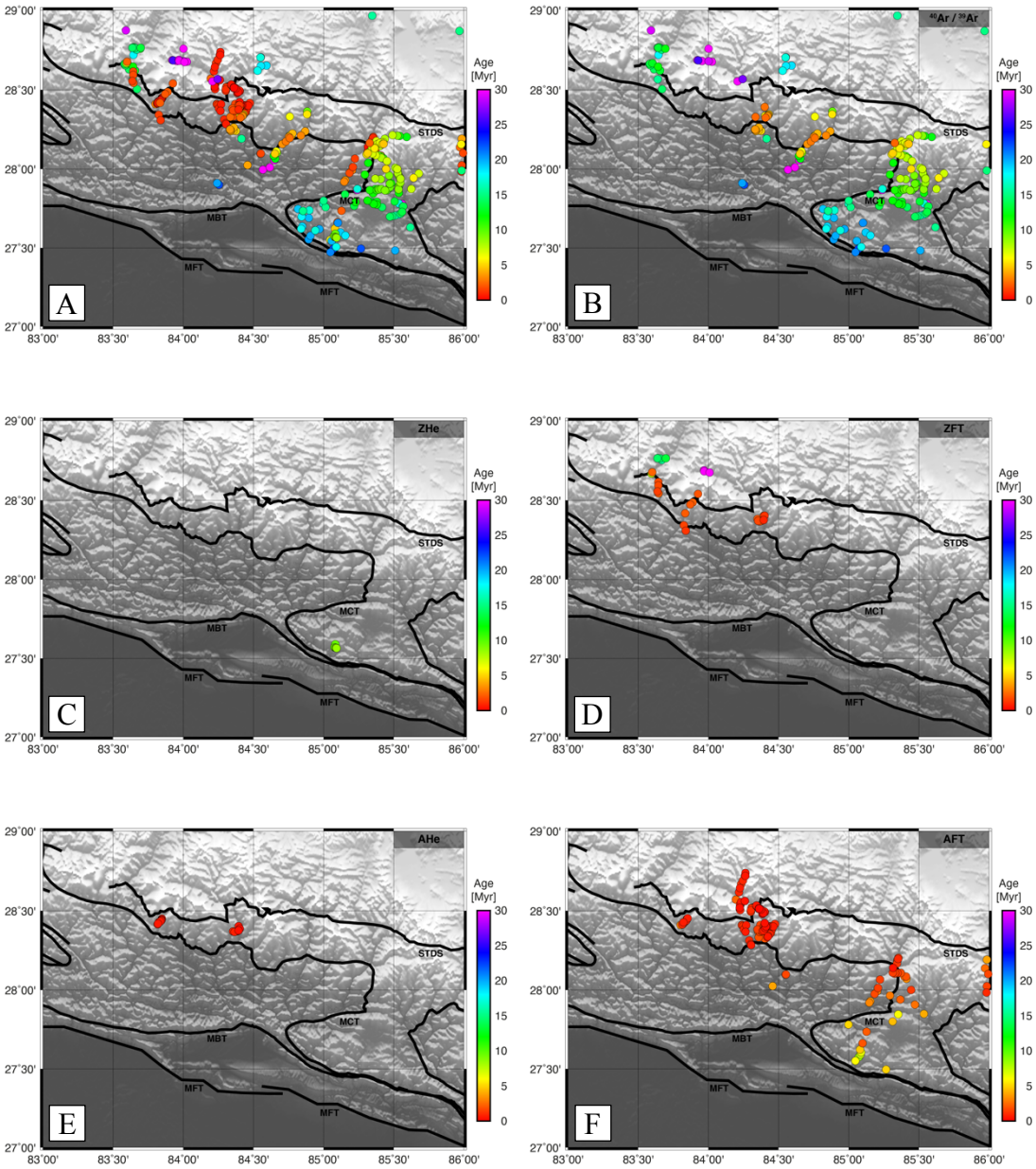

Fig. 3: ***A.*** *Compilation of all thermochronometric ages from* ***B.*** $^{40}Ar/^{39}Ar$ *on muscovite,* ***C.*** *ZHe,* ***D.*** *ZFT,* ***E.*** *AHe, and* ***F.*** *AFT. Ages from the world data base file of Herman et al. (2013). AHe – apatite (U-Th)/He; ZHe – zircon (U-Th)/He; AFT – apatite fission track; ZFT – zircon fission track.*

Resolution of the exhumation rates from thermochronometric ages is determined by the range of ages, the number and range of the closure temperature and the distribution of samples (Fig. 4B). This means that even though resolution is dependent on the age of the sample, its location is a main factor influencing resolution. A resolution of 1 implies that the thermochronometric ages perfectly describe the exhumation rates.

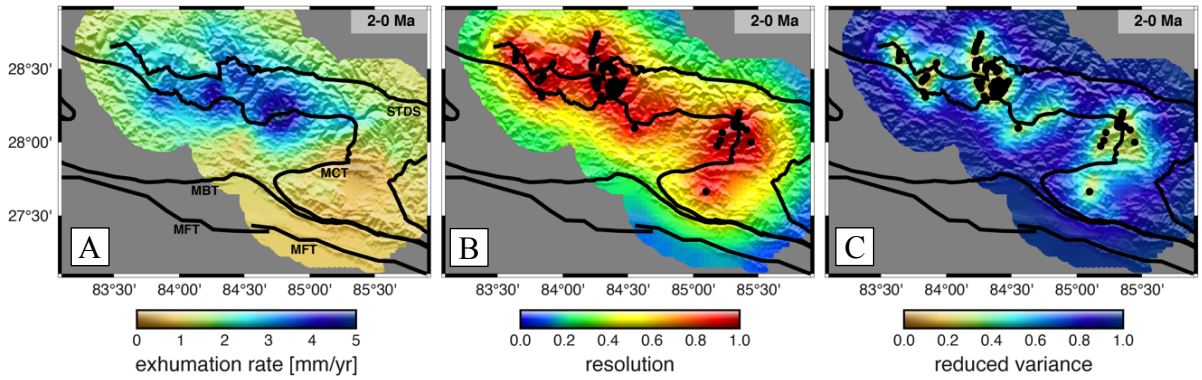

Fig. 4: *Modelling results by inverting thermochronometric ages.* ***A.*** *Map of exhumation rates during the last 2 Myr, with* ***B.*** *its resolution, and* ***C.*** *its reduced variance, derived from the Bayesian inversion of thermochronometric ages of Herman et al. (2013) with GLIDE (Fox et al., 2014). A resolution (dimensionless) of 1 and a reduced variance (dimensionless) of 1 imply that the thermochronometric ages perfectly describe the exhumation rates derived in A.*

3.2. Luminescence measurements

The luminescence thermochronometry method has been exhaustively described previously (e.g., King et al., 2016a; Ogata et al., 2022; Bouscary and King, 2022) and we only briefly describe our luminescence measurements here. Samples were prepared to extract K-feldspar under subdued red light using standard methods (e.g., King et al., 2016a) before measurement using a multi-elevated temperature post-infrared infrared-stimulated luminescence (MET-pIR-IRSL) protocol (Li and Li, 2011; King et al, 2016a), using four IRSL temperatures at 50, 100, 150, and 225 °C. Samples of the Buri Gandaki were measured using only two IRSL stimulations at 50 and 225 °C, as preliminary investigations showed that the post-IR IRSL signals at 100 and 150 °C were too dim or were absent.

Following the approach of Bouscary and King (2022), three measurements were done to describe luminescence signal growth and decay for each sample. Luminescence dose response curve were measured in a single aliquot regenerative dose method to measure the natural luminescence signal of the sample. Anomalous fading rates were determined using fading tests, and isothermal decay experiments were used to measure the thermal sensitivity of the sample. Individual luminescence signals were rejected when aliquots did not pass the acceptance criteria (i.e., signal greater than 3σ above background, recycling ratio within 10 % of unity, maximum test dose uncertainty < 10 %, and recuperation < 10 % of the natural signal) and when the measurements were not reproducible within error for each sample (n = 3). Samples that did not yield a residual-subtracted dose recovery ratio within 15 % of unity were also rejected.

Data were fitted using the same approach as Bouscary et al. (In review). A single-saturating exponential function was used to fit luminescence dose response, allowing constraint

of the natural luminescence signal of the sample, $\tilde{n}_{nat}$. The band-tail states model was used to fit the isothermal decay data, allowing derivation of the thermal kinetic parameters whilst the model of Huntley (2006) was used to fit the fading data.

Luminescence signals were also rejected when they exhibited field saturation, which was evaluated in two ways; for athermal steady-state, and for surface temperature. The approach of Kars et al. (2008) was used to screen whether the samples were in athermal steady-state, $\tilde{n}_{SS}$, or whether they exhibited disequilibrium (i.e. contained a thermal signal). A second screening was done to remove samples that were potentially in thermal equilibrium with surface temperature. A temperature at 10 °C (for samples at lower latitude and/or elevation) or 5 °C (for samples at higher latitude and/or elevation), reflecting the approximate average surface temperature throughout the Holocene (last few meters of exhumation of the rocks) was chosen. In both cases, natural luminescence $\tilde{n}_{nat}$ values were compared with those predicted for athermal steady-state $\tilde{n}_{SS}$, or those predicted for surface temperature $\tilde{n}_{Tmin}$. Samples were considered saturated when $\tilde{n}_{nat} \geq 0.86.\tilde{n}_{SS}$, or $\tilde{n}_{nat} \geq 0.86.\tilde{n}_{Tmin}$.

3.3. Luminescence exhumation rates derived from inverse modelling

Average exhumation histories are calculated for each non-saturated IRSL signal. Models were run for 1 Myr, between 1 Ma and 0 Ma (today), with a time step of 1000 yr (nstep = 1001). Time-temperature cooling paths were calculated for fixed exhumation rates between 0 mm/yr (no exhumation) and 30 mm/yr, in increments of 0.1 mm/yr, assuming a fixed homogeneous geothermal gradient at 50 °C/km, and a surface temperature of 5 or 10 °C. As the samples experienced monotonic cooling since formation, maximum temperature was fixed at 120 °C not to bias the luminescence signal.

For each exhumation rate-derived time-temperature path (Fig. 5A), a forward model calculates the modelled trap occupancy values, $\tilde{n}_{mod}$, for each IRSL signal, using the sample specific natural kinetic parameters and equation 5 of King et al. (2016a) (Fig. 5B). Final $\tilde{n}_{mod}$ values, $\tilde{n}_{mod}(end)$, were extracted and compared to the natural luminescence signals of the samples, $\tilde{n}_{nat}$. Only exhumation rates that yielded $\tilde{n}_{mod}(end)$ values within uncertainty of $\tilde{n}_{nat}$ ($s\tilde{n}_{nat}$, fixed at a minimum of 5 % of $\tilde{n}_{nat}$) were retained (Fig. 5B). Exhumation rates are then extracted from the minimum difference between $\tilde{n}_{mod}(end)$ and $\tilde{n}_{nat}$ for each IRSL signal. Errors on the exhumation rates are calculated in the same way, from the minimum and maximum exhumation rates that correspond to the minimum and maximum $\tilde{n}_{nat}$ values including error ($\tilde{n}_{nat}$ - $s\tilde{n}_{nat}$ and $\tilde{n}_{nat}$ + $s\tilde{n}_{nat}$) (Fig. 5C). Sample-specific exhumation rates are then averaged over the different non-saturated luminescence signals of the samples.

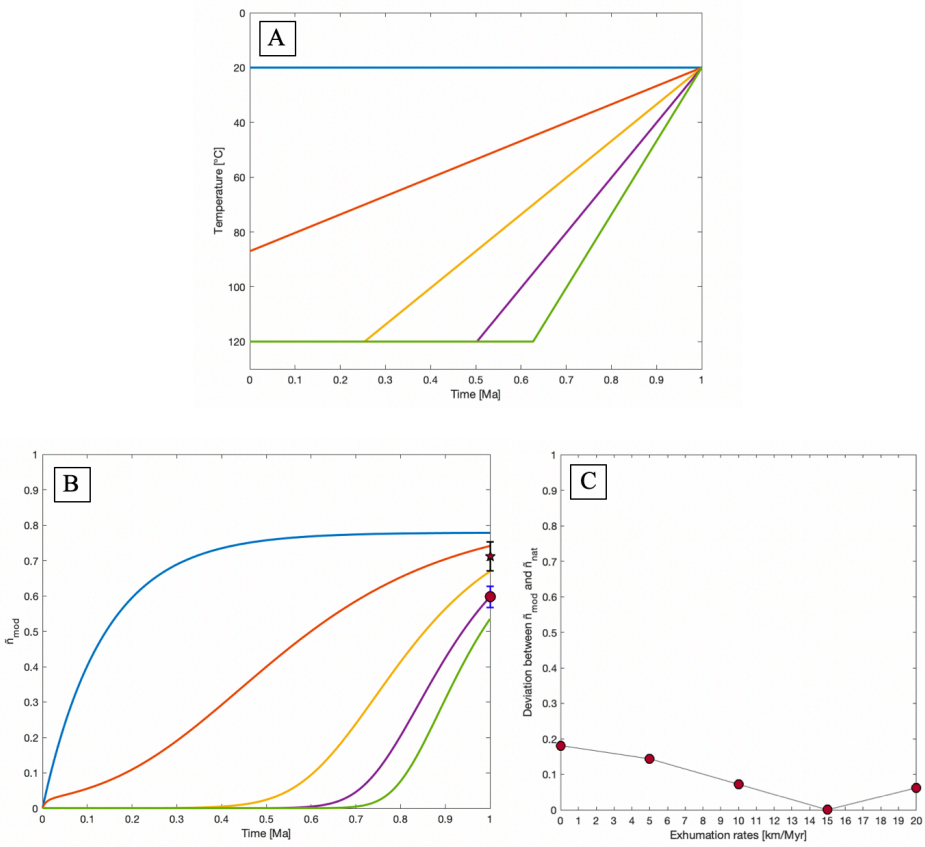

Fig. 5: *Modelled average exhumation rates for an IRSL signal of a sample (from the Supplementary material of Bouscary et al., In review).* ***A.*** *Example of a few time-temperature paths corresponding to 5 exhumation rates at 0 (blue), 5 (orange), 10 (yellow), 15 (purple), and 20 mm/yr (green). The time 1 Ma corresponds to the present day.* ***B.*** $\tilde{n}_{mod}$ *signals for each exhumation rate. The red circle and star represent the* $\tilde{n}_{nat}$ *and 0.86**$\tilde{n}_{SS}$ *values for the IRSL of the sample, and their error range* $s\tilde{n}_{nat}$ *and* $s\tilde{n}_{SS}$ *in blue and black respectively. The time 1 Ma corresponds to the present day.* ***C.*** *Deviation between the final* $\tilde{n}_{mod}$ *value,* $\tilde{n}_{mod}$*(end), and the natural signal of the sample,* $\tilde{n}_{nat}$*, for each exhumation rate. When the misfit is closest to the x-axis, it corresponds to the exhumation rate that generates an* $\tilde{n}_{mod}$*(end) value closest to* $\tilde{n}_{nat}$ *for the sample signal, i.e., here to 15 mm/yr.*

4. Results

4.1. Saturation of the luminescence signals

Of the 61 samples investigated in the Himalayan hinterland of central Nepal, 5 samples (HIM.0, HIM.6, HIM.6A, HIM.6C, HIM.6D) did not have enough K-feldspar to be fully measured, and were thus rejected from the study. Out of the 56 remaining sampled, 26 are in field saturation, and 46 have at least one of their IRSL signals that did not pass the rejection criteria or that is in field saturation. However, a clear pattern emerges when the distribution of

saturated and non-saturated samples is considered (Fig. 6). Almost all samples south of the MCT are saturated. In contrast, north of the MCT, only a few samples are totally saturated.

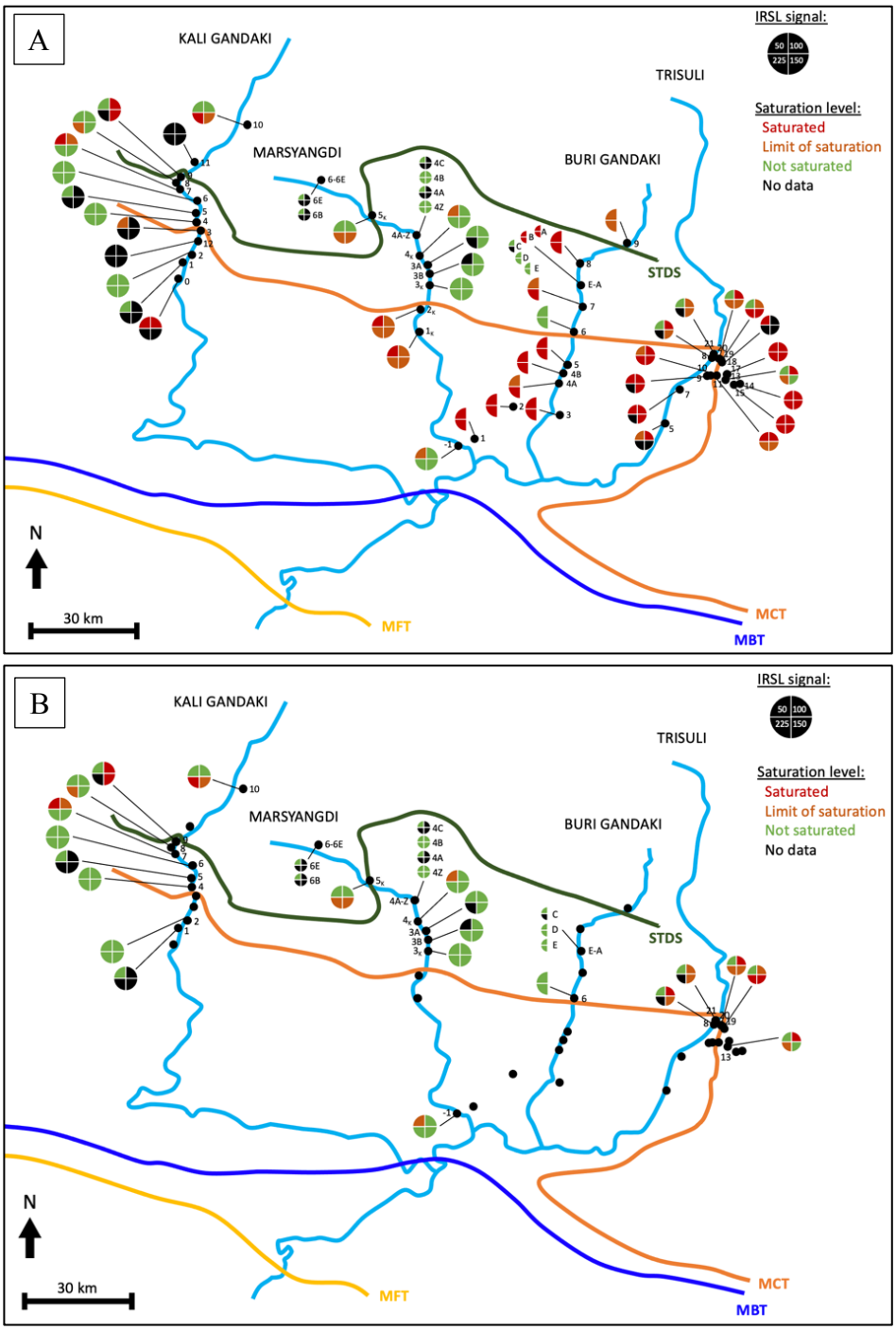

Fig. 6: *Schematic maps showing the saturation of each individual IRSL signal of all sample for* ***A.*** *all the samples, and* ***B.*** *the samples that have at least one of their IRSL signal not saturated. Luminescence signals that are totally saturated (i.e.,* $\tilde{n}_{nat} \geq \tilde{n}_{ss}$*) are shown in dark red, within the limit of saturation (i.e.,* $\tilde{n}_{nat} \geq 0.86*\tilde{n}_{ss}$*) in dark orange, and non-saturated signals are in green. When signals are in black, it means that for this signal, the data did not pass the rejection criteria, and were rejected from the study.*

4.2. Apparent ages

The average of the non-saturated IRSL signals of each sample was taken to obtain apparent ages for the studied samples (Fig. 7B). The High Himalayan samples yield an average age of ~100 ka, which is younger than the average age of ~200 ka previously reported for luminescence thermochronometry measurements of samples from the Sub-Himalayas (Bouscary et al., In review). Ages of < 100 ka are generally clustered just north of the MCT, although some ages of < 100 ka are found south of the MCT in the Kali Gandaki and in the lower Marsyangdi (Fig. 7B).

Two samples of the Marsyangdi valley, HIM.3A and HIM.3B and one sample from the Kali Gandaki (KG.2), show ages far younger (age of 15 kyr for the HIM.3A and 3B samples, and of 39 kyr for KG.2) than samples from the same transect, or even from the High Himalayas. However, these samples were strategically collected near thermal hot springs to evaluate impact of hot springs on the luminescence thermochronometry data.

The published low and medium-temperature thermochronometric data of Herman et al. (2013) (Fig. 3 and Fig. 7A) have apparent ages extending to the Oligocene (~23-34 Ma). Compiling all thermochronometers together (Fig. 7A) reveals a trend of younger ages in the MCT thrust sheet, with samples increasing in ages toward the north (north of the STDS), and towards the south (south of the MCT). In the east of the study area, a different pattern is observed, with younger ages on the MBT thrust sheet, and a scatter of increasing ages on the MCT thrust sheet from north to south. A sharp transition in age is also present for this Trisuli transect, west of the MCT zone.

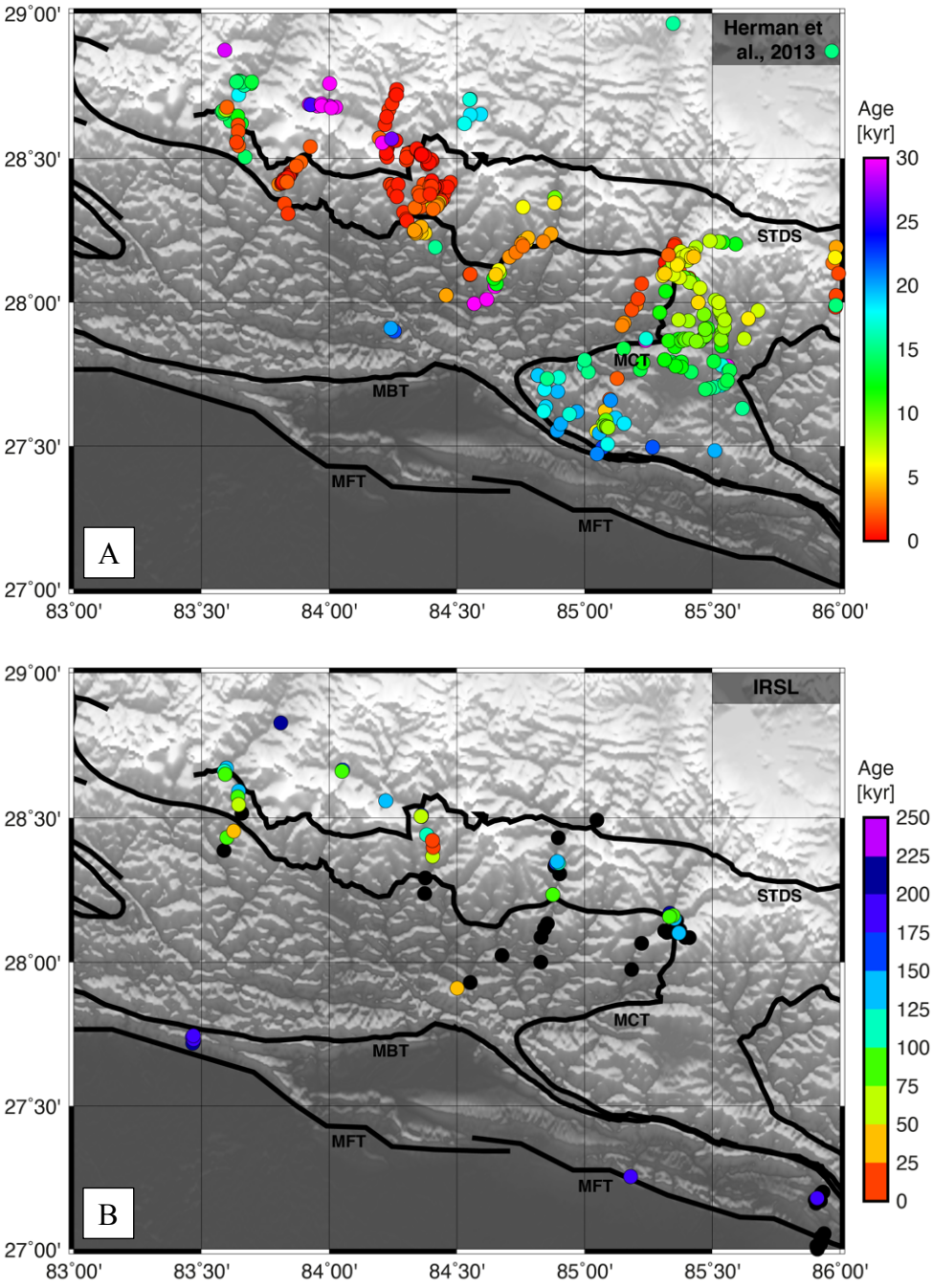

Fig. 7: A. *Compilation of all thermochronometric ages from $^{40}Ar/^{39}Ar$ on muscovite, ZHe, ZFT, AHe, and AFT from the world data base of Herman et al. (2013).* ***B.*** *Apparent ages derived from luminescence thermochronometry (IRSL). Data points in black represent saturated samples for which no age can accurately be derived.*

4.3. Exhumation rates

The inversion results of the thermochronometric data of Herman et al. (2013) with GLIDE (Fig. 8A) suggests that since 2 Ma, the exhumation rates have been well resolved for most parts of the studied area. From 2 to 0 (today) Ma, exhumation rates are ≤ 5 mm/yr, with higher exhumation rates focussed around the MCT thrust sheet in the vicinity of the Kali Gandaki, Marsyangdi, and Buri Gandaki valleys, in the west of the studied area. The Trisuli valley, in the east, records exhumation rates that are lower, < 1.5 mm/yr. No sharp transition in exhumation rate can be observed on each part of the thrust systems.

Luminescence thermochronometry exhumation rates (Fig. 8B) were derived from each sample using their non-saturated IRSL signals, and the modelling approach presented in the method (Bouscary et al., In review / Chapter 2). Exhumation rates of ~3-23 mm/yr are recorded for the High Himalayas of central Nepal during the last 100 kyr (Fig. 8B). Samples HIM.3A and HIM.3B did not converge towards an exhumation rate within the limit of the modelling (0 to 30 mm/yr), they record exhumation rates > 30 mm/yr. KG.2, also situated near a hot spring, yields an exhumations rate of 23.5 ± 4.9 mm/yr, ~5 to 10 mm/yr above the next highest exhumation rate. Sample HIM.-1 also seems to be an outlier, having only one of its IRSL signal giving an exhumation rate of 17.7 ± 2.7 mm/yr, whereas its IRSL.150 and IRSL.225 signals give exhumation > 30 mm/yr. Removing these four samples that are likely explained by hot-spring activity, the High Himalayas of the Annapurna and Ganesh regions experienced exhumation rates of 3-16 mm/yr (~7.2 mm/yr on average) over the last 100 kyr. Samples from the MCT thrust sheet yield an average exhumation rate of ~8.7 mm/yr, whereas the MBT thrust sheet has an average exhumation rate of ~6.3 mm/yr, and the only sample north of the STDS records an exhumation rate of ~6 mm/yr.

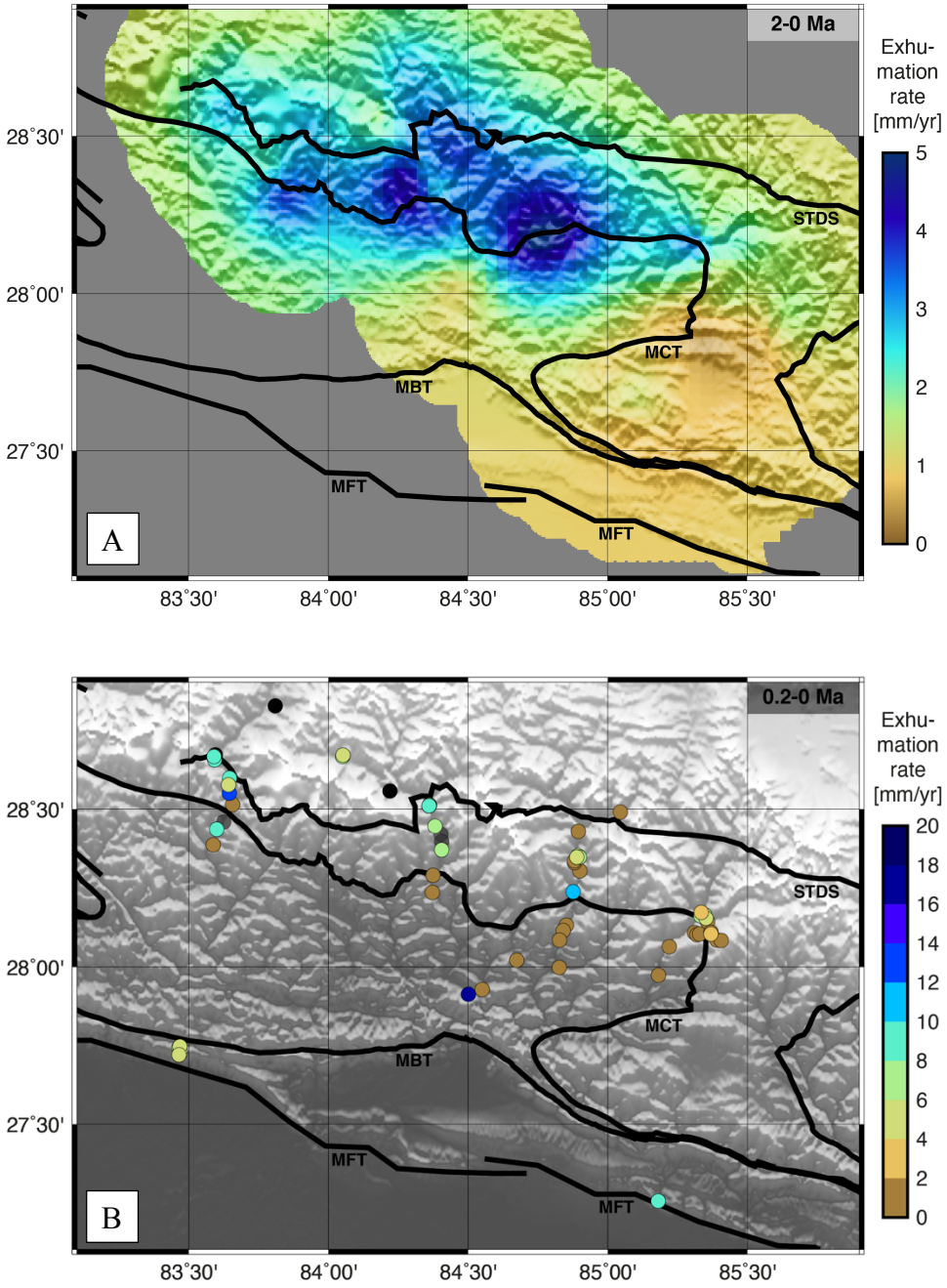

Fig. 8: ***A.*** *Exhumation rates during the last 2 Myr, derived from the Bayesian inversion of thermochronometric ages of Herman et al. (2013) with GLIDE (Fox et al., 2014).* ***B.*** *Distribution of sample-specific exhumation rates on the last ~200 kyr (0.2 Myr), derived from luminescence thermochronometric data (IRSL). Exhumation rates in the Sub-Himalayas are from Bouscary et al. (In review). Brown data points indicate samples that are saturated, and thus record exhumations < 2 mm/yr. The three data points corresponding to the hot spring samples (HIM.3A, HIM.3B, and KG.2) were greyed out to avoid the bias towards young, and thus high exhumation rates due to thermal depletion of the luminescence signal.*

5. Discussion

Our new luminescence thermochronometry data and modelling of exhumation rates complete the existing higher temperature thermochronometer data for the High Himalayas, and suggest an increase in exhumation rates since ~0.2 Ma.

When looking at luminescence thermochronometry data (Fig. 6), a pattern emerges with almost all samples south of the MCT being saturated, whereas north of the MCT, only a few samples are totally saturated. This pattern is also seen in the apparent luminescence age of the samples (Fig. 7B), for which ages are on 50 to 200 kyr timescales, with young ages of < 100 ka generally clustered just north of the MCT, and more saturated samples (black dots on Fig. 7B, and saturated data on Fig. 6) south of the MCT. This is consistent with the trend that is observed for higher closure temperature thermochronometers (AFT, ZFT, AHe, ZHe, $^{40}Ar/^{39}Ar$; Fig. 3 and Fig. 7A), that present younger ages in the MCT thrust sheet, and increase in age towards the north (north of the STDS). This sharp transition in ages on each side of the MCT zone indicates that we are in the presence of an active fault on Quaternary timescales, samples record different thermal histories depending on if they are located on the hanging wall (north of the MCT) or the footwall (south of the MCT) of the MCT thrust. The only difference being the Trisuli transect that presents a sharp transition in ages, but shifted to the west, potentially indicating that the location of the MCT is not correct, or that the tectonic activity of another fault system creates this abrupt change in ages.

It is interesting to note that luminesce samples with young ages, with the exception of HIM.-1, correlate with the location of hot springs (HIM.3A, HIM.3B, and KG.2). Independently of whether those samples are situated on the MBT or MCT thrust sheet, they record young apparent ages < 40 kyr. These anomalously young ages correspond to the influence of the temperature of the hot springs, that thermally depleted some/most of the samples' luminescence signal. These samples cannot be used to derive exhumation rates, as they will yield anomalously high values, that have nothing to do with the exhumation history of the rocks, but instead reflect the temperature of the hot springs.

Converting the higher temperature thermochronometric ages to exhumation rates (Fig. 8A), the pattern of marked transition on each side of the MCT disappears. From 2 to 0 (today) Ma, modelled exhumation rates are ≤ 5 mm/yr, with higher exhumation rates focussed around the MCT thrust sheet in the vicinity of the Kali Gandaki, Marsyangdi, and Buri Gandaki valleys, in the west of the studied area. The Trisuli valley, in the east, records exhumation rates that are lower, < 1.5 mm/yr. No abrupt transition in exhumation rate can be observed on each part of the thrust systems. This indicates that the MCT fault zone is likely not active on this timescale, or that if it is active, the resolution of these thermochronometers is not enough, or we are within their limit of detection. However, a pattern seems to exist between the east and the west, with lower exhumation rates recorded in the east of the studied area, two times lower than that recorded in the west, around the Annapurna region (Kali Gandaki to Marsyangdi, Buri Gandaki). One might be careful, as when looking at the resolution map, it is to be noted

that even though the resolution seems to be good (~1) in these areas, only a few thermochronometers give information on the exhumation rates south of the MCT in areas other than the Trisuli valley (east).

Luminescence thermochronometry records exhumation rates of 3-16 mm/yr (~7.2 mm/yr on average) over the last 100 kyr (Fig. 8B). Considering that saturated samples imply exhumation rates < 2 mm/yr, the MCT marks a sharp transition between low exhumation rates in the south (< 2 mm/yr), and high exhumation rates in the north, with the samples from the MCT thrust sheet recording an average exhumation rate of ~8.7 mm/yr. Removing samples that seem to be impacted by hot springs and saturated samples that record exhumation rates < 2 mm/yr, averaged exhumation rates for the four different valleys are of 8.8 ± 2.5 mm/yr for the Kali Gandaki, 7.5 ± 3.9 mm/yr for the Marsyangdi, 7.1 ± 2.5 mm/yr for the Buri Gandaki, and 5.0 ± 1.9 mm/yr for the Trisuli. These late Quaternary luminescence thermochronometry exhumation rates (Fig. 8B) show a decrease from west to east of the studied area, whereas for the period 2-0 Ma (Fig. 8A), increased exhumation rates were more focussed on the central part of the studied area, at the Buri Gandaki and Marsyangdi valleys.

This spatial and temporal variability between the four valleys of central Nepal at different timescales implies that exhumation rates are highly transient, suggesting an intermittency of exhumation signal due to geomorphological processes. Higher exhumation rates can have several origins, including: the flat-to-ramp transition of the MHT (which is coincidently at the 3500 m elevation delimitation, and corresponds in some places to the MCT zone), an extensive basal accretion which may correspond to the formation of a duplex at depth, an increased erosion due to isostatic processes, an increase in precipitation with a focussed monsoon at the front of the orographic transition, slope instabilities, an increase in steam power due to precipitation or deglaciation, the presence of river anticlines where largely erosive rivers flow along structural highs (due to localised uplift and plastic deformation of the crust in response to regional compression) and incision of a relatively weak crust creating tectonic aneurysms (e.g., Montgomery and Stolar, 2006).

These results suggest that the in-sequence model, with exhumation rates linked to increased erosion of a duplex formed below the Higher Himalayas, coincidently at the MCT location in some areas, is the best model describing the thermochronometric ages on Myr timescales. However, for the late Quaternary period, the transition from low to high exhumation rates, and saturated to unsaturated samples on each side of the MCT could potentially suggest a change in tectonic regime, possibly with an activity of the MCT area during the last 100 kyr, in the Annapurna and Ganesh regions.

Burbank et al. (2003) measured apatite fission-track cooling ages from the Marsyangdi valley. They record cooling ages < 0.9 Ma on the hanging wall of the MCT, whereas those from the footwall are > 1.9 Ma. These data are evidence for substantial Pleistocene slip on the MCT system. Hodges et al. (2004) also argue that the difference in cooling ages in the Marsyangdi is due to an uplift discontinuity that has been active within the past 100 kyr. This discontinuity is marked by changes in river channel geometry, responding quickly to changes

in bedrock uplift rate, and is close to a surface expression of the MCT thrust, suggesting that this Marsyangdi strand of the MCT accommodated shortening during the Quaternary. Wobus et al. (2003) found the same pattern in their $^{40}Ar/^{39}Ar$ muscovite cooling ages further east, that they relate to higher uplift rates in the Higher Himalaya than in the Lower Himalaya related to fault activity.

These studies and our luminescence data seem to be more sensitive to changes in exhumation rates on each side of the MCT, highlighting the possibility of an active MCT on sub-Quaternary periods. If this is the case, activity of the MCT must be carefully considered as it could have a devasting impact on the seismic hazard, putting the local population at risk.

6. Conclusions

We report new luminescence thermochronometry data along four transects in the Nepalese-Himalayan hinterland, enabling the resolution of deformation on sub-Quaternary timescales (10^4 yr 10^5 yr). Modelling published low to medium thermochronometric data and comparison with luminescence thermochronometry data reveals enhanced exhumation since ~0.2 Myr, with the location of the highest exhumation rates varying spatially and temporally.

When compared with higher temperature thermochronometers, luminescence thermochronometric ages highlight spatial and temporal variation in exhumation rates since the Oligocene (~30 Myr). This spatial variability between the four different valleys at different timescales suggests an intermittency of exhumation signal due to geomorphological processes. This suggests that the in-sequence model, with exhumation rates linked to increased erosion and the formation of a duplex below the Higher Himalayas, coincidently at the MCT location in some areas, is the best model describing the thermochronometric ages of this study. However, when looking at the cooling ages, and more particularly to the young cooling ages derived from luminescence thermochronometry, the MCT seem to be a natural boundary that separate older ages south of the MCT to younger ages north of the MCT, to older ages north of the STDS. This sharp transition is also recorded by various authors in the Marsyangdi valley, and is seen in the luminescence thermochronometry exhumation rates, highlighting the possibility of an active MCT on 100-kyr timescales.

Acknowledgements

The authors would like to thanks people that helped collecting samples in the field: Kristel Chanard, and Shiba Subedi.

Supplementary data

Supplementary data are available at an online depository:
>>>> Please ask for the Dropbox link if needed. >>>>

Table SD.1: Compilation of the published low and medium-temperature thermochronometric data from the world data file of Herman et al. (2013) used in this study, with their respective locations, elevations, apparent ages, and references.

Table SD.2: Sample names, thrust sheet, locations, elevations, and transect name.

Table SD.3: Radioisotope concentrations, grain size range, and calculated total environmental dose rate ($\dot{D}$). Errors are calculated as 3 % of the values.

Table SD.4: Summary of kinetic and fitted parameters for all four IRSL temperatures, using kinetic parameters derived from four isothermal temperatures between 190 and 250 °C (Bouscary and King, 2022). Uncertainties are listed at 1σ for all values, except for D_e, for which errors are listed as 5 % of D_e. Fading rates are expressed both as ρ' and as g-values normalised to 2 days, g_{2d}, Huntley and Lamothe (2001). Saturated samples are shown in grey.

Table SD.5: Saturation indicator values, and age of the samples for all four IRSL temperatures. Saturated samples are shown in grey.

Table SD.6: Samples with their IRSL signal specific apparent age, and their sample specific apparent age, i.e., the average of the non-saturated IRSL signal specific apparent age.

Table SD.7: Samples with their IRSL signal specific exhumation rate, and their sample specific exhumation rate, i.e., the average of the non-saturated IRSL signal specific exhumation rates.

Fig. SD.1.1-6: Luminescence measurement and model fit results for all samples. (A, D, G, J) Anomalous fading data fitted using equations 3 and 4 of King et al. (2016a), for the IRSL at 50, 100, 150, and 225 °C respectively. (B, E, H, K) Luminescence dose response accounting for fading, fitted using equation 5 of King et al. (2016a). The black solid line is the unfaded dose response curve, and the yellow dots represent the $\tilde{n}_{nat}$ values of each aliquot. (C, F, I, L) Isothermal decay data fitted with the BTS model, using equations 6 and 7 of King et al. (2016a).

Fig. SD.2.1-6: Steady-state saturation plots (Kars plots) for all samples, contrasting natural luminescence values, $\tilde{n}_{nat}$, with steady-state luminescence values, $\tilde{n}_{SS}$, predicted for each of the samples. The 1:1 line delimits saturated samples (blue area) to unsaturated samples (white area), with the saturation limit indicated by the blue line.

Fig. SD.3.1-6: Surface temperature saturation plots for all samples, contrasting natural luminescence values, $\tilde{n}_{nat}$, with the luminescence values for a surface temperature of 10 °C or 5 °C, $\tilde{n}_{Tmin} = \tilde{n}_{10}$ or $\tilde{n}_{Tmin} = \tilde{n}_{5}$ depending on sample location, predicted for each of the samples. The 1:1 line delimits saturated samples (blue area) to unsaturated samples (white area), with the saturation limit indicated by the blue line.

Chapter 4

Research: behind the curtain

In this chapter, I present some of the research done and experiments that were made throughout my PhD, but that did not lead to a publication or to a full chapter in this thesis. Some of the research presented here might be published later: 'To publish or not to publish, that is the question?'.

1. Luminescence thermochronometry of feldspar minerals: towards a uniform set of thermal kinetic parameters.

1.1. Isothermal decay of infrared stimulated luminescence in feldspar: how variable are the kinetic parameters?

In this thesis, the parameters that describe the thermal stability of feldspar, E_t, E_u, and s, are constrained from isothermal decay data. However, the isothermal decay measurements, conventionally used to extract the kinetic parameters describing thermal decay, are highly time consuming (~5 days per sample using an automated reader). The new protocol for the derivation of thermal kinetic parameters with isothermal decay experiments, presented in the article of Bouscary and King (2022), and here in Chapter 1, permitted this measurement time to be reduced by ~2 days per sample, by decreasing the number of isothermal temperatures used from 7 temperatures to 4. However, in thermochronometry, precise results are often obtained by the analysis of multiple samples on different transects, and a large number of samples sometimes need to be measured, which still takes a large amount of measurement time. To remedy to this issue, another direction was first explored to try to optimise and reduce the time necessary to obtain thermal kinetic parameters.

Riedesel et al. (2019) recently found that the trap depth and band-tail width (respectively E_t and E_u) are broadly similar for a suite of feldspar samples, despite large variations in chemical composition, possibly indicating that a single set of values could be appropriate for all feldspars. Following their research and the fact that other thermochronometric methods only use a single reference set of thermal kinetic parameters (cf., Reiners and Brandon, 2006), we sought to optimise the luminescence thermochronometry measurements by exploring whether a single set of thermal kinetic parameters can describe thermal decay in feldspar. If successful, this approach could allow a fast screening of luminescence samples by measuring their luminescence signals based on average kinetic parameters. This would reduce luminescence thermochronometry measurement times by c.50%, allowing higher resolution sampling and measurement.

A set of K-feldspar samples from the Himalayas, including sandstones samples from the Sub-Himalayas on transects along the Tinau (BUT), Ratu (RA-P) and Kamala (RA-K) rivers, as well as crystalline metamorphic rock samples from the High Himalaya, collected along the Marsyangdi river (HIM) were first analysed. These samples were then joined by four Na-feldspar samples of the KTB borehole (KTB) presented in Chapter 1. Samples were prepared using standard methods and four different IRSL signals were measured at increasing stimulation temperatures (50, 100, 150, and 225 °C) using a multi-elevated temperature post-IR-IRSL protocol (MET-pIRIR) (Li and Li, 2011). The isothermal decay of each signal was measured using storage temperatures in the range 170-350 °C, with isothermal delay times of 1 to 10,000 s. All data were fitted using the band-tail states model (Li and Li, 2013).

Results show that even though it is not possible to generalise the kinetic parameters between IRSL signals measured at different temperatures, similarities exist between the same temperature IRSL measurements of samples from the same area (Fig. 1).

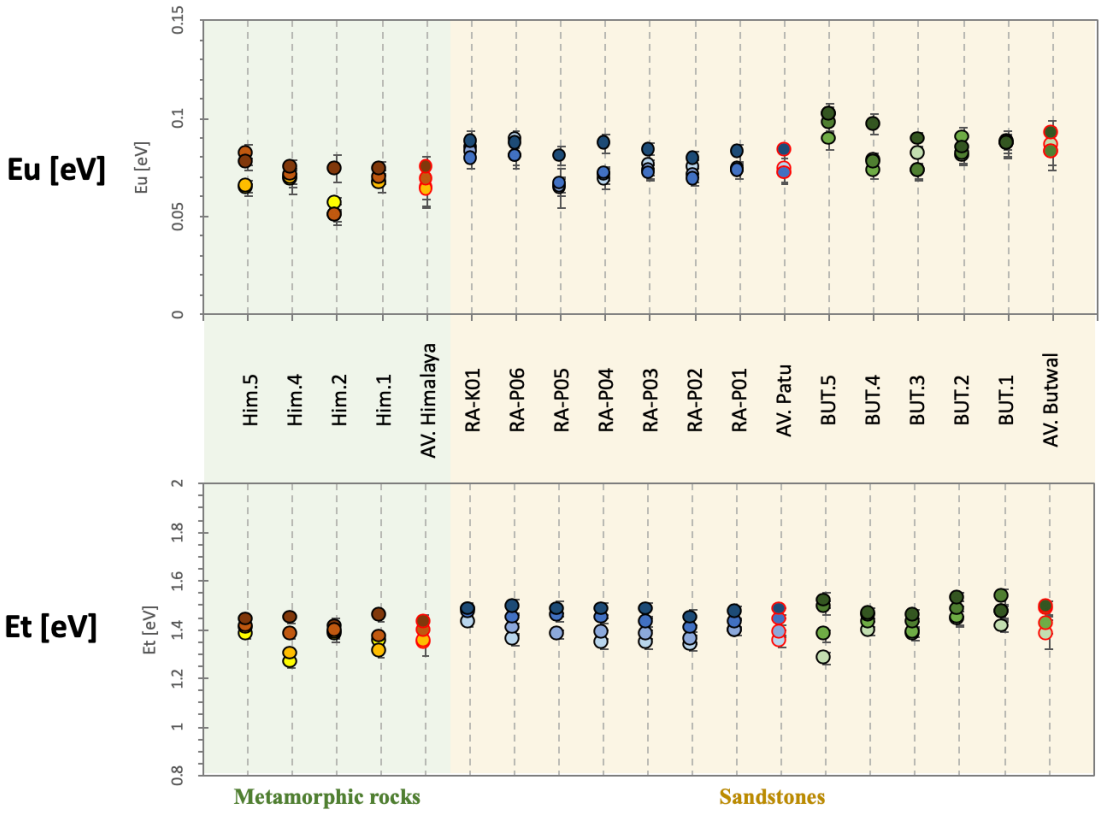

Fig. 1: *Average kinetic parameters Et and Eu for samples of the Sub-Himalayas (RA-K, RA-P, BUT) and of the Marsyangdi valley (Him). The gradient of colour for each sample shows the different MET temperature of the IRSL measurements, with the darker colour representing the IRSL 225 °C and the lightest colour the IRSL 50 °C.*

Comparisons were done between the kinetic parameters of each IRSL signal depending on different variables such as transect, crystal type, or lithology of the rock (Fig. 2). Despite slight differences between the Na-feldspars and K-feldspars thermal kinetic parameters, the deviation between the kinetic parameters of different samples from the same site is within the range of measurement error (i.e. <2-10 % depending of the kinetic parameter), suggesting that regional, rather than sample-specific values may be appropriate.

Fig. 2: *Average kinetic parameters E (=Et-Eu), Et, Eu, s, and rhop (ρ′) for samples of the Sub-Himalayas along the Ratu Khola (RA-P) and the Tinau Khola (BUT), of the High Himalaya along the Marsyangdi river (HIM), and of samples from the KTB borehole (KTB). The dots represent the values for the IRSL 50 °C signal, and the lines show the average values for the signal depending on different variables such as transect, crystal type, or lithology of the rock (see legend). The other IRSL temperatures present the same trends, but are not shown here for clarity of the figure.*

rhop [-]
s [s-1]
Eu [eV]
Et [eV]
E=Et-Eu [eV]
AV-Him-50
AV-Patu-50
AV-Butwal-50
AV-KTB-50
AV-Crystalline-50
AV-Sandstone-50
AV-Gneiss-50
AV-K-Feldspar-50
AV-NA-Feldspar-50
Him 5
Him 4
Him 2
Him 1
RA-P06
RA-P05
RA-P04
RA-P03
RA-P02
RA-P01
BUT 5
BUT 4
BUT 3
BUT 2
BUT 1
KTB 250F
KTB 380C
KTB 428B
KTB 481B

1.2. Impact of average thermal kinetic parameters on thermochronometry

1.2.1. Forward modelling of signal growth

The impact of taking the average kinetic parameters instead of the sample-specific kinetic parameters is evaluated with forward modelling. Two forward models are run (fixed D0, Ddot, rhop) for given cooling histories (Fig. 3). One model is run with the natural sample-specific kinetic parameters KP_nat, and the other is run with the average kinetic parameters KP_AV. For each cooling history, the maximum modelled luminescence signals obtained, nNsim_nat for the forward model with the KP_nat, and nNsim_AV for the forward model with the KP_AV, are compared using:

$$nNsim_{Diff} = \frac{abs(nNsim_{nat} - nNsim_{AV})}{nNsim_{nat}}$$

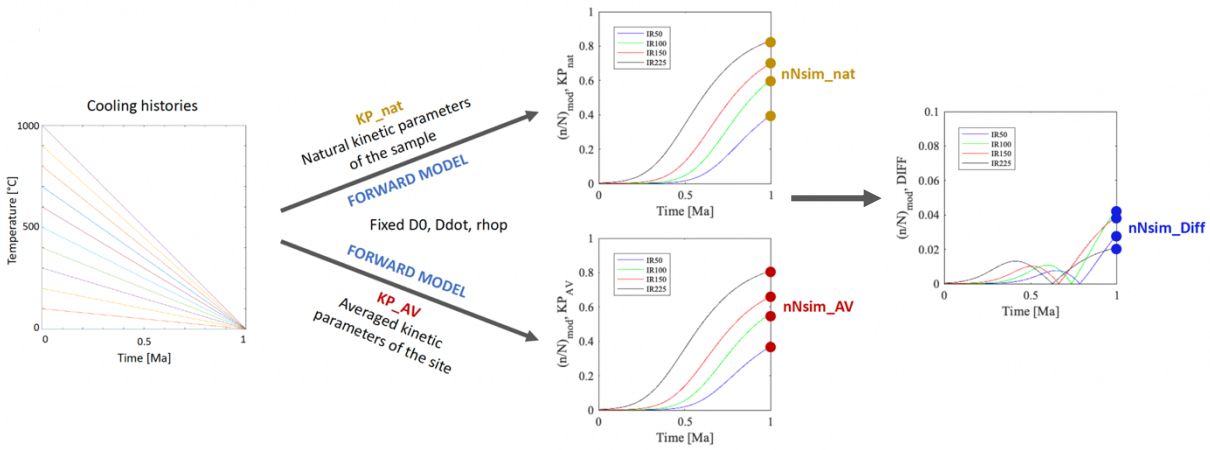

Fig. 3: *Forward models for the comparison of the luminescence signal obtained with the natural kinetic parameters of the samples KP_nat, and with the averaged kinetic parameters of the studied site KP_AV.*

When the deviation between these luminescence values (n/N) is below 0.06, the difference between the two forward models lies within the range of analytical error (i.e. the typical uncertainty of n/N for these samples). The average kinetic parameters are then considered suitable for cooling history inversion of the samples.

Himalaya transect – High Himalaya bedrock

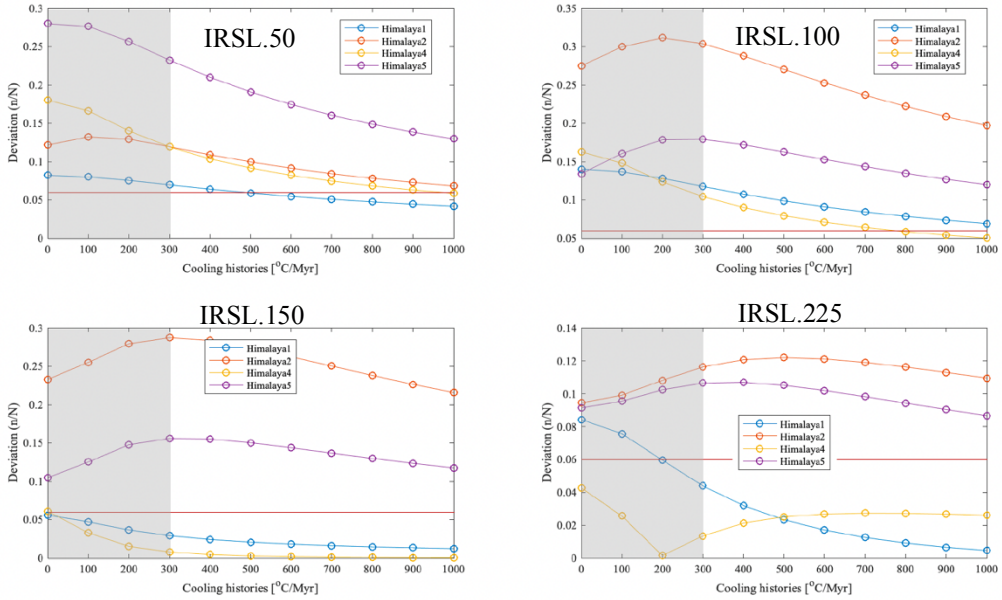

Patu transect – Siwaliks sandstones

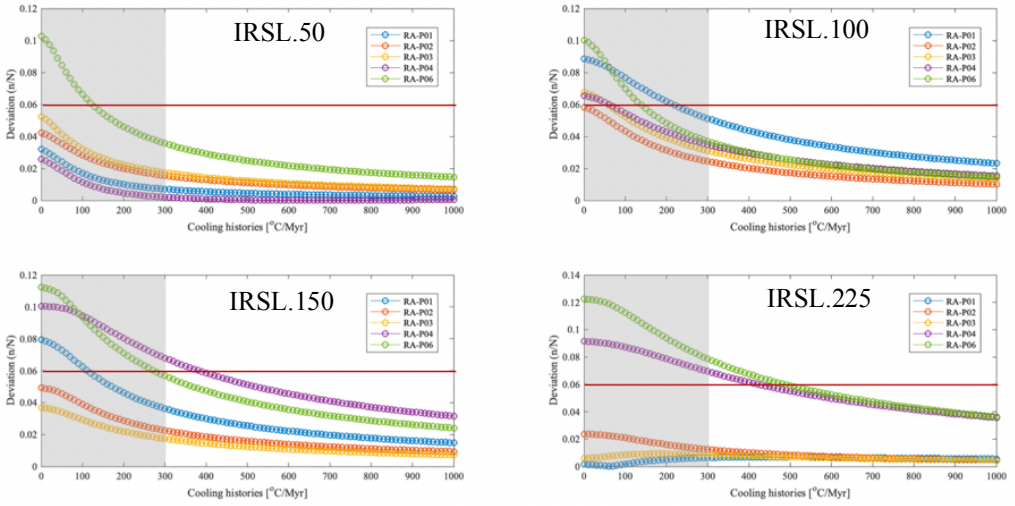

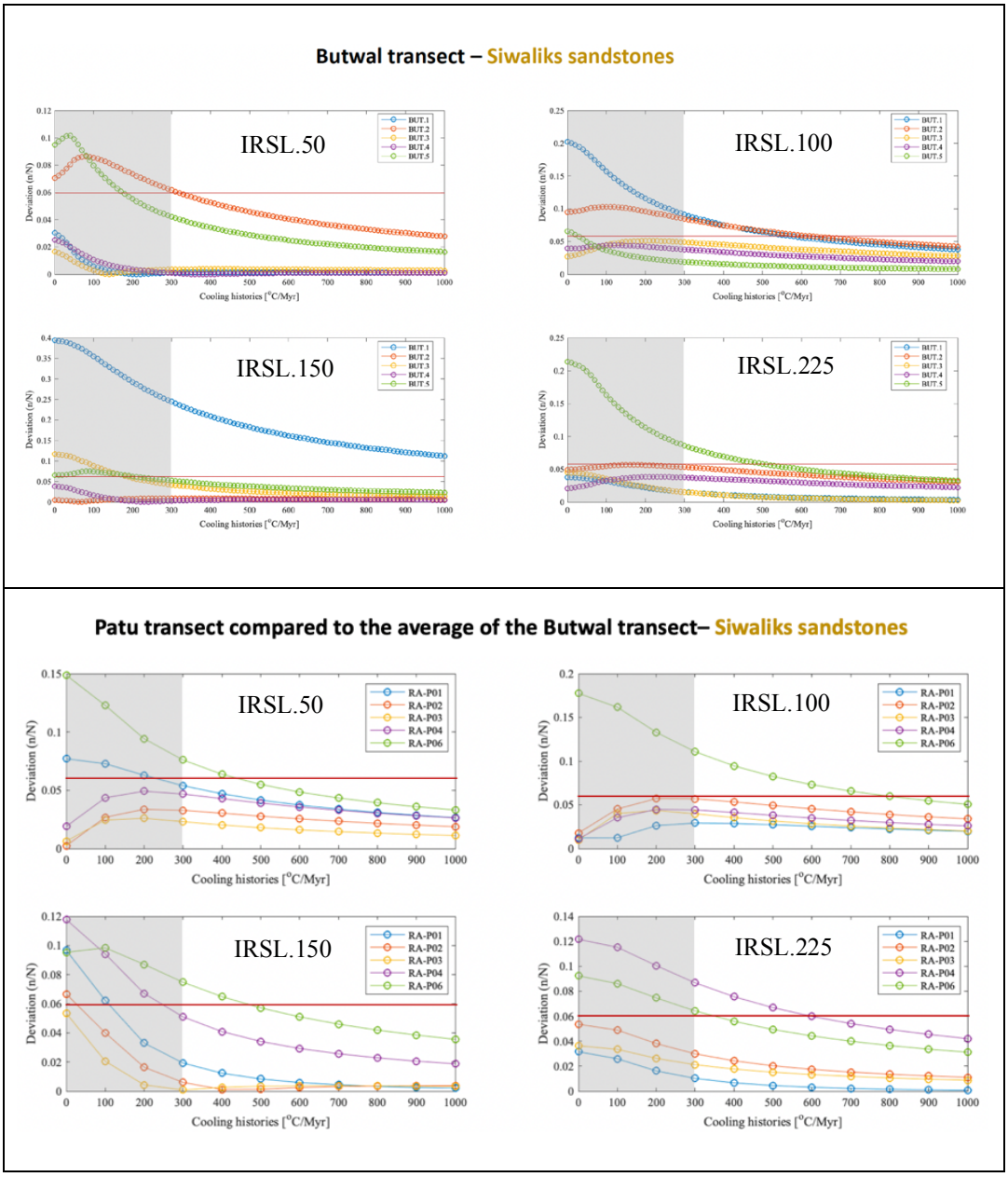

Fig. 4: *Results of the forward modelling. Deviation between the forward modelling done with the sample-specific kinetic parameters, and with the average site-specific kinetic parameters. The red line indicates the typical n/N measurement uncertainty for these samples (0.06). The grey area indicates cooling histories that cannot be measured as they will be too slow for luminescence thermochronometry and give saturated signals.*

The results of this study show that for the Siwaliks samples, it does not matter if we take the sample-specific kinetic parameters or the average site-specific kinetic parameters. It would even be possible to take the average kinetic parameters of the Butwal transect to analyse the samples of the Patu transect that is located around 250 kilometres away (Fig. 4). However, for the High Himalaya samples, the results are inconclusive. This may be linked to the fact that there are multiple lithologies, or the limited samples available when these analyses were done.

1.2.2. Cooling histories, impact of an average set of thermal kinetic parameters

To test the impact of using average thermal kinetic parameters on the derivation of cooling histories, an approach combining forward models and inverse modelling was used. Sample RA-P02 was investigated with the average thermal kinetic parameters of the Patu transect.

Taking a fixed cooling history of 600 °C/Myr, a forward model was used to generate the corresponding (n/N)sim_nat values with the natural kinetic parameters of the sample KP_nat, and the (n/N)sim_AV values with the average site-specific kinetic parameters KP_AV (Fig. 3). An inversion for cooling was then done for each set of (n/N)sim values, and the two resulting inverted cooling histories were then compared by subtracting one from the other (Fig. 5). The residual difference in temperature was also calculated for the median cooling histories (red lines in Fig. 5).

Variation between the two cooling histories is minimal, and the differences in temperatures between the two median cooling histories (red lines) are < 10 °C, largely within analytical error.

This study indicates that it should be possible to take an average set of thermal kinetic parameters for some of the samples from the same site. However, changes in lithology, and/or origin of the mineral can have an impact on the kinetic parameters of the sample. Despite the promising perspectives of this study, it remains necessary to fully measure some samples at each new site investigated in order to determine if averaged kinetic parameters will be appropriate and to determine them.

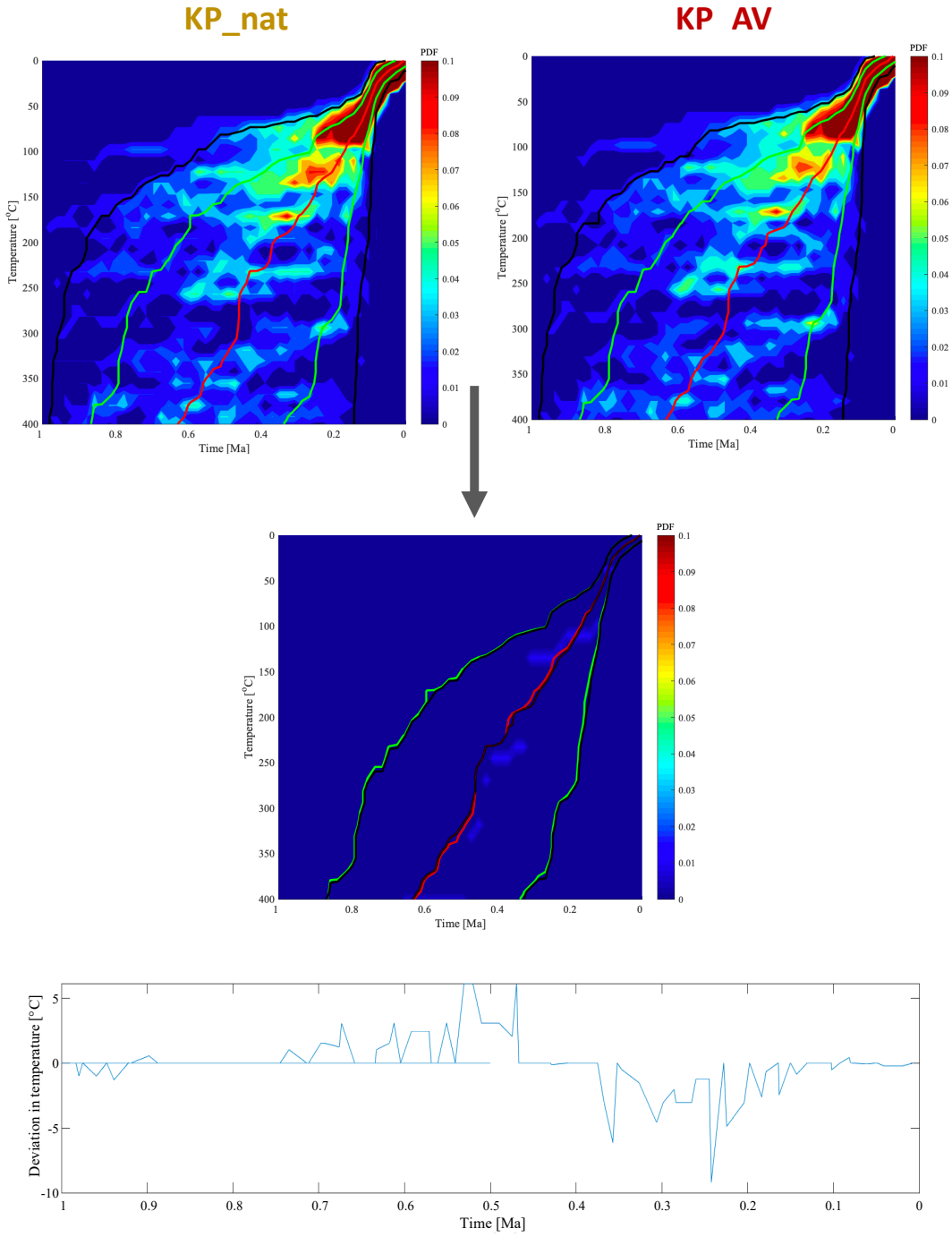

Fig. 5: *Cooling history plots derived from the natural thermal kinetic parameters of the sample KP_nat, and from the average site-specific thermal kinetic parameters KP_AV. Subtracting the cooling history plots, and median cooling histories (red lines) from one another allows the temperature deviation (lower plots) to be computed.*

2. Luminescence parameters and their interplay

2.1. Lifetime

The thermal stability of a luminescence signal is given by the lifetime of the thermal decay. This lifetime, τ [s], can be calculated for each IRSL signal with a trap depth energy E_t. The lifetime corresponds to the time it takes for all trapped electrons to be thermally evicted from their traps at a certain temperature. The lifetime can be defined by (Li and Li, 2013; adapted for the BTS model from Aitken, 1985):

$$\tau = s^{-1}.e^{-\frac{E_t - E_b}{k_b T}}$$

with s [s^{-1}] the frequency factor or electron escape probability, E_t [eV] the activation energy or the electron trap depth below the conduction band, E_b [eV] a particular band-tail energy within the Urbach band-tail of width E_u [eV], k_B [eV/K] the Boltzmann constant (k_B = 8.617 * 10^{-5} eV/K), and T [K] the absolute isothermal temperature.

In order to account for the band-tail states of energy below the conduction band of the BTS model, a MATLAB code was created to calculate the lifetime of thermal decay of the luminescence signal of K-feldspars, directly from the thermal kinetic parameters of the IRSL signal of a sample (E_t, E_u, and s). Following Poolton et al. (2002b, 2009) and Li and Li (2013), in the band-tail states model (BTS), the density ρ of band-tail states E_b is exponentially distributed below the conduction band edge (E_c) as:

$$\rho(E_b) = \rho_0 . e^{-\frac{E_b}{E_u}}$$

with ρ_0 the density of the sub-conduction band states. When $E_b \approx E_c$, $\rho_0 = 0$, and when $E_b = E_t$, $\rho_0 = 1$. E_b is sampled between 0 and E_t, and $\rho(E_b)$ is calculated for each band-tail state energy level E_b (Fig. 6). The lifetime is then calculated for each band-tail state energy level E_b, and divided by the probability/density of this band-tail state $\rho(E_b)$. The lifetimes of all the band-tail state energy levels E_b are then summed together and divided by the sum of all the probabilities/densities $\rho(E_b)$ to obtain the lifetime of the luminescence signal as the electrons are thermally evicted and pass by the band-tail states below the conduction band.

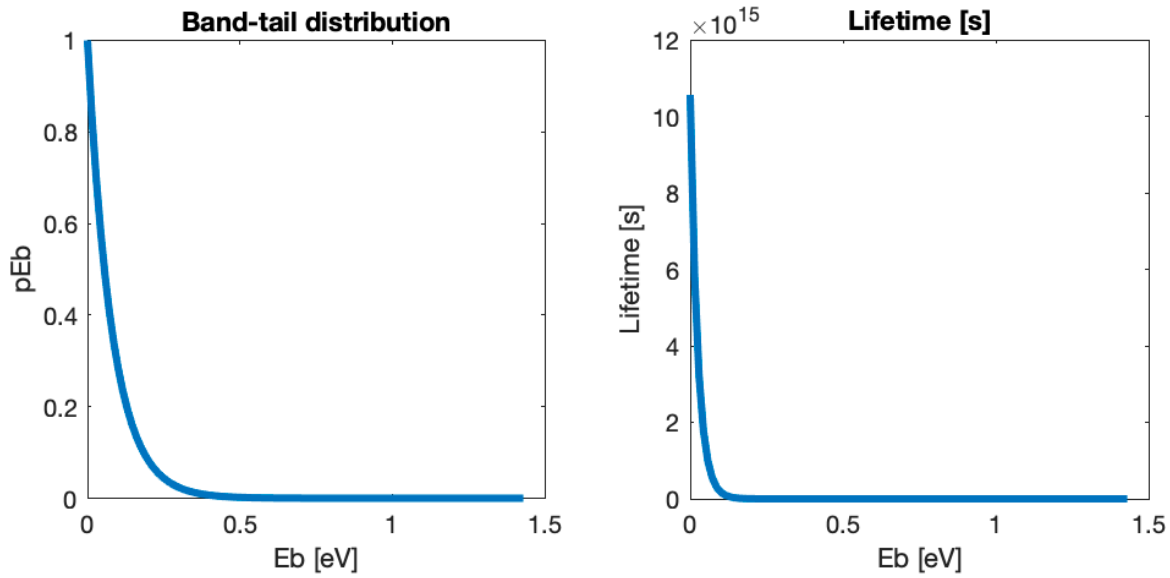

Fig. 6: ***A.*** *Band-tail states distribution, with* E_b *representing the different band-tail state energy levels between 0 and* E_t. ***B.*** *Lifetimes calculated for each band-tail state energy level* E_b *for the IRSL.50 signal of K-felspars from sample BUT.2.*

Using MATLAB the lifetime was calculated for different isothermal temperatures, using the thermal kinetic parameters of the IRSL signal, E_t, E_u, and s. Calculations were made using thermal kinetic parameters derived from seven isothermal holding temperatures for two samples: a K-feldspar sample for the Sub-Himalayas BUT.2, and a Na-feldspar sample of the KTB borehole KTB.428B (Fig. 7).

Lifetime of the luminescence signal decreases with increased temperature. At ambient temperature, i.e., 20 °C, the IRSL.50 signal of the samples BUT.2 and KTB.428B has a lifetime of respectively ~23.1 Myr and ~1.3 Myr. These lifetimes decrease drastically for higher temperatures, with lifetimes of ~36 min for BUT.2 and ~11 min for KTB.428B at 300 °C. This illustrates the thermal stability/instability of the luminescence signal with regard to temperature. It also shows that the Na-feldspars seem to have lower thermal stabilities than the K-felspars.

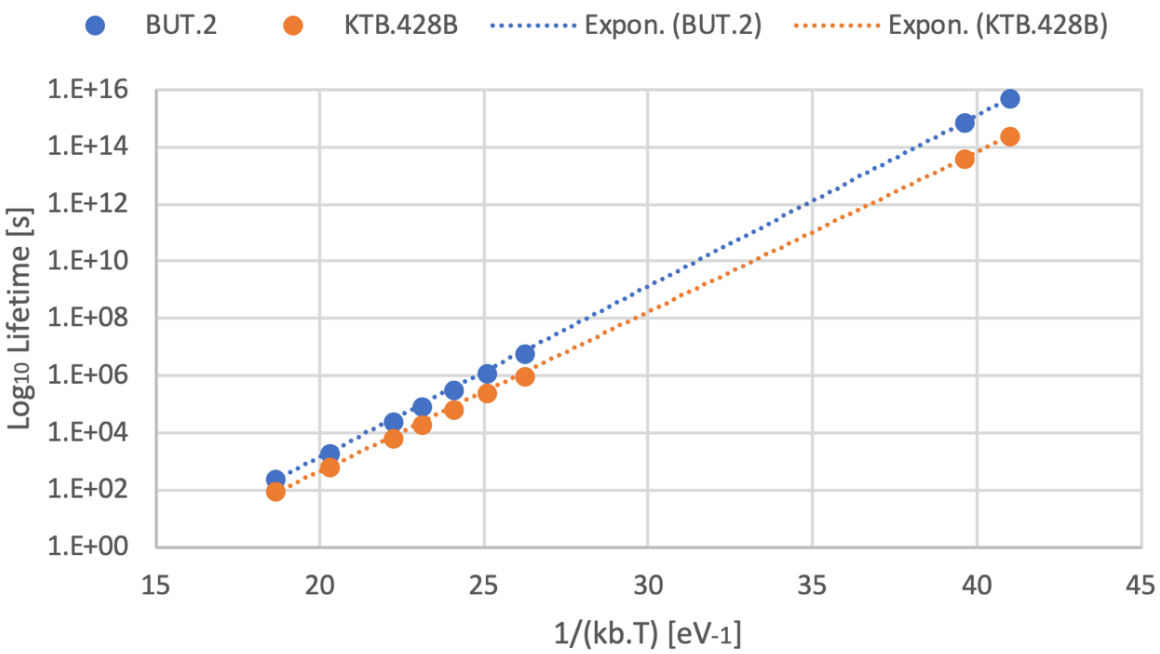

Fig. 7: *Variation of apparent lifetime with inverse storage temperature (T = 10, 20, 170, 190, 210, 230, 250, 300, 350 °C) for the isothermal decay data of the IRSL.50 signal, for sample BUT.2 (K-feldspar) and KTB.428B (Na-feldspar). The data points have been fitted with an exponential function.*

For a lifetime calculated assuming an isothermal temperature of 10 °C, I find $\tau_K = 1.6 * 10^8$ yr ≈ 164 Myr for K-felspars (sample BUT.2), and $\tau_{Na} = 8.0 * 10^6$ yr ≈ 8 Myr for Na-feldspars (sample KTB.428B). When compared to published data, these two samples give lifetimes of approximately in the same order of magnitude as Tso and Li (1996), that found a lifetime at 10 °C of $\tau_K = 1.0 * 10^9$ yr ≈ 1 Gyr for K-felspars, and $\tau_{Na} = 0.9 * 10^4$ yr $\approx$ 9 kyr for Na-feldspars, and Li and Tso (1997), that found a lifetime at 10 °C of $\tau_K = 6.6 * 10^8$ yr ≈ 660 Myr for the IRSL signal of K-felspars. These data reinforce the difference in thermal stability found between K-feldspars and Na-feldspars. Na-feldspars seem to have lower thermal stabilities than the K-felspars. This difference in thermal stability is more pronounced for lower temperatures (e.g., 10, 20 °C), but the thermal stability at higher temperatures is more critical as the luminescence signal will be evicted from the traps at faster rates. This is of particular importance as these high temperatures are used for isothermal decay experiments to derive kinetic parameters. It suggests that lower isothermal holding temperatures are probably more appropriate for the Na-feldspars for a better constraint of the thermal decay. This also demonstrate that K-feldspars will be thermally reset later than Na-feldspars when exposed to high temperatures, e.g., when sediments are exposed to a natural fire, or when ceramics/potteries are heated.

2.2. Anomalous fading

All of the kinetic parameters derived from the feldspar samples under investigation seem to be linked, and to be temperature dependant (MET IRSL signals). I explored the effects of anomalous fading on the thermal stability of the traps. For this, thermal kinetic parameters were calculated including and excluding fading (Fig. 8).

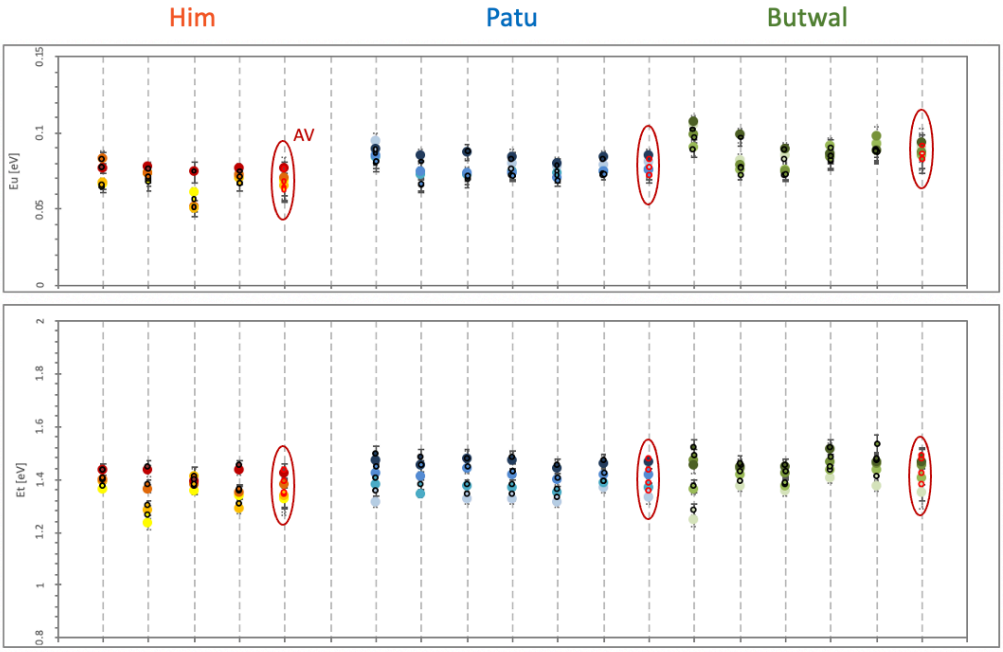

Fig. 8: *Average kinetic parameters Et and Eu for samples of the Sub-Himalayas (transect of the Patu thrust sheet and of the Butwal area) and of samples from the Marsyangdi valley (Him). Full dots with borders are thermal kinetic parameters including fading, and full dots without border are the thermal kinetic parameters calculated not accounting for fading. The gradient of colour for each sample shows the different MET temperature of the IRSL measurements, with the darker colour representing the IRSL 225 °C and the lightest colour the IRSL 50°C.*

When compared to Fig. 1, Fig. 8 does not show any significant differences between the thermal kinetic parameters calculated with or without fading for all of the samples. Where fading is not corrected for, thermal kinetic parameters Et and s, are underestimated whereas Eu is overestimated relative to when fading is included in the calculation (Fig. 9).

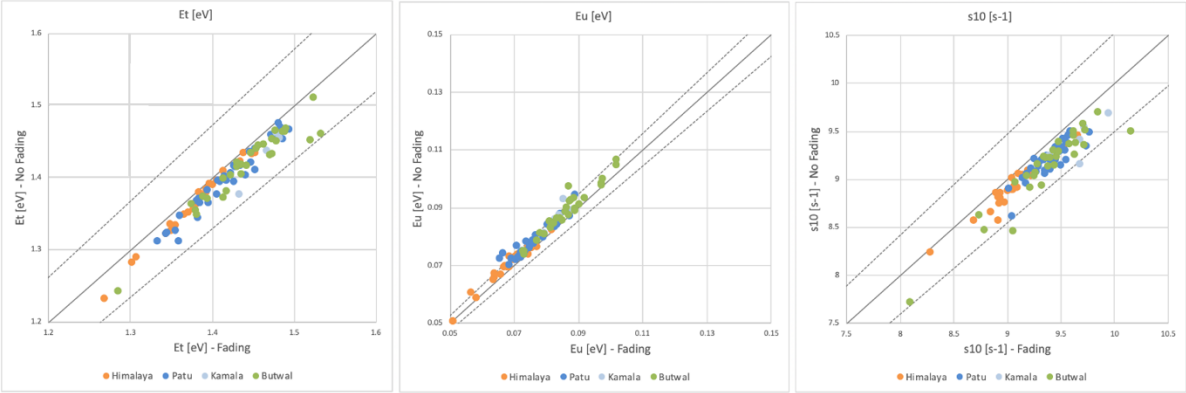

Fig. 9: *Comparison of the thermal kinetic parameters Et, Eu, and s, calculated including vs. excluding anomalous fading. The lines represent the 1:1 line, on which the thermal kinetic parameters are the same when including and excluding fading, and on each side, the 5 % difference lines.*

Although this difference in thermal kinetic parameters is subtle, it may have significant implications for the derivation of cooling histories. However, in this study, the Siwaliks and High Himalaya samples do not have independent cooling histories and so the implications of including or excluding fading for these samples could not be tested. Nevertheless, preliminary investigations on the KTB samples, which have low fading rates, indicated that the effect was not significant.

2.3. Trade-off between the thermal kinetic parameters

The relationship between the thermal kinetic parameters was explored to see if a single set of values capable of describing the thermal history of all the samples could be isolated. For this a Monte Carlo approach was used. All three thermal kinetic parameters (Et, Eu, and s) were randomly sampled between two extreme fixed values. Every set of randomly selected kinetic parameters was then used to fit the isothermal decay data of a samples (ITLpred, Fig. 10A), and the misfit with the natural kinetic parameters (ITLori) was calculated. Misfit values for all sets of thermal kinetic parameters were plotted on a 3D-plot (Fig. 10B), highlighting the change in fit depending on the value of the kinetic parameters. The best fits are highlighted in yellow and red.

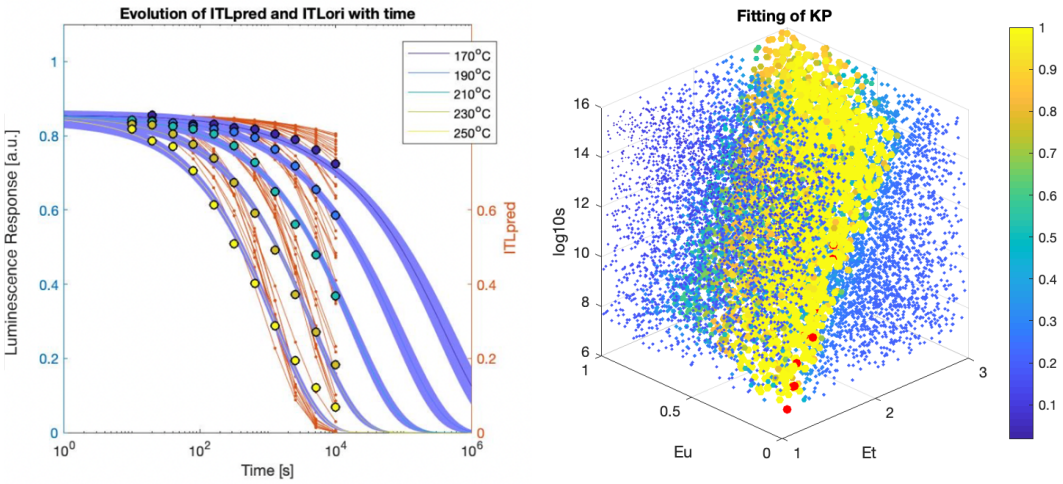

Fig. 10: A. *Fit of the isothermal decay data. The dots represent the measured data, the blue lines are the fit of the isothermal decay data with the BTS model and the natural kinetic parameters of the samples (ITLori), and the orange lines represent the fit of the isothermal decay data with sets of random kinetic parameters (ITLprep) and the BTS model.* ***B.*** *3D-plot of the thermal kinetic parameters depending on their fit to measured isothermal holding experiment data. The red dots represent the 10 best fitting trio of thermal kinetic parameters (modelled data with the lowest misfit), and the colour bar indicates the fitting of the model (1 being the best fit). In yellow we can see the plane that defines the trade-off between the three thermal kinetic parameters.*

There seems to be a unique range of values representing the relationship between the kinetic parameters that can correctly fit the equation for thermal detrapping. Et, Eu, s and ρ' are closely linked, and there is a covariance between these parameters. The stability of the traps depends on the distance between the kinetic parameters Et and Eu, and is linked to the electron escape probability *s*. If this distance (Et-Eu) is smaller, there is logically a higher probability for the electrons to escape (higher s). In the same way, ρ' and Et are linked by the depth of the traps. The deeper is a trap (higher value of Et), the more stable it will be (lower ρ'). Same for the different MET signals: the higher the measurement temperature, the more stable are the traps measured (higher Et, lower ρ'). For different MET signals, there are different stabilities of the traps, and different fading rates.

Further work could investigate whether other samples can be described by the same plane between parameters, offering an alternative method of data fitting to derive common kinetic parameters that could also constrain fading rate. There was insufficient time to do this work within the present thesis.

2.4. Plateau test for the thermal kinetic parameters

During the research for Chapter 1, instead of looking at temperatures, I initially explored directly evaluating the impact of the number of isothermal temperatures used on the derivation of thermal kinetic parameters (Figs. 11 and 12). Different plateaus, corresponding to different kinetic parameter values, can be identified. These plateaus, i.e., these changes in thermal kinetic parameter values, seem to be influenced by the temperature of the highest isothermal holding temperature, similar to the results of Chapter 1. However, these plateau tests have no control in terms of expected values for the samples, i.e., it is not clear which values are incorrect, only that they are sensitive to the isothermal temperatures used for their derivation. For this reason, the study instead investigated the recovery of in-situ temperatures, cf. Chapter 1.

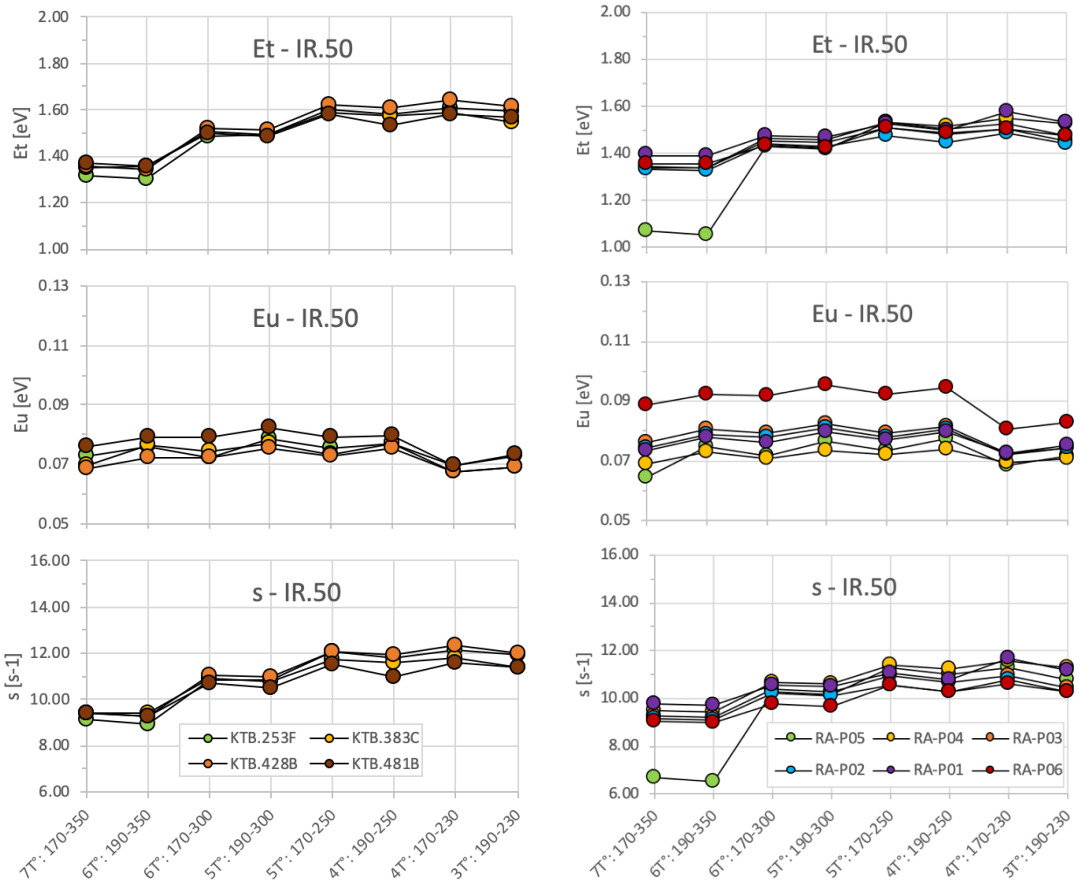

Fig. 11: *Evolution of the thermal kinetic parameters Et, Eu, and s depending on the number of isothermal holding temperatures used to derive them from the fitting of the isothermal decay data of the IRSL.50 signal, for the samples from the KTB borehole, Germany (KTB), and the samples of the Patu thrust sheet, Sub-Himalayas (RA-P).*

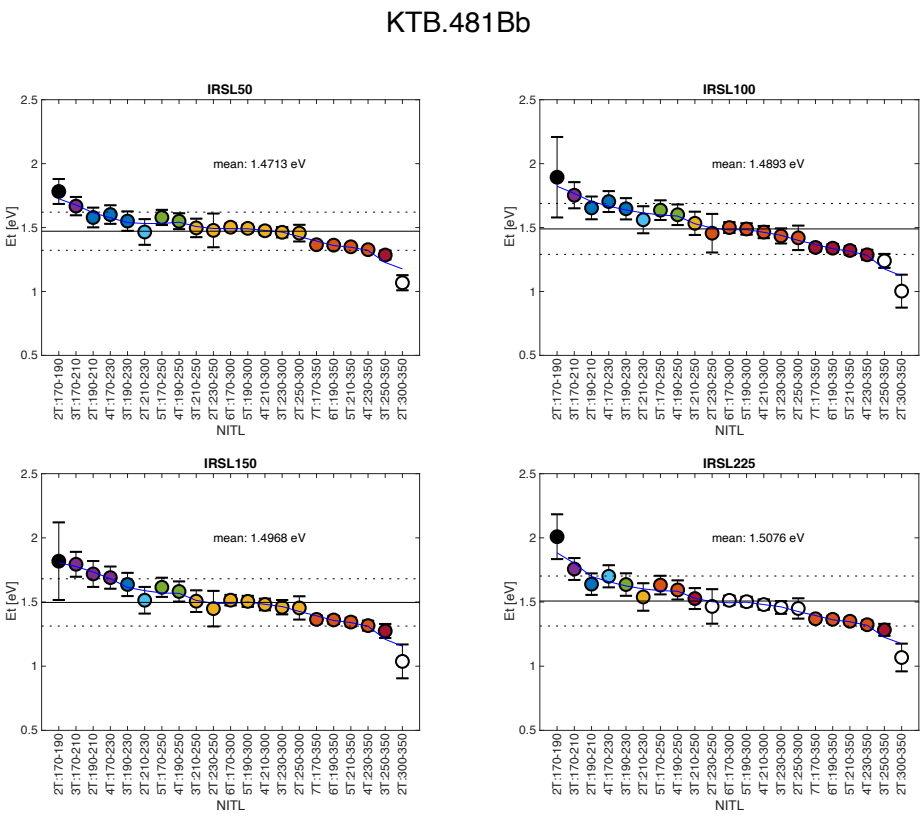

Fig. 12: *Kinetic parameter Et for the sample KTB.481B, for different ITL temperature combinations. The colours represent the different steps, it changes colour each time the difference between two consecutive Et point is superior to 0.06 (detection limit). The black line represents the average Et value, and the dotted lines are the standard deviation interval. The blue line is the moving average on three consecutive points.*

3. Different models: BTS/GOK/GAUSS, KTB samples

Most of the research done during my PhD project focused on K-feldspar luminescence, fitted with the band-tail states model (Li and Li, 2013) to define the thermal kinetic parameters from the isothermal holding experiments. But as described in the presentation of the luminescence method (cf., Introduction), different models exist to extract the thermal kinetic parameters. For example, Guralnik et al. (2015a) used a general order kinetic model, and Lambert et al. (2018) developed the Gaussian model.

Taking the four samples of the KTB borehole presented in details in Chapter 1, luminescence signals were inverted for isothermal temperature using the three thermal decay models (BTS, GOK, GAUSS) to fit the seven isothermal decay data. The three models yield similar temperatures but the KTB in-situ temperatures are not recovered, modelled temperatures being underestimated by more than 10 °C (Fig. 13).

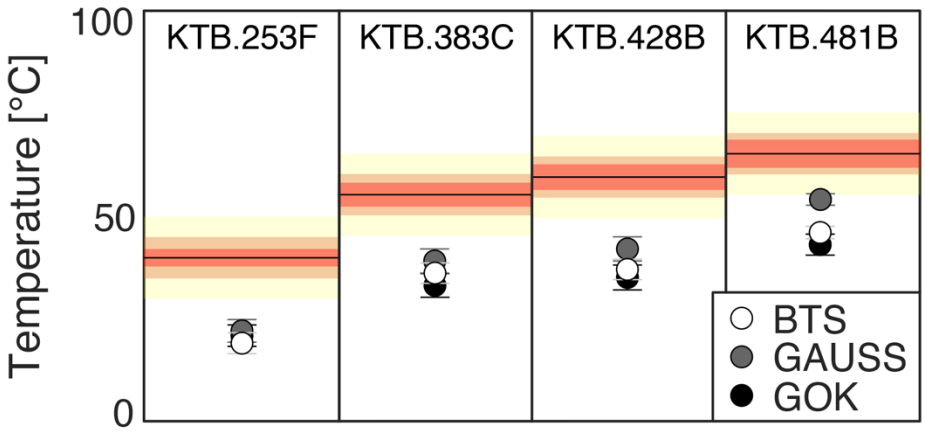

Fig. 13: *Modelled temperatures for the IRSL.50 signal of four Na-feldspar samples from the study of Guralnik et al. (2015b). The temperature was modelled for the three thermal decay models (BTS, GAUSS, GOK), using 7 isothermal holding temperatures. In red are the measured in-situ temperatures and their error range.*

Seeing as the KTB temperatures are also not recovered with seven isothermal holding temperatures, the same methodology as in Chapter 1 was applied for the GOK and the GAUSS models (Fig. 14). Note that the results for the BTS model are already presented in Chapter 1 but are presented here for comparison.

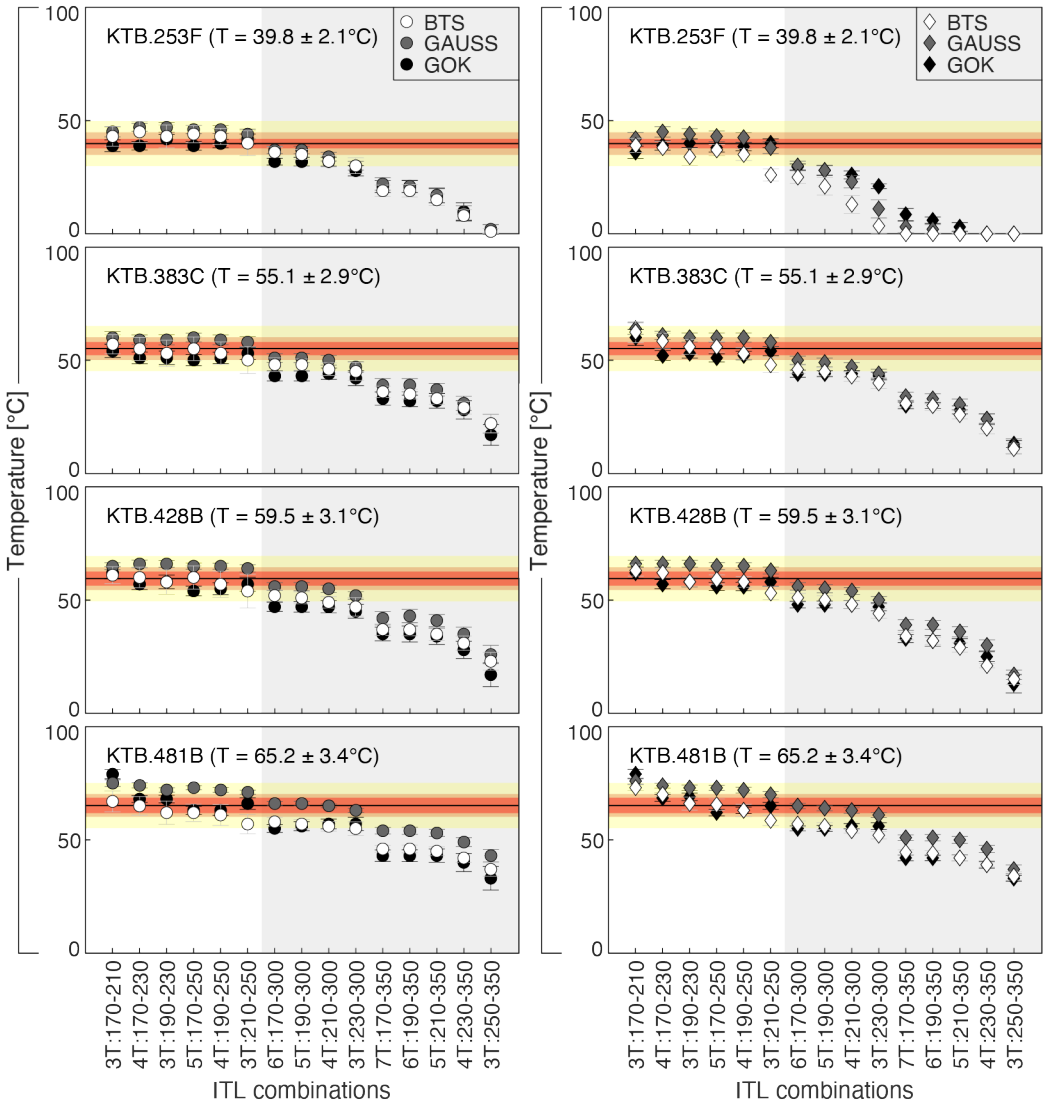

Fig. 14: *Results of the inversion for isothermal temperatures for the KTB borehole samples with the three thermal decay models (BTS, GAUSS, GOK), for* ***A.*** *the IRSL.50 signal, and* ***B.*** *the average of all four MET-IRSL signals. Different combinations of ITL temperatures are tested. The different colours represent how close the inverted temperatures are to the target in-situ temperature. The red area and the red dots are modelled temperatures within the error range of the in-situ temperature, the orange area and dots are within 5 °C of the target-temperature, and the yellow area and dots are within 10 °C of the target-temperature. The green dots have a difference of 10 to 20 °C with the in-situ temperature, 20 to 30 °C for the blue dots, and above 30 °C for the grey dots. The solid black line is the target in-situ temperature, and the red-coloured areas represent the error on this temperature. The grey area highlights the ITL combinations that do not successfully recover the in-situ temperature of the KTB borehole, within error.*

The results obtained are the same as in Chapter 1; the inclusion of isothermal holding data above 250 °C result in kinetic parameters that underestimate modelled temperature. This trend was true for the BTS model for the KTB samples, but is also true for the GAUSS and the GOK models. The Gaussian model also seems to give higher modelled temperature than the two other thermal decay models, particularly for deeper samples (higher in-situ temperature). Furthermore, these results reinforce the validation of the MET-pIR-IRSL measurement protocol for luminescence thermochronometry through the successful recovery of in-situ borehole temperatures with all thermal decay fitting models. It also confirms that using four isothermal temperatures at 190, 210, 230 and 250 °C to determine thermal kinetic parameters from isothermal holding experiments seems to be a good option for the recovery of accurate modelled temperature with luminescence thermochronometry.

4. Invert for surface temperature / palaeothermometry

Given the sensitivity of the IRSL signal to low temperatures (e.g., Guralnik et al., 2015b), it is necessary to consider the surface temperature when inverting the luminescence thermochronometry data. To test whether the measured luminescence data are saturated for surface temperature rather than reflect a rock cooling (and thus exhumation), we calculated the $\tilde{n}_{Tmin}$ value that each sample would correspond to if it stayed at surface temperature.

The method used in Chapters 2 and 3 is to calculate the $\tilde{n}_{Tmin}$ that isothermal holding at the surface temperature of the study area would give, and to contrast the natural luminescence value, $\tilde{n}_{nat}$, of the sample relative to signal saturation for surface temperature, i.e. $0.86*\tilde{n}_{Tmin}$. If the natural luminescence sample is equal or above $0.86*\tilde{n}_{Tmin}$, the sample is considered saturated for surface temperature and is removed from the study. This saturation for surface temperature may not mean that the sample reflects surface temperature. It just means that it should not be possible for the natural luminescence signal of the sample to have a natural luminescence signal above the $\tilde{n}_{Tmin}$ value, or more strictly above $0.86*\tilde{n}_{Tmin}$ value of the sample (Fig. 15). This is because the $\tilde{n}_{Tmin}$ value is the highest trapped-charge value that the sample should have, given that the T_{min} temperature is the lowest that the sample experienced (the lower the temperature is, the bigger the luminescence signal can be). All samples that present natural luminescence values above the $\tilde{n}_{Tmin}$ value for surface temperature are saturated, and show anomalous behaviour, possibly related to measurement uncertainties. The luminescence signals that are in saturation regarding surface temperature T_{min} are excluded from the exhumation rate inversion results. Whilst this criterion is strict and resulted in the exclusion of significant amounts of data, we opted to do this to avoid the determination of spurious exhumation rates.

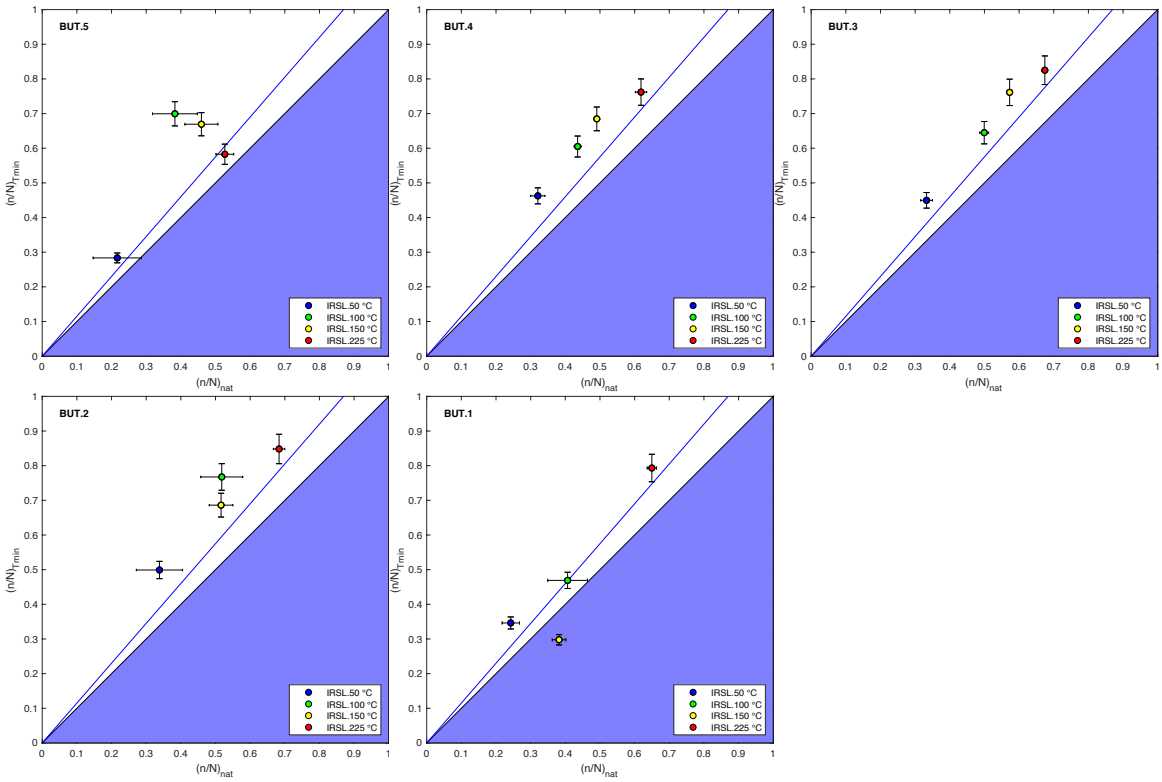

Fig. 15: *Surface temperature saturation plots for the BUT transect, contrasting natural luminescence values, $\tilde{n}_{nat}$, with the luminescence values for a surface temperature of 20 °C, $\tilde{n}_{Tmin} = \tilde{n}_{20}$, predicted for each of the samples. The 1:1 line delimits saturated samples (blue area) to unsaturated samples (white area), with the saturation limit 0.86*$\tilde{n}_{Tmin}$ indicated by the blue line. All samples falling below this line are considered saturated for surface temperature.*

Another way to reach the same conclusion is by calculating the isothermal temperature T_{iso} that the luminescence signal of the sample could invert to. We did this through determining the isothermal temperature that the $\tilde{n}_{nat}$ signals of the sample would reflect. The same method as that described in Chapter 1 to recover the temperature of the KTB borehole samples was used. Isothermal holding was assumed for 1 Myr at temperatures from 100 to 0 °C in 0.1 °C increments. If the modelled T_{iso} is below the surface temperature T_{min}, the luminescence signal is rejected as reflecting saturation (Fig. 16).

For the High Himalaya, whereas samples from the BG and TRI transects exhibit saturation, samples from the KG and HIM transects are generally not saturated. In contrast, for the Sub-Himalaya, only samples from the BUT and SJT transects are not saturated. There is no trend between saturation and elevation.

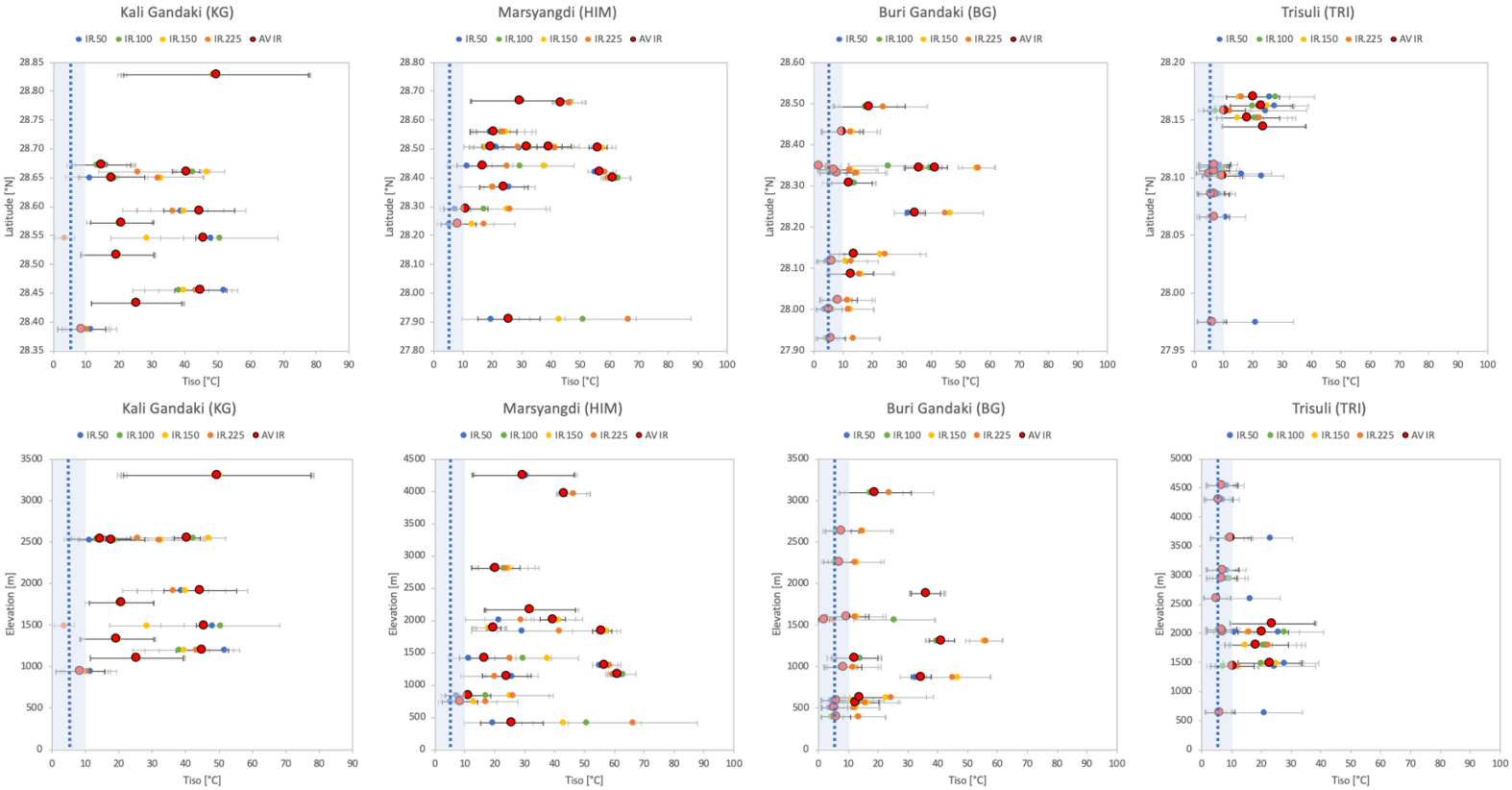
Kali Gandaki (KG)
Marsyangdi (HIM)
Buri Gandaki (BG)
Trisuli (TRI)
IR.50 IR.100 IR.150 IR.225 AV IR
Latitude [°N]
Elevation [m]
Tiso [°C]

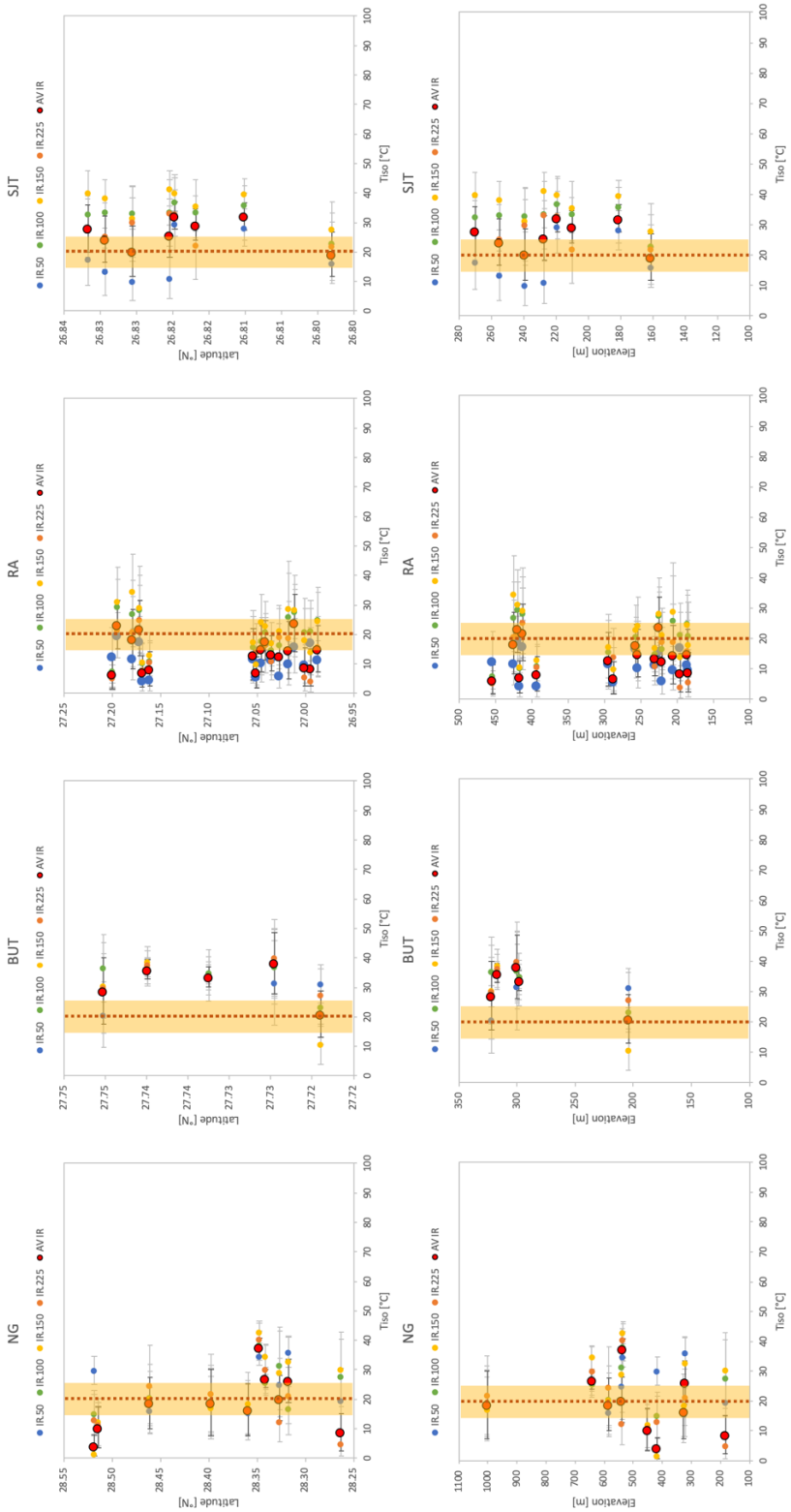

Fig. 16: *Results of the inversions for surface temperature for the four transects of the High Himalayas (KG, HIM, BG, TRI), and for four transects of the Sub-Himalayas (NG, BUT, RA, SJT). Average surface temperature is fixed at 5 ± 5 °C for the High Himalayas (in blue), and at 20 ± 5 °C for the Sub-Himalayan fold-and-thrust belt (in orange). Results are represented for each transect as a function of latitude (left panels) and elevation (right panels).*

Conclusions

In this PhD thesis, I presented the results of the work I carried out through the acquisition, processing and interpretation of different data sets with the aim to quantify the recent late Quaternary deformation of the Himalayas of Nepal and Bhutan. This thesis is articulated around two main lines of research including (1) the optimisation and validation of the luminescence thermochronometry protocol for a multi-thermochronometer approach for feldspar minerals, and (2) the use of luminescence thermochronometry as a tool to study the spatial and temporal distribution of exhumation rates throughout the Himalayas. These different aspects allowed me to combine various disciplines and to employ a multidisciplinary approach combining fieldwork, analysis in the laboratory and numerical modelling, in order to bring new constraints on the thermal histories, and thus exhumation/erosion histories derived from luminescence thermochronometry, to (i) fill the temporal gap in geological constraint between the Holocene and geologic data, that (ii) would contribute to the improvement of the tectonics models of the Himalayas for the Quaternary, and (iii) increase our knowledge on tectonics and the seismic cycle.

Luminescence thermochronometry is a recently developed low-temperature thermochronometer sensitive to low temperatures (< 120 °C) allowing the reconstruction of the thermal histories of the upper first few kilometres of the Earth's crust on sub-Quaternary timescales; a spatial and temporal scale hitherto at the sensitivity limit of other methods. However, despite this advantage, the method was not validated outside of the study of Guralnik et al. (2015b), that showed that using three isothermal holding temperatures (ITL) between 190 and 230 °C, and fitting luminescence decay data with a general order kinetic model, resulted in thermal kinetic parameters that accurately recover temperature for known-thermal history calibration samples from the KTB borehole, Germany. Following the work of Guralnik et al. (2015b), in **Chapter 1** (Bouscary and King, 2022) and in Chapter 4.3, I tested the validity and refined the luminescence thermochronometry method for a multi-thermochronometer approach using K-feldspar minerals. I analysed three sets of samples: samples with independently known thermal histories (KTB borehole samples), synthetic thermal history samples created following irradiation at high temperature in the laboratory, and unknown-thermal history samples, and used a multi-elevated-temperature infrared stimulated luminescence (MET-IRSL; Li and Li, 2012) measurement protocol for feldspar.

As thermal histories depend on the thermal stability of the MET signal and are based on the thermal kinetic parameters extracted from isothermal decay experiments, I tested the validity of thermal kinetic parameters obtained from different combinations of isothermal holding data by trying to recover the temperature of our samples. I found that the temperatures inferred from inverting the data vary depending on the combination of isothermal holding temperatures used for thermal kinetic parameter derivation. The Na-feldspar minerals were more sensitive to changing thermal kinetic parameters constraint, and samples of the same locality exhibit similar behaviour. Results revealed that the inclusion of isothermal holding data above 250 °C result in kinetic parameters that underestimate modelled temperatures.

Focussing mainly on the KTB samples, and on the scatter between all modelled temperatures, I recommended using a new protocol with four isothermal holding temperatures between 190 and 250 °C for appropriate thermal kinetic parameter derivation. This temperature combination allowed validation of the MET-pIR-IRSL measurement protocol for luminescence thermochronometry through the successful recovery of in-situ borehole temperatures.

In Chapter 1, I also attempted to develop artificial luminescence calibration samples in the laboratory, through irradiating a K-feldspar (BUT) and Na-feldspar (KTB) sample at elevated temperature. However, as the laboratory dose rate is nine orders of magnitude greater than that experienced in nature, the effect of changes in the kinetic parameters caused by their calculation with different sub-sets of isothermal data was masked, limiting the use of these synthetic thermal history samples as calibration samples.

Chapter 1 fulfilled the first objective of the PhD project by optimising and validating the multi-luminescence thermochronometry approach for feldspar minerals. The main results of this Chapter are:

- Thermal kinetic parameters, and thus thermal histories, are impacted by the number of isothermal holding temperature used to derive them.

- Artificial luminescence calibration samples cannot be created in the laboratory, the laboratory dose rate being too high.

- Samples from the same locality tend to exhibit similar behaviour.

- Na-feldspar minerals seem to be more affected by change in thermal kinetic parameters than K-feldspars.

- The multi-luminescence thermochronometry approach for feldspar minerals is validated.

- A new protocol with four isothermal holding temperatures between 190 and 250 °C is proposed for accurate thermal history recovery.

A big part of my PhD research has focused on the development of the luminescence thermochronometry method by working on the sample measurement protocol as well as on forward and inverse models using MATLAB (c.f., Bouscary and King, 2002 / Chapter 1, Chapter 4, Appendix). This work has resulted in an improvement in the resolution and accuracy of the thermal histories derived from the luminescence method.

During my PhD, I successfully measured and analysed 116 samples, from which 4 are from the KTB borehole, 12 are control samples from all around the world (c.f., Chapter 1), and 100 are from the Himalayas (5 more samples were sampled but did not have enough K-feldspar minerals to be fully measured).

The improved multi-luminescence thermochronometry protocol was used as a tool to constrain the exhumation history of the Himalayas to better understand the recent late Quaternary (timescales of 10^4 to 10^5 years) tectonics of this tectonically active region. From the 105 rocks sampled from the Himalayas of Nepal and Bhutan, 100 were successfully measured and analysed, from which 44 are from the Sub-Himalayas (33 are presented in Chapter 2 / Bouscary et al. (In review), and 11 others in Chapter 4), and 56 are from the High Himalayas (Chapter 3). All these sample greatly contributes to the existing thermochronological database of the Himalayan chain, filling the temporal gap between modern GPS measurement, palaeoseimic ($\leq 10^2$ yr), Holocene fluvial terrace records ($10^{3\text{-}4}$ yr) and geological estimates ($\geq 10^6$ yr) of exhumation rates.

Chapter 2 focusses on the Sub-Himalayas, the most frontal fold-and-thrust belt of the Himalayan orogen. Samples from western Nepal to eastern Bhutan, collected between the MFT and the MBT, yield exhumation rates of ~3-11 mm/yr over the past ~200 kyr, which convert to minimum cumulative thrust slip rates and horizontal shortening rates of ~6-22 mm/yr and ~5-19 mm/yr, assuming a thrust dip angle of 30°. Comparing these rates with geodetic convergence rates indicates that at least ~55 % of the Himalayan convergence is accommodated by the Sub-Himalayan fold-and-thrust belt, and particularly by the MFT, since the late Quaternary, consistent with this fault being a high seismic hazard zone.

A major uncertainty of the study comes from the conversion of the luminescence thermochronometry data to slip and shortening rates because of the depths over which the thrust geometry must be known. The luminescence signals are constrained on ~200 kyr; considering the exhumation of the rocks along the fault through time, the geometry of the fault needs to be constrained over a few hundred meters to kilometres (dependent on the apparent sample age and its exhumation rate). The fault dip has a major influence on the slip and shortening rates estimated from geological records, and consequently on estimates of strain partitioning. Further constraint of thrust geometry at depth, which is not straight-forward, would be needed to accurately constrain the proportion of late Quaternary convergence accommodated by the MFT relative to the proportion of strain partitioning.

However, even though strain partitioning on other thrusts north of the MFT cannot be excluded, part of the shortening recorded is accommodated by the Main Dun Thrusts (MDT), internal-wedge thrusts between the MFT and the MBT, during the late Quaternary. This implies that internal deformation of the orogenic wedge and strain partitioning may have occurred. Differentiating between an activity out-of-sequence, the MDT accommodating the full convergence rate for a short period, or a coeval activity of the MFT and the MDT, is challenging as luminescence thermochronometry thrust slip rates are averaged over ~200 kyr, rendering a temporal resolution of these late Quaternary deformation rates impossible.

Chapter 3 focussed on the High Himalayas of central Nepal, with more than 50 samples collected and analysed along four transects (from west to east: Kali Gandaki,

Marsyangdi, Buri Gandaki, Trisuli) on each side of the MCT zone. A pattern emerges with almost all samples south of the MCT being saturated, whereas north of the MCT, only a few samples are totally saturated. This pattern is also seen in the apparent luminescence ages of the samples, with young ages of < 100 ka generally clustered just north of the MCT. This follows the trend that is observed for higher closure temperatures thermochronometers, that present younger ages in the MCT thrust sheet, with samples increasing in age towards the north (north of the STDS). However, this pattern in age distribution disappears for the higher temperature thermochronometers when exhumation rates are calculated.

From 2 to 0 (today) Ma, modelled exhumation rates are ≤ 5 mm/yr, with higher exhumation rates focussed around the MCT thrust sheet in the vicinity of the Kali Gandaki, Marsyangdi, and Buri Gandaki valleys, in the west of the studied area. The Trisuli valley, in the east, records exhumation rates that are lower, < 1.5 mm/yr. No sharp transition in exhumation rate can be observed on each part of the thrust systems.

Luminescence thermochronometry records exhumation rates of 3-16 mm/yr (~7.2 mm/yr on average) over the last 100 kyr. Considering that saturated samples imply exhumation rates < 2 mm/yr, the MCT marks a sharp transition between low exhumation rates in the south (< 2 mm/yr), and high exhumation rates in the north, with the samples from the MCT thrust sheet recording an average exhumation rate of ~8.7 mm/yr.

Late Quaternary luminescence thermochronometry exhumation rates show a decrease from west to east of the studied area, whereas for the period 2-0 Ma, increased exhumation rates were more focussed on the central part of the studied area, at the Buri Gandaki and Marsyangdi valleys. This spatial and temporal variability between the four valleys of central Nepal at different timescales suggest an intermittency of exhumation signal due to geomorphological processes. Higher exhumation rates can have several origins, including: the flat-to-ramp transition of the Main Himalayan Thrust (MHT, which is coincidently at the 3500 m elevation delimitation, and corresponds in some places to the MCT zone), extensive basal accretion which may correspond to the formation of a duplex at depth, increase erosion due to isostasic processes, increase in precipitations with a focussed monsoon at the front of the orographic transition, slope instabilities, increase in steam power due to precipitation or deglaciation, presence of a river anticline where largely erosive rivers flow along structural highs (due to localised uplift, plastic deformation of the crust in response to regional compression) and incision of relatively weak crust creating tectonic aneurysms (e.g., Montgomery and Stolar, 2006).

These results suggest that the in-sequence model, with exhumation rates linked to increased erosion of a duplex formed below the Higher Himalayas, coincidently at the MCT location in some areas, is the best model describing the thermochronometric ages of this study on Quaternary timescales. However, for the late Quaternary period, the transition for low to high exhumation rates, and saturated to unsaturated samples on each side of the MCT could potentially suggest a change in tectonic regime, possibly with activity of the MCT area during the last 100 kyr, in the Annapurna and Ganesh regions. If this is the case, activity of the MCT

must be carefully considered as it could have a devasting impact on the seismic hazard, putting the local population at risk.

When combining the results of Chapters 2 and 3 a few key points can be extracted that fulfil the PhD objectives:

- Precise sub-Quaternary (last 200 kyr, timescale of 10^4-10^5) exhumation rates were determined through using a multi-luminescence thermochronometry approach on feldspar minerals, allowing the temporal gap between geophysics / palaeoseismic data ($\leq 10^2$), Holocene geomorphological studies (10^{3-4}), and geological constraints ($\geq 10^6$) to be bridged.

- High exhumation rates are recorded for the High Himalaya and for the Sub-Himalaya during the late Quaternary period. The High Himalayan samples yield an average age of ~100 ka, which is younger than the average age of ~200 ka previously reported for luminescence thermochronometry measurements of samples from the Sub-Himalayas (Bouscary et al., In review), with luminescence thermochronometry rates of ~3-11 mm/yr recorded for the Sub-Himalayas (~6.7 mm/yr on average) over the last 200 kyr, and of ~3-16 mm/yr (~7.2 mm/yr on average) for the High Himalaya over the last 100 kyr.

- The MFT accommodates at least 55 % of the convergence since 200 ka, but activity of faults internal to the Sub-Himalayan FTB is recorded, giving evidence for strain partitioning at least in the Sub-Himalayan fold-and-thrust belt.

- Modelling of the thermochronometric data reveals enhanced exhumation since ~200 kyr, with the location of the highest exhumation rates varying spatially and temporally. This suggests an intermittency of exhumation due to geomorphological processes, favouring the in-sequence model with the development of a duplex structure below the High Himalayas.

- However, the high exhumation rates in the MCT area, and the difference in apparent age and exhumation rates on each side of the MCT fault system during the late Quaternary could potentially indicate out-of-sequence fault reactivation, proving strain partitioning on thrusts on the Himalayan hinterland.

- These results contribute to and improve our understanding of the temporal and spatial evolution of first-order fault systems, and unravel which mechanisms account for the change in exhumation style and pattern during the Quaternary. This contributes to understanding the seismic activity of the Nepalese faults during the Quaternary, and will help to improve contemporary seismic hazard models.

Perspectives

The results presented in this manuscript open up perspectives, both in methodological development of the luminescence thermochronometry technique, and in the application of luminescence thermochronometry as a tool for geomorphological and geological questions. These perspectives provide a framework for future studies on the advancement of luminescence thermochronometry for a better understanding of the processes shaping Earth's topography throughout the Quaternary period.

1. Development and calibration of the luminescence thermochronometry method

1.1. Calibration

Even though the development of luminescence thermochronometry started around fifteen to twenty years ago, a lot remains to be done.

Following the study of Guralnik et al. (2015b) that validated luminescence thermochronometry for the IRSL.50 signal using a general order kinetic model, this thesis successfully optimised and validated the multi-thermochronometer approach (IRSL.50, 100, 150, 225) for feldspar minerals, using the band-tail states model to fit the thermal kinetic parameters (Bouscary and King, 2022). Ogata et al. (2022) also recently used this approach to investigate a deep borehole in the granite of the Tono region, Japan. These studies highlight the importance of having a robust calibration of the luminescence thermochronometry method. However, as different mineralogies and lithologies might influence the sample's kinetic parameters, it is important to find independently constrained thermal history samples that reflect the diversity of the minerals used for luminescence studies. Future studies must focus on verifying and developing luminescence thermochronometry through applications in a variety of settings and mineralogies and lithologies. It would also be necessary to validate the different models used for luminescence thermochronometry, and to do a comparative study of the results obtained with each one of them for the same samples.

Chapter 1 also raised questions on the importance of the measurement temperature, and on the temperature calibration of the measurement instrument. Tests using different preheat temperatures and the impact they can have on isothermal decay experiments need to be done. Do we have thermal transfer only when the isothermal decay temperatures are higher than the pre-heat temperature, or is it independent, and is it just linked to the fact that the TL preheat has no impact on luminescence signals for temperatures < 250 °C, meaning that the reduction in temperature observed in Chapter 1 for the KTB samples is due to a partial annealing of the luminescence signal by the TL preheat at high temperature during the high temperature ITL?

1.2. Inclusion of the measurement error in the calculation of the luminescence signal

The MATLAB codes presented in the Appendix do not include error on the luminescence measurements. Some of the IRSL signals for various reasons, can have high dark counts before measurements, or high background counts, low brightness and high uncertainties on the measured values, but this is totally ignored once the data are analysed in MATLAB. Including these errors on the measurements would allow accurate error propagation, which would provide better quality control on the parameters, and on the luminescence derived results.

1.3. Impact of the hot springs

King et al. (2020) studied some samples from a high temperature tunnel in Japan. In their study, they mention that two samples that were collected had been exposed to temperatures of 165 °C when the tunnel was dug in the 1930s. These samples have an ESR and IRSL signal that is zeroed, showing the impact that these high temperatures have on the trapped-charge methods. Similarly, in Chapter 3, we showed that samples HIM.3A and HIM.3B are impacted by the proximity of a hot spring. The temperature of the water was not as high as 165 °C, however, 50-70 °C was enough to influence the luminescence signal of these two samples, reducing their $\tilde{n}_{nat}$ values drastically.

These kinds of samples provide an important source of information on the thermal stability of the trapped-charge systems, demonstrating that all charge can be evicted from the traps at sufficiently high temperatures. This statement and Chapters 1 and 4 raise question on the thermal stability of the luminescence signals, further studies focussing on thermal transfer and thermal sensitivity for feldspar IRSL are needed to continue to improve our understanding of luminescence-thermochronometry, and the accuracy of the thermal histories extracted.

1.4. Luminescence as a multi-thermochronometer

Over the past few years, my PhD research has focused on the development of the luminescence thermochronometry method by working on the sample measurement protocol as well as on forward and inverse models through MATLAB. This work has resulted in an improvement in the resolution and accuracy of the exhumation rates derived from the luminescence method.

However, even though the multi-luminescence approach is promising, and manages to recover in-situ temperatures, it did not fulfil all of its promises. In this study, the MET protocol data were averaged, yielding a single thermochronometric result. More work needs to be done

to constrain each luminescence signal, and their closure temperatures, to have a better idea in which context the multi-thermochronometer approach would be more appropriate (samples far from saturation, having experienced burial to high temperatures that resets the luminescence signal …).

In theory, differences between the luminescence signals should give information about potential complex burial/exhumation histories. However, what does it mean when an IRSL signal is saturated whereas the other signals are far from saturation for the same sample? Why do we record different exhumation histories, have different apparent ages, that do not follow the logic of the thermal stability of the sample?

1.5. Improving the efficiency of luminescence-thermochronometry measurements

As described in Chapters 1 and 4, luminescence thermochronometry is time consuming, in terms of measurement time, but also in terms of preparation time. Indeed, today one luminescence thermochronometry sample needs approximately one week to be prepared (sawing the rock to remove the parts that were potentially exposed to light, crushing and sieving to the desired grain size, chemical treatment with HCl and H_2O_2, and then two density separations to extract the K-feldspar minerals), and then an estimated measurement time of eleven days per sample (~ 3.5 days for the SAR-MET, ~ 2 days for the FTEST- MET, ~ 5.5 days for the ITL-MET, plus dose recovery, extended fading test…). It is almost twenty days of work to have the results of one single sample.

The isothermal holding protocol proposed in Chapter 1 allows the measurement time to be cut by ~2 days, making total measurement of the sample ~10 % faster. To improve the efficiency of the method, it would be interesting to explore different approaches, such as the construction of a standardised dose response curve, or, as proposed in Chapter 4, to have average kinetic parameters for some lithologies or sites. Another approach, this time concerning sample preparation, would be to directly work on rock slices to measure the luminescence thermochronometry signal. If the results of such a study are conclusive, it could change the way luminescence thermochronometry is done. Making slices instead of preparing aliquots only takes one day per sample! The luminescence signal of the rock slices could also be evaluated with a CCD camera, which would enable the quantification of the luminescence potential of a rock surface, giving control of heterogeneity, grain size, lithology, and mineralogy of the slice measured.

2. Luminescence thermochronometry as a tool for geomorphological and geological questions

Although many new thermochronological ages have been produced in this study, some areas still remain understudied. It would be useful to have samples from each side of the thrusts, having transects that cross from south of the MFT to north of the STDS. Resolution of the exhumation rates also depends heavily on how many thermochronometric systems are being analysed per sample, and on their thermochronological age differences. More data will improve the exhumation rate histories in certain areas, but not necessarily its resolution. Samples also need to be analysed with other thermochronometric systems, and the results need to be coupled with field studies relating exhumation to local topography, climate and surface processes.

The thrusts also need to be mapped more precisely to have a better constrain on the stratigraphy, and the relation between the sample and the tectonics. This could be useful to be able to have better constraints on the maximum burial depth (initial temperature for the thermochronometric models) and local geothermal gradient, particularly for the sample of the Sub-Himalayas.

Following the results of Chapter 2, we showed that for Sub-Quaternary timescales, the sub-surface geometry of the thrust also needs to be constrained on km-scales in order to be able to derive accurate thrust slip rates and horizontal shortening rates from thermochronometric data or exhumation estimates coming from geological studies, and consequently have better estimates of strain partitioning. Further studies are thus necessary to image and constrain near-surface (~few hundred m to km) fault geometries.

2.1. Variation of the geothermal gradient

Further studies should also focus on the code used to derived cooling histories, to allow variation in the geothermal gradient through time, and to be able to have non-monotonic and non-linear geothermal gradient, accounting for the reduced temperatures in the first few meters closer to the Earth's surface, and for the advection of the isotherm by tectonic structures. Even more considering that some of the samples were probably located in glaciated or para-glaciated areas, probably presenting permafrost, seasonally influencing the temperature in the first few meters of the Earth's surface. The change in surface temperature due to climate change is also detectable down to a depth of over 200 m (e.g., Pollack and Huang, 2000).

2.2. Assessing the Himalaya's seismic behaviour from modelling of its sub-Quaternary tectonics

The different tectonic hypotheses presented in Chapters 2 and 3 could be tested with a set of numerical models. These models would combine the thermochronometric data obtained during this PhD using luminescence thermochronometry with previously published low- and medium-temperature thermochronometric, and geomorphic observations to eventually gain a better understanding of the temporal and spatial evolution of the Himalayan fault system since the Quaternary. The different kinematics and geometries of the faults that can explain the accommodation of the convergence between the Indian and Eurasian tectonic plates during the Quaternary could be tested, by changing the mechanical parameters (i.e., friction coefficient, strain, etc.) and the geometry (e.g., slope, fault ramp, presence of an anticline, etc.) of the major tectonic structures. This would allow the out-of-sequence and the in-sequence/duplex hypotheses to be differentiated (at least during the Quaternary period), and to unravel which mechanisms between the tectonic (e.g., location and stage of advancement of the faults, differences in convergences rates), the climate (e.g., precipitation gradients, influence of the fluvial and glacial valleys), and the geology (e.g., lithology, geometry, rock properties) account for the differences in exhumation style and pattern between the foreland (south) and hinterland (north), as well as in between the different valleys of Nepal and Bhutan (east-west).

The relative movements of the different thrusts and the MHT could be assessed in a thermo-kinematic numerical model (inspired by Herman et al., 2010) as a function of the controlling parameters listed above to (1) match the thermochronometry data, and to (2) assess the associated seismic behaviour of the Nepalese mountain belts during the Quaternary.

(a) Landscape evolution model: Prior to building thermo-kinematic models, a range of numerical experiments need to be done using a landscape evolution model such as CASCADE (developed by Braun and Sambridge, 1997; Braun et al., 1999), and then using a thermal model (e.g., PECUBE, Braun, 2003; Herman et al., 2007) to calculate the thermal history of the study area. This should be done to assess if the response can be approximated with a simple analytical function that would be more amenable to inversion.

(b) 1-D thermo-kinematic model: A thermo-kinematic model could utilise the transient solution to episodic uplift (Carretier et al., 2009; Godard et al., 2011, 2013). The transient aspect would come from the erosional response and the thermal adjustment, the erosional response being driven by river entrenchment and hillslope adjustment or directly through landslides triggered by the seismic events themselves (Huerta et al., 1999; Parker et al., 2011; Hovius et al., 2011). This transient solution could have different input parameters, including the geometry and location of the faults, as well as the geothermal gradient at the location of the model (e.g., temperatures logged in wells and their 1-D modelling, Cermak et al., 1993), the parameters being constrained from literature data. These 1-D thermo-kinematic models could be based on initial thermal histories and on the exhumation/erosion rates obtained from luminescence

thermochronometry. Various modelling inversion approaches could be used to find the thermal histories that correspond best to the data.
(c) 2-D thermo-kinematic model: A nonlinear inversion of the data using a Neighborhood Algorithm (following the approach of Herman et al., 2007, and 2010, who used the thermo-kinematic model PECUBE, Braun, 2003; Herman et al., 2007), or any other similar nonlinear inversion method where the algorithm optimizes the misfit function (depending on the changing parameters) as the Monte Carlo iterations proceed can be used for constraining the model. These 2-D thermo-kinematic models could then be compared to the results obtained from existing thermo-mechanical 2-D models, such as the Seismo-thermo-mechanical (STM) code of Dal Zilio et al. (van Dinther et al., 2013, Dal Zilio et al., 2018).
(d) 3-D landscape evolution model: It would then be possible to couple a landscape evolution model such as CASCADE (Braun and Sambridge, 1997; Braun et al., 1999) with the 2-D thermo-kinematic models to simulate regional landscape evolution for the setting of the Central Himalayas, and assess to which extent the proposed kinematics can explain the morphology of the area. Such a 3-D modelling approach would enable to integrate vertical and horizontal displacement trajectories based on fault geometries and their capacity to simulate surface processes at the scale of the mountain range.

2.3. Link with the active seismicity

Mountain building processes and the seismic cycle are closely linked, and earthquakes are the physical response to crustal deformation and fault movements driven by the convergence of tectonic plates (Avouac et al., 2001; Avouac, 2007; Ader et al., 2012; Dal Zilio et al., 2018, 2019, 2020). In the Himalayas, the link between earthquakes and surface uplift has been investigated by various authors. For example, articles by Lavé et al. (2005), Sapkota et al. (2013), and Bollinger et al. (2014) suggest that large earthquakes break the surface along the MFT and lead to plurimetric surface uplift. However, most of these articles focus on short timescales which might not be representative on the seismic behaviour over the long run given that the largest events may have a millenary return period.
Luminescence thermochronometry data could help simulating the temporal and spatial evolution of the Himalayan fault system during the sub-Quaternary, as well as the variations in surface uplift during this period. This Quaternary geochronologic signal could be extracted from the 3-D thermo-kinematic models described above, and based on the current knowledge of earthquakes kinematics, a numerical code to simulate the Quaternary seismic history of the Nepalese faults could be built. This history could then be compared to the seismic history inferred from the return time of earthquakes (Bollinger et al., 2014, 2016; Dal Zilio et al., 2018, 2019). Doing so would allow to have a better understanding of the link between the tectonic activity/fault movements and the seismic cycles, and to therefore improve the existing seismic hazard models (e.g., Stevens et al., 2018).

All of this would improve our understanding of the temporal and spatial evolution of first-order fault systems, and unravel which mechanisms account for the change in exhumation style and pattern. This could ultimately provide a currently absent key piece of information regarding the seismic activity of the Nepalese and Bhutanese-Himalayan faults during the Quaternary, and contribute to the improvement of today's seismic hazard models.

Placing these data in the context of globally available thermochronological ages and models could allow the general role of climate and tectonics in exhumation/erosion and seismicity to be discussed. It will call for subsequent investigations into the link between all these processes related to the formation and evolution of mountainous landscapes.

Appendix

LumiThermo and ESRThermo: Libraries of codes for trapped-charge thermochronometry

---

C. Bouscary, G.E. King, et al.

Table of contents

This pseudo-chapter will be submitted to *AncientTL* or as a *Technical Note for Geochronology*:
Bouscary, C., Bartz, M., Biswas, R., Bossin, L., Duverger, A., Guralnik, B., Lambert, R., Licul, A., Nanni, U., Stalder, N., Valla, P., Visnjevic, V., Wen, X., Herman, F., and King, G.E. *(in prep.)*, LumiThermo and ESRThermo: Libraries of codes for trapped-charge thermochronometry. *AncientTL / Technical Note for Geochronology*.

Abstract

Over the past fifteen years, trapped-charge thermochronometry has been established as an ultra-low temperature (< 80 °C) thermochronometric system. Its novelty is its ability to resolve rock cooling within the final km of Earth's surface, as well as air temperature changes since the Last Glacial Maximum to the present day. In order to derive temperature histories from the luminescence or electron spin resonance signals of feldspar or quartz minerals, it is necessary to model both signal accumulation and signal loss in response to mineral exposure to ionizing radiation and temperature, as well as athermal signal losses. Two libraries have been developed in MATLAB that allow different numerical models to be used for this purpose, the first is applicable to the infrared stimulated luminescence of feldspar minerals (LumiThermo) and the second to the electron spin resonance signal of quartz minerals (ESRThermo). These libraries have been made available in GITHUB and this contribution describes their broad structure, the models that have been implemented and their practical use.

Keywords: low-temperature thermochronometry, luminescence, feldspar, kinetic parameters, MATLAB

1. Introduction

The development of trapped-charge thermochronometry over the past fifteen years (e.g., Herman et al., 2010; Guralnik et al., 2015a; Wu et al., 2015; King et al., 2016a; Brown et al., 2017; Biswas et al., 2018; King et al., 2020) and recent investigations of trapped-charge thermometry (e.g., Guralnik and Sohbati, 2019; Biswas et al., 2020) have built upon both previous applications of the method (e.g., Houtermans et al., 1957; Grün et al., 1999) and earlier fundamental research describing the accumulation and loss of trapped-charge signals (e.g., Prokein and Wagner, 1994; Toyoda and Ikeya, 1991). Recent reviews of the technique are given by King et al. (2016c) and Herman and King (2018). The premise of the technique is that as the luminescence and electron spin resonance (ESR) signals of quartz and feldspar minerals are thermally sensitive, they can be used to determine temperature histories. Temperature changes occur, for example, as rocks are exhumed towards the surface (e.g., King et al., 2016b) or as atmospheric temperature changes (Guralnik and Sohbati, 2019; Biswas et al., 2020).

Luminescence and ESR thermochronometry rely on the combination of laboratory measurements with numerical models, that allows the conversion of trapped-charge concentrations into thermal histories. Two or three laboratory experiments are typically used to make an ESR or luminescence thermochronometry measurement, respectively (e.g., Herman et al., 2010; Guralnik et al., 2015b; King et al., 2016a; Biswas et al., 2018; Fang and Grün, 2000; King et al., 2020). The first experiment measures the amount of trapped charge within the sample, and is usually done using a single aliquot regenerative dose method (e.g., Murray and Wintle, 1999; Tsukamoto et al., 2015). As trapped-charge thermochronometry data are often described as saturation ratios, i.e. the proportion of electrons trapped, relative to the maximum possible number of trapped electrons, laboratory dose response curves are generally measured until signal saturation. For some samples, the very high saturation level of the quartz ESR Al-centre makes this impractical, and for this signal the system may be treated as non-saturating. The second experiment measures the thermal decay of the luminescence or ESR signals in response to temperature and generally comprises an isothermal decay experiment whereby signal loss relative to a fixed temperature is measured following different time points (e.g., Bouscary and King, 2022). The final experiment is only applicable to the luminescence of feldspar minerals and consists of measuring the rate of anomalous fading (Wintle, 1973; Visocekas, 1994) by measuring signal loss at ambient temperature following delays of different durations.

Fitting these experimental data using models that describe signal accumulation, thermal or athermal decay, allows the experimental data to be reduced to several kinetic parameters, as illustrated in equation 1:

$$\frac{\mathrm{d}\tilde{n}}{\mathrm{d}t} = \frac{\dot{D}}{D_0}\,(1-\tilde{n})^{\alpha} - \; s\,\tilde{n}^{\beta}\,\exp\left(\frac{-E_a}{k_B T}\right) - \; \tilde{s}\,\tilde{n}\,\exp\left(-{\rho'}^{-\frac{1}{3}} r'\right) \qquad [1]$$

The trapped-charge population $\tilde{n}$ at a given time t (Ma) is given by three terms, the first term on the right-hand side of the equation describes trapped-charge accumulation where $\dot{D}$ is the environmental dose rate (Gy/Ma), D_0 is the characteristic dose of saturation (Gy) and α is an exponent ≥ 1, depending on whether electron trapping is described as first or general order. The second term describes thermal loss at a given temperature, T (K), where s (Ma^{-1}) is the frequency factor, E_a is the activation energy of the electron trap (eV), k_B is the Boltzmann constant ($eV.K^{-1}$) and β the order of kinetics ($1 \leq \beta \leq 2$). The final term describes athermal loss where $\tilde{s}$ is a frequency factor (3×10^{-15} s^{-1}), ρ' is a dimensionless description of the density of recombination centers and r' is a dimensionless distance between traps and recombination centers (Huntley, 2006).

A variety of different models describing signal accumulation and athermal or thermal signal loss have been investigated for use in trapped-charge thermochronometry/thermometry applications (e.g., Guralnik et al., 2015b; Biswas et al., 2018; Biswas et al., 2020; King et al., 2020) and have been validated against data collected in the laboratory as well as independent temperature measurements (e.g., Lambert, 2018). These kinetic parameters can then be used together with equation 1, to predict a trapped-charge concentration for a particular temperature-time history, allowing the natural trapped charge concentration of a sample to be inverted for its thermal history.

In this contribution we first outline the models implemented in the codes. We then describe the structure of the LumiThermo and ESRThermo libraries as well as the input format of experimental data required. Note that we do not comment on the suitability of different models for specific datasets, but rather list those models that have been implemented in the libraries at present. We anticipate that new models of trapped-charge systems will be integrated in the future.

2. Model overview

In this section the specific models that have been implemented in the LumiThermo and ESRThermo libraries are described. Although athermal signal losses are usually one of the first measurement done, here we begin with these models as athermal losses must also be accounted for when constraining the trapped-charge concentration and fitting isothermal decay data of feldspar minerals in the LumiThermo library.

2.1. Athermal signal loss

This part of the code is only available in the LumiThermo library.

Athermal signal losses are known to affect the infrared stimulated luminescence of feldspar minerals (Visocekas, 1994) and must be accounted for when fitting luminescence data to derive the kinetic parameters of signal dose response and thermal decay. The model of Huntley (2006) as implemented by Kars et al. (2008) is used in the LumiThermo library as it allows the natural dose response curve of feldspar signals to be computed as well as the natural steady-state luminescence signal, $\tilde{n}_{ss}$. This signal is expressed as the ratio between the trapped-charge concentration, n, and the maximum possible trapped-charge concentration in the absence of anomalous fading, N. Signal saturation is the main limitation of luminescence thermochronometry (e.g., Valla et al., 2016) and accurate screening of luminescence signals for saturation is essential.

The rate of anomalous fading induced signal loss can be calculated from:

$$n(t^*) = n(0) \cdot \varphi(t^*) \quad [2]$$

where $n(0)$ is the initial trapped-charge concentration at time 0, and $n(t^*)$ is the signal remaining after fading time t^* which is calculated from the mid-point of the irradiation time, following Auclair et al. (2003), and

$$\varphi(t^*) = \mathrm{e}^{-\rho' \ln(1.8\,\tilde{s}\,t^*)^3} \quad [3]$$

in which $\rho' \equiv \frac{4\pi\rho}{3\alpha^3}$, where ρ is the density of recombination centres and α is a constant (Huntley, 2006; Kars et al., 2008).

To compute the athermal steady-state value for feldspar luminescence signals, $\tilde{n}_{ss}$, the following equation is used (Li and Li, 2008; King et al., 2016a):

$$\tilde{n}_{ss} = \int_{r'=0}^{\infty} \frac{3r'^2 e^{-r'^3}}{1+\frac{D_0}{D}\tilde{s}e^{-\rho'^{-1/3}r'}} dr' \quad [4]$$

where dimensionless distance $r' \equiv \left\{\frac{4\pi\rho}{3}\right\}^{\frac{1}{3}} r$, and the probability that the nearest recombination centre is at a distance between r' and $r' + dr'$ is given by $p(r')dr = 3r'^2 e^{-r'^3} dr'$ (Huntley, 2006).

2.2. Signal growth

Trapped-charge signals accumulate in response to the exposure of quartz and feldspar minerals to ionizing radiation. Various models have been proposed for luminescence and electron spin resonance signal growth. In the LumiThermo library, the single-saturating exponential growth (SSE) and general order kinetic growth (GOK) functions have been implemented. In the ESRThermo library in addition to SSE and GOK, a linear growth (LIN) function has also been implemented for signals that do appear to experience saturation (King et al., 2020).

In trapped-charge thermochronometry, the saturation ratio of the centre under investigation is usually considered, rather than the age, consequently, $\tilde{n}$ ratios are calculated for all of the signal growth fitting options with the exception of the LIN model, where N cannot be constrained. For this model, rather the equivalent dose, D_e (Gy) of the natural sample is considered.

The different dose response models are given below:

(i) Single saturating exponential growth (SSE)

$$\tilde{n}(t) = \varphi(t^*) \cdot A\left(1 - e^{-\frac{\dot{D}_{lab}t}{D_0}}\right) \quad [5]$$

where $\tilde{n}(t)$ is the amount of trapped electrons at time (t), A is a pre-exponential multiplier, $\dot{D}_{lab}$ is the laboratory dose rate (Gy/s) and φ accounts for athermal detrapping (Eq. 2 and 3). Note that athermal detrapping is only applicable for luminescence signals from feldspar and this term is not incorporated in the models implemented in the ESRThermo library. Single saturating exponential fits have been used previously to fit both luminescence (e.g., Herman et al., 2010) and ESR thermochronometry data (e.g., Grün et al., 1999).

(ii) General order kinetic growth (GOK)

$$\tilde{n}(t) = \varphi(t^*) \cdot A\left(1 - \left(1 + \left(\frac{\dot{D}_{lab}}{D_0}\right)ct\right)\right)^{-1/\alpha} \quad [6]$$

where α is the kinetic order (Guralnik et al., 2015b). General order kinetic models have been used to fit both infrared stimulated luminescence data (e.g., Guralnik et al., 2015a) and thermoluminescence data (Biswas et al., 2018).

(iii) Linear growth (LIN)

$$D = mt\dot{\mathrm{D}}_{lab} \quad [7]$$

Linear growth has been used to describe the ESR response of the Al-centre within the context of ESR-thermochronometry (King et al., 2020), with m the gradient of the slope.

2.3. Thermal signal loss

The thermal sensitivity of trapped-charge signals is well known (e.g., Aitken, 1985). The following models have been implemented in the LumiThermo and ESRThermo libraries: (i) General-order kinetics (GOK; Guralnik et al., 2015a), (ii) the Band-tail states model (BTS; Li and Li, 2011), and (iii) the Gauss distribution model (GAUSS; Lambert, 2018). The mathematical basis of the models is described below:

(i) General order kinetics (GOK)

$$\frac{n(t)}{n(0)} = \varphi(t^*) \cdot \left[n(0)^{1-b} - (1-b) \frac{1}{s^{-1}\, exp^{\frac{E_a}{k_B T(t)}}} \right]^{\frac{1}{1-b}} \quad [8]$$

Note that if the kinetic order, b, is fixed at 1 or 2, the model reverts to first or second order kinetics respectively. Guralnik et al. (2015b) used general order kinetic thermal decay to fit their infrared stimulated luminescence thermochronometry for samples from the KTB-borehole whilst Biswas et al. (2018) used a similar approach to fit their thermoluminescence thermochronometry data for samples from the KTB-borehole and from Namche Barwa. Wu et al. (2015) used first order kinetics to fit quartz luminescence data for samples from Taiwan and Toyoda (1991) used second order kinetics to describe the thermal decay of the Al- and Ti-ESR centres of quartz minerals and noted their potential for thermochronometry.

(ii) Band-tail states (BTS)

$$\frac{n(t)}{n(0)} = \varphi(t^*) \cdot \int_0^{\max(E_a)} P(E_b)\, e^{\left(-ste^{-\frac{E_a}{k_B T}}\right)} dE_b \quad [9]$$

Where $E_a = E_t - E_b$, E_t being the trap depth of the electron trap (eV) and E_b the depth of the band-tail state (eV). The probability of thermally evicting electrons into the band-tail states of energy in the range of $E_b + dE_b$, $P(E_b)\, dE_b$, is given by (Poolton et al., 2009; Li and Li, 2013):

$$P(E_b)\,dE_b = C\,e^{\left(-\frac{E_b}{E_u}\right)}dE_b \quad [10]$$

where C is a pre-exponential multiplier and E_u is the width of the Urbach tail (eV). King et al. (2016a, 2016b), Herman and King (2018), King et al. (2020), Bouscary and King (2022) and Ogata et al. (2022) used the band-tail states model to describe their multi-luminescence-thermochronometry data from feldspar minerals.

(iii) Gauss distribution model (GAUSS)

The Gauss distribution model assumes a Gaussian distribution of trap depths, with mean trap depth $\mu(E_t)$ (eV) and width $\sigma(E_t)$ (eV) (Lambert, 2018), with

$$\frac{n(t)}{n(0)} = \varphi(t^*) \cdot \int_0^{E_t} P_t(E_t)\, e^{\left(-ste^{-\frac{E_t}{k_B T}}\right)} dE_t \quad [11]$$

and the probability of eviction $P_t(E_t)$ given by:

$$P_t(E_t) = \frac{1}{\sigma(E_t)\sqrt{2\pi}} \exp\left(-\frac{1}{2}\left(\frac{E_t-\mu(E_t)}{\sigma(E_t)}\right)^2\right) \quad [12]$$

Lambert (2018) used the Gauss model to describe thermal losses from the IRSL signals of feldspar minerals from the Mont Blanc massif, whilst King et al. (2020) used the GAUSS model to describe thermal signal losses from the ESR Al- and Ti-centres of samples from Japan.

2.4. Data inversion

Using the kinetic parameters derived from fitting experimental data with the models described above, it is possible to invert the data to derive a thermal history using equation 1, where the kinetic orders α and β are equal to 1 for a SSE fit or where the BTS or GAUSS models are used, and where $E_a = E_t$ for the GOK, $E_a = E_t - E_b$ for the BTS model, or $E_a = E_t - \mu(E_t)$ for the GAUSS model. For the luminescence of feldspar, the model must be integrated over the range of recombination centre distances *r'* and, for the BTS and GAUSS models, over the range of activation energies E_a described by equations 9 and 11. In contrast for quartz ESR data the third term on the right-hand side of the equation that accounts for anomalous fading can be removed, and it is only necessary to integrate over the range of activation energies:

$$\frac{\mathrm{d}\tilde{n}}{\mathrm{d}t} = \frac{\dot{D}}{D_0}\,(1-\tilde{n})^{\alpha} - s\,\tilde{n}^{\beta}\exp\left(\frac{-E_a}{k_B T}\right) \quad [13]$$

Finally, for a non-saturating system exhibiting linear dose response, equation 14 is used:

$$\frac{\mathrm{d}\tilde{n}}{\mathrm{d}t} = \dot{D} - s\,\tilde{n}\,\exp\left(\frac{-(E_t-\mu(E_t))}{kT}\right) \qquad [14]$$

3. Structure of LumiThermo and ESRThermo

The two libraries described here are structured in a similar manner (Table 1), that allow the input of partially processed trapped-charge data into MATLAB, before the data are fitted to derive the kinetic parameters that describe signal growth and decay. These parameters can then be used to invert thermal histories from the natural trapped-charge concentrations of the sample under investigation.

Table 1: *Overview of the structure of the LumiThermo and ESRThermo libraries.*

	Script name	***Description***	***Output***
Data fitting	LumiThermo/ ESRThermo	A single script that calls the other scripts, allowing the user to input the filename and select the models that they would like to use to fit their data.	
	Stage 1_ExceltoStruct	Uploads the data from a pre-defined Excel spreadsheet format.	filename.mat containing the structure, 'records', which contains the raw data
	Stage 2a_Fitparameters	The raw data are fitted with the selected models yielding the kinetic parameters that will be used to later invert the data.	fitpar.mat containing the structure, 'records.params', which contains the kinetic parameters
	Stage2b_PlotFit	The raw data are plotted relative to the model fits, allowing visual inspection of the data.	Figures of the data fitting
Inversion	Stage3a	The data can be inverted to obtain a cooling history, using the specific selected models and the kinetic parameters output from Stage 2a.	'Tt.mat', structure containing the inversion results
	Stage3b	The inversion results are plotted allowing visual inspection of the data.	Figures of the inversion

4. Experimental data

The LumiThermo and ESRThermo libraries are designed for the following three experimental data types but could be modified for different types of experimental data if required. (i) Luminescence or ESR dose response data measured in a regenerative dose protocol until saturation, i.e. the luminescence/ESR response to a range of laboratory irradiation doses including zero dose. The laboratory irradiation source dose rate (Gy/s) must be listed in the data input file, as well as the irradiation times (ks) (Fig. 1). (ii) Isothermal decay data for a minimum of three temperatures. The isothermal holding temperatures (°C) must be listed in the data input file together with the isothermal holding times (ks) (Fig. 1). (iii) Anomalous fading data for feldspar luminescence data only. The delay times (t*, ks) between the mid-point of irradiation and measurement should be calculated after Auclair et al. (2003).

The data format for the Excel data input file that is required is shown in Fig. 1 for an example luminescence sample. Templates populated with the example data shown here are available for download from GitHub here:insertlink. Where fewer dose response or isothermal holding temperatures have been measured, the rows should be deleted and the values of 'na'/'nSARA' and number of isothermal measurements 'NITL' updated in the LumiThermo/ESRThermo script (see below). Similarly, additional measurements can be included by inserting additional rows in the appropriate section and updating the NITL and na/nSARA values. This spreadsheet must be saved in the "Data" folder of the MATLAB library so that it can be called by the script (see further details below). It should then only be necessary for the user to modify the LumiThermo/ESRThermo script to both fit and invert their data.

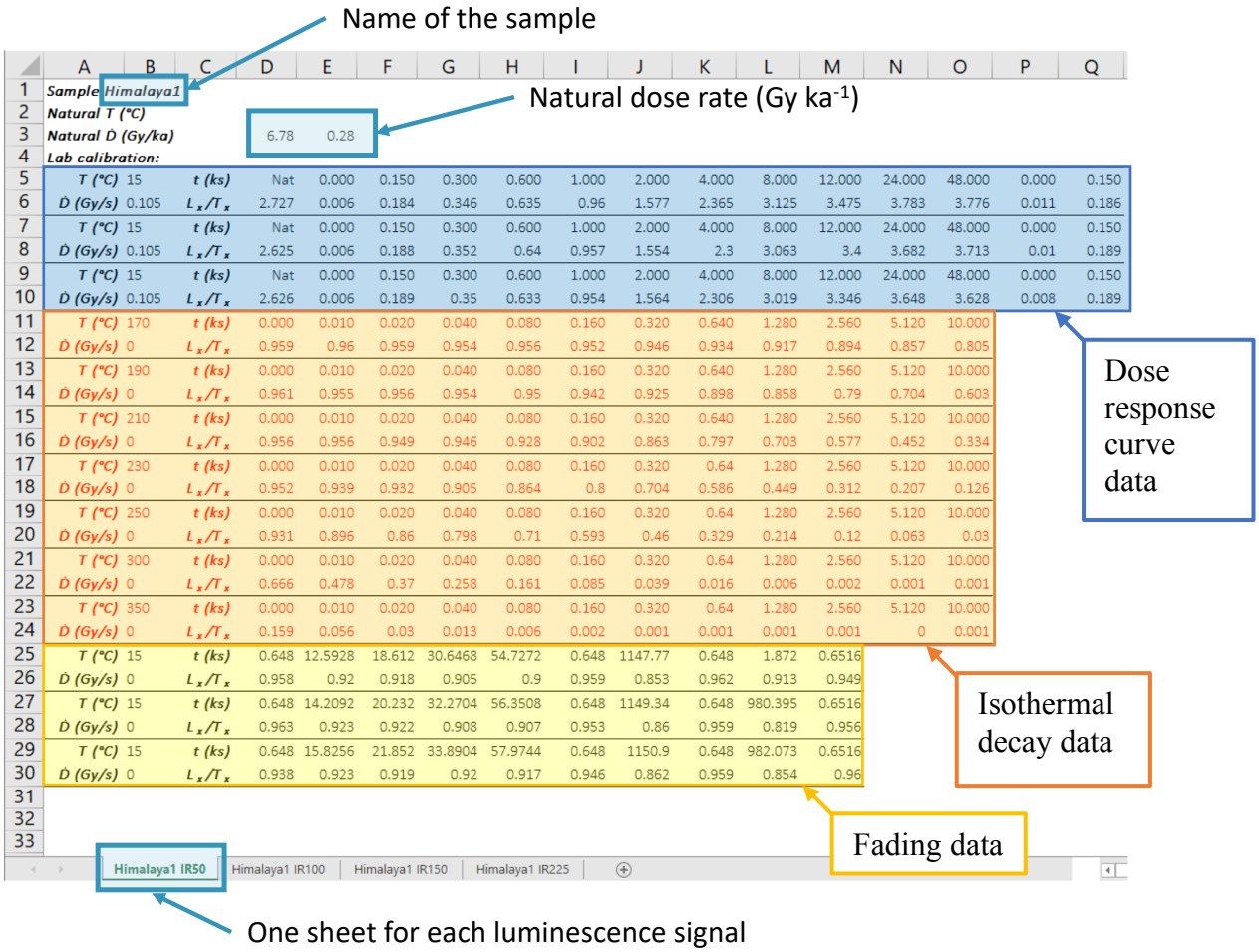

Fig. 1: *Example of an Excel input sheet for the LumiThermo library.*

5. Running the code

The code is available from GitHub here:insertlink. Users will need both a MATLAB license and the statistics toolpack to run the code. Example datasets are provided from King et al. (2016a) and Bartz et al. (2022).

5.1. LumiThermo/ESRThermo

In LumiThermo/ESRThermo the user must provide the filename and select which models will be used to fit the data and invert the data. The number of aliquots and number of isothermal temperatures investigated must also be stated.

```
filenamevec={'TTY-A01-Ti_2022'};   %name of Excel data file
NITL=3;                            %number of isothermal decay temperatures
nSARAvec={3};                      %number of SARA measurements
SARA_fittype=[1];                  %1=SSE; 2=GOK; 3=LIN
ITLmat=[8 8 8];                    %shape of ITL data
ITL_fittype=[1];                   %1=GOK; 2=Gauss;
```

The user then selects which codes should be run for that particular sample, e.g., *Stage1_ExcelToStruct*, *Stage 2a_Fitparameters*. Once a code has been run for a sample, the output is saved (see Table 1) so it is not necessary to run the code again unless the raw data have changed, or the data should be fitted with a different model.

5.2. Stage1_ExcelToStruct

This function imports the Excel data into MATLAB and creates a structure called 'records' that is called in *Stage2a_Fitparameters*:

```
run Stage1_ExcelToStruct2022

>>records
  struct with fields:
        id: 'TTY-A01-Ti'
        params: [1×1 struct]
        rawdata: [1×14 struct]

>>records.rawdat
  1×14 struct array with fields:
        T
        Ddot
        t
        ESR
```

This structure is also saved as a .mat file in the subfolder "ComputeData", with the name filename.mat, and can be accessed without running *Stage1_ExcelToStruct* again. If multiple sheets are present in the Excel file, 'records' will comprise multiple datasets, which can be accessed separately by inputting records(*i*) where *i* is the record number, into the MATLAB Command Window. The different rows of raw data (*j*) can also be accessed directly, for

example to access the duration of dose/isothermal annealing time (Table 2), one can input *records(i).rawdata(j).t* into the command line.

Table 2: *Variable names and description of data stored in MATLAB after running Stage1_ExcelToStruct.*

Excel ID	MATLAB ID	Description
Sheet name	records(i).id	Excel sheet name
Natural T (°C)	records(i).params.natT	Natural temperature (°C)
Natural $\dot{D}$ (Gy/ka)	records(i).params.natDdot	Natural environmental dose rate (Gy/ka)
T (°C)	records(i).rawdata(j).T	Measurement temperature
$\dot{D}$ (Gy/s)	records(i).rawdata(j).Ddot	Instrument dose rate (Gy/s)
t (ks)	records(i).rawdata(j).t	Duration of dose/isothermal annealing
Lx/Tx	records(i).rawdata(j).L	Luminescence data (LumiThermo only)
ESR	records(i).rawdata(j).ESR	ESR data (ESRThermo only)

5.3. Stage2a_Fitparameters

This script calls *filename.mat* created by *Stage1a_ExcelToStruct* and fits the raw data using the models specified in the ESRThermo/LumiThermo script. The kinetic parameters output by the script depend on the model used and are summarised in Table 3. The parameters are stored in the structure 'records' as 'records.params'. In addition to the kinetic parameters, the modelled data fits are stored in the structure 'records' as 'records.plot' for plotting in *Stage2b_PlotFit*.

```
>> records
struct with fields:
        id: 'TTY-A04-Al'
        params: [1×1 struct]
        rawdata: [1×14 struct]
        SARA_fittype: 1
        ITL_fittype: 2
        plot: [1×1 struct]

>> records.params
struct with fields:
        natT: [NaN NaN]
        natDdot: [1.3883e-10 1.3730e-11]
        Et_GAUSS: [1.5578 0.0880]
```

s10_GAUSS: [13.7442 0.9927]
sigmaEt_GAUSS: [0.0845 0.0060]
SARADeGy: [1.4192e+03 54.9701]
SARAnNnat: [0.1787 0.0051]
D0: [7.2085e+03 351.4857]

Table 3: *Parameters output by Stage2a_Fitparameters by model.*

Model	Params	LumiThermo MATLAB ID	ESRThermo MATLAB ID
Trapping model			
SSE	D_e, D_0, $(n/N)_{nat}$	De, D0, nNnat	SARADeGy, D0, SARAnNnat
GOK	D_e, D_0, a, $(n/N)_{nat}$	De, D0, nNnat, GOK_a	SARADeGy, D0, SARAnNnat, GOKgrowthorder
LIN	D_e	-	SARADeGy
Thermal detrapping model			
GOK	E_t, s, b	Et, s10, GOK_b	Et_GOK, s10_GOK, GOKorder
BTS	E_t, E_u, s	Et,Eu, s10	-
GAUSS	$\mu(E_t)$, $\sigma(E_t)$, s	Et, sigmaEt, s10	Et_GAUSS, sigmaEt_GAUSS, s10_GAUSS
Athermal detrapping model			
Huntley (2006)	ρ', $(n/N)_{ss}$	rhop, nNss	-

5.4. Stage2b_PlotFit

This script calls *filename.mat,* created in *Stage1_ExcelToStruct* and updated in *Stage2a_Fitparameters*. *Stage2b_PlotFit* plots the raw data and the model fits to the data. In the LumiThermo library, the output of the Huntley (2006) model to test for luminescence signal saturation due to anomalous fading (Kars et al., 2008; Valla et al., 2016) is also plotted. The figures produced for the two example datasets are shown in Fig. 2 and are automatically saved as .eps files to the subfolder "Figures". Whilst it is not necessary to run *Stage2b_PlotFit* prior to running *Stage3a_Inversion* as no additional data fitting occurs in the script, it is good practice to make a visual inspection of the quality of data fitting before proceeding to the data inversion.

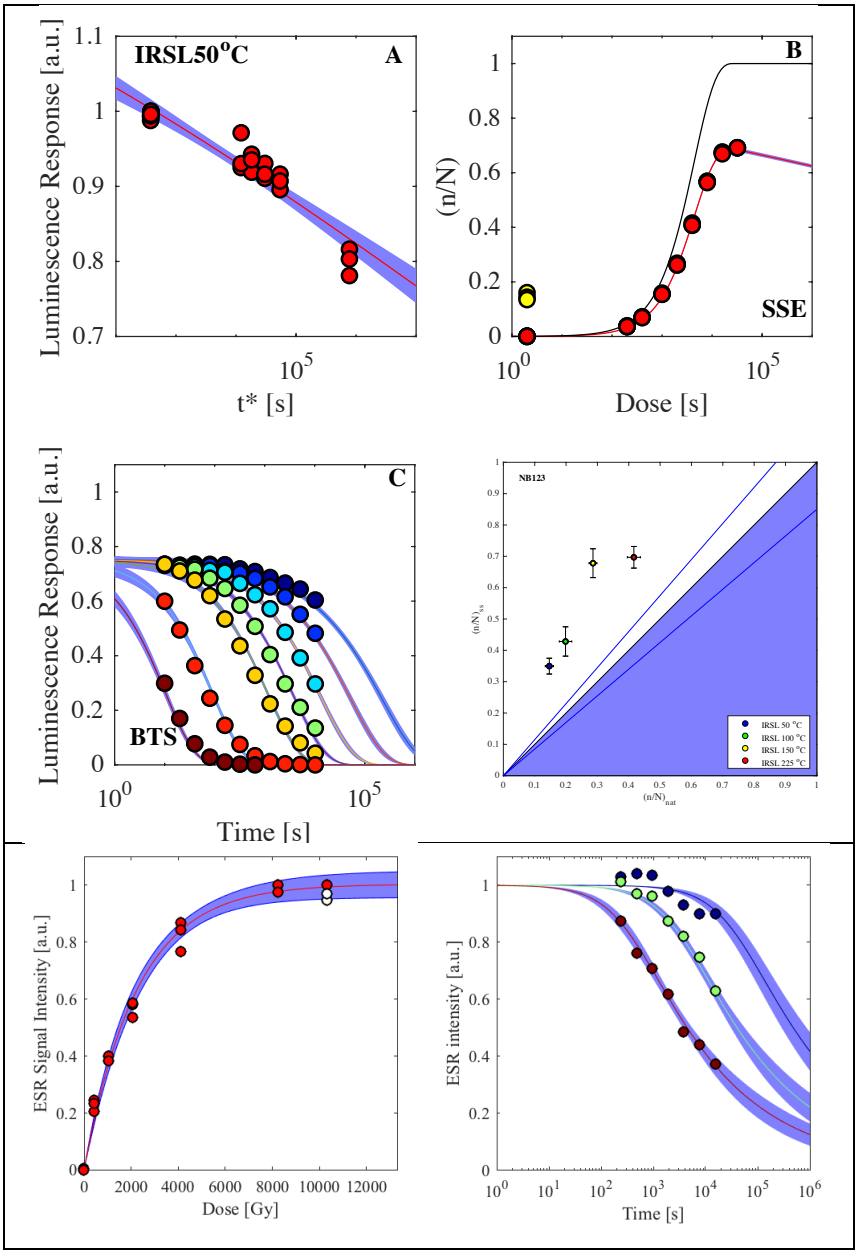

Fig. 2: *IRSL and ESR data fitting. (a) Athermal signal loss, (b) dose response, (c) isothermal decay and (d) comparison of luminescence $(n/N)_{nat}$ values with those calculated for athermal steady-state $(n/N)_{ss}$ for the $IRSL_{50}$ signal of the K-feldspar extract of sample NB123 (King et al., 2016a). (e) Dose response and (f) isothermal decay for the Ti-centre of sample TTY-A01 (Bartz et al., 2022).*

5.5. Stage3a_Inversion

This script allows the inversion of trapped-charge data, using the parameters calculated in *Stage2a_Fitparameters* assuming monotonic rock cooling. The model is setup to run for the time *tmax* - *tmin* (here1 Myr), assuming cooling from *Tmax* (here 200 °C) to *Tmin* (here 10

± 5 °C) using *niter* (here 2000) iterations. It is also setup to invert all of the data from a single Excel spreadsheet together, e.g., in the case of multi-luminescence thermochronometry data measured at different infrared stimulation temperatures. These conditions can be changed by editing the following lines of code.

```
ntmin=1;
nt = length(records);          % number of traps
ntmax=nt;
niter = 2000;                  % number of random realisations
Tmax = 200;                    % Maximum temperature in °C
tmax = 1;                      % Time in Ma
tmin = 0;                      % Time in Ma
Tmin = 10-(5*randn);           % Minimum temperature in °C, and its error
```

More iterations will require a longer computational time. The principles of the inversion are fully described in King et al. (2016a) and King et al. (2020) and are outlined briefly here. Random monotonic cooling histories are generated and for each history, the accumulation of trapped-charge is calculated using the model and sample specific kinetic parameters determined in *Stage2a_Fitparameters*. The quality of each model fit to the natural measured data are assessed by comparing the final modelled $\tilde{n}$ value, $\tilde{n}_{mod,f}$ (i.e. the value calculated after 1 Ma) to the natural measured value $\tilde{n}$ using a misfit function, M. This function has been updated since King et al. (2016a) following Wheelock et al. (2015) and as described by King et al. (2020) and Biswas et al. (2020), where:

$$M = \frac{1}{2} \cdot \frac{\tilde{n}}{\delta\tilde{n}} \cdot \left(\log \left(\frac{\tilde{n}}{\tilde{n}_{mod,f}} \right) \right)^2 \quad [15]$$

with $\delta\tilde{n}$ is uncertainty on $\tilde{n}$.

The results of the inversion (time-temperature paths, $\tilde{n}$ vectors and misfit values) are saved in a MATLAB structure called 'Tt' which is saved in the 'ComputeData' subfolder.

```
>>Tt
struct with fields:
        misfit: [1000×1 double]
        time: [1000×500 double]
        temp: [1000×500 double]
        nNmod: [1000×500 double]
        nNnat: 0.6203
        snNnat: 0.0620
```

In addition to investigating rock cooling, it is also possible to investigate isothermal histories or specific thermal histories by replacing the random cooling history generated using the randpathAD function with a specific temperature history.

```
% create a random path
tT = randpathAD([tmin Tmax],[tmax Tmin]);

% patch to keep model strictly monotonic
for ii=1:length(tT)-1
        if (tT(ii+1)==tT(ii) || tT(ii+1)<tT(ii))
                tT(ii+1)=tT(ii)+1e-7;
        end
end

% interpolates the random path on a regular grid
temp = interp1(tT(:,1),tT(:,2),time,'linear');
```

5.6. Stage3b_PlotTt

The final script, Stage3b_PlotTt uses the output from Stage3a_Inversion and computes a probability density function from the inversion results. The likelihood, L, of a particular cooling history is computed from the misfit scores,

$$L = \exp(-M) \quad [16]$$

and these values are passed through a rejection algorithm whereby values of L are contrasted with a random number between 0 and 1, and only values that are greater than the random number are retained. Those cooling histories that are retained are then used to compute a probability density function. The results of inverting the example datasets are shown in Fig. 3.

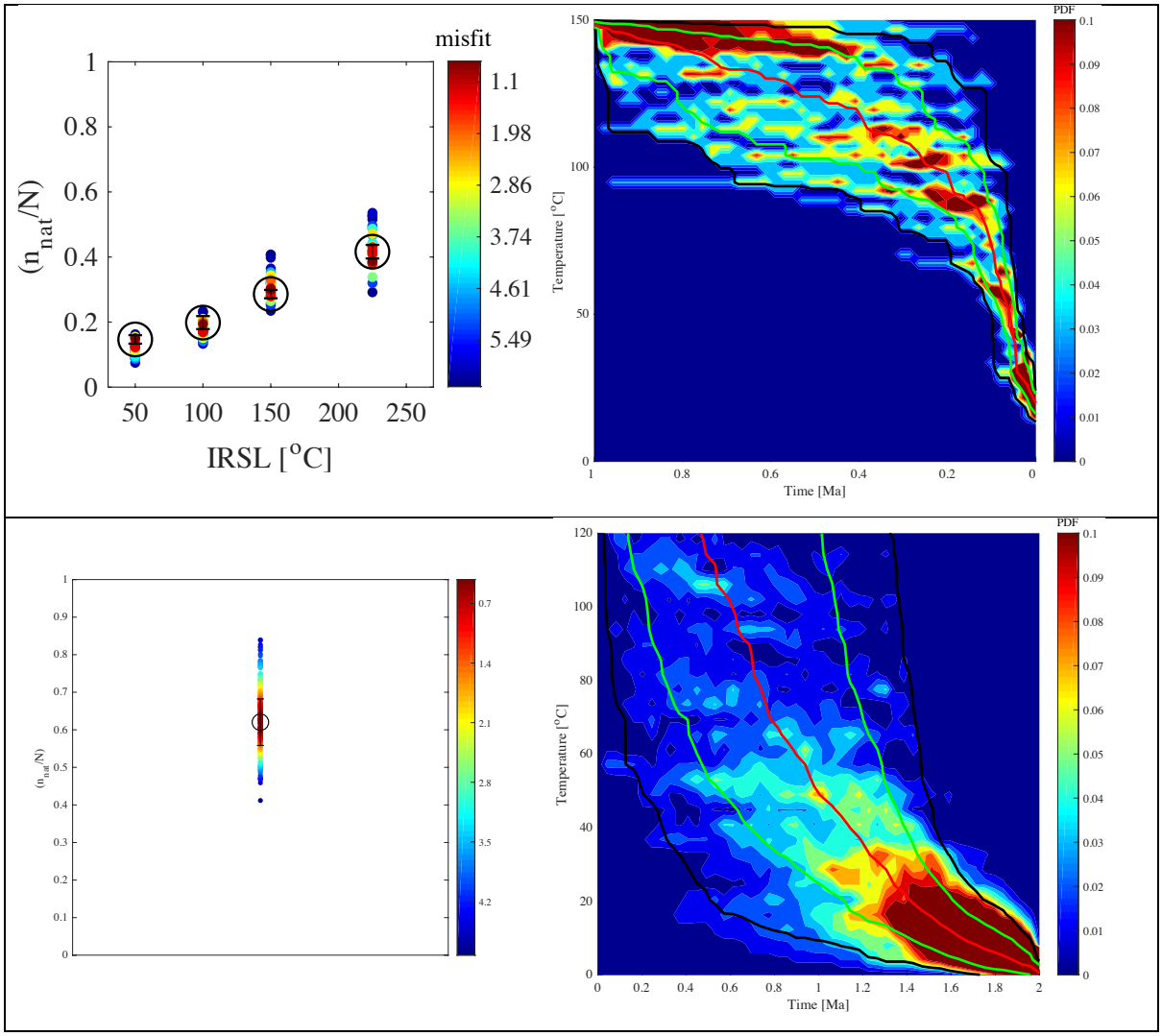

Fig. 3: *Inversion of luminescence (IRSL) and ESR data for cooling histories. (a) and (c) misfit between observed and accepted modelled n/N values and (b) and (e) resultant probability density functions for the luminescence (IRSL) signal of the K-feldspar extract of sample NB123 (King et al., 2016a) and the ESR signal of the Ti-centre of sample TTY-A01 (Bartz et al., 2022) respectively.*

6. Outlook

We hope that by sharing the codes that we have developed for the modelling of trapped-charge thermochronometry data, that we will motivate other members of our community to apply and develop the trapped-charge thermochronometry/thermometry technique. In addition to the three stages outlined in this manuscript, a range of other scripts are available from our GitHub page, which follow approximately the same structure. We will continue to update the LumiThermo and ESRThermo libraries as our research further refines the technique.

References

Adams, B., Dietsch, C., Owen, L.A., Caffee, M.W., Spotila, J., and Haneberg, W.C., 2009. *Exhumation and incision of the Lahul Himalaya, northern India, based on (U-Th)/He thermochronometry and terrestrial cosmogenic nuclide method*s. Geomorphology, 107, 285-299.
doi:10.1016/j.geomorph.2008.12.017

Ader, T., Avouac, J.P., Liu-Zeng, J., Lyon-Caen, H., Bollinger, L., Galetzka, J., Genrich, J., Thomas, M., Chanard, K., Sapkota, S.N., Rajaure, Su., Shrestha, P., Ding, L., and Flouzat, M., 2012. *Convergence rate across the Nepal Himalaya and interseismic coupling on the Main Himalayan Thrust: Implications for seismic hazard.* Journal of Geophysical Research: Solid Earth, 117(B4), B04403.
doi:10.1029/2011JB009071

Aitken, M.J., 1998. *Introduction to Optical Dating, The Dating of Quaternary Sediments by the Use of Photon-stimulated Luminescence*. Clarendon Press, Oxford University Press, Oxford Science Publications, 280 pp.
ISBN: 0-19-854092-2

Aitken, M.J., 1985. *Thermoluminescence dating*. Academic Press, Harcourt Brace Jovanovich Publishers, 351 pp.
ISBN 0-12-046381-4

Almeida, R.V., Hubbard, J., Liberty, L., Foster, A., and Sapkota, S.N., 2018. *Seismic imaging of the Main Frontal Thrust in Nepal reveals a shallow décollement and blind thrusting.* Earth and Planetary Science Letters, 494, 216-225.
doi:10.1016/j.epsl.2018.04.045

Arita, K., and Ganzawa, Y., 1997. *Thrust tectonics and uplift process of the Nepal Himalaya revealed from fission-track ages.* Journal of Geography (Chigaku Zasshi), 106(2), 156-167.
doi:10.5026/jgeography.10

Arita, K., Dallmeyer, R., and Takasu, A., 1997. *Tectonothermal evolution of the Lesser Himalaya, Nepal: Constraints from $^{40}Ar/^{39}Ar$ ages from the Kathmandu Nappe.* Island Arc, 6(4), 372-385.
doi:10.1111/j.1440-1738.1997.tb00047.x

Auclair, M., Lamothe, M., and Huot, S., 2003. *Measurement of anomalous fading for feldspar IRSL using SAR.* Radiation Measurements, 37, 487-492.
doi:10.1016/S1350-4487(03)00018-0

Ault, A.K., Gautheron, C., and King, G.E., 2019. *Innovations in (U–Th)/He, fission track, and trapped charge thermochronometry with applications to earthquakes, weathering, surface-mantle connections, and the growth and decay of mountains.* Tectonics, 38(11), 3705-3739.
doi:10.1029/2018TC005312

Avouac, J.P., 2003. *Mountain building, erosion, and the seismic cycle in the Nepal Himalaya.* Advances in Geophysics, 46, 1-80.
doi:10.1016/S0065-2687(03)46001-9

Avouac, J.P., Bollinger, L., Lavé, J., Cattin, R., and Flouzat, M., 2001. *Le cycle sismique en Himalaya.* Compte Rendus de l'Académie des Sciences, Paris, Series IIA-Earth and Planetary Science, 333(9), 513-529.
doi:10.1016/S1251-8050(01)01573-7

Balescu, S., and Lamothe, M., 1994. *Comparison of TL and IRSL age estimates of feldspar coarse grains from waterlain sediments.* Quaternary Science Reviews, 13(5-7), 437-444.
doi:10.1016/0277-3791(94)90056-6

Bartz, M., Peña, J., Grand, S., and King, G.E., 2022 (in review). *Potential impacts of chemical weathering on feldspar luminescence dating properties.* Geochronology Discussions, Preprint.
doi:10.5194/gchron-2022-3

Berger, A.L., Gulick, S.P., Spotila, J.A., Upton, P., Jaeger, J.M., Chapman, J.B., Worthington, L.A., Pavlis, T.L., Ridgway, K.D., Willems, B.A., and McAleer, R.J., 2008. *Quaternary tectonic response to intensified glacial erosion in an orogenic wedge.* Nature Geoscience, 1(11), 793-799.
doi:10.1038/ngeo334

Bernet, M., van der Beek, P., Pik, R., Huyghe, P., Mugnier, J.L., Labrin, E., and Szulc, A., 2006. *Miocene to Recent exhumation of the central Himalaya determined from combined detrital zircon fission-track and U/Pb analysis of Siwalik sediments, western Nepal.* Basin Research, 18, 393-412.
doi:10.1111/j.1365-2117.2006.00303.x

Berthet, T., Ritz, J.F., Ferry, M., Pelgay, P., Cattin, R., Drukpa, D., Braucher, R., and Hetényi, G., 2014. *Active tectonics of the eastern Himalaya: new constraints from the first tectonic geomorphology study in southern Bhutan.* Geology, 42(5), 427-430.
doi:10.1130/G35162.1

Bilham, R., Mencin, D., Bendick, R., and Bürgmann, R., 2017. *Implications for elastic energy storage in the Himalaya from the Gorkha 2015 earthquake and other incomplete ruptures of the Main Himalayan Thrust.* Quaternary International, 462, 3-21.
doi:10.1016/j.quaint.2016.09.055

Biswas, R.H., Herman, F., King, G.E., Lehmann, B., and Singhvi, A.K., 2020. *Surface paleothermometry using low-temperature thermoluminescence of feldspar.* Climate of the Past, 16(6), 2075-2093.
doi:10.5194/cp-16-2075-2020

Biswas, R.H., Herman, F., King, G.E., and Braun, J., 2018. *Thermoluminescence of feldspar as a multi-thermochronometer to constrain the temporal variation of rock exhumation in the recent past.* Earth and Planetary Science Letter, 495, 56-68.
doi:10.1016/j.epsl.2018.04.030

Blythe, A.E., Burbank, D.W., Carter, A., Schmidt, K.M., and Putkonen, J., 2007. *Plio-Quaternary exhumation history of the central Nepalese Himalaya: 1. Apatite and zircon fission track and apatite (U-Th)/He analyses.* Tectonics, 26, TC3002.
doi:10.1029/2006TC001990

Bollinger, L., Tapponnier, P., Sapkota, S.N., and Klinger, Y., 2016. Slip deficit in central Nepal: omen for a repeat of the 1344 AD earthquake? Earth, Planets and Space, 68(1), 1-12.
doi:10.1186/s40623-016-0389-1

Bollinger, L., Sapkota, S.N., Tapponnier, P., Klinger, Y., Rizza, M., van der Woerd, J., Tiwari, D.R., Pandey, R., Bitri, A., and Bes de Berc, S., 2014. *Estimating the return times of great Himalayan earthquakes in eastern Nepal: Evidence from the Patu and Bardibas strands of the Main Frontal Thrust.* Journal of Geophysical Research: Solid Earth, 119(9), 7123-7163.
doi:10.1002/2014JB010970

Bollinger, L., Henry, P., and Avouac, J.P., 2006. *Mountain building in the Nepal Himalaya: Thermal and kinematic model.* Earth and Planetary Science Letter, 244, 8-71.
doi:10.1016/j.epsl.2006.01.045

Bollinger, L., Avouac, J.P., Beyssac, O., Catlos, E.J., Harrison, T.M., Grove, M., Goffe, B., and Sapkota, S., 2004. *Thermal structure and exhumation history of the Lesser Himalaya in central Nepal.* Tectonics, 23, TC5015.
doi:10.1029/2003TC001564

Bookhagen, B., and Burbank, D.W., 2010. *Toward a complete Himalayan hydrological budget: Spatiotemporal distribution of snowmelt and rainfall and their impact on river discharge.* Journal of Geophysical Research: Earth Surface, 115(F3). doi:10.1029/2009JF001426

Bouscary, C., King, G.E., Grujic, D., Lavé, J., Almeida, R., Hetényi, G., and Herman F. (In review, 2022). *Sustained deformation across the Sub-Himalayas since 200 ka.* Geology.

Bouscary, C., and King, G.E., 2022. *Luminescence thermochronometry of feldspar minerals: Optimisation of measurement conditions for the derivation of thermal kinetic parameters using isothermal holding experiments.* Quaternary Geochronology, 67, 101240, 1-14. doi:10.1016/j.quageo.2021.101240

Braun, J., 2003. *Pecube: A new finite element code to solve the heat transport equation in three dimensions in the earth's crust including the effects of a time-varying, finite amplitude surface topography.* Computers & Geosciences, 29(6), 787-794. doi:10.1016/S0098-3004(03)00052-9

Braun, J., 2002. *Estimating exhumation rate and relief evolution by spectral analysis of age-elevation datasets.* Terra Nova, 14(3), 210-214. doi:10.1046/j.1365-3121.2002.00409.x

Braun, J., Zwartz, D., and Tomkin, J.H., 1999. *A new surface-processes model combining glacial and fluvial erosion.* Annals of Glaciology, 28, 282-290. doi:10.3189/172756499781821797

Braun, J., and Sambridge, M., 1997. *Modelling landscape evolution on geological time scales: A new method based on irregular spatial discretization.* Basin Research, 9(1), 27-52. doi:10.1046/j.1365-2117.1997.00030.x

Brennan, B.J., Lyons, R.G., and Phillips, S.W., 1991. Attenuation of alpha particle track dose for spherical grains. International Journal of Radiation Applications and Instrumentation, Part D, Nuclear Tracks and Radiation Measurements, 18(1-2), 249-253. doi:10.1016/1359-0189(91)90119-3

Brocklehurst, S.H., and Whipple, K.X., 2002. Glacial erosion and relief production in the Eastern Sierra Nevada, California. Geomorphology, 42(1-2), 1-24. doi:10.1016/S0169-555X(01)00069-1

Brown, N.D., Rhodes, E.J., and Harrison, T.M., 2017. Using thermoluminescence signals from feldspars for low-temperature thermochronology. Quaternary Geochronology, 42(6967), 31-41. doi:10.1016/j.quageo.2017.07.006

Burbank, D.W., Blythe, A.E., Putkonen, J., Pratt-Sitaula, B., Gabet, E., Oskin, M., Barros, A., and Ojha, T., 2003. Decoupling of erosion and precipitation in the Himalayas. Nature, 426, 652-655.
doi:10.1038/nature02187

Burg, J.P. and Chen, G.M., 1984. *Tectonics and structural zonation of southern Tibet, China.* Nature, 311(5983), 219-223.
doi:10.1038/311219a0

Burgess, W. P., Yin, A., Dubey, C. S., Shen, Z.K., and Kelty, T. K., 2012. *Holocene shortening across the Main Frontal Thrust zone in the eastern Himalaya.* Earth and Planetary Science Letters, 357, 152-167.
doi:10.1016/j.epsl.2012.09.040d

Buscombe, D., 2013. *Transferable wavelet method for grain-size distribution from images of sediment surfaces and thin sections, and other natural granular patterns.* Sedimentology, 60, 1709-1732.
doi:10.1111/sed.12049

Carretier, S., Poisson, B., Vassallo, R., Pepin, E., and Farias, M., 2009. *Tectonic interpretation of transient stage erosion rates at different spatial scales in an uplifting block.* Journal of Geophysical Research: Earth Surface, 114, F02003.
doi:10.1029/2008JF001080

Cassadanne, J.P., and Roditi, M., 1996. *The location, geology and mineralogy of gem tourmalines in Brazil.* Journal of Gemmology, 25(4), 263-298.
doi:10.15506/jog.1996.25.4.263

Catlos, E.J., Harrison, T.M., Kohn, M., Grove, M., Ryerson, M., Manning, C.E., and Upreti, B.N., 2001. *Geochronologic and thermobarometric constraints on the evolution of the Main Central Thrust, central Nepal Himalaya.* Journal of Geophysical Research: Solid Earth, 106(B8), 16177–16204.
doi:10.1029/2000JB900375

Catlos, E.J., 2000. *Geochronologic and thermobarometric constraints on the evolution of the main central thrust, Himalayan orogen*. PhD. thesis, University of California, Los Angeles, USA.

Cattin, R., and Avouac, J.P., 2000. *Modeling mountain building and the seismic cycle in the Himalaya of Nepal.* Journal of Geophysical Research: Solid Earth, 105(B6), 13389-13407.
doi:10.1029/2000JB900032

Cermak, V., Kukkonen, I.T., and Safanda, J., 1993. *Temperature logs in deep wells – a useful tool for past climatic reconstruction.* Terra Nova, 5(2), 134-143.
doi:10.1111/j.1365-3121.1993.tb00238.x

Champagnac, J.D., Molnar, P., Sue, C., and Herman, F., 2012. *Tectonics, climate, and mountain topography.* Journal of Geophysical Research: Solid Earth, 117(B2).
doi:10.1029/2011JB008348, 2012

Champel, B., van der Beek, P., Mugnier, J.L, and Leturmy, P., 2002. *Growth and lateral propagation of fault-related folds in the Siwaliks of western Nepal: Rates, mechanisms, and geomorphic signature.* Journal of Geophysical Research: Solid Earth, 107(B6).
doi:10.1029/2001JB000578

Chirouze, F., Huyghe, P., van der Beek, P., Chauvel, C., Chakraborty, T., Dupont-Nivet, G., and Bernet, M., 2013. *Tectonics, exhumation, and drainage evolution of the eastern Himalaya since 13 Ma from detrital geochemistry and thermochronology, Kameng River Section, Arunachal Pradesh.* GSA Bulletin, 125(3-4), 523-538.
doi:10.1130/B30697.1

Chirouze, F., Dupont-Nivet, G., Huyghe, P., van der Beek, P., Chakraborti, T., Bernet, M., and Erens, V., 2012. *Magnetostratigraphy of the Neogene Siwalik Group in the far eastern Himalaya: Kameng section, Arunachal Pradesh, India.* Journal of Asian Earth Sciences, 44, 117-135.
doi:10.1016/j.jseaes.2011.05.016

Clauser, C., Giese, P., Huenges, E., Kohl, T., Lehmann, H., Ryback, L., Safanda, J., Wilhelm, H., Windloff, K., and Zoth, G., 1997. *The thermal regime of the crystalline continental crust: implications from the KTB.* Journal of Geophysical Research: Solid Earth, 102(B8), 18417-18441.
doi:10.1029/96JB03443

Coleman, M.E., and Hodges, K.V.,1998. *Contrasting Oligocene and Miocene thermal histories from the hanging wall and footwall of the south Tibetan detachment in the central Himalaya from $^{40}Ar/^{39}Ar$ thermochronology, Marsyandi Valley, central Nepal.* Tectonics, 17, 726-740.
doi:10.1029/98TC02777

Copeland, P., Harrison, T.M., Hodges, K.V., Maruejol, P., Lefort, P., and Pêcher, A., 1991. *An early Pliocene thermal disturbance of the Main Central Thrust, central Nepal: Implications for Himalayan tectonics.* Journal of Geophysical Research: Solid Earth, 96(B5), 8475-8500.
doi:10.1029/91JB00178

Coutand, I., Barrier, L., Govin, G., Grujic, D., Hoorn, C., Dupont-Nivet, G., and Najman, Y., 2016. *Late Miocene-Pleistocene evolution of India-Eurasia convergence partitioning between the Bhutan Himalaya and the Shillong Plateau: New evidences from foreland basin deposits along the Dungsam Chu section, eastern Bhutan.* Tectonics, 35(12), 2963-2994.
doi:10.1002/2016TC004258

Coyle, D.A., Wagner, G.A., Hejl, E., Brown, R., and van den Haute, P., 1997. *The Cretaceous and younger thermal history of the KTB site (Germany): apatite fission-track data from the Vorbohrung.* Geologische Rundschau, 86(1), 203-209.
doi:10.1007/s005310050132

Dal Zilio, L., van Dinther, Y., Gerya, T.V., and Pranger, C.C., 2018. *Seismic behaviour of mountain belts controlled by plate convergence rate.* Earth and Planetary Science Letters, 482, 81-92.
doi:10.1016/j.epsl.2017.10.053

Dal Zilio, L., van Dinther, Y., Gerya, T.V., and Avouac, J.P., 2019. *Bimodal seismicity in the Himalaya controlled by fault friction and geometry.* Nature Communications, 10(1).
doi:10.1038/s41467-018-07874-8

Dal Zilio, L., Joliver, R., and van Dinther, Y., 2019. *Segmentation of the Main Himalayan Thrust illuminated by Bayesian inference and interseismic coupling.* Geophysical Research Letters, 47(4).
doi:10.1029/2019GL086424

de Sigoyer, J., Chavagnac, V., Blichert-Toft, J., Villa, I.M., Luais, B., Guillot, S., Cosca, M. and Mascle, G., 2000. *Dating the Indian continental subduction and collisional thickening in the northwest Himalaya: Multichronology of the Tso Morari eclogites.* Geology, 28(6), 487-490.
doi:10.1130/0091-7613(2000)28<487:DTICSA>2.0.CO;2

DeCelles, P.G., Robinson, D.M., Quade, J., Ojha, T., Garzione, C., Copeland, P., and Upreti, B.N., 2001. *Stratigraphy, structure, and tectonic evolution of the Himalayan fold-thrust belt in western Nepal.* Tectonics, 20, 487-509.
doi:10.1029/2000TC001226

Delcaillau, B., Carozza, J.M., and Laville, E., 2006. *Recent fold growth and drainage development: the Janauri and Chandigarh anticlines in the Siwalik foothills, northwest India.* Geomorphology, 76(3-4), 241-256.
doi:10.1016/j.geomorph.2005.11.005

Dey, S., Thiede, R.C., Schildgen, T.F., Wittmann, H., Bookhagen, B., Scherler, D., and Strecker, M.R., 2016. *Holocene internal shortening within the northwest Sub-Himalaya: Out-of-sequence faulting of the Jwalamukhi Thrust, India.* Tectonics, 35(11), 2677-2697. doi:10.1002/2015TC004002

Ding, L., Kapp, P., and Wan, X., 2005. *Paleocene–Eocene record of ophiolite obduction and initial India-Asia collision, south central Tibet.* Tectonics, 24(3), TC3001. doi:10.1029/2004TC001729

Dhital, M.R., 2015. *Geology of the Nepal Himalaya: regional perspective of the classic collided orogen.* Springer, Regional Geology Reviews, 498 pp. ISBN 9783319352053

Drukpa, D., Gautier, S., Cattin, R., Namgay, K., and Le Moigne, N., 2018. *Impact of near-surface fault geometry on secular slip rate assessment derived from uplifted river terraces: Implications for convergence accommodation across the frontal thrust in southern Central Bhutan.* Geophysical Journal International, 212(2), 1315-1330. doi:10.1093/gji/ggx478.

Duller, G.A.T., 2008. *Luminescence Dating: Guidelines on using luminescence dating in archaeology.* Swindon: English Heritage.

Durcan, J.A., King, G.E., and Duller, G.A.T., 2015. *DRAC: dose rate and age calculator for trapped charge dating.* Quaternary Geochronology, 28, 54-61. doi:10.1016/j.quageo.2015.03.012

Edwards, M., Kidd, W.S.F., Li, J., Yue, Y., and Clark, M., 1996. *Multistage development of the southern Tibet detachment system near Khula Kangri. New data from Gonto La.* Tectonophysics, 260(1-3), 1-19. doi:10.1016/0040-1951(96)00073-X

England, P. and Molnar, P., 1990. *Surface uplift, uplift of rocks, and exhumation of rocks.* Geology, 18(12), 1173-1177. doi:10.1130/0091-7613(1990)018<1173:SUUORA>2.3.CO;2

Fang, F., and Grün, R., 2020. *ESR thermochronometry of Al and Ti centres in quartz: A case study of the Fergusons Hill-1 borehole from the Otway Basin, Australia.* Radiation Measurements, 139, 106447. doi:10.1016/j.radmeas.2020.106447

Finnegan, N.J., Schumer, R., and Finnegan, S., 2014. *A signature of transience in bedrock river incision rates over timescales of 10^4–10^7 years.* Nature, 505(7483), 391-394. doi:10.1038/nature12913

Finnegan, N., Hallet, B., Montgomery, D., Zeiter, P., Stone, J., Anders, A., and Yuping, L., 2008. *Coupling of rock uplift and river incision in the Namche Bara-Gyala Peri massif, Tibet.* GSA Bulletin 120(1-2), 142-155.
doi:10.1130/B26224.1

Fitzgerald, P.G., and Gleadow, A.J.W., 1988. *Fission-track geochronology, tectonics and structure of the Transantarctic Mountains in northern Victoria Land, Antarctica.* Chemical Geology: Isotope Geoscience section, 73(2), 169-198.
doi:10.1016/0168-9622(88)90014-0

Fox, M., Herman, F., Kissling, E., and Willet, S.D., 2015. *Rapid exhumation in the Western Alps driven by slab detachment and glacial erosion.* Geology, 43(5), 379-382.
doi:10.1130/G36411.1

Fox, M., Herman, F., Willett, S.D., and May, D.A., 2014. *A linear inversion method to infer exhumation rates in space and time from thermochronometric data.* Earth Surface Dynamics, 2(1), 47-65.
doi:10.5194/esurf-2-47-2014

Gallagher, K., 2012. *Transdimensional inverse thermal history modeling for quantitative thermochronology.* Journal of Geophysical Research: Solid Earth, 117, B2408.
doi:10.1029/2011JB008825

Garcia-Guinea, J., Townsend, P.D., Sanchez-Muños, L., and Rojo, J.M., 1999. *Ultraviolet-blue ionic luminescence of alkali feldspars from bulk and interfaces.* Physics and Chemistry of Minerals, 26(8), 658-667.
doi:10.1007/s002690050231

Gautam, P., and Apple, E., 1997. *Magnetic-polarity stratigraphy of Siwalik Group sediments of Tinau Khola section in west central Nepal, revisited.* Geophysical Journal International, 117(1), 223-234.
doi:10.1111/j.1365-246X.1994.tb03314.x

Gibson, R., Godin, L., Kellett, D.A., Cottle, J.M., and Archibald, D., 2016. *Diachronous deformation along the base of the Himalayan metamorphic core, west-central Nepal.* GSA Bulletin, 128(5-6), 860-878.
doi:10.1130/B31328.1

Godard, V., Tucker, G.E., Burch Fisher, G., Burbank, D.W., and Bookhagen, B., 2013. *Frequency-dependent landscape response to climatic forcing.* Geophysical Research Letters, 40(5), 859-863.
doi:10.1002/grl.50253

Godard, V., and Burbank, D.W., 2011. Mechanical analysis of controls on strain partitioning in the Himalayas of central Nepal. Journal of Geophysical Research, 116, B10402. doi:10.1029/2011JB008272

Govindaraju, K., 1995. *Update (1984-1995) on two GIT-IWG geochemical reference samples: albite from Italy, Al-I and iron formation sample from Greenland, IF-G.* Geostandards Newsletter, 19(1), 55-96. doi:10.1111/j.1751-908X.1995.tb00152.x

Grün, R., Tani, A., Gurbanov, A., Koshchug, D., Williams, I., and Braun, J., 1999. *A new method for the estimation of cooling and denudation rates using paramagnetic centers in quartz: A case study on the Eldzhurtinskiy Granite, Caucasus.* Journal of Geophysical Research: Solid Earth, 104(B8), 17531-17549. doi:10.1029/1999JB900173

Guérin, G., Mercier, N., Nathan, R., Adamiec, G., and Lefrais, Y., 2012. *On the use of the infinite matrix assumption and associated concepts: a critical review.* Radiation Measurements, 47(9), 778-785. doi:10.1016/j.radmeas.2012.04.004

Guérin, G., Mercier, N., and Adamiec, G., 2011. *Dose-rate conversion factors: update.* Ancient TL, 29(1), 5-8.

Guillot, S., Garzanti, E., Baratoux, D., Marquer, D., Mahéo, G., and de Sigoyer, J., 2003. *Reconstructing the total shortening history of the NW Himalaya.* Geochemistry, Geophysics, Geosystems, 4(7). doi:10.1029/2002GC000484

Guralnik, B., and Sohbati, R., 2019. *Fundamentals of luminescence photo-and thermochronometry.* Advances in Physics and Applications of Optically and Thermally Stimulated Luminescence, Chapter 11, 399-437. doi:10.1142/9781786345790_0011

Guralnik, B., Li, B., Jain, M., Chen, R., Paris, R.B., Murray, A.S., Li, S.H., Pagonis, V., Valla, P.G., and Herman, F., 2015.a. *Radiation-induced growth and isothermal decay of infrared-stimulated luminescence from feldspar.* Radiation Measurements, 81, 224-231. doi:10.1016/j.radmeas.2015.02.011

Guralnik, B., Jain, M., Herman, F., Ankjærgaard, C., Murray, A.S., Valla, P.G., Preusser, F., King, G.E., Chen, R., Lowick, S.E., Kook, M., and Rhodes, E.J., 2015.b. *OSL-thermochronology of feldspar from the KTB borehole, Germany.* Earth and Planetary Science Letters, 423, 232-243. doi:10.1016/j.epsl.2015.04.032

Guralnik, B., Jain, M., Herman, F., Paris, R.B., Harrison, T.M., Murray, A.S., Valla, P.G., and Rhodes, E.J., 2013. *Effective closure temperature in leaky and/or saturating thermochronometers.* Earth and Planetary Science Letters, 384, 209-218. doi:10.1016/j.epsl.2013.10.003

Hallet, B., Hunter, L., and Bogen, J., 1996. *Rates of erosion and sediment evacuation by glaciers: A review of field data and their implications.* Global and Planetary Change, 12(1-4), 213-235. doi:10.1016/0921-8181(95)00021-6

Harrison, T.M., Grove, M., Lovera, O.M., and Catlos, E.J., 1998. *A model for the origin of Himalayan anatexis and inverted metamorphism.* Journal of Geophysical Research: Solid Earth, 103(B11), 27017-27032. doi:10.1029/98JB02468

Heim, A., and Gansser, A., 1939. *Central Himalaya.* Hindustan Publishing, Delhi.

Herman, F., and King, G.E., 2018. *Luminescence thermochronometry: investigating the link between mountain erosion, tectonics and climate.* Elements: An International Magazine of Mineralogy, Geochemistry, and Petrology, 14(1), 33-38. doi:10.2138/gselements.14.1.33

Herman, F., Seward, D., Valla, P.G., Carter, A., Kohn, B., Willett, S.D., and Ehlers, T.A., 2013. *Worldwide acceleration of mountain erosion under a cooling climate.* Nature, 504(7480), 423-426. doi:10.1038/nature12877

Herman, F., Copeland, P., Avouac, J.-P., Bollinger, L., Mahéo, G., Le Fort, P., Rai, S., Foster, D., Pêcher, A., Stüwe, K., and Henry, P., 2010. *Exhumation, crustal deformation, and thermal structure of the Nepal Himalaya derived from the inversion of thermochronological and thermobarometric data and modeling of the topography.* Journal of Geophysical Research: Solid Earth, 115, B06407. doi:10.1029/2008JB006126

Herman, F., Rhodes, E.J., Braun, J., and Heiniger, L., 2010. *Uniform erosion rates and relief amplitude during glacial cycles in the Southern Alps of New Zealand, as revealed from OSL-thermochronology.* Earth and Planetary Science Letters, 297(1-2), 183-189. doi:10.1016/j.epsl.2010.06.019

Herman, F., Braun, J., and Dunlap, W., 2007. *Tectonomorphic scenarios in the Southern alps of New Zealand.* Journal of Geophysical Research: Solid Earth, 112, B04201. doi:10.1029/2004JB003472

Hirschmiller, J., Grujic, D., Bookhagen, B., Coutand, I., Huyghe, P., Mugnier, J.L., and Ojha, T., 2014. *What controls the growth of the Himalayan foreland fold-and-thrust belt?* Geology, 42(3), 247-250.
doi:10.1130/G35057.1

Hodges, K.V., Wobus, C., Ruhl, K., Schildgen, T., and Whipple, K.X., 2004. *Quaternary deformation, river steepening, and heavy precipitation at the front of the Higher Himalayan ranges.* Earth and Planetary Science Letters, 220(3-4), 379-389.
doi:10.1016/S0012-821X(04)00063-9

Hodges, K.V., Hurtado, J.M., and Whipple, K.X., 2001. *Southward extrusion of Tibetan crust and its effect on Himalayan tectonics.* Tectonics, 20(6), 799-809.
doi:10.1029/2001TC001281

Hodges, K.V., 2000. *Tectonics of the Himalaya and southern Tibet from two perspectives.* GSA Bulletin, 112(3), 324-350.
doi:10.1130/0016-7606(2000)112<324:TOTHAS>2.0.CO;2

Hossler, T., Bollinger, L., Sapkota, S.N., Lavé, J., Gupta, R. M., and Kandel, T.P., 2016. *Surface ruptures of large Himalayan earthquakes in Western Nepal: Evidence along a reactivated strand of the Main Boundary Thrust.* Earth and Planetary Science Letters, 434, 187-196.
doi:10.1016/j.epsl.2015.11.042

Houtermans, F., Jager, E., Schon, M., and Staufer, H., 1957. *Measurements of the thermoluminescence as a means to investigate the thermal and radiation history of the natural minerals and rocks.* Annals of Physics, 20, 283.

Hovius, N., Meunier, P., Lin, C.W., Chen, H., Chen, Y.G., Dadson, S., Horng, M.J., and Lines M., 2011. *Prolonged seismically induced erosion and the mass balance of a large earthquake.* Earth and Planetary Science Letters, 304(3-4), 347-355.
doi:10.1016/j.epsl.2011.02.005

Huerta, A.D., Royden, L.H., and Hodges, K.V., 1999. *The effects of accretion, erosion and radiogenic heat on the metamorphic evolution of collisional orogens.* Journal of Metamorphic Geology, 17, 349-366.
doi:10.1046/j.1525-1314.1999.00204.x

Huerta, A.D., Royden, L.H., and Hodges, K.V., 1996. *The interdependence of deformational and thermal processes in mountain belts.* Science, 273(5275), 637-639.
doi:10.1126/science.273.5275.637

Huntington, K.W., and Hodges, K.V., 2006. *A comparative study of detrital mineral and bedrock age-elevation methods for estimating erosion rates.* Journal of Geophysical Research: Earth Surface, 111, F03011.
doi:10.1029/2005JF000454

Huntley, D.J., 2006. *An explanation of the power-law decay of luminescence.* Journal of Physics: Condensed Matter, 18(4), 1359-1365.
doi:10.1088/0953-8984/18/4/020

Huntley, D.J., Lamothe, M., 2001. *Ubiquity of anomalous fading in K-feldspars and the measurement and correction for it in optical dating.* Canadian Journal of Earth Sciences, 38(7), 1093-1106.
doi:10.1139/e01-013

Huntley, D.J., Godfrey-Smith, D.I., and Thewalt, M.L., 1985. *Optical dating of sediments.* Nature, 313(5998), 105-107.
doi:10.1038/313105a0

International Atomic Energy Agency, 1999 International Atomic Energy Agency, Analytical Quality Control Services, Seibersdorf (Austria), 1999. *IAEA AQCS Catalogue for Reference Materials and Intercomparison Exercises 1998/1999 (INISxa–131).* International Atomic Energy Agency (IAEA).

Kars, R.H., Wallinga, J., and Cohen, K.M., 2008. *A new approach towards anomalous fading correction for feldspar IRSL dating — tests on samples in field saturation.* Radiation Measurements, 43(2-6), 786-790.
doi:10.1016/j.radmeas.2008.01.021

King, G.E., Tsukamoto, S., Herman, F., Biswas, R.H., Sueoka, S., and Tagami, T., 2020. *Electron spin resonance (ESR) thermochronometry of the Hida range of the Japanese Alps: validation and future potential.* Geochronology, 2(1), 1-15.
doi:10.5194/gchron-2-1-2020

King, G.E., Herman, F., Lambert, R., Valla, P.G., and Guralnik, B., 2016.a. *Multi-OSL thermochronometry of feldspar.* Quaternary Geochronology, 33, 76-87.
doi:10.1016/j.quageo.2016.01.004

King, G.E., Herman, F., and Guralnik, B., 2016.b. *Northward migration of the eastern Himalayan syntaxis revealed by OSL thermochronometry.* Science, 353(6301), 800-804.
doi:10.1126/science.aaf2637

King, G.E., Guralnik, B., Valla, P.G., and Herman, F., 2016.c. *Trapped-charge thermochronometry and thermometry: A status review.* Chemical Geology, 446, 3-17. doi:10.1016/j.chemgeo.2016.08.023

Kook, M.H., Lapp, T., Murray, A.S., and Thiel, C., 2012. *A Risø XRF Attachment for Major Element Analysis of Aliquots of Quartz and Feldspar Separates.* UK Luminescence and ESR Meeting, Aberystwyth, p.37. September 2012 (abstract).

Kumar, S., Wesnousky, S.G., Rockwell, T.K., Briggs, R.W., Thakur, V.C., and Jayangondaperumal, R., 2006. *Paleoseismic evidence of great surface rupture earthquakes along the Indian Himalaya.* Journal of Geophysical Research: Solid Earth, 111(B3). doi:10.1029/2004JB003309

Lambert R., 2018. *Investigating thermal decay in K-feldspar for the application of IRSL thermochronometry on the Mont Blanc massif.* PhD. thesis, University of Lausanne, Faculty of Geoscience and Environment, Lausanne, Switzerland.

Lavé, J., Yule, D., Sapkota, S., Basant, K., Madden, C., Attal, M., and Pandey, R., 2005. *Evidence for a great medieval earthquake (~ 1100 A.D.) in the Central Himalayas, Nepal.* Science, 307(5713), 1302-1305. doi:10.1126/science.1104804

Lavé, J., and Avouac, J.P., 2001. *Fluvial incision and tectonic uplift across the Himalayas of central Nepal.* Journal of Geophysical Research: Solid Earth, 106(B11), 26561-26591. doi:0148-0227/01/2001JB000359509

Lavé, J., and Avouac, J.P., 2000. *Active folding of fluvial terraces across the Siwaliks Hills, Himalayas of central Nepal.* Journal of Geophysical Research, 105(B3), 5735-5770. doi:0148-0227/00/1999JB900292

Law, R.D., Stahr, D.W., Francsis, M.K., Ashley, K.T., Grasemann, B., and Ahmad, T., 2013. *Deformation temperatures and flow vorticities near the base of the Greater Himalayan Series, Sutlej Valley and Shimla Klippe, NW India.* Journal of Structural Geology, 54, 21-53. doi:10.1016/j.jsg.2013.05.009

Le Roux-Mallouf, R., 2016. *Déformation Holocène de l'Himalaya du Bhoutan. Apport de la géomorphologie et de la paléosismologie.* PhD. thesis, Université de Montpellier, Montpellier, France.

Lénard, S.J.P., Lavé, J., France-Lanord, C., Aumaître, G., Bourlès, D.L., and Keddadouche, K., 2020. *Steady erosion rates in the Himalayas through late Cenozoic climatic changes.* Nature Geoscience, 13(6), 448-452.
doi:10.1038/s41561-020-0585-2

Lénard, S.J.P., 2019. *The evolution of the Himalaya since the Late Miocene, as told by the history of its erosion.* PhD. thesis, CRPG – Centre de Recherches Pétrographiques et Géochimiques, Université de Lorraine, Nancy, France.

Li, S., Wang, Q., Chen, G., He, P., Ding, K., Chen, Y., and Zou, R., 2019. *Interseismic Coupling in the Central Nepalese Himalaya: Spatial Correlation with the 2015 Mw 7.9 Gorkha Earthquake.* Pure and Applied Geophysics, 176(9), 3893-3911.
doi:10.1007/s00024-019-02121-7

Li, B., and Li, S.H., 2013. *The effect of band-tail states on the thermal stability of the infrared stimulated luminescence from K-feldspar.* Journal of Luminescence, 136, 5-10.
doi:10.1016/j.jlumin.2012.08.043

Li, B., Li, S.H., 2012. *Determining the cooling age using luminescence-thermochronology.* Tectonophysics, 580, 242-248.
doi:10.1016/j.tecto.2012.09.023

Li, B., Li, S.H., 2011. *Luminescence dating of K-feldspar from sediments: a protocol without anomalous fading correction.* Quaternary Geochronology, 6(5), 468-479.
doi:10.1016/j.quageo.2011.05.001

Li, B., Li, S.H., 2008. *Investigations of the dose-dependent anomalous fading rate of feldspar from sediments.* Journal of Physics D: Applied Physics, 41(22), 225502.
doi:10.1088/0022-3727/41/22/225502

Li, S.H., and Tso, M.Y.W., 1997. *Lifetime determination of OSL signals from potassium feldspar.* Radiation Measurements, 27(2), 119-121.
doi:10.1016/S1350-4487(96)00145-X

Long, S.P., Gordon, S.M., Young, J.P., and Soignard, E., 2016. *Temperature and strain gradients through Lesser Himalayan rocks and across the Main Central thrust, south central Bhutan: Implications for transport-parallel stretching and inverted metamorphism.* Tectonics, 35(8), 1863-1891.
doi:10.1002/2016TC004242

Lyon-Caen, H., and Molnar, P., 1985. *Gravity anomalies, flexure of the Indian plate, and the structure, support and evolution of the Himalaya and Ganga Basin.* Tectonics, 4(6), 513-538.
doi:10.1029/TC004i006p00513

Macfarlane A., 1993. *Chronology of tectonic events in the crystalline core of the Himalaya, Langtang National Park, central Nepal.* Tectonics, 12(4), 1004-1025.
doi:10.1029/93TC00916

Macfarlane, A., Hodges, K. V., and Lux, D., 1992. *A structural analysis of the Main Central Thrust zone, Langtang National Park, central Nepal Himalaya.* GSA Bulletin, 104(11) 1389-1402.
doi:10.1130/0016-7606(1992)104<1389:ASAOTM>2.3.CO;2

Malavieille, J., Marcoux, J., and de Wever, P., 2002. *L'océan perdu.* Himalaya-Tibet, Le choc des continents, Musée National d'Histoire Naturelle: CNRS éditions, Paris, 32-39.

Mandal, S.K., Scherler, D., and Wittmann, H., 2021. *Tectonic accretion controls erosional cyclicity in the Himalaya.* AGU Advances, 2(3), e2021AV000487.
doi:10.1029/2021AV000487

Marechal, A., Mazzotti, S., Cattin, R., Cazes, G., Vernant, P., Drukpa, D., Thinley, K., Tarayoun, A., Le Roux-Mallouf, R., Thapa, B.B., and Pelgay, P., 2016. *Evidence of interseismic coupling variations along the Bhutan Himalayan arc from new GPS data.* Geophysical Research Letters, 43(24), 12-399.
doi:10.1002/2016GL071163

Martin, A.J., 2017. *A review of definitions of the Himalayan Main Central Thrust.* International Journal of Earth Sciences, 106(6), 2131-2145.
doi:10.1007/s00531-016-1419-8

Mathew, G., De Sarkar, S., Pande, K., Dutta, S., Ali, S., Rai, A., and Netrawali, S., 2013. *Thermal metamorphism of the Arunachal Himalaya, India: Raman thermometry and thermochronological constraints on the tectono-thermal evolution.* International Journal of Earth Sciences, 102(7), 1911-1936.
doi:10.1007/s00531-013-0904-6

Metcalfe, I., 1996. *Gondwanaland dispersion, Asian accretion and evolution of eastern Tethys.* Australian Journal of Earth Sciences, 43(6), 605-623.
doi:10.1080/08120099608728282

Molnar, P., and England, P., 1990. *Late Cenozoic uplift of mountain ranges and global climate change: chicken or egg?* Nature, 346(6279), 29-34.
doi:10.1038/346029a0

Molnar, P., and Stock, J.M., 2009. *Slowing of India's convergence with Eurasia since 20 Ma and its implications for Tibetan mantle dynamics.* Tectonics, 28(3), TC3001.
doi:10.1029/2008TC002271.

Molnar, P., Boos, W.R., and Battisti, D.S., 2010. *Orographic controls on climate and paleoclimate of Asia: Thermal and mechanical roles for the Tibetan Plateau.* Annual Review of Earth and Planetary Sciences, 38(1), 77-102.
doi:10.1146/annurev-earth-040809-152456

Montgomery, D.R., and Stolar, D.B., 2006. *Reconsidering Himalayan river anticlines.* Geomorphology, 82(1-2), 4-15.
doi:10.1016/j.geomorph.2005.08.021

Mugnier, J.L., Huyghe, P., Leturmy, P., and Jouanne, F., 2004. *Episodicity and rates of thrust-sheet motion in the Himalayas (Western Nepal).* In K.R. McClay, ed., Thrust tectonics and hydrocarbon systems: AAPG Memoir, 82, 91-114.
doi:10.1306/M82813C6.

Mugnier, J.L., Leturmy, P., Mascle, G., Huyghe, P., Chalaron, E., Vidal, G., Husson, L., and Delcaillau, B., 1999. *The Siwaliks of western Nepal: I. Geometry and kinematics.* Journal of Asian Earth Sciences, 17(5-6), 629-642.
doi:10.1016/S1367-9120(99)00038-3

Mugnier, J.L., Chalaron, E., Mascle, G., Pradier, B., and Herail, G., 1995. *Structural and thermal evolution of the Siwaliks of western Nepal.* Journal of Nepal Geological Society, 11, 171-178.
doi:10.3126/jngs.v11i0.32791

Mukherjee, S., 2015. A review on out-of-sequence deformation in the Himalaya. Geological Society, London, Special Publications, 412(1), 67-109.
doi:10.1144/SP412.13

Murray, A.S., Wintle, A.G., 1999. *Isothermal decay of optically stimulated luminescence in quartz.* Radiation Measurements, 30(1), 119-125.
doi:10.1016/S1350-4487(98)00097-3

O'Brien, P.J., 2001. *Subduction followed by collision: Alpine and Himalayan examples.* Physics of the Earth and Planetary Interiors, 127(1-4), 277-291.
doi:10.1016/S0031-9201(01)00232-1

Ogata, M., King, G.E., Herman, F., and Sueoka, S., 2022. *Reconstructing the thermal structure of shallow crust in the Tono region using multi-OSL-thermometry of K-feldspar from deep borehole core.* Earth and Planetary Science Letters, 591, 117607. doi:10.1016/j.epsl.2022.117607

Pandey, M.R., Tandukar, R.P., Avouac, J.P., Lavé, J., and Massot, J.P., 1995. *Interseismic strain accumulation on the Himalayan crustal ramp (Nepal).* Geophysical Research Letters, 22(7), 751-754. doi:10.1029/94GL02971.

Parker, R.N., Densmore, A.L., Rosser, N.J., De Michele, M., Li, Y., Huang, R., Whadcoat, S., and Petley, D.N., 2011. *Mass wasting triggered by the 2008 Wenchuan earthquake is greater than orogenic growth.* Nature Geoscience, 4(7), 449-452. doi:10.1038/NGEO1154

Pollack, H.N., and Huang, S., 2000. Climate reconstruction from subsurface temperatures. Annual Review of Earth and Planetary Science, 28, 339-365. doi:10.1146/annurev.earth.28.1.339

Poolton, N.R.J., Kars, R.H., Wallinga, J., and Bos, A.J.J., 2009. *Direct evidence for the participation of band-tails and excited-state tunnelling in the luminescence of irradiated feldspars.* Journal of Physics: Condensed Matter, 21(48), 485505. doi:10.1088/0953-8984/21/48/485505

Poolton, N.R.J., Wallinga, J., Murray, A.S., Bulur, E.N.V.E.R., and Bøtter-Jensen, L., 2002.a. *Electrons in feldspar I: on the wavefunction of electrons trapped at simple lattice defects.* Physics and Chemistry of Minerals, 29(3), 210-216. doi:10.1007/s00269-001-0217-3

Poolton, N.R.J., Ozanyan, K.B., Wallinga, J., Murray, A.S., and Bøtter-Jensen, L., 2002.b. *Electrons in feldspar II: a consideration of the influence of conduction band-tail states on luminescence processes.* Physics and Chemistry of Minerals, 29(3), 217-225. doi:10.1007/s00269-001-0218-2

Powers, P.M., Lillie, R.J., and Yeats, R.S., 1998. *Structure and shortening of the Kangra and Dehra Dun reentrants, sub-Himalaya, India.* GSA Bulletin, 110(8), 1010-1027. doi:10.1130/0016-7606(1998)110<1010:SASOTK>2.3.CO;2

Preusser, F., Chithambo, M.L., Götte, T., Martini, M., Ramseyer, K., Sendezera, E.J., Susino, G.J., and Wintle, A.G., 2009. *Quartz as a natural luminescence dosimeter.* Earth-Science Reviews, 97(1-4), 184-214. doi:10.1016/j.earscirev.2009.09.006

Prokein, J., and Wagner, G.A., 1994. *Analysis of thermoluminescent glow peaks in quartz derived from the KTB-drill hole.* Radiation Measurements, 23(1), 85-94. doi:10.1016/1350-4487(94)90026-4

Rai, S.M., Guillot, S., Le Fort, P., and Upreti, B.N., 1998. *Pressure-temperature evolution in the Kathmandu and Gosainkund regions, central Nepal.* Journal of Asian Earth Sciences, 16(2-3), 283-298. doi:10.1016/S0743-9547(98)00019-1

Reiners, P.W., and Brandon, M.T., 2006. *Using thermochronology to understand orogenic erosion.* Annual Review of Earth and Planetary Sciences, 34(1), 419-466. doi:10.1146/annurev.earth.34.031405.125202

Reiners, P.W., Ehlers, T.A., Mitchell, S.G., and Montgomery, D.R., 2003. *Coupled spatial variations in precipitation and long-term erosion rates across the Washington Cascades.* Nature, 426(6967), 645-647. doi:10.1038/nature02111

Rendell, H.M., and Clarke, M.L., 1997. *Thermoluminescence, radioluminescence and cathodoluminescence spectra of alkali feldspars.* Radiation Measurements, 27, 263-272. doi:10.1016/S1350-4487(96)00128-X

Rhodes, E.J., 2011. *Optically stimulated luminescence dating of sediments over the past 200,000 years.* Annual Review of Earth and Planetary Sciences, 39(1), 461-488. doi:10.1146/annurev-earth-040610-133425

Riedesel, S., Bell, A.M.T., Duller, G.A.T., Finch, A.A., Jain, M., King, G.E., Pearce, N.J., and Roberts, H.M., 2021. *Exploring sources of variation in thermoluminescence emissions and anomalous fading in alkali feldspars.* Radiation Measurements, 141, 106541. doi:10.1016/j.radmeas.2021.106541

Riedesel, S., King, G.E., Prasad, A.K., Kumar, R., Finch, A.A., and Jain, M., 2019. *Optical determination of the width of the band-tail states, and the excited and ground state energies of the principal dosimetric trap in feldspar.* Radiation Measurements, 125, 40-51. doi:10.1016/j.radmeas.2018.08.019

Riedesel, S., Brill, D., Roberts, H.M., Duller, G.A.T., Garrett, E., Zander, A.M., King, G.E., Tamura, T., Burow, C., Cunningham, A., Seeliger, M., De Batist, M., Heyvaert, V.M.A., Fujiwara, O., Brückner, H., and the QuakeRecNankai Team, 2018. *Single-grain luminescence chronology of historical extreme-wave event deposits recorded in a coastal lowland, Pacific coast of central Japan.* Quaternary Geochronology, 45, 37-49. doi:10.1016/j.quageo.2018.01.006

Ring, U., Brandon, M.T., Willett, S.D., and Lister, G.S., 1999. *Exhumation processes.* Geological Society, London, Special Publications, 154(1), 1-27.
doi:10.1144/GSL.SP.1999.154.01.0

Robert, X., van der Beek, P., Braun, J., Perry, C., Dubille, M., and Mugnier, J.L., 2009. *Assessing Quaternary reactivation of the Main Central thrust zone (central Nepal Himalaya): New thermochronologic data and numerical modeling.* Geology, 37, 731-734.
doi:10.1130/ G25736A.1

Robinson, D.M., DeCelles, P.G., Garzione, C.N., Pearson, O.N., Harrison, T.M., and Catlos, E.J., 2003. *Kinematic model for the Main Central Thrust in Nepal.* Geology, 31, 359-362.
doi:10.1130/0091-7613(2003)031<0359:KMFTMC>2.0.CO;2

Robinson, D.M., DeCelles, P.G., and Copeland, P., 2006. *Tectonic evolution of the Himalayan thrust belt in western Nepal: Implications for channel flow models.* GSA Bulletin, 118(7-8), 865-885.
doi:10.1130/B25911.1

Rowley, D.B., 1996. *Age of initiation of collision between India and Asia: A review of stratigraphic data.* Earth and Planetary Science Letters, 145(1-4), 1-13.
doi:10.1016/S0012-821X(96)00201-4

Sapkota, S.N., Bollinger, L., Klinger, Y., Tapponnier, P., Gaudemer, Y., and Tiwari, D., 2013. *Primary surface ruptures of the great Himalayan earthquakes in 1934 and 1255.* Nature Geoscience, 6(1), 71-76.
doi:10.1038/NGEO1669

Schelling, D., and Arita, K., 1991. *Thrust tectonics, crustal shortening, and the structure of the far eastern Nepal Himalaya.* Tectonics, 10(5), 851–862.
doi:10.1029/91TC01011

Schelling, D., 1992. *The tectonostratigraphy and structure of the eastern Nepal Himalaya.* Tectonics, 11(5), 925-943.
doi:10.1029/92TC00213

Searle, M.P., Law, R.D., Godin, L., Larson, K.P., Streule, M.J., Cottle, J.M., and Jessup, M.J., 2008. *Defining the Himalayan main central thrust in Nepal.* Journal of the Geological Society, 165(2), 523-534.
doi:10.1144/0016-76492007-081

Searle, M., Avouac, J.P., Elliott, J., and Dyck, B., 2017. *Ductile shearing to brittle thrusting along the Nepal Himalaya: Linking Miocene channel flow and critical wedge tectonics to 25th April 2015 Gorkha earthquake.* Tectonophysics, 714, 117-124.
doi:10.1016/j.tecto.2016.08.003

Sohbati, R., Murray, A.S., Chapot, M.S., Jain, M., and Pederson, J., 2012. *Optically stimulated luminescence (OSL) as a chronometer for surface exposure dating.* Journal of Geophysical Research: Solid Earth, 117, B09202.
doi:10.1029/2012JB009383

Sreejith, K.M., Sunil, P.S., Agrawal, R., Saji, A.P., Rajawat, A.S., and Ramesh, D.S., 2018. *Audit of stored strain energy and extent of future earthquake rupture in central Himalaya.* Scientific reports, 8(1), 1-9.
doi:10.1038/s41598-018-35025-y

Srivastava, P., and Mitra, G., 1994. *Thrust geometries and deep structure of the outer and lesser Himalaya, Kumaon and Garhwal (India): Implications for evolution of the Himalayan fold-and-thrust belt.* Tectonics, 13(1), 89-109.
doi:10.1029/93TC01130

Stevens V.L., Shrestha S.N., and Maharjan D.K., 2018. *Probabilistic Seismic Hazard Assessment of Nepal.* Bulletin of the Seismological Society of America, 108(6), 3488-3510.
doi:10.1785/0120180022

Stevens, V.L., and Avouac, J.P., 2015. *Interseismic coupling on the main Himalayan thrust.* Geophysical Research Letters, 42(14), 5828-5837.
doi:10.1002/2015GL064845.

Stüwe, K., and Barr, T.D., 1998. *On uplift and exhumation during convergence.* Tectonics, 17(1), 80-88.
doi:10.1029/97TC02557

Szulc, A.G., Najman, Y., Sinclair, H.D., Pringle, M., Bicke, M., Chapman, H., Garzanti, E., Andò, S., Huyghe, P., Mugnier, J.L., Ojha, T., and DeCelles, P., 2006. *Tectonic evolution of the Himalaya constrained by detrital ^{40}Ar-^{39}Ar, Sm-Nd and petrographic data from the Siwaliks foreland basin succession, SW Nepal.* Basin Research, 18(4), 375-391.
doi:10.1111/j.1365-2117.2006.00307.x

Tachiya, M., and Mozumder, A., 1974. *Decay of trapped electrons by tunnelling to scavenger molecules in low-temperature glasses.* Chemical Physics Letters, 28(1), 87-89.
doi:10.1016/0009-2614(74)80022-9

Tarantola, A., 2005. *Inverse problem theory and methods for model parameter estimation.* Society for Industrial and Applied Mathematics, 342 pp.
ISBN:978-0-89871-572-9

Thiede, R., Robert, X., Stübner, K., Dey, S., and Faruhn, J., 2017. *Sustained out-of-sequence shortening along a tectonically active segment of the Main Boundary thrust: The Dhauladhar Range in the northwestern Himalaya.* Lithosphere, 9(5), 715-725.
doi:10.1130/L630.1

Tokuoka, T., Takeda, S., Yoshida, M., and Upreti, B.N., 1988. *The Churia (Siwalik) Group in the Western Part of the Arung Khola Area, West Central Nepal.* Memoir of the Faculty of Science, Shimane University, 22, 131-140.

Toyoda, S., and Ikeya, M., 1991. *Thermal stabilities of paramagnetic defect and impurity centers in quartz: Basis for ESR dating of thermal history.* Geochemical Journal, 25(6), 437-445.
doi:10.2343/GEOCHEMJ.25.437

Tso, M.Y.W., Wong, N.W.L., and Li, S.H., 1996. *Determination of lifetime of infrared stimulated signals from potassium and sodium feldspars.* Radiation protection dosimetry, 66(1-4), 387-389.
doi:10.1093/oxfordjournals.rpd.a031760

Tsukamoto, S., Toyoda, S., Tani, A., and Oppermann, F., 2015. *Single aliquot regenerative dose method for ESR dating using X-ray irradiation and preheat*. Radiation Measurements, 81, 9-15.
doi:10.1016/j.radmeas.2015.01.018

Valla, P.G., Lowick, S.E., Herman, F., Champagnac, J.D., Steer, P., and Guralnik, B., 2016. *Exploring $IRSL_{50}$ fading variability in bedrock feldspars and implications for OSL thermochronometry*. Quaternary Geochronology, 36, 55-66.
doi:10.1016/j.quageo.2016.08.004

van der Beek, P., Robert, X., Mugnier, J.L., Bernet, M., Huyghe, P., and Labrin, E., 2006. *Late Miocene - Recent exhumation of the central Himalaya and recycling in the foreland basin assessed by apatite fission-track thermochronology of Siwalik sediments, Nepal.* Basin Research, 18 (4), 413-434.
doi:10.1111/j.1365-2117.2006.00305.x

van Dinther, Y., Gerya, T.V., Dalguer, L.A., Mai, P.M., Morra, G., and Giardini, D., 2013. *The seismic cycle at subduction thrusts: Insight from seismo-thermo-mechanical models.* Journal of Geophysical Research: Solid Earth, 118(12), 6183-6202.
doi:10.1002/2013JB010380

Vannay, J.C., Grasemann, B., Rahn, M., Frank, W., Carter, A., Baudraz, V., and Cosca, M., 2004. *Miocene to Holocene exhumation of metamorphic crustal wedges in the NW Himalaya: Evidence for tectonic extrusion coupled to fluvial erosion.* Tectonics, 23(1). doi:10.1029/2002TC001429

Vernant, P., Bilham, R., Szeliga, W., Drukpa, D., Kalita, S., Bhattacharyya, A.K., Gaur, V.K., Pelgay, P., Cattin, R., and Berthet, T., 2014. *Clockwise rotation of the Brahmaputra Valley relative to India: Tectonic convergence in the eastern Himalaya, Naga Hills, and Shillong Plateau.* Journal of Geophysical Research: Solid Earth, 119(8), 6558-6571. doi:10.1002/2014JB011196

Visocekas, R., Spooner, N.A., Zink, A., and Blanc, P., 1994. *Tunnel afterglow, fading and infrared emission in thermoluminescence of feldspars.* Radiation Measurements, 23(2-3), 377-385. doi:10.1016/1350-4487(94)90067-1

Wagner, G.A., Coyle, D.A., Duyster, J., Henjes-Kunst, F., Peterek, A., Schröder, B., Stöckhert, B., Wemmer, K., Zulauf, G., Ahrendt, H., Bischoff, R., Hejl, E., Jacobs, J., Menzel, D., Lal, N., van den Haute, P., Vercoutere, C., and Welzel, B., 1997. *Post-Variscan thermal and tectonic evolution of the KTB site and its surroundings.* Journal of Geophysical Research, Solid Earth, 102(B8), 18221-18232. doi:10.1029/96JB02565

Wagner, G.A., and Reimer, G.M., 1972. *Fission track tectonics: the tectonic interpretation of fission track apatite ages.* Earth and Planetary Science Letters, 14(2), 263-268. doi:10.1016/0012-821X(72)90018-0

Wallinga, J., Murray, A.S., Wintle, A.G., and Bøtter-Jensen, L., 2002. *Electron-trapping probability in natural dosemeters as a function of irradiation temperature.* Radiation Protection Dosimetry, 101(1-4), 339-344. doi:10.1093/oxfordjournals.rpd.a005997

Warnock, A.C., and Zeitler, P.K., 1998. *$^{40}Ar/^{39}Ar$ thermochronometry of K-feldspar from the KTB borehole, Germany.* Earth and Planetary Science Letters, 158(1-2), 67-79. doi:10.1016/S0012-821X(98)00044-2

Webb, A.A.G., 2013. *Preliminary balanced palinspastic reconstruction of Cenozoic deformation across the Himachal Himalaya (northwestern India).* Geosphere, 9(3), 572-587. doi:10.1130/GES00787.1

Webb, A.A.G., Yin, A., and Dubey, C.S., 2013. *U-Pb zircon geochronology of major lithologic units in the eastern Himalaya: Implications for the origin and assembly of Himalayan rocks.* GSA Bulletin, 125(3-4), 499-522.
doi:10.1130/B30626.1

Wesnousky, S.G., Kumar, S., Mohindra, R., and Thakur, V.C., 1999. *Uplift and convergence along the Himalayan Frontal Thrust of India.* Tectonics, 18(6), 967-976.
doi:10.1029/1999TC900026

Wheelock, B., Constable, S., and Key, K., 2015. *The advantages of logarithmically scaled data for electromagnetic inversion.* Geophysical Journal International, 201(3), 1765-1780.
doi:10.1093/gji/ggv107

Whipp, D.M., Ehlers, T.A., Blythe, A., Huntington, K., Hodges, K., and Burbank, D.W., 2007. *Plio-Quaternary exhumation history of the central Nepalese Himalaya: 2. Thermokinematic and thermochronometer age prediction model.* Tectonics, 26, TC3003.
doi:10.1029/2006TC001991

Whipple, K.X., Shirzaei, M., Hodges, K.V., and Arrowsmith, J.R., 2016. *Active shortening within the Himalayan orogenic wedge implied by the 2015 Gorkha earthquake.* Nature Geoscience, 9(9), 711-718.
doi:10.1038/NGEO2797

Whipple, K.X., 2009. *The influence of climate on the tectonic evolution of mountain belts.* Nature Geoscience, 2(2), 97-104.
doi:10.1038/ngeo413

Willett, S.D., 1999. *Orogeny and orography: The effects of erosion on the structure of mountain belts.* Journal of Geophysical Research: Solid Earth, 104(B12), 28957-28981.
doi:10.1029/1999JB900248

Willett, S.D., and Brandon, M.T., 2002. *On steady states in mountain belts*. Geology, 30(2), 175-178.
doi:10.1130/0091-7613(2002)030<0175:OSSIMB>2.0.CO;2

Wintle, A.G., 1977. *Detailed study of a thermoluminescent mineral exhibiting anomalous fading.* Journal of Luminescence, 15(4), 385-393.
doi:10.1016/0022-2313(77)90037-0

Wintle, A.G., 1973. *Anomalous fading of thermo-luminescence in mineral samples.* Nature, 245(5421), 143-144.
doi:10.1038/245143a0

Wobus, C.W., Whipple, K.X., and Hodges, K.V., 2006. *Neotectonics of the central Nepalese Himalaya: Constraints from geomorphology, detrital $^{40}Ar/^{39}Ar$ thermochronology and thermal modeling.* Tectonics, 25, TC4011.
doi:10.1029/2005TC001935

Wobus, C.W., Heimsath, A.M., Whipple, K.X., and Hodges, K.V., 2005. *Active out-of-sequence thrust faulting in the central Nepalese Himalaya.* Nature, 434(7036), 1008-1011.
doi:10.1038/nature03499

Wobus, C.W., Hodges, K.V., and Whipple, K.X., 2003. *Has focused denudation sustained active thrusting at the Himalayan topographic front?* Geology, 31(10), 861-864.
doi:10.1130/G19730.1

Wu, T.S., Jain, M., Guralnik, B., Murray, A.S., and Chen, Y.G., 2015. *Luminescence characteristics of quartz from Hsuehshan Range (Central Taiwan) and implications for thermochronometry.* Radiation Measurements, 81, 104-109.
doi:10.1016/j.radmeas.2015.03.002

Yeats, R.S., and Thakur, V.C., 2008. *Active faulting south of the Himalayan Front: Establishing a new plate boundary.* Tectonophysics, 453(1-4), 63-73.
doi:10.1016/j.tecto.2007.06.017

Yin, A., Dubey, C.S., Kelty, T.K., Webb, A.A.G., Harrison, T.M., Chou, C.Y., and Célérier, J., 2010. *Geologic correlation of the Himalayan orogen and Indian craton: Part 2. Structural geology, geochronology, and tectonic evolution of the Eastern Himalaya.* GSA Bulletin, 122(3-4), 360-395.
doi:10.1130/B26461.1

Yin, A., 2006. *Cenozoic tectonic evolution of the Himalayan orogen as constrained by along-strike variation of structural geometry, exhumation history, and foreland sedimentation.* Earth-Science Reviews, 76(1-2), 1-131.
doi:10.1016/j.earscirev.2005.05.004

Yin, A., and Harrison, T.M., 2000. *Geologic evolution of the Himalayan-Tibetan orogen.* Annual Review of Earth and Planetary Sciences, 28(1), 211-280.
doi:10.1146/annurev.earth.28.1.211

Yin, A., 2000. *Mode of Cenozoic east-west extension in Tibet suggesting a common origin of rifts in Asia during the Indo-Asian collision.* Journal of Geophysical Research: Solid Earth, 105(B9), 21745-21759.
doi:10.1029/2000JB900168